UNIVERSITÀ DEGLI STUDI DI PADOVA
Dipartimento di Scienze Chimiche

Scuola di dottorato in Scienza ed Ingegneria dei Materiali
XXVIII CICLO

TESI DI DOTTORATO

Study and control of drop motion on inclined surfaces

Direttore della scuola: Prof. Gaetano Granozzi
Supervisore: Prof. Giampaolo Mistura
Co-supervisore: Dott. Matteo Pierno

Dottoranda: Silvia Varagnolo

Contents

List of Figures

List of Tables

Riassunto

Questa tesi raccoglie una serie di lavori sperimentali che si collocano nell'ambito della microfluidica aperta e dei fenomeni interfacciali di bagnamento e fondamentalmente studiano il comportamento di gocce depositate su superfici. Lo scopo principale di questo tipo di ricerca è lo sviluppo di superfici che presentino proprietà particolari, come ad esempio superfici autopulenti, antinebbia o antiriflesso, o di tecniche di manipolazione di gocce finalizzate ad applicazioni nel campo biologico o chimico.
In particolare questo lavoro considera metodi attivi e passivi atti a controllare sia la statica che la dinamica di gocce poste su superfici inclinate e quindi soggette ad una forza esterna costante, la forza di gravità. Tra le tecniche passive basate sull'utilizzo di superfici strutturate sono state studiate le proprietà di adesione di superfici polimeriche geometricamente nano/microstrutturate. Inoltre, campioni chimicamente eterogenei formati da regioni idrofiliche e idrofobiche di geometria diversa (strisce, quadrati, triangoli) si sono dimostrati uno strumento efficace per la regolazione passiva della velocità di scivolamento delle gocce. Questo tipo di superfici può influire non solo sulla velocità, ma anche sulla traiettoria della goccia. Per analizzare più nel dettaglio come si può deviare una goccia è stato studiato lo scivolamento su una superficie formata da due sole regioni di diversa bagnabilità, cioè una sorta di gradino chimico. D'altra parte, un controllo attivo implica l'applicazione di un campo esterno, ad esempio elettrico, magnetico o acustico. Come tecnica attiva in questa tesi è stata considerata l'applicazione di vibrazioni asimmetriche del substrato, capaci di indurre comportamenti dinamici interessanti e sorprendenti: piccole goccioline poste su un piano inclinato che oscilla verticalmente possono non solo rimanere ferme o scivolare, ma addirittura risalire contro la forza di gravità.
Anche se la maggioranza di questi esperimenti riguarda liquidi ordinari, in particolare acqua e soluzioni acquose, una parte della ricerca è stata dedicata allo scivolamento di fluidi complessi, più precisamente soluzioni polimeriche, caratterizzati da proprietà reologiche (ad esempio viscosità o effetti elastici) che dipendono dallo sforzo applicato sul fluido.

Parole chiave: Microfluidica, microfluidica aperta, gocce, microfabbricazione, PDMS, soft-litografia, fotolitografia, bagnabilità, adesione, linea di contatto, scivolamento.

Abstract

This PhD thesis collects different experimental studies in the field of wetting phenomena and open microfluidics, which analyze the behavior of liquid drops on free open surfaces. The main goal of such a research is to develop smart coatings featuring useful wetting properties (e. g. water repellent, antifogging and antireflection materials) or techniques aimed at manipulating droplets for chemical or biological applications.

In particular this work considers both passive and active methods to control the statics and dynamics of drops deposited on an inclined plane and consequently subject to an external constant force, the gravity force. Among the passive techniques based on surface patterning, we investigated the adhesion properties of multiscale nano- and microstructured hairy surfaces made of polymers having different elasticity. Also, chemically patterned surfaces, formed by hydrophilic and hydrophobic regions of different shape (stripes, squares and triangles), have found to be an effective tool to passively tune drop sliding velocity. Chemically heterogeneous surfaces can affect not only sliding velocity, but also drop trajectory. To further investigate the deviation of a drop by means of a chemical pattern we considered a sample formed by only two regions featuring different wettability, i. e. a chemical step characterized by a linear interface. On the other hand, an active manipulation implies the application of an external field, as, for instance, electric, magnetic or acoustic. As active technique we considered asymmetric vibrations of the substrate, able to induce interesting and surprising dynamical behaviors: small droplets placed on a vertically oscillating inclined plane can stay pinned, slide down, but even climb up the surface against gravity.

Even if the vast majority of our experiments involves ordinary liquids, in particular water and aqueous solutions, our research about sliding includes also the study of complex fluids, more precisely polymer solutions, exhibiting rheological properties (e. g. viscosity and elastic behaviors) depending on the applied stress.

Keywords: Microfluidics, open microfluidics, droplets, microfabrication, PDMS, soft-lithography, photo-lithography, wetting, pinning, contact line, sliding.

Introduction

The study of the behavior of drops on open surfaces is fundamental for the production of surfaces featuring useful wetting properties and droplet manipulation in microfluidic platforms aimed at biological or chemical applications.

Special wettability properties. The realization of ”smart” coatings can arise from the observation of nature, where many examples of interesting properties have been developed by plants and animals to meet the enviromental conditions [1].
The first and very famous example is the self-cleaning effect of the lotus leaf (see figure 1a), which needs to be always clean in order to capture the sun light: water drops are very mobile and roll on this surface removing all the dust. Such a behavior, also known as superhydrophobicity, is due to the roughness (see figure 1b) and hydrophobicity of the leaf surface, as discovered by the botanist Barthlott who first observed a lotus leaf under a scanning electron microscope [2]. Since this analysis, many studies have been performed to produce self-cleaning water repellent surfaces with different textures and materials to cover a wide range of applications, e. g. textile, building and car industry [3–19].

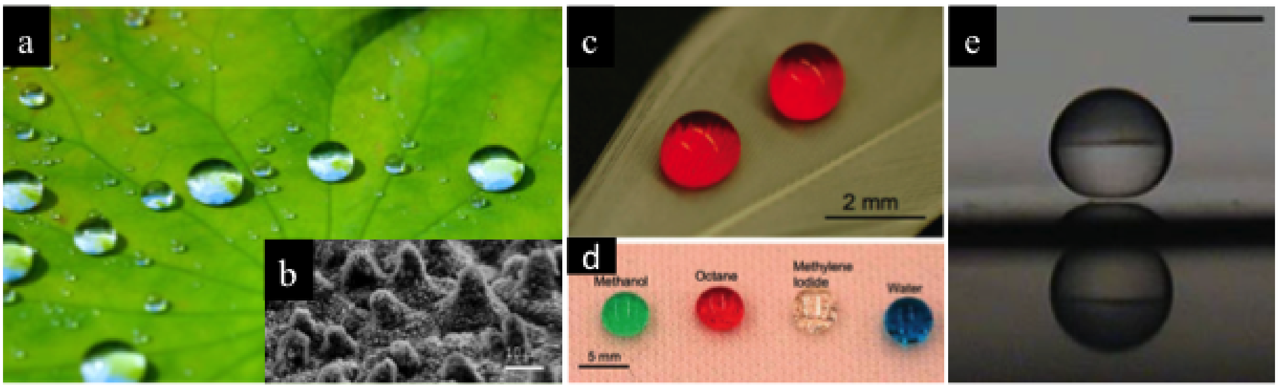

Figure 1 : Examples of superlyophobic behaviors: a) water repellent lotus leaf and b) corresponding surface morphology [18]; c) and d) superoleophobic surfaces [20, 21] and e) levitating droplet in Leidenfrost regime (scale bar corresponds to 1 mm) [22, 23].

In addition, superoleophobic surfaces (see figures 1c and 1d) are even more difficult to achieve because oil intrinsically tends to spread and wet very well many kind of materials, indeed it is used as lubricant. Surface structures with particular shapes are necessary to repel oil [20, 21, 24–36].
Another case where drops are very mobile is the so-called Leidenfrost effect occurring on very hot surfaces: a cushion of vapour appears between the substrate and the drop which actually levitates without touching the surfaces, as shown in figure 1e, and this is the cause of its huge motility [23, 37–40].

An interesting even if opposite behavior is the petal effect, characterized by a strong adhesion with water droplets, in spite of a high static hydrophobicity, that is droplets do not spread on the surface but assume an almost spherical shape, as shown in figure 2. The high adhesion between petals and water is common to many flowers which, indeed, require to be wet to avoid drying [41]. Furthermore, pronounced stickiness is also typical of the gecko's feet allowing to climb up vertical walls (see figure 2) [42]. In this case the observation under the microscope shows the presence of hierarchical microstructures covered by nanohairs [41, 43, 44]. Again, mimicking nature, several works realized patterned surfaces reproducing the petal effect [9, 45–48]. High adhesive but hydrophobic surfaces can be exploited, for instance, to stop drops moving on a sample or to transfer drops from a sticky surface to a different substrate with minimal volume losses [49–51].

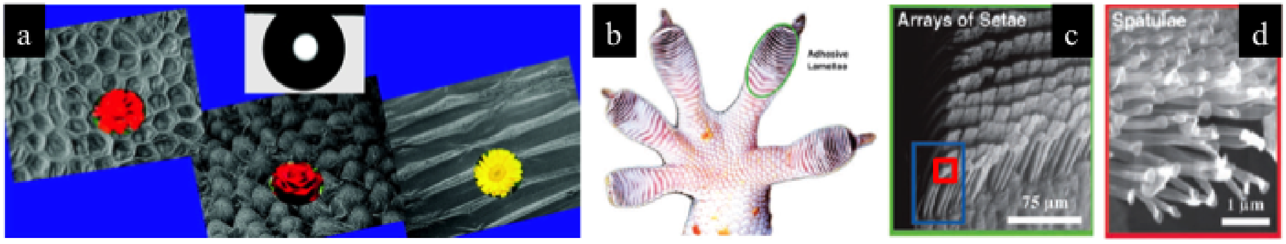

Figure 2 : Examples of sticky surfaces: a) petal effect in many flowers [41]; b) Gecko's foot with adhesive lamellae; c) portion of a single lamella formed by an array of setae; d) nanostructures in the tip of a seta [44].

Another quite useful property, mainly for drivers and glass-wearers, is antifogging. Fogging occurs when condensation produces droplets of size larger than half of the shortest wavelength of visible light. There are three kinds of surfaces where the formation of such droplets is suppressed: oleophobic [52, 53], superhydrophilic [54] and superhydrophobic [55–58]. In this case the source of inspiration from nature is the mosquito eye which has a composite structure formed by microscale hemispheres covered by nanoscale nipples organized in a hexagonal array preventing the formation of fog droplets (see figure 3) [59]. Indeed, the surface of mosquito eyes is always dry and clear even if exposed to moisture in watery and dim habitats, entailing an excelent sight.

Antireflection coatings can be exploited in many optical applications, such as lenses, solar cells, electrooptical devices and sensors, thanks to the efficiency in enhancing transmitted light and removing ”ghost images”. Antireflectivity is an important feature present, for instance, in the eyes of some insects, to allow a good sight in low-light conditions, or in the wings for camouflage by reducing reflection from transparent surfaces [60–62]. Again, such property is related to the particular morphology of the surface, being formed by arrays of nanoscale nipples, as observed in the moth eyes or in the cicada wings, as depicted in figure 3. Inspired by these examples, superhydrophobic antireflection coatings have been produced by means of several micro and nanofabrication techniques [63–68].

In desert enviroments the development of technologies for harvesting water from the atmosphere is fundamental. Obviously, nature has already evolved a large variety of systems for water collection in arid places as can be observed, for instance, in the *Stipagrostis sabulicola* (Namib dune bushman grass) [69], in cactus [70, 71], in lizards [72] and in the *Stenocara sp.* beetle or in the spider web (see figure 3) [73]. Different water harvesting samples have been realized mimicking the complex structures on the *Stenocara* beetle's back, composed by bumps featuring a smooth and hydrophilic peak in a superhydrophobic background [73–76]. An alternative interesting approach considers fibers [77] or surfaces covered by fiber nanomats [78].

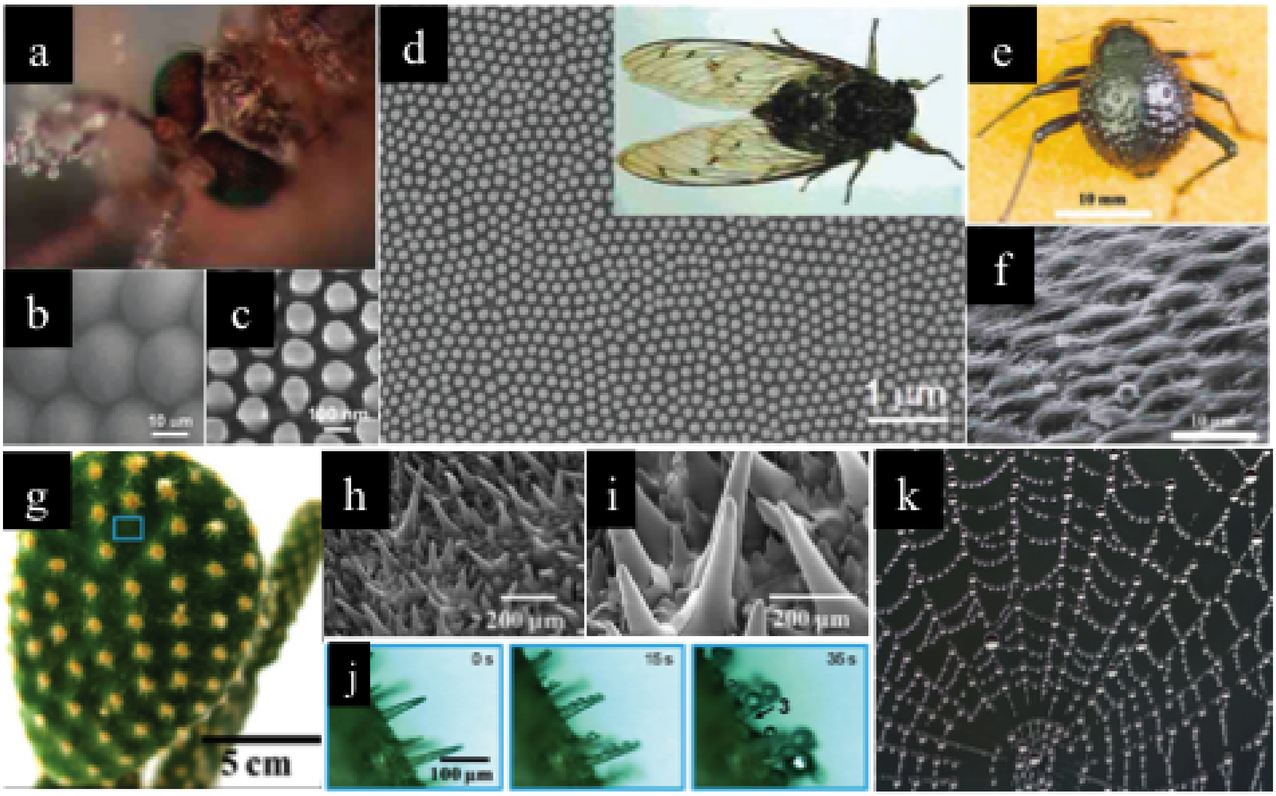

Figure 3 : Smart textured surfaces featuring different properties: a) antifogging mosquito's eyes and b) and c) corresponding surfaces structure [59]; d) antireflection cicada's wings [79]; e) water collecting *Stenocara sp.* beetle and f) related surface texture [73]; g) cactus leaf and h) and i) microscope picture of its needles harvesting water through th mechanism shown in sequence j) [71]; k) water drops trapped on a spider web.

Open microfluidics. The second very important field involving drops is the so-called "open microfluidics", which studies the behavior of small amounts of liquid (typically in the nanoliter/microliter range) deposited on free surfaces. Open microfluidics moves from the traditional microfluidics [80,81], dealing with the handling of fluids in devices formed by closed microchannels, with the purpose to solve some inconveniences: for instance in closed chips small channels are easily clogged, there is not accessibility to liquids, flows through pipes of very small cross section are very difficult because of high fluidic resistance and fabrication is more complicated [82].

The real challenge in the field of open microfluidics is to achieve a complete control of drops, including their formation, emission frequency, volume [83], morphology [84–86], and, above all, motion, in order to exploit such technology for biological or chemical applications, as already done for closed microfluidics [81,87–90]. There are two main categories of methods devised to control droplets: passive techniques, based, for example, on surface geometrical or chemical patterning, and active techniques hinging on the application of external fields, e. g. electrical, magnetic or acoustic.

Among passive methods we can find, for instance, asimmetrical textures, where levitating Leidenfrost drops spontaneously move in a direction depending on the structures shape [37, 91].
Drop self-propulsion can be obtained also by means of surfaces featuring a wettability gradient: droplets deposited on the more hydrophobic part of the sample move towards the more hydrophylic region [92–96]. If the sample is tilted and the more hydrophilic part is upward, the drop can also climb against gravity [97]. A similar effect can occur on homogeneous substrates heated with a thermal gradient because of the relation between surface tension (and accordingly wettability) and temperature [98, 99].
Chemical patterns can be exploited even to affect drop trajectories: self-propelling droplets can be spatially confined in the hydrophilic pathways drawn on a hydrophobic background [100] and drops sliding down an inclined surface featuring stripes oblique with respect to the gravity direction deviate following the lines [101, 102].
Another very peculiar phenomenon making droplets spontaneously move is the "long" and "short" range interactions between droplets made of a two-component solution, i. e. water and propylen glycol [103] (see figure 4c). "Long-range" interactions involve the vapour clouds surrounding droplets deposited at distances of up to several radii apart, while "short-range" interactions occurs when droplets meet. The vapour-mediated "long range" interaction is attractive, then the "short range" interaction can be either repulsive, causing drop propulsion (figure 4d), or attractive (figure 4e), leading to drop merging, according to the propylen glycol concentration in the two droplets.

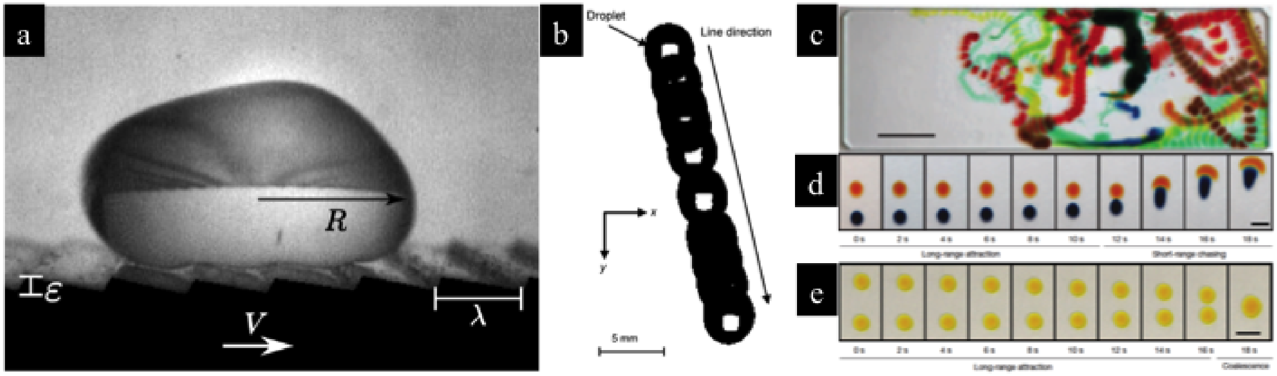

Figure 4 : Examples of passive methods to control drop motion: a) Leidenfrost drop on a hot ratchet (λ=1,5 mm) [91]; b) chemical pattern formed by stripes [101] and c) vapour-mediated interactions between droplets leading either to d) propulsion or e) merging (scale bars correspond to 10, 3 and 5 mm, respectively) [103].

On the other hand, active methods involve the application of external fields. The first and most common example is electrowetting (see figure 5 a-c): the shape of a polar fluid drop can be changed through the application of a potential difference between the surface and the liquid [104] in such a way to induce the motion of the contact line in the desired direction. This technology can perform dried blood spot analysis [105], extraction and quantification of estrogen in biological samples [106] and cell culture and analysis [107, 108], for example (see figure 5b and 5c). Actually, such a device takes a place halfway between closed and open microfluidics, indeed drops are usually sendweeched between two plates and fluid accessibility is limited; moreover electrical field application could damage cells in biologic mixtures.

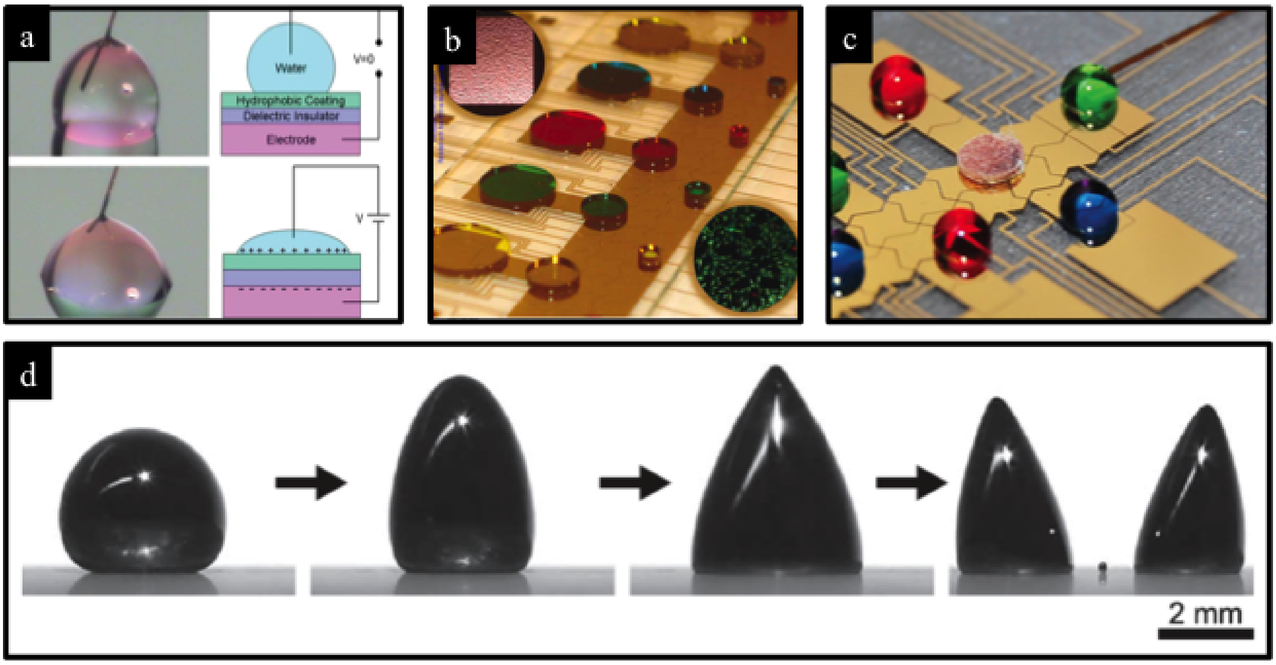

Figure 5 : Drops subject to external fields: box a) basic principle of electrowetting [104]; box b) application of electrowetting for complete mammalian cell colture [108]; box c) analysis of a dried blood spot through electrowetting [105]; box d) shapes assumed by a ferrofluid drop subject to a magnetic field of magnitude increasing from left to right. For a high enough field the drop splits into daughter droplets [109].

Magnetic fields can affect ferrofluids, i. e. colloidal suspensions of ferromagnetic nanoparticles in a solvent containing surfactants (i. e. molecules formed by a polar head and an apolar chain which avoid particle clustering and precipitation). Ferrofluid drops subject to a magnetic field markedly deform their interface (spherical when the field is absent) to balance surface tension and magnetic forces. Unusual shapes are assumed (elongated, stretched or with spikes) according to the kind of ferrofluid, the field gradient and intensity, as reported in figure 5. Drops can even split into a regular number of daughter droplets (Rosensweig effect) [110] which can move on the surface [109]. Droplets covered by a ferrofluid layer impregnating a textured surface are attracted by magnets [111] and Leidenfrost oxigen drops can be deviated by means of permanent magnets.

The effectiveness of electrowetting and magnetowetting is restricted only to particular kinds of fluids: polar liquids and ferrofluids respectively. Such a limit can be overcome, for example, by means of acoustic vibrations applied to the substrate, which couple with liquid inertia, independently from particular physical or chemical fluid properties, therefore providing the possibility to handle any kind of liquid (see figure 6). Pure vertical (pumping mode) or pure horizontal (rocking mode) oscillations of the substrate cannot produce a net motion of the drop because of their intrinsic simmetry. To break this simmetry a combination of these two modes is required and can be obtained by using two independent orthogonal shakers [112] or by applying vibrations obliquely to the substrate, e. g. vertical vibrations to an inclined plane [113]. In the first case the direction of drop motion has been found to depend on the phase shift between the two vibrations. In the second case the drop can be pinned, slide down or also climb uphill against gravity according to the combination of amplitude and frequency of oscillation. While the amplitude of these mechanical oscillations required for droplet displacemnt is in the millimetric range, much smaller amplitudes (up to hundreds of microns) are enough to move droplets through surface acoustic waves (SAW). Ultrasonic SAWs generated by means of transducers on piezoelectric substrates can either agitate the internal flow of a drop with pinned contact line, or induce a motion in the direction of the wave, accompanied by internal flow [114, 115]. The details of drop behavior depend on the combination of several parameters, such as wave frequency and amplitude, surface wettability, drop size and viscosity. The application of SAWs could be a further valid tool to handle droplets in discrete microfluidic devices [116, 117].

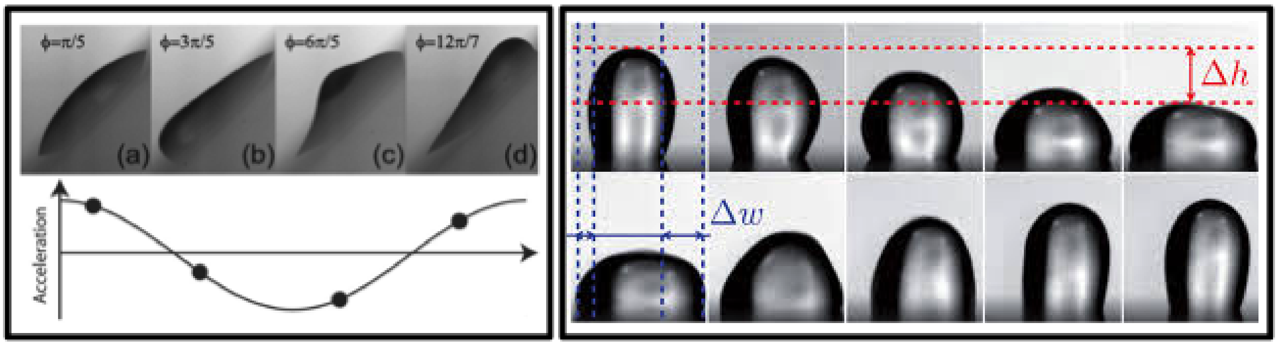

Figure 6 : Droplets subject to vibrations. Left panel: climbing drop on a inclined surface vibrating vertically [113]. Right panel: sequence of deformetions of a drop actuated by surface acoustic waves [115].

Obviously passive and active methods can be combined to find more reliable ways to control drops. For example electrowetting is often paired with patterned surfaces [105] and vibrations can be applied to chemical heterogeneous samples [118] or to a fluidic network [119].

Despite the large variety of studies about drop behavior, this is still an active, fermenting and hot topic where further research is necessary to better understand wetting mechanisms and where new ideas can lead to the production of surfaces with special wetting properties and to a complete handling of drops in digital-microfluidic platforms applied in chemical or biomedical processes.

This work. This thesis collects experiments about drops of millimetric size (featuring a volume typically of the order of microliters or tens of microliters) on inclined surfaces and, as a consequence, subject to a constant force (i. e. the gravity force). In particular different kinds of surfaces (homogeneous, heterogeneous and textured) and different types of fluids (pure liquids, solutions and complex fluids) have been investigated. Experimental observations are in some cases complemented by numerical simulations performed by theoretical coworkers.
The manuscript is organized as follows:

- Chapter 1 describes the theory explaining wetting and drop dynamics on inclined planes;
- the experimental setups used for the observation of drop behavior are described in Chapter 2;

- Chapter 3 deals with the adhesion properties of surfaces covered by hairy structures;
- Chapters 4 and 5 report new results about sliding on chemically homogeneous and heterogeneous samples, respectively;
- Chapter 6 is devoted to the passage of drops through a chemical step;
- non-newtonian complex fluids are the subject of Chapter 7;
- Chapter 8 shows the interesting dynamics of droplets on inclined vibrating substrates;
- finally Conclusions summarize the main results of this work.

Chapter 1

Basic concepts about liquid drops

The following chapter deals with the theory underlying wetting phenomena and drop behavior on surfaces, starting from the fundamental concept of surface tension, explained in Section 1.1. Section 1.2 describes the static wettability of drops deposited on different kinds of horizontal surfaces (flat, rough or heterogeneous). Section 1.3 further analyzes drop shape considering also the size. Dynamical contact angles and contact angle hysteresis are the object of Section 1.4. The sliding of drops down inclined surfaces is treated in Section 1.5. Finally, Section 1.6 gives an overview of the main numerical methods applied for the simulation of drop statics and dynamics: lattice Boltzmann, Surface evolver and Cahn-Hilliard / Navier-Stokes (CHNS) model.

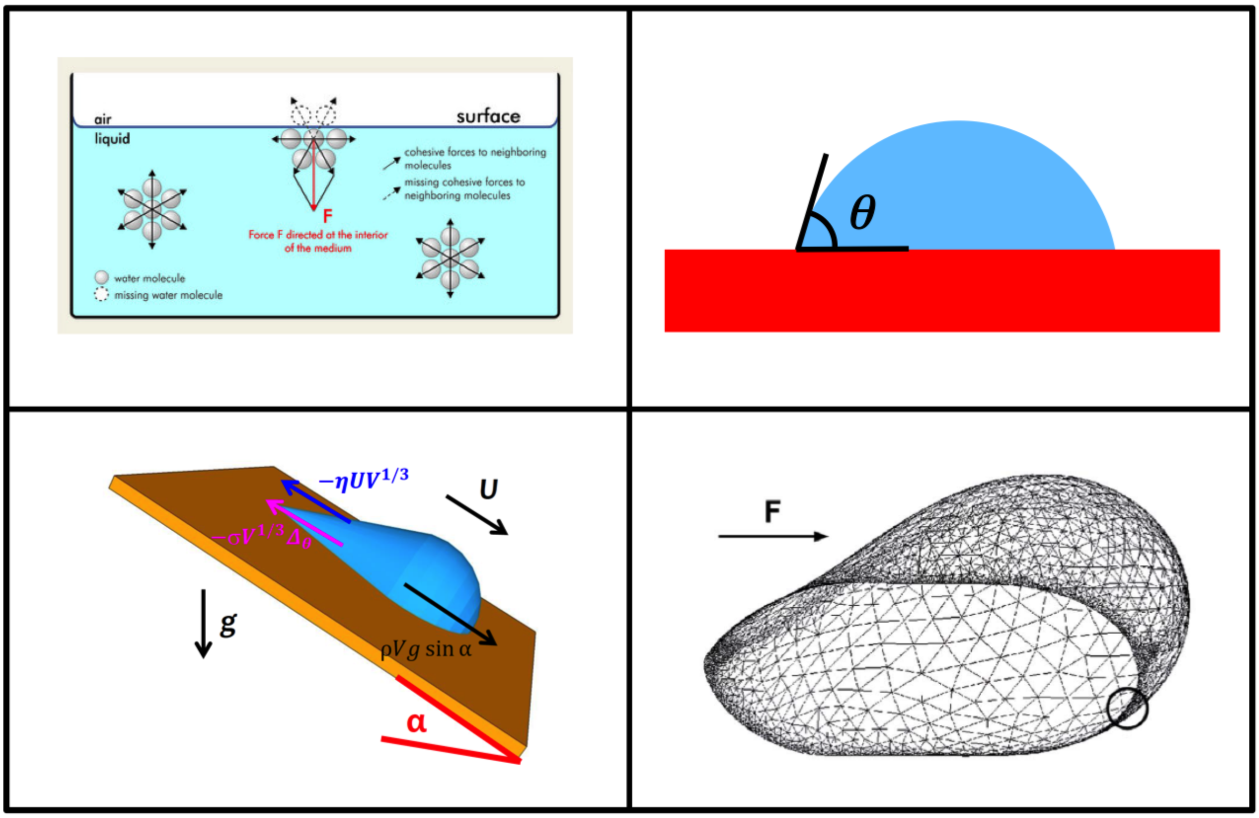

§ 1.1. Surface tension

A liquid surface is smooth on an atomic scale and assumes the shape minimizing the surface energy. It can also be seen as a stretched membrane featuring a surface tension which opposes its distorsion. The physical origin of the presence of surface tension can be understood by considering a fluid at the molecular scale (see figure 1.1): a molecule in the bulk interacts with all its neighbours, on the other hand a molecule on the surface loses parts of these cohesive interactions and is in an unfavorable energy state. This is the reason why liquids adjust their shape in order to reduce the exposed surface area as much as possible. From this microscopic picture we can evaluate the surface tension for some fluids: if we define E as the cohesion energy per molecule inside the liquid, a molecule at the surface has an energy of roughly $E/2$ less and surface tension is a direct measurement of the energy shortage per unit surface area. More precisely, if a is the dimension of a molecule a^2 is its exposed area and the surface tension is of order

$$\sigma \sim E/(2a^2). \tag{1.1}$$

For instance, oils are characterized by van der Waals interactions and $E \sim kT$ which is the thermal energy (where k is the Boltzmann constant and T the temperature expressed in K). At room temperature (25° C) $kT = 1/40$ eV and the corresponding surface tension is σ=20 mJ/m^2. The surface tension of water is higher ($\sigma \sim 72$ mJ/m^2) due to the hydrogen bonds. An example of very high surface tension liquid is mercury ($\sigma \sim 500$ mJ/m^2), which is a strongly cohesive liquid metal.
As surface tension characterizes a surface in open air, systems formed by two immiscible phases a and b feature an interfacial tension σ_{ab} and all the considerations valid for surface tension hold also for interfacial tension.

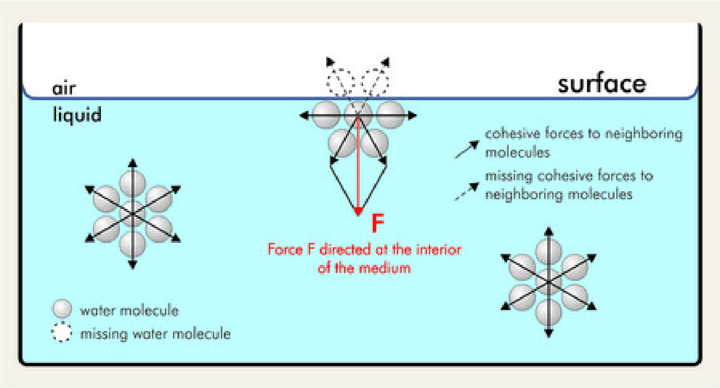

Figure 1.1 : Physical origin of surface tension: molecules at the interface interact with less neighbours than molecules in the bulk.

Even if the concept of surface tension finds its explanation at the microscopic level, it is a macroscopic parameter which can be defined on a macroscopic scale in two main ways: taking into consideration surface work or capillary forces.
In order to create a surface, energy is required because some intermolecular bonds have to be broken to bring a molecule from the bulk to the surface. From a macroscopic point of view, the work necessary to increase the surface area of a liquid by an amount dA is proportional to the number of molecules

which have to be brought to the surface, i. e. dA itself:

$$\delta W = \sigma dA, \tag{1.2}$$

where the surface tension is the energy that must be supplied to increase the surface area by one unit and is expressed in mJ/m^2.

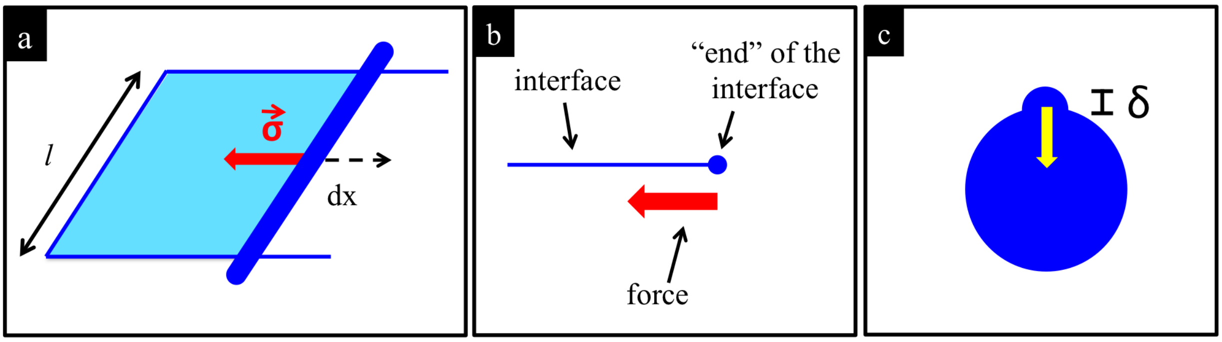

Figure 1.2 : a) Surface tension as a force per unit length normal to the mobile rod; b) surface tension applied in the ending point of an interface is parallel to the interface and directed inward to reduce surface area; c) elastic reply to a generic surface deformation δ, due to the presence of surface tension (yellow arrow).

In addition, surface tension can be thought also as a force per unit length, as can be understood from the example shown figure 1.2a. Such a system is a frame formed by three fixed sides and a rod of length l free to move on the two parallel fixed sticks. If this apparatus is dipped in a viscous fluid to form a liquid mambrane inside the rectangle, as soon as the frame is removed from the liquid, the mobile rod spontaneously moves in the direction of its opposite fixed side (see the arrow in figure 1.2a) in order to reduce the membrane surface area. The work done for a rod displacement equal to dx is:

$$\delta W = F dx = 2\sigma l dx, \tag{1.3}$$

where the factor 2 refers to the presence of two interfaces. As a consequence σ is a force per unit length normal to the rod, lying in the plane of the surface and directed toward the liquid. Indeed, the most common dimensional units used for surface tension are mN/m.
In a particular situation where a surface has an ending point, as sketched in figure 1.2b, the force applied in such point is parallel to the surface and directed "inwards", as indicated by the arrow, in order to minimize the interface.
Generally, a surface deformed by δ, as depicted in figure 1.2c, reacts through a restoring force $F \sim \sigma\delta$ and a corresponding energy $E \sim \sigma\delta^2$, resembling elastic systems where surface tension represents the spring constant.

Furthermore, surface tension can be related even to a pressure associated to curved surfaces, the *Laplace pressure*.

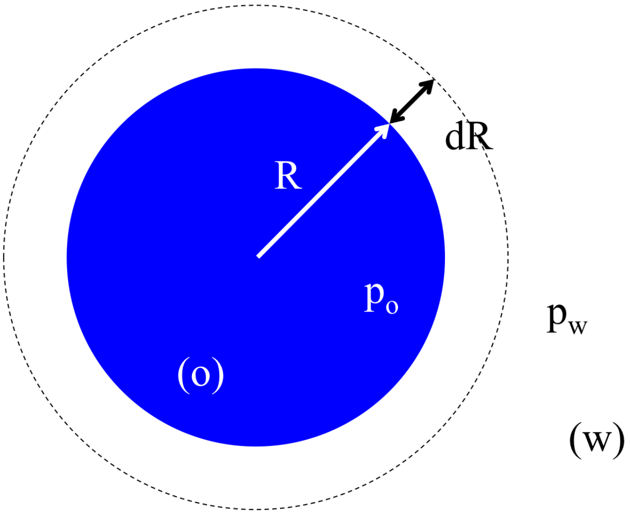

Figure 1.3 : Sketch of an oil droplet (o) immersed in water (w). Inside the drop there is a pressure p_o higher than the pressure in water p_w. The pressure jump is related to surface interface and drop curvature.

In the simplified example of an oil (o) drop immersed in water (w) depicted in figure 1.3, the shape adopted by the droplet to decrease its surface energy is a sphere of radius R. If the oil/water interface is displaced by dR, the corresponding work done by pressure and capillary forces is

$$\delta W = -p_o dV_o - p_w dV_w + \sigma_{ow} dA, \tag{1.4}$$

where $dV_o = 4\pi R^2 dR = -dV_w$ and $dA = 8\pi R dR$ are the volume and surface increase, respectively, p_o and p_w are pressures in oil and water and σ_{ow} is the interfacial tension between oil and water. The equilibrium condition $\delta W = 0$ implies

$$\Delta p = p_o - p_w = \frac{2\sigma_{ow}}{R} : \tag{1.5}$$

smaller droplets undergo a higher inner pressure.

More generally, according to the *Laplace theorem*, the pressure increase Δp that occurs upon traversing the boundary between two fluids is equal to the product of the surface tension σ and the curvature of the surface C:

$$\Delta p = \sigma C = \sigma\left(\frac{1}{R} + \frac{1}{R'}\right), \tag{1.6}$$

where R and R' are the radii of curvature of the surface.

§ 1.2. Static wettability

This section deals with the theory about wetting, distinguishing between different kinds of surfaces: flat homogeneous substrates (1.2.1), heterogeneous samples (5) and finally rough surfaces (1.2.3).

§ 1.2.1. Flat homogeneous surfaces

A liquid drop deposited on an ideal flat homogeneous surface is a system composed by three interfaces (solid/liquid, solid/air and liquid/air), where, due to the simmetry of the problem, the contact area is circular and the liquid/air interface forms a static contact angle θ with the liquid/solid interface (see figure 1.4), which is the only parameter necessary to describe surface wetting.

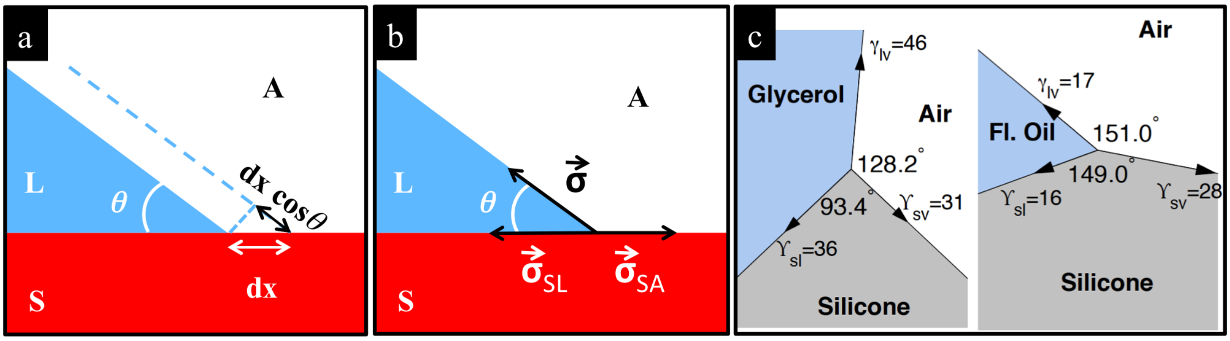

Figure 1.4 : Cartoons of systems formed by three phases (A=air, L=liquid and S=solid): determination of θ through a) energy minimization and b) force balance. c) example of soft substrate deformed by the normal component of surface tension (image from [120] where surface tension is denoted by γ).

A way to determine the value of θ is to consider the work (normalized to a unit length) done to displace the contact line by dx along the solid surface, as sketched in figure 1.4a:

$$\delta W = \sigma_{SL} dx - \sigma_{SA} dx + \sigma dx cos\theta, \tag{1.7}$$

where σ_{SL}, σ_{SA} and σ are the solid/liquid, solid/air and liquid/air interfacial tensions respectively. This work must be 0 at equilibrium, giving the Young's equation:

$$cos\theta = \frac{\sigma_{SA} - \sigma_{SL}}{\sigma}. \tag{1.8}$$

Equivalently, the triple contact line can be seen as formed by the ending points of three interfaces and, as already explained in Section 1.1, the forces applied in the contact points are tangent to the interfaces, as shown in figure 1.4b. At equilibrium the contact line does not move and the in-plane component of the resultant of such forces must be 0:

$$\sigma \cos\theta = \sigma_{SA} - \sigma_{SL}, \tag{1.9}$$

leading again to the Young's equation 1.8. This picture gives further information: the component of the force perpendicular to the solid surface ($\sigma \sin\theta$) is not 0 and, consequently, interesting behaviors

can be observed in droplets on soft deformable substrates [120, 121] (see figure 1.4c).
While the solid/liquid and solid/air interface tensions are not accessible values, the directly measurable quantity is θ, which is adopted to define the wettability of a surface (see figure 1.5):

- if a static contact angle $\theta < 5°$ is reached almost instantaneously (within less than 1 second), the surface is superhydrophilic;
- if water drops feature $\theta < 90°$, the surface is hydrophilic;
- if water drops have $\theta > 90°$, the surface is hydrophobic;
- if water drops are characterized by $\theta > 150°$, the surface is superhydrophobic.

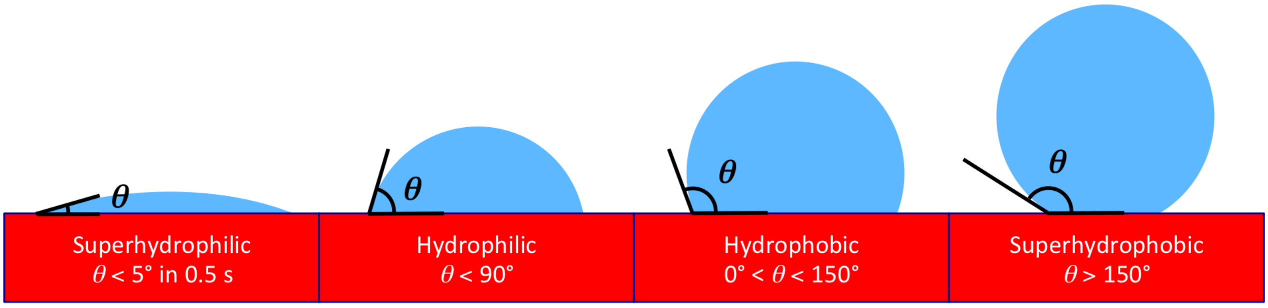

Figure 1.5 : Wettability characterization through the value of the static contact angle assumed by a water drop deposited on the surface.

For a smooth surface, θ is always smaller than 120° and higher contact angles can be obtained by introducing roughness on the surfaces (see Section 1.2.3). More generally, a surface is defined lyophilic/lyophobic if the static contact angle of a liquid different from water is lower/higher than 90°.

§ 1.2.2. Heterogeneous surfaces

The static contact angle of a drop on a heterogeneous surface formed by areas of different wettability depends on the relative size of the drop with respect to the dimension of the domains. The statics of droplets featuring a size comparable with the dimensions of the patterns varies according to the position where the droplet is deposited. On the other hand, drops large enough to cover an area representative of the whole sample assume a static contact angle given by the weighted average of the wettability characterizing the different materials forming the surface. The precise evaluation of such apparent contact angle, θ_{CB}, is given by the Cassie-Baxter model [122], which considers a flat smooth surface formed by two materials, labeled as 1 and 2, characterized by different static contact angles θ_1 and θ_2 , obeying the corresponding Young's equation 1.8, and fractions f_1 and f_2 with respect to the whole surface area.

To calculate θ_{CB} we can evaluate the work necessary to move (a unitary length of) the contact line by dx, covering species 1 and 2 with probability f_1 and f_2 respectively, as sketched in figure 1.6:

$$\delta W = f_1(\sigma_{SL} - \sigma_{SA})_1 dx + f_2(\sigma_{SL} - \sigma_{SA})_2 dx + \sigma dx \cos\theta_{CB}, \tag{1.10}$$

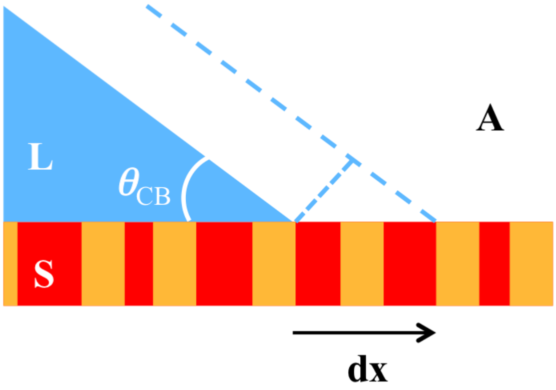

Figure 1.6 : Static contact angle on a heterogeneous surface formed by two different materials represented by red (dark) and yellow (light) colors. The drop is much bigger than surface domains and the resulting contact angle θ_{CB} is an average between the contact angles characterizing the two materials.

The equilibrium condition required for determining the *static* contact angle is $\delta W = 0$ and leads to:

$$
\begin{aligned}
0 &= f_1(\sigma_{SL} - \sigma_{SA})_1 dx + f_2(\sigma_{SL} - \sigma_{SA})_2 dx + \sigma dx cos\theta_{CB} && (1.11)\\
0 &= -f_1 cos\theta_1 dx - f_2 cos\theta_2 dx + cos\theta_{CB} && (1.12)\\
& && (1.13)
\end{aligned}
$$

where in the second passage the Young's equation 1.8 holding on each material has been applied. By rearranging equation 1.13 we obtain the Cassie-Baxter relation:

$$cos\theta_{CB} = f_1 cos\theta_1 + f_2 cos\theta_2 \tag{1.14}$$

The apparent contact angle θ_{CB} lies between θ_1 and θ_2, depending on the average of the *cosines* of the contact angles weighted according to the fractions of the two materials of the surface.

§ 1.2.3. Rough surfaces

There are two different kinds of wetting on a rough sample: the basic Wenzel model [123] (Section 1.2.3), where the liquid touches the whole exposed surface, and the model by Bico et al. [124, 125] (Sections 1.2.3 and 1.2.3), distinguishing between hydrophilic and hydrophobic cases and considering composite rough surfaces: on a hydrophilic surface where the liquid spontaneously fills the holes, a drop is in contact with a mixed solid/liquid wet substrate; on the other hand, on a hydrophobic surface, air is trapped between the structures under the droplet, which rests on a composite of solid and air. This last case is also known as Cassie state.

Wenzel model

The roughness of a surface can be described by the parameter $r \geq 1$, defined as the ratio between the real surface area to the apparent surface area, which is equal to 1 in the case of a flat smooth surface. To evaluate the apparent angle θ^* on a rough but chemically homogeneous surface we assume that the local contact angle θ is given by the Young's equation 1.8 and the drop completely touches the surfaces and features a size much bigger than the roughness scale.

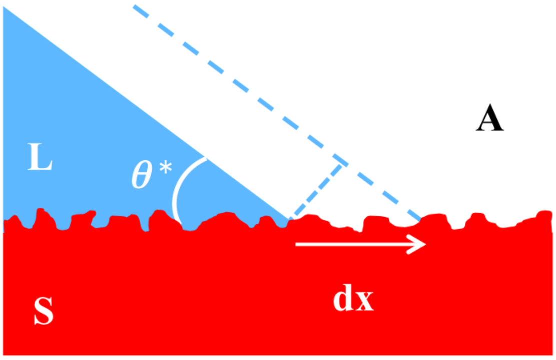

Figure 1.7 : Static contact angle on a rough surface according to the Wenzel model: the drop touches the whole solid surface formed by a texture featuring a typical dimension much smaller than drop size [126].

The surface energy variation (per unit length of contact line) corresponding to a displacement dx of the line of contact in a direction parallel to the surface is (see figure 1.7):

$$\Delta E = r(\sigma_{SL} - \sigma_{SA})dx + \sigma dx cos\theta^*. \tag{1.15}$$

The equilibrium condition is the minimum of E, that is $dE = 0$, leading to the Wenzel relation:

$$cos\theta^* = rcos\theta. \tag{1.16}$$

Indeed, for $r = 1$, i. e. for a smooth surface, these formulas returns to the Young's case 1.8, while for $r > 1$ there are two possible behaviors:

- $\theta^* < \theta$ if $\theta < 90°$;
- similarly, $\theta^* > \theta$ if $\theta > 90°$.

Surface roughness always magnifies the underlying wetting properties: both hydrophilic and hydrophobic characteristics are reinforced by surface textures. Another consequence of Wenzel model is the presence of wetting and drying transitions. Since r is not bounded, there should exist a threshold value $r^* = 1/cos\theta$ beyond which wetting becomes either total or zero according to the value of θ. However this simplified view is arguable and actually there are restrictions to the domain of validity of Wenzel's relation, as explained in the next sections.

Composite rough surfaces: hydrophilic

A rough hydrophilic surface can be thought as a thin porous medium where some liquid escapes from the drop to fill the surface structures, as shown in figure 1.8. As a consequence, the drop finds a mixed wet substrate formed by solid and liquid areas. To simplify the calculation of the apparent contact angle θ^* we consider a sample made of an array of regular tiles where the exposed solid edges are dry and the liquid fills the holes mantaining a horizontal interface (see figure 1.8) so that the whole substrate results to be flat.

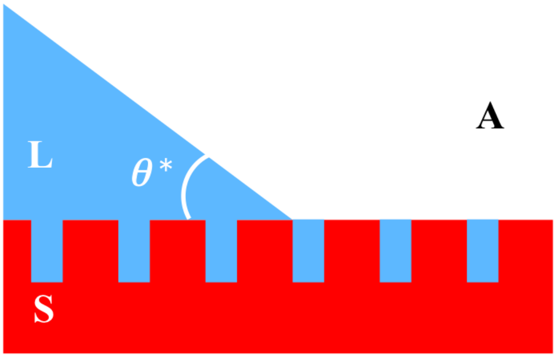

Figure 1.8 : Static contact angle on a hydrophilic porous surface where the liquid spontaneously fills the grooves: the drop feels a heterogeneous surfaces formed by liquid and solid domains.

If we define f_s and (1-f_s) the relative fractions of solid and liquid phases under a drop much bigger than surface structures and we apply the Cassie-Baxter relation 1.14 with contact angles θ and 0° respectively, we find:

$$cos\theta^* = 1 - f_s + f_s cos\theta. \tag{1.17}$$

Differently from Wenzel's prediction, it appears clear that the condition of total wetting (θ^*=0) cannot be obtained simply by introducing surface roughness, since *theta* $\neq$ 0°. In addition, this picture is valid if a penetrating film can develop in the textured surface. Considering again the sketch in figure 1.8, we can evaluate the condition required for the impregnation of the surface. If the wetting film advances by a distance dx, the wet surface area (per unit length of the film) is rdx, but this displacement also leaves a dry solid area $f_s dx$. The corresponding energy variation per unit length is

$$dE = (r - f_s)(\sigma_{SL} - \sigma_{SA})dx + (1 - f_s)\sigma dx. \tag{1.18}$$

The formation of the impregnating film is energetically favorable, i. e. $dE < 0$ if the following inequality is satisfaied:

$$cos\theta > \frac{1 - f_s}{r - f_s} = cos\theta_c. \tag{1.19}$$

Such a condition defines a critical angle θ_c below which a film impregnate the texture. θ_c is comprised between 0° and 90° and can be derived by calculating the intersection between equations 1.16 and 1.17, as reported in the graph of figure 1.9:

- if $\theta_c < \theta < 90°$ the solid remains dry and the correct description is given by the Wenzel model;
- when $0° < \theta < \theta_c$ the formation of the penetrating film is promoted and the right equation is 1.17, derived from the picture by Bico et al [124, 125].

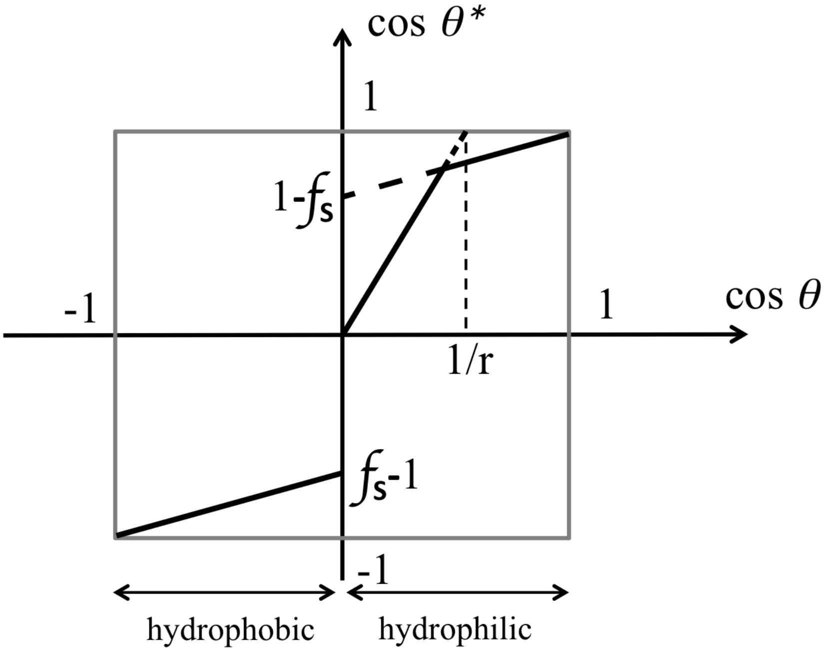

Figure 1.9 : Relation between the apparent contact angle θ^* and the Young's angle θ for a liquid drop lying on a textured surface [124–126].

Composite rough surfaces: hydrophobic (Cassie state)

A parallel approach can be adopted also for hydrophobic surfaces: in this case the energy of the dry solid is lower than that of the wet solid and, as a consequence, air pockets are trapped between surface structures, as depicted in figure 1.10 [127].

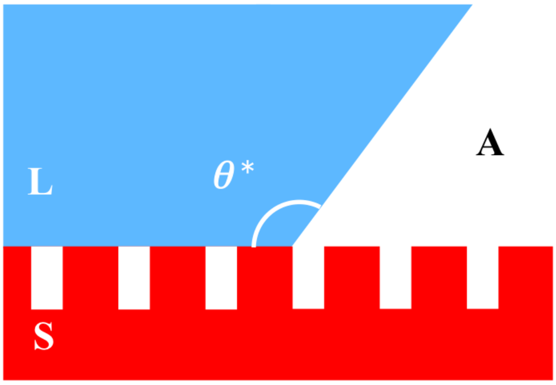

Figure 1.10 : Static contact angle on a hydrophobic porous surface where air pockets are trapped between the grooves: the drop rests on a mixed air/solid surface.

The static contact angle θ^* is then an average between the value on air (θ_{air}=180°) and on the flat solid (θ) [128], applying again the Cassie-Baxter relation 1.14:

$$\begin{aligned} \cos\theta^* &= f_A \cos\theta_{air} + f_S \cos\theta \\ &= (1-f_S)(-1) + f_S \cos\theta \\ &= -1 + f_S(1+\cos\theta) \qquad (1.20) \end{aligned}$$

$$(1.21)$$

where $f_A = 1 - f_S$ and f_S denotes the fraction of the drop base touching the solid surface. This result is much different from the Wenzel's prediction: as soon as air is trapped in the surface holes, cosθ^* suddenly jumps to values lower than $(f_s - 1)$, approaching the value -1 as the solid fraction get smaller, as shown in figure 1.9. However, the ideal condition $\theta^* = 180°$ is not physically realizable because it would mean f_s=0 or $\theta = 180°$. Moreover in this "fakir regime" the drop is not affected by surface defects, being largely sustained by a defect-free cushion of air.

§ 1.3. Drop size

A sessile drop is subject to capillary and gravity force and its shape is a spherical cap if the capillarity contribution is dominant, whereas the drop is a flattened puddle when gravity is stronger (see figure 1.11).

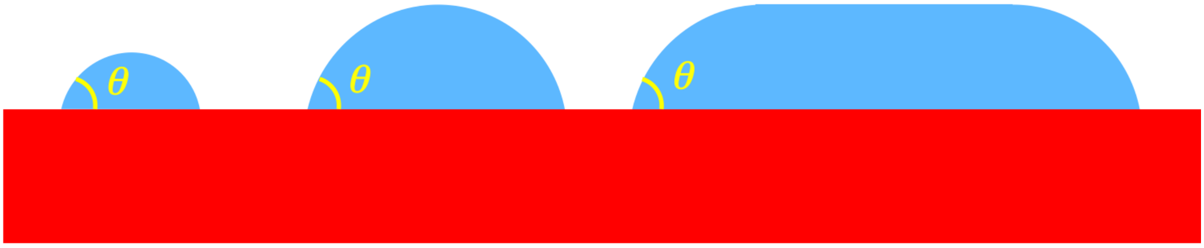

Figure 1.11 : Sessile drops of increasing size: the shape is a spherical cap or a puddle depending on whether the dimension is smaller or bigger than the capillary length, but the contact angle is always the same.

The characteristic length discriminating between these two possible morphologies is the capillary length K^{-1} defined by the balance between surface and potential energy ($\sigma R^2 \sim \rho R^3 g R$) or by comparing the Laplace pressure with the hydrostatic pressure ($\sigma/R \sim \rho g R$):

$$K^{-1} = \sqrt{\frac{\sigma}{\rho g}} \qquad (1.22)$$

where ρ is the liquid density and g is the gravity acceleration. The value of K^{-1} is generally around a few millimeters.

In addition, the static contact angle θ is a local quantity independent of drop volume even if gravity is dominant, as shown in figure 1.11 and as discussed in section 1.4 where gravity has not been considered.

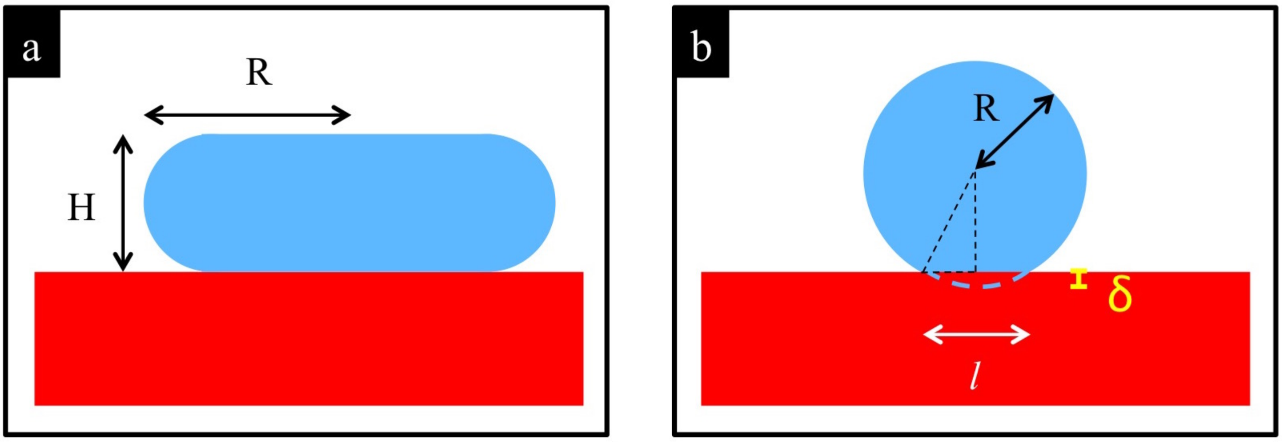

Figure 1.12 : Characteristic lengths of drops on a superhydrophobic surface with typical size a) larger or b) smaller than the capillary length.

In the particular case of a superhydrophobic surface the evaluation of drop shape can be simply derived considering the sketches in figure 1.12:

size above K^{-1}: the drop assumes a fattened shape, as depicted in figure 1.12a. The corresponding volume can be approximated with $V = \pi R^2 H$ and, as a consequence, the energy of this drop is

$$E \sim \pi R^2\sigma + \pi R^2\sigma + (1/2)\rho\pi R^2 H^2 g \sim 2\sigma V/H + (1/2)\rho V H g, \tag{1.23}$$

whose minimum is obtained for $H = 2K^{-1}$: the height of the puddle is the same, regardless drop volume;

size below K^{-1}: the drop is deformed as shown in figure 1.12b because of the gravity force. Surface tension opposes to such deformation and the equilibrium shape can be determined by equating gravity force and surface tension ($\sigma\delta \sim \rho R^3 g$) leading to $\delta \sim R^3/K^{-2}$ and $l \sim R^2/K^{-2}$.

On the other hand, the calculations for a partially wetting drop of generic angle θ is much more complex and we refer to [126] for a complete dissertation.

§ 1.4. Dynamic contact angles

Real surfaces are characterized by chemical or physical defects and, consequently, the static contact angle is not a single value, but rather there is a range of possible contact angles assumed by the drop mantaining the contact line pinned.

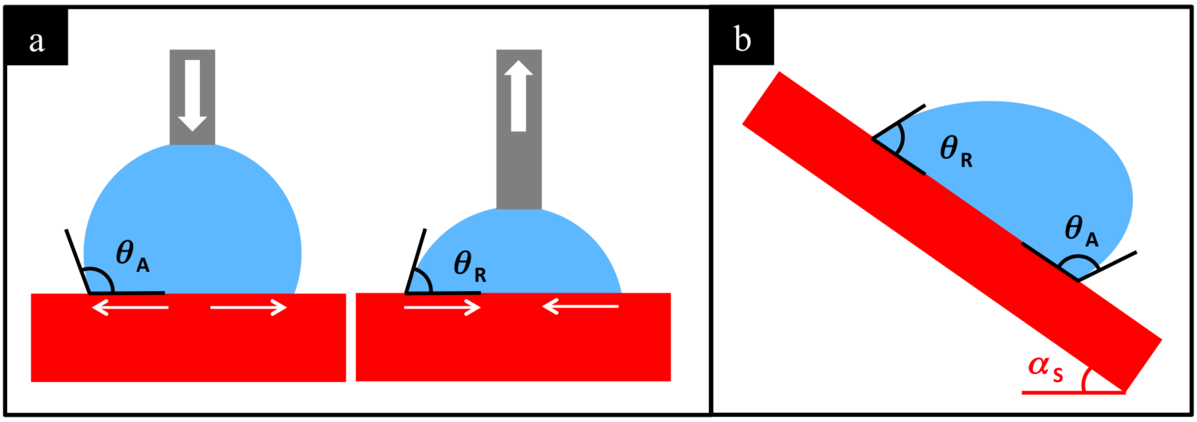

Figure 1.13 : Advancing (θ_A) and receding (θ_R) contact angles defined a) by inflating or deflating a sessile drop or b) from the shape of a drop lying on a surface inclined by α_s, the smallest inclination angle necessary to observe sliding.

If a sessile drop is inflated as shown in figure 1.13, the contact angle increases with the contact line initially pinned, then the contact points start moving when the threshold *advancing contact angle* θ_A is exceded. Likewise, when the drop is deflated (see figure 1.13), the contact angle decreases but the contact line does not move untill the threshold *receding contact angle* θ_R is reached. The static contact angle on a real surface can assume every value within these two threshold angles. The difference between the advancing and receding contact angles $\Delta\theta = \theta_A - \theta_R$ is denoted as contact angle hysteresis and quantifies the degree of pinning on the surface.

Although the static contact cangle can be predicted for several kinds of systems, as described in Section 1.2, dynamic contact angles cannot be theoretically calculated because of their dependence on the adhesion between liquid and substrate which is inimately connected to the details of defects and roughness of the surface. Advancing and receding contact angles appear also in drops lying on inclined surfaces: the shape is no more symmetric [129], that is the front assumes a blunt shape and the rear becomes thinner (see figure 1.13). As the surface inclination increases, the front contact angle increases, while the rear contact angle decreases.

The different curvature of the front and rear parts of the drop implies the presence of a force pointing upward due to the Laplace pressure which is larger downstream, where the curvature is higher, and lower upstream, where the curvature is smaller. Indeed, for small inclinations, drops usually stand still because the adhesion to the surface is stronger than the gravitational force: this pinning occurs for inclination angles lower than a critical angle called sliding angle (the smallest angle beyond which the drop starts moving). To find the relation between the sliding angle (α_S) and contact angle hysteresis we can consider the work done to move the drop by a distance dx along the plane [130]. For sake of simplicity we assume an almost rectangular shape of the contact area of width w, as sketched in figure

1.14.

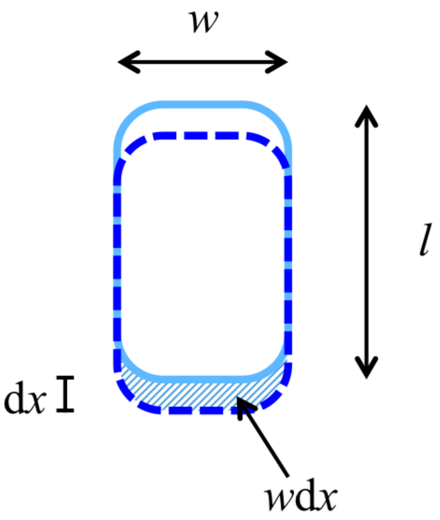

Figure 1.14 : Plane view of a liquid drop having a parallel sided contact line. The dashed line represents the same contact line after a displacement of the drop equal to dx.

The force leading to drop sliding is the gravity force and the corresponding work relative to a displacement equal to dx is

$$W = mgsin\alpha_S dx, \tag{1.24}$$

where m is drop mass, g the gravity acceleration and α_S the sliding angle. In moving down by dx, a surface area wdx is wetted in the front of the drop and an equal area is dewetted by the rear edge. The work done in wetting a unit area of solid surface is equal to $\sigma(1+cos\theta_A)$ and similarly, the work for dewetting a unit area of surface is $\sigma(1+cos\theta_R)$. Hence the total work associated to capillary forces is:

$$W = \sigma wdxcos\theta_R - \sigma wdxcos\theta_A. \tag{1.25}$$

Combining equations 1.24 and 1.25 we obtain:

$$\frac{mg\sin\alpha_S}{w} = \sigma(\cos\theta_R - \cos\theta_A). \tag{1.26}$$

More generally, for drops with different shapes we have:

$$mg\sin\alpha_S = kR\sigma(\cos\theta_R - \cos\theta_A), \tag{1.27}$$

where R is drop radius and k is a dimensionless prefactor depending on the geometry of the contact area [131]. In equation 1.27 the threshold dynamic angles appear, giving an evaluation of the smallest inclination angle necessary to observe sliding, which increases as the hysteresis increases. Actually, such formula holds also for inclination angles α higher than the sliding angle, if the critical angles θ_R and θ_A are respectively replaced by θ_r and θ_a, i. e. receding and advancing contact angles assumed

by the drop sliding on the plane inclined by α.
In addition, rearranging equation 1.27 we can provide a criterion to evaluate surface adhesion, which is proportional to $\Delta\theta$:

$$\frac{V}{R} \propto (\cos\theta_R - \cos\theta_A) : \tag{1.28}$$

if we fix the inclination, the volume V supported by the surface (devided by the contact area width) is proportional to the contact angle hysteresis and so a measurement of the maximum sustained volume can give a valuation of surface stickiness.

§ 1.5. Drops sliding on inclined surfaces

This section is divided into two parts describing the sliding of drops down homogeneous partially wetted surfaces (Section 1.5.1) and down superhydrophobic samples (Section 1.5.2).

§ 1.5.1. Sliding on partially wetted surfaces

Drops on a surface inclined by more than the sliding angle move on the plane being subject to three forces, whose in-plane components are [132, 133], as depicted in figure 1.15:

- gravitational pull along the plane $\sim \rho V g \sin\alpha$;
- viscous drag on the surface $\sim -\eta U V^{1/3}$;
- interfacial forces $\sim -\sigma V^{1/3}\Delta_\theta$.

where ρ is the fluid density, η is its viscosity, σ is the surface tension, V is the droplet volume, U is its velocity, α is the plate inclination and Δ_θ is a non dimensional factor depending on the contact angle distribution along the perimeter and on the perimeter shape.

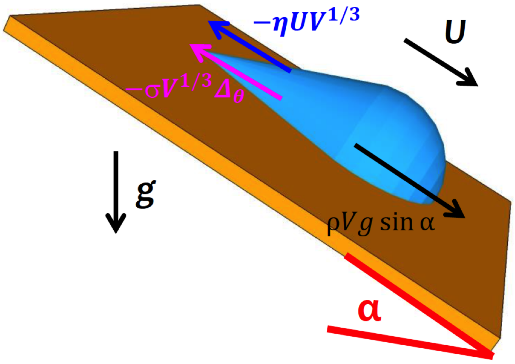

Figure 1.15 : Cartoon of a sliding drop on a partially wetted plane tilted by an angle α. The characteristic sliding velocity U is governed by the down-plane component of the gravitational acceleration $g\sin\alpha$, the viscous drag and capillary forces.

Initial motion can be both accelerated and at constant velocity, depending on many surface properties such as chemical composition, surface roughness or affinity with water [134], however the process

is dissipative: after a transient phase, forces balance and the drop reaches a steady state with a constant velocity and almost a constant shape [132], [135], [136].
Force balance implies a scaling law of the form:

$$Ca \simeq Bo - Bo_c \tag{1.29}$$

where

- $Ca = \dfrac{\eta U}{\sigma}$ is the capillary number;
- $Bo = V^{2/3}\dfrac{\rho g}{\sigma}\sin\alpha$ is the effective Bond number based on the component of gravity parallel to the plane;
- Bo_c is a constant depending on the wetting hysteresis through Δ_θ.

Further details about the sliding of drops partially wetting smooth homogeneous surfaces are reported in Section 4.1.
With regards to drops internal fluidity, both theoretical studies [135], [137] and experimental observations [138], [139], [140] were lately conducted. Gao and McCarthy [141] postulated two mechanisms for droplets movement:

- a sliding motion, where particles near the solid-liquid interface exchange their position with those at the gas-liquid interface, while the bulk of the liquid rigidly translates. Particles in the rotating layer undergo a movement similar to the motion of a tread of a caterpillar tank;
- a rolling motion, where the whole fluid mass assumes a circulatory movement.

Even if simulations predict a rolling motion [135] [137], PIV (Particle Imaging Velocimetry) [138], [140] and PTV (Particle Tracking Velocimetry) [139] reveal two different components in water droplets internal motion: caterpillar-like rotation flow (rolling) and slippage at the solid-liquid boundary (slipping), as depicted in figure 1.16. Indeed behavior in regions inside a drop is a very recently studied phenomenon which needs further research to be completely understood.

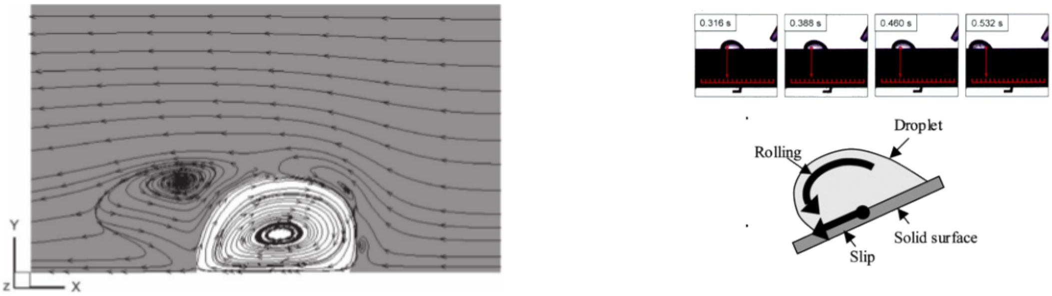

(a) (b)

Figure 1.16 : Internal flow of water droplets moving on homogeneous hydrophobic surfaces: (a) simulation prediction [135], (b) example of internal fluidity measurement [139] (above) and cartoon of droplet movement (below) [139].

§ 1.5.2. Sliding on superhydrophobic surfaces

Liquid drops move very easily on superhydrophobic surfaces due to the very low contact angle hysteresis [142,143] (lotus leaf effect [19]): the sliding angle α_s is much lower than on hydrophilic or hydrophobic surfaces. In this case, sliding angles depend on factors such as surface wettability and texture geometry and roughness, being very different on various surfaces: for example in [144] the sliding angle of a 5 μl water droplet was found to be between 5° and 30° depending on the area fraction of the solid liquid interface; Miwa *et al.* [145] produced instead a substrate featuring a sliding angle of 1° for 7 μl water droplets.

The behavior of drops moving on superhydrophobic inclined surfaces is strictly related to the viscosity of the fluid and the two cases of low viscosity, i. e. similar to water, and high viscosity, i. e. much higher than water, are discussed below in two distinct sections.

Low viscosity fluids

Initial sliding motion of low viscosity small droplets consists of an uniformly accelerated motion. Acceleration is constant because at this stage air friction is negligible and forces acting on the drop are the gravitational force F_g and a resistance force R, due to interaction with the surface, independent on drop velocity, which can be considered as a dynamic friction. The resulting equation of motion is:

$$\begin{aligned} ma &= F_g - R \\ &= mg\sin\alpha - \mu N \\ &= mg\sin\alpha - \mu mg\cos\alpha \end{aligned} \tag{1.30}$$

$$\tag{1.31}$$

where m is the droplet mass, a is its acceleration, g is the gravity acceleration, α is the inclination angle of the plane, μ is the dynamic friction coefficient and N is the normal force [146].

The consequent motion law is very simple:

$$x(t) = \frac{1}{2}g(\sin\alpha - \mu\cos\alpha)t^2 \tag{1.32}$$

where x is the coordinate along the plane and t is time.

If also R can be ignored [147], the motion law becomes even simpler:

$$x(t) = \frac{1}{2}gt^2\sin\alpha \tag{1.33}$$

where x is the coordinate along the plane and t is time.

These equations suggest that, in the early phase of motion, drops behave as a mass point system, exhibiting a very small deformation and above all a pure sliding motion (this behavior has been confirmed observing internal fluidity through PIV [146] (see figure 1.17(a))). Then, the motion can be still accelerated, but with a smaller speed for a given position because the droplet starts rolling with a moment of inertia equal to $(2/5)mR$ where R is drop radius. Accordingly, the new law for free fall is $x = (5/14)gt^2 \sin\alpha$ [148].

Due to the very low friction droplets can move very fast ($U \sim 1$ m/s) and a terminal constant velocity can be reached after travelling very long distances (up to around a meter [148]) and when air friction becomes important. In this terminal regime drops elongate developing a trail in their rear part which bends up, more or less perpendicularly to the surface, as depicted in figure 1.18, and so liquid deposition at the rear of the drop does not occur, leaving the substrate completely dry after water passage [147, 148].

Internal motion is no more uniquely translational, but drops slide down the surface both sliding and rolling: more precisely PIV and PTV measurements [144] show two different behaviors inside water drops (see figure 1.17(b)):

- particles in the inner part move following the motion direction of the droplets, i. e. inner regions are characterized by a pure translational motion;
- particles near the edge change their vertical position during drops movement, meaning that rotational motion affects only a liquid layer at the edge of the drop.

Despite the complexity of shape and internal fluidity, a scaling law for the terminal velocity can be obtained by balancing friction and drop weight. The Reynolds number of this system is $Re = \rho_a RU/\eta_a \approx 10$, where the subscript a refers to air, and consequently the friction should be inertial, i. e. of the form $\rho_a R^2 U^2$, leading to a terminal velocity scaling as

$$U \sim \left(\frac{\rho g R \sin\alpha}{\rho_a}\right)^{1/2} \tag{1.34}$$

and resulting around a few meters per second, as found in the experiments.
On the other hand, inertia would tend to expand a drop in the direction perpendicular to its trajectory [149], while the droplet elongates, a behavior typical of viscous dissipation (see Section 4.1 for more details). A construction based only on inertial friction does not consider that drops are moving on a film of air. The viscous friction associated to the presence of an air layer of thickness δ is of the order of $\eta_a(U/\delta)R^2$ and the corresponding descent velocity is:

$$U \sim \frac{\rho g R \delta \sin\alpha}{\eta_a} \tag{1.35}$$

which is equal to a few meters per second for δ ranging between 1 and 10 μm [148]. However a measurement of δ is very challenging, because of its very small size comparable with the height of structures forming superhydrophobic surfaces.
The complete understanding of the sliding terminal velocity of drops with low viscosity would require a further experimental investigation, but, to the best of our knowledge, such a work has not appeared in literature yet.

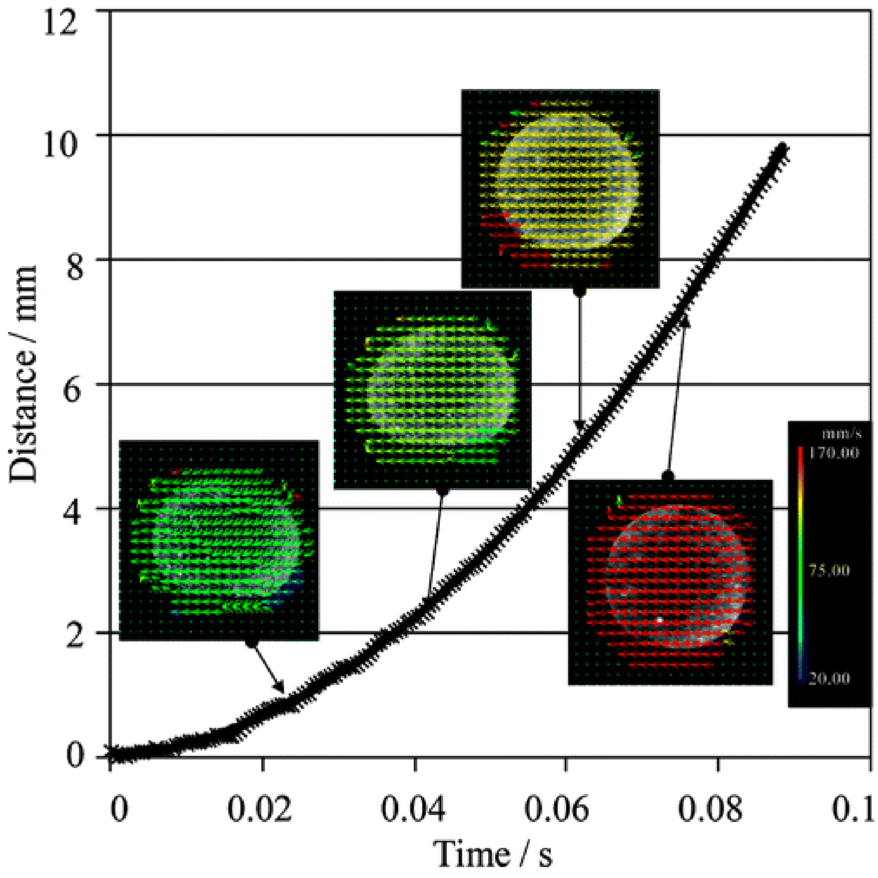

(a)

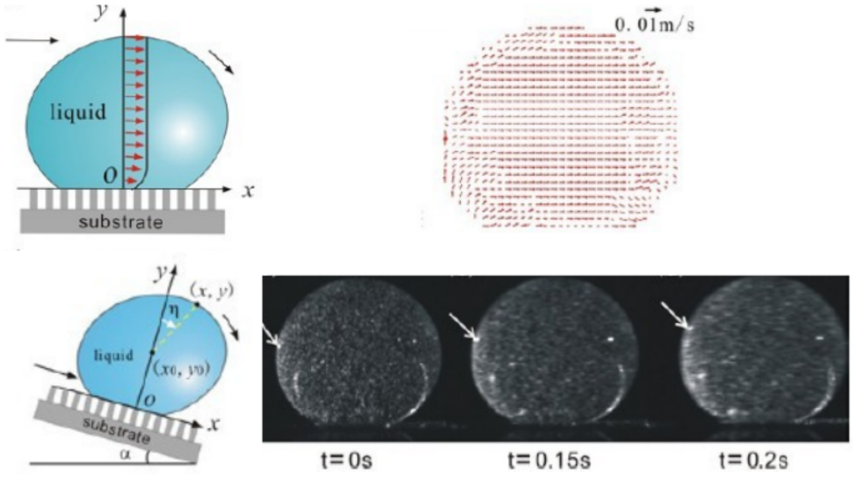

(b)

Figure 1.17 : (a) internal fluidity in the early stage of motion on superhydrophobic surfaces: only sliding [146]; (b) PTV revealing both translational and rolling motion inside a water drop on a superhydrophobic surface [144].

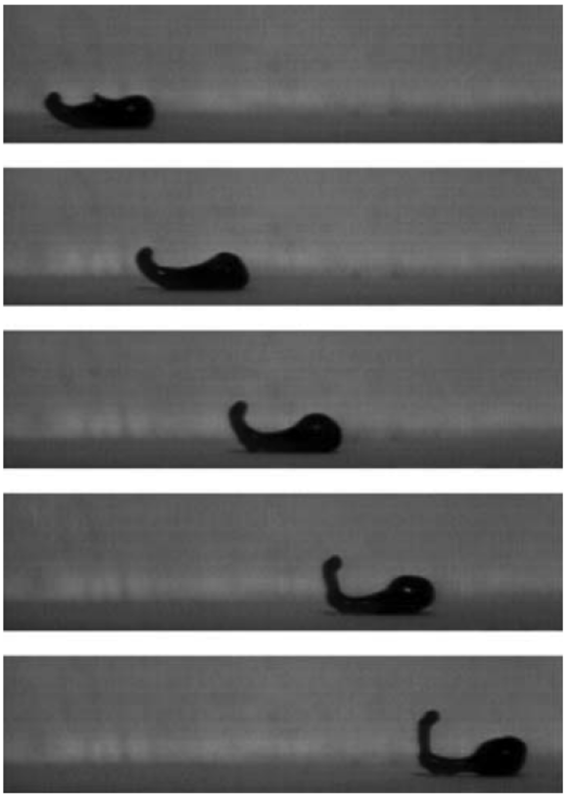

Figure 1.18 : Successive snapshots of a water drop (initial radius R $\sim$ 2.5 mm) running down a superhydrophobic plate inclined by $\alpha = 60°$. The picture width is 41 mm, the interval between snapshots 2.8 ms, and the drop speed $U \sim 2.5$ m/s. At such a high velocity, the drop elongates up to almost a centimeter and the tail in the rear bends up and leaves the substrate, which remains dry behind the drop despite the speed [148].

High viscosity fluids

The behavior of drops featuring a high viscosity (typically much bigger than water) depends on drop size, discriminated/classified according to the capillary length K^{-1}, as reported in Section 1.3.

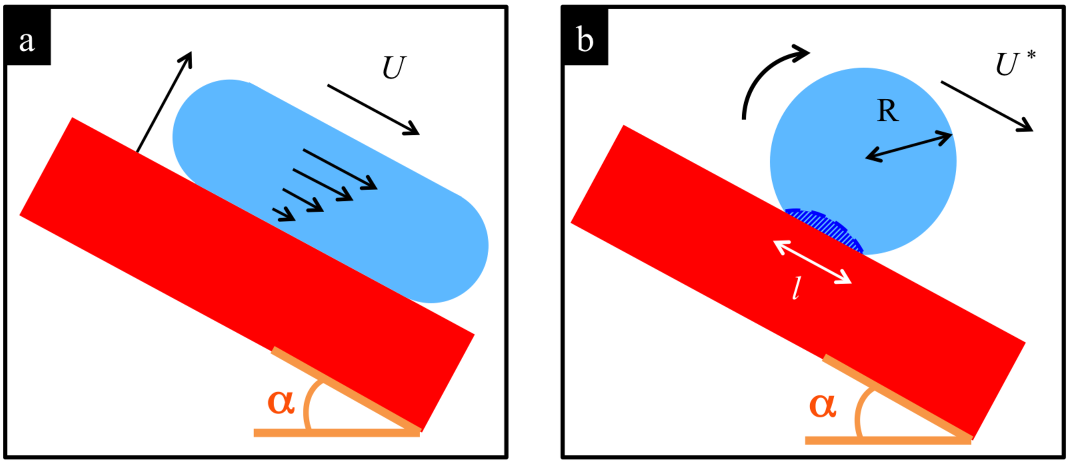

Figure 1.19 : Cartoons of viscous drops sliding down a superhydrophobic surface: a) big drop with size higher than the capillary length; b) droplet with radius smaller than the capillary length, where the viscous dissipation occurrs in the dashed region near the contact area.

Big drops sliding down a plane tilted by α with stationary velocity U feature a velocity gradient inside the drop of order U/K^{-1}, as shown in figure 1.19a. The value of U can be determined from the comparison between gravity and viscous force (derived by Huh and Scriven [150]):

$$\rho R^2 K^{-1} g\alpha \sim \eta \frac{U}{K^{-1}} R^2 \tag{1.36}$$

leading to

$$U \sim \frac{\rho g}{\eta} K^{-2} \alpha \sim \frac{\sigma}{\eta} \alpha : \tag{1.37}$$

U does not depend neither on ρ nor on g because gravity determines both the height of the puddle (and consequently the velocity gradient related to dissipation) and the force causing drop sliding.

Small droplets roll on the surface in order to minimize viscous dissipation which is relegated in the region near the contact line, as depicted in figure 1.19b [151]. In this case the torque balance has to be considered:

$$\rho R^3 g\alpha R \sim \eta \frac{U}{R} l^2 l \tag{1.38}$$

and, consequently,

$$U^* \sim \frac{\rho g \alpha}{\eta} \frac{R^5}{l^3}. \tag{1.39}$$

The terminal velocity U^* assumed by a rolling droplet is higher than the corresponding velocity associated to the sliding where viscous dissipation occurs in the whole drop [150, 152] (cfr. equation 1.37):

$$U^* \sim U\frac{K^{-1}}{R} > U. \tag{1.40}$$

More interestingly, equation 1.39 hides a counterintuitive and surprising scaling of the velocity:

$$U^* \sim \frac{1}{R} \tag{1.41}$$

considering that $l \sim R^2$ (see Section 1.3). Smaller droplets move faster than bigger drops [151]!

§ 1.6. Numerical simulations

The behavior of sessile drops on horizontal or inclined surfaces can be modelled through a huge variety of numerical methods as, for instance, lattice Boltzmann [153–156], Surface Evolver [157,158], molecular-dynamics [159, 160], lubrication theory [161, 162], smoothed particle hydrodynamics [137], boundary element method [163], Cahn-Hilliard/Navier-Stokes model [164] ....
In this section we briefly describe the numerical techniques implemented by our coworkers (prof. mauro Sbragaglia, dr. Ciro Semprebon and prof. Carlo Massimo Casciola) to explain and complete our experimental work: lattice Boltzmann simulations, modelling based on the Surface Evolver program and the Cahn-Hilliard / Navier-Stokes (CHNS) approach.

§ 1.6.1. Lattice Boltzmann simulations

The lattice Boltzmann (LB) model [153–156] allows to reproduce the diffuse-interface hydrodynamic equations for a binary mixture of 2 components [164,165], say A and B, with A indicating the "rich" phase inside the droplet. The LB equation evolves in time the discretized probability density function $f_{\zeta i}(\mathbf{r}, t)$ to find at position $\mathbf{r}$ and time t a fluid particle of component $\zeta = A, B$ with velocity $\mathbf{c}_i$ according to the LB updating scheme

$$f_{\zeta i}(\mathbf{r} + \mathbf{c}_i, t + 1) - f_{\zeta i}(\mathbf{r}, t) = \Delta_{\zeta i} + \Delta^g_{\zeta i} \tag{1.42}$$

expressing the streaming of the probability density function (lhs of equation (1.42)) together with a relaxation towards a local equilibrium ($f^{(eq)}_{\zeta j}$)

$$\Delta_{\zeta i} = \sum_j \mathcal{L}_{ij}(f_{\zeta j} - f^{(eq)}_{\zeta j}) \tag{1.43}$$

with $\mathcal{L}_{ij}$ a relaxation operator whose properties have been described in many papers (see [166, 167] and references therein). The term $\Delta^g_{\zeta i}$ represents a forcing term used to introduce the volume force ($\mathbf{g}$, gravity) and the immiscibility between the two components [156,167,168]. The distribution functions are related to the physical variables, i.e. the fluid densities $\rho_{A,B} = \sum_i f_{A,Bi}$, and the total momentum

$\rho\mathbf{u} = \sum_i f_{A,Bi}\mathbf{c}_i$ with $\rho = \rho_A + \rho_B$ the total density. It can be shown (see [167] and references therein) that with a suitable choice of the equilibrium distribution function $f^{(eq)}_{\zeta j}$ and the forcing term $\Delta^g_{\zeta i}$, equations (1.42-1.43) reproduce the continuity equation for the total density $\rho = \rho_A + \rho_B$

$$\partial_t \rho + \nabla \cdot (\rho \mathbf{u}) = 0 \tag{1.44}$$

plus an advection-diffusion equation for the order parameter $\phi = \rho_A - \rho_B$

$$\partial_t \phi + \nabla \cdot (\phi \mathbf{u}) = \nabla \cdot (M \nabla \mu).$$

The mobility M is the constant of proportionality in the linear phenomenological law relating the thermodynamic flux to the thermodynamic force expressed by the gradient of the chemical potential μ [169]. In the case of a drop on an inclined plane the Navier-Stokes equation for the fluid velocity $\mathbf{u}$ is:

$$\rho \left(\partial_t \mathbf{u} + \mathbf{u} \cdot \nabla \mathbf{u}\right) = -\nabla \cdot \bar{\bar{P}} + \nabla \cdot \bar{\bar{\tau}} + \rho_A \mathbf{g} \sin\alpha \tag{1.45}$$

where $\bar{\bar{\tau}}$ is the viscous stress tensor with components $\tau_{ij} = \eta(\partial_i u_j + \partial_j u_i)$, with η the dynamic viscosity. Both the pressure tensor $\bar{\bar{P}}$ in equation (5.1) and the chemical potential μ in equation (1.44) can be made compliant with a continuum free energy (see [169] for the explicit expression of the free energy) by suitably choosing the forcing term in equation (1.42). The free energy regulates the immiscibility and drives the system towards the segregation of the two fluids. The resulting physical domain is partitioned into two different subdomains, each occupied by a pure fluid with the interface between the two fluids described as a thin layer of thickness ℓ where the fluid properties change smoothly. The surface tension [169] at the free interface of the drop and the wetting properties [153–155] at the fluid-solid interface are input via such a free energy. The values of the interface thickness ℓ and the mobility M need to be larger than those suggested by physical considerations in order to make the simulations affordable [164, 165]; they are therefore empirically tuned in comparison with experimental results [167]. Another control parameter is the viscous ratio $\chi = \eta_A/\eta_B$: a proper choice of the relaxation operator in (1.43) allows to tune the viscosity inside (η_A) and outside (η_B) the droplet, as the viscosity coefficients depend on the eigenvalues of $\mathcal{L}_{ij}$ [166]. Numerical simulations with very large χ are quite unstable and technical improvements are needed to cure such numerical instabilities. Nevertheless, the viscous ratio can be changed by one order of magnitude, from $\chi = 20$ to $\chi = 1$, without suffering simulation artefacts. The gravity in equation (5.1) is only projecting in the down-plane direction and is only applied to the A phase (the rich phase inside the drop). Such body force monotonously decreases to zero across the fluid-fluid interface: this accounts for the fact that the outer phase remains inert in the limit of zero drop size.

The LB model is a *mesoscopic model* retaining the essential supramolecular details of fluid-fluid and fluid-solid interactions (surface tension, wetting angle, etc.) without surrendering -actually boosting- the computational efficiency of continuum methods. This simulations escape a purely continuum treatment, and yet, still exhibit sufficient universality to do away with a fully atomistic description.

§ 1.6.2. Surface Evolver

The public domain software Surface Evolver, developed by Ken Brakke [170], allows to determine the equilibrium shape of the interface by minimizing the total energy [158, 171]. For a drop moving on an inclined plane at small capillary numbers, the energy is mostly dissipated at the contact line, while in the bulk and at the free liquid interface the contribution is less relevant. As a consequence, a suitable model to describe this system is the Contact Line Dominated Dynamics model (CLDD) which assumes that the free liquid interface relaxes at a much smaller timescale than the contact line, and therefore at each instant its shape is simply dictated by the Laplace law

$$\Delta P + \rho\, g\, \langle x \rangle \ = \sigma \kappa \tag{1.46}$$

where g is the acceleration of gravity acting in the x direction and σ is the liquid-vapour tension of an interface with mean curvature κ. For a given contour Γ of the contact line, the shape Σ of the liquid interface is obtained by minimizing the energy

$$E\{\Sigma\} = \sigma\, A_{\mathrm{lv}} - \rho\, g\, V\, \langle x \rangle \tag{1.47}$$

where A_{lv} is the area of the free interface, and where the liquid volume V is fixed by an additional constraint. Equation (1.47) can be solved with standard minimization algorithms by means of the Surface Evolver software representing the liquid-vapor interface by a mesh of small triangles, as shown in figure 1.20.

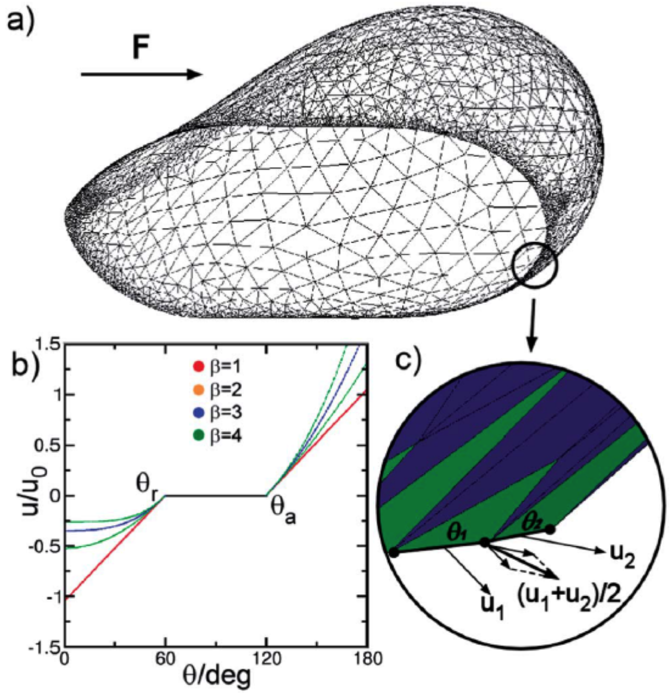

Figure 1.20 : (a) Snapshot of a sliding drop in a Surface Evolver simulation illustrating the different levels of the mesh refinement. (b) Functional dependence of the model for the contact line velocity for different exponents β. (c) Magnification of the region close to the contact line to illustrate the implementation of the dynamic law. The local contact angle is computed from the surface normal of the triangles sharing an edge with the contact line (shown in green) [158].

The motion of the contact line is performed by normally displacing the elements in contact with the substrate (see figure 1.20c), depending on the local contact angles θ and the relation between contact angle and contact line velocity u (see figure 1.20b):

$$u = \begin{cases} \dfrac{u_\mathrm{a}}{\beta\theta_\mathrm{a}^{\beta-1}}(\theta^\beta - \theta_\mathrm{a}^\beta) & \text{for} \quad \theta \geq \theta_\mathrm{a} \\ \dfrac{u_\mathrm{r}}{\beta\theta_\mathrm{r}^{\beta-1}}(\theta^\beta - \theta_\mathrm{r}^\beta) & \text{for} \quad \theta \leq \theta_\mathrm{r} \end{cases} . \tag{1.48}$$

The friction coefficients u_a and u_r are phenomenological parameter, accounting for the energy dissipation in the wedge [152], which could be deduced from the experiments. The exponent β mimics the leading order scaling of certain models proposed for the contact line motion. The linearized relationship around the static values of the contact angles θ_a and θ_r reduces to a friction law, taking $\beta = 1$; $\beta = 2$ corresponds to the molecular kinetic theory according to Blake [172], while $\beta = 3$ corresponds to the continuum hydrodynamic model of Voinov [173] and Cox [174].

§ 1.6.3. Cahn-Hilliard / Navier-Stokes (CHNS) model

The Cahn-Hilliard / Navier-Stokes (CHNS) model describes the flow of two immiscible fluids where capillary effects and contact line motion play a crucial role on the fluid dynamics [164, 175, 176].
The binary system constituted by two pure, immiscible fluids of density ρ_A and ρ_B, respectively, is described by a scalar function, the *phase field* $\Phi(\mathbf{x}, t)$, defined as $\Phi(\mathbf{x}, t) = 2\left[\rho(\mathbf{x}, t) - (\rho_A + \rho_B)/2\right] / (\rho_A - \rho_B)$, where $\rho(\mathbf{x}, t)$ is the local density of the mixture, such that $-1 \leq \Phi \leq 1$. The Cahn-Hilliard model corresponds to a non-local free energy functional

$$\mathcal{F}[\Phi] = \int_\Omega \left(f_{bulk}(\Phi) + \frac{\lambda}{2} |\boldsymbol{\nabla}\Phi|^2 \right) dV + \int_{\partial\Omega} f_w(\Phi)\, dS \,, \tag{1.49}$$

where $\lambda = 3\sigma\epsilon/\sqrt{8}$ is a coefficient related to the surface tension σ and to the interface thickness ϵ, combined with the constraint of mass conservation of the two species. In equilibrium conditions the free-energy is a minimum and, away from the wall, the double-well shaped bulk free energy density, $f_{bulk} = \lambda(\Phi^2 - 1)^2/(4\epsilon^2)$ with two minima in $\Phi = \pm 1$, drives the system towards the segregation of the two species. Conversely, the gradient excess term $\lambda/2|\boldsymbol{\nabla}\Phi|^2$ energetically penalizes the formation of sharp interfaces. As a consequence of these two counteracting mechanisms, a finite thickness interface (width of order ϵ), across which Φ varies smoothly, separates the two bulk fluids in such a way to minimize the interfacial energy. The presence of the wall modifies this equilibrium, as prescribed by the last term, $f_w(\Phi) = -\sigma\cos(\theta)\Phi(3 - \Phi^2)/4 + (\sigma_{wA} + \sigma_{wB})/2$, which describes the fluid-wall interaction. The wall energy, away from the contact line (i.e. in the portion of the wall where $\Phi = \pm 1$), provides the fluid-wall interfacial tensions $\sigma_{wA} = f_w(\Phi = 1)$ and $\sigma_{wB} = f_w(\Phi = -1)$. Apparently, $\sigma_{wB} - \sigma_{wA} = \sigma\cos(\theta)$ recovers the Young's equation for the equilibrium contact angle.
The model can be extended to unsteady isothermal conditions in presence of fluid motion described by the velocity field $\mathbf{u}$. Under the assumption of a small density variation, i.e. $2\,(\rho_A - \rho_B)\,/\,(\rho_A + \rho_B) \ll 1$, the velocity field is solenoidal to first order in the density variation, and the dimensionless form of the system reads

$$\boldsymbol{\nabla} \cdot \mathbf{u} = 0 \,, \tag{1.50}$$

$$\frac{D\Phi}{Dt} = \frac{\mathrm{M}}{\mathrm{Cn}}\nabla^2\mu_c\,, \tag{1.51}$$

$$\frac{D\mathbf{u}}{Dt} = -\frac{1}{\rho}\boldsymbol{\nabla}p + \frac{1}{\mathrm{We}\,\mathrm{Cn}}\mu_c\boldsymbol{\nabla}\Phi + \frac{1}{\mathrm{Re}}\nabla^2\mathbf{u} + \tilde{f}\,. \tag{1.52}$$

The chemical potential μ_c is defined as the functional derivative of the free energy (1.49) with respect to the phase field, $\mu_c = \delta\mathcal{F}/\delta\Phi = \Phi^3 - \Phi - \mathrm{Cn}^2\nabla^2\Phi$ where $\mathrm{Cn} = \epsilon/L$ is the Cahn number, ratio of interface thickness and macroscopic length scale L. In equations (1.51,1.52) $\dfrac{D(\cdot)}{Dt} = \partial(\cdot)/\partial t + \mathbf{u}\cdot\boldsymbol{\nabla}(\cdot)$ is the material derivative, $\mathrm{Re} \sim \rho RU/\eta$ is the Reynolds number with R and U typical drop radius and velocity, $\mathrm{We} \sim \rho U^2 R/\sigma$ is the Weber number, $\tilde{f}$ is the external force per unit mass. Finally $\mathrm{M} \sim M^*\sigma/(L^2U)$ is the dimensionless *mobility coefficient* with M^* the *mobility.* In ordinary conditions the physical interface thickness is on the nanometer scale and the model cannot be exploited for macroscopic flows unless an artificial thickening of the interface is introduced. It is crucial that such artificial thickening does not alter the dynamics. Indeed the *sharp interface limit* is obtained when the macroscopic solution becomes independent of Cn and M at decreasing their values. In [164] the scaling law $\mathrm{M} \propto \mathrm{Cn}^2$ is shown to be crucial in approaching the physically meaningful solution in the limit of decreasing Cahn number, which is recovered at $\mathrm{Cn} = \mathcal{O}(10^{-2})$.

Chapter 2

Experimental system to study drop behavior

The experimental analysis of drop behavior on inclined surfaces is based on two imaging setups: an apparatus for the wettability characterization of the samples and an apparatus for measurements on tilted surfaces.

The setup adopted for standard wettability analysis is described in detail in Section 2.1 and provides the evaluation of static and dynamic contact angles of sessil droplets deposited on the horizontal surface. Section 2.2 reports a detaild description of the fundamental instrument for our study: the apparatus formed by a motorized stage inclining the samples by the desired angle. Such setup is used mainly for two kinds of measurements: sliding and stickiness. Finally Section 2.3 deals with two programs used for images analysis, aimed at finding drops contour to be interpolated.

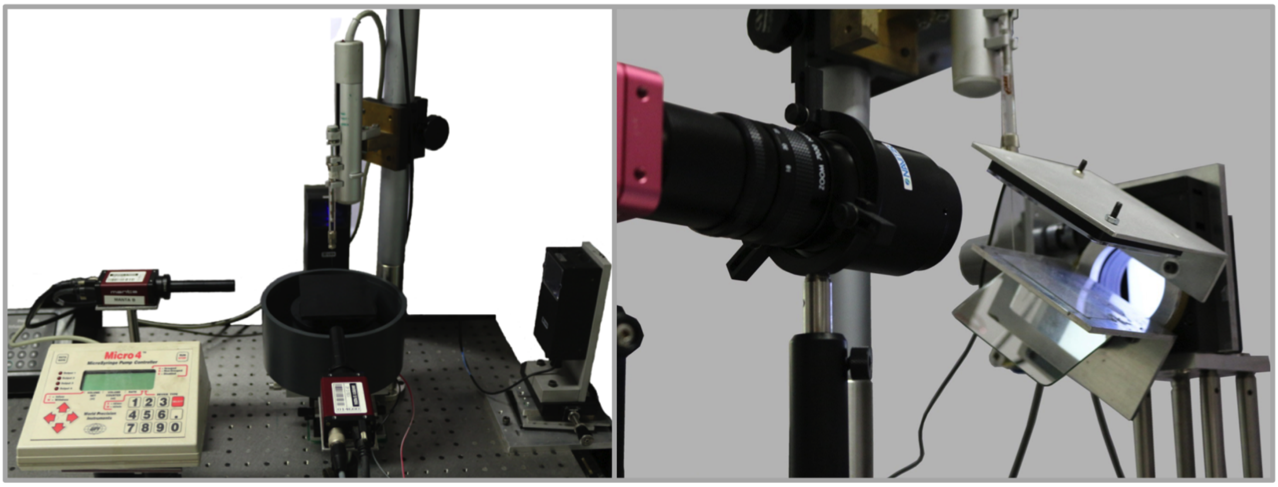

§ 2.1. Experimental setup for wettability characterization

The setup used to measure both the static and the dynamic contact angles of a sessile drop is depicted in figure 2.1

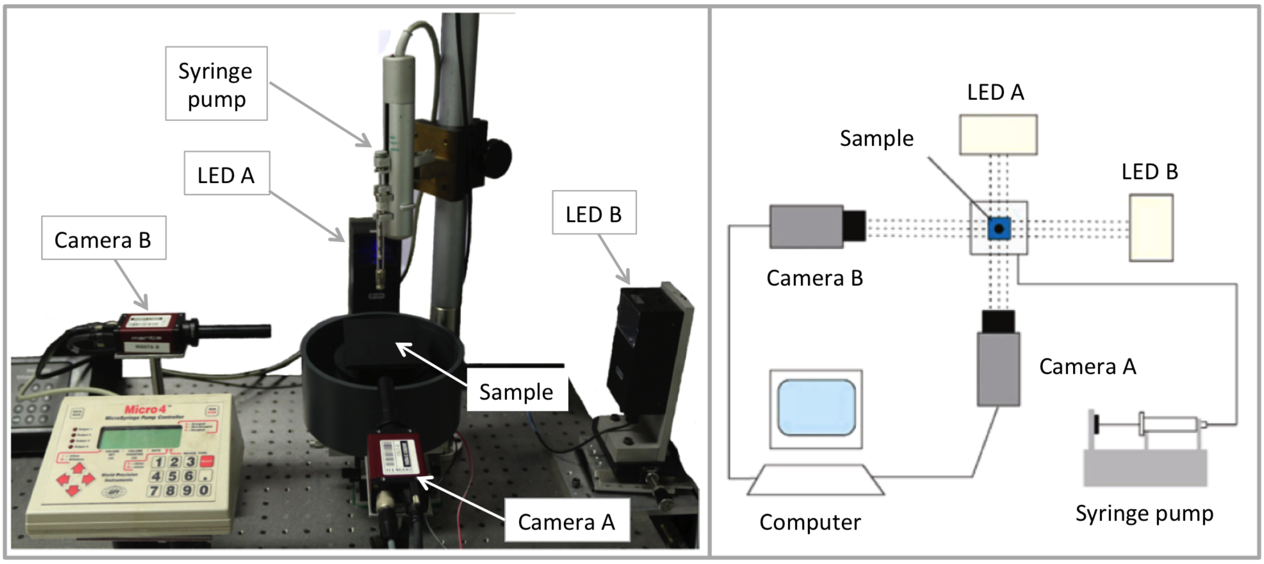

Figure 2.1 : Photograph (left panel) and cartoon (right panel) of the experimental setup used for sessile drops measurements.

A known volume of liqiuid is gently deposited on the surface by means of a vertical syringe pump (World Precision Instruments, Inc.). The drop is simultaneously viewed by two CCD cameras (Manta G-146, Allied Vision Technologies) equipped with a telecentric objective 2X looking at two perpendicular directions. Correspondingly, the drop is back-enlighted by two blue LED sources focused in the cener of the sample holder. This configuration is useful to characterize the wetting properties of anisotropic samples featuring, for instance, grooves, stripes or rectangular domains.
The two cameras can acquire single images, for the evaluation of the static contact angle , or sequences of images working up to 17 fps, to measure the advancing or receding contact angles by pregressively increasing or reducing the droplet volume at the desired flow rate.

§ 2.2. Apparatus for sliding measurements

The experimental apparatus is imaged in figure 2.2.

Droplets of the desired volume are leant on the surface through a syringe pump (World Precision Instruments, Inc.). The sample is placed on a tiltable support whose inclination can be set with a 0.1° accuracy. A mirror mounted under the sample stage at 45° with respect to the surface allows to view the contact line and the lateral side of the drop simultaneously. The drop is illuminated by two white LED backlights (Phlox). The sample stage, the mirror and the light above the drop rotate together, while the light behind the drop is fixed.
To record drop motion on the inclined sample different cameras and objective lens are used according to the kind of required measurement:

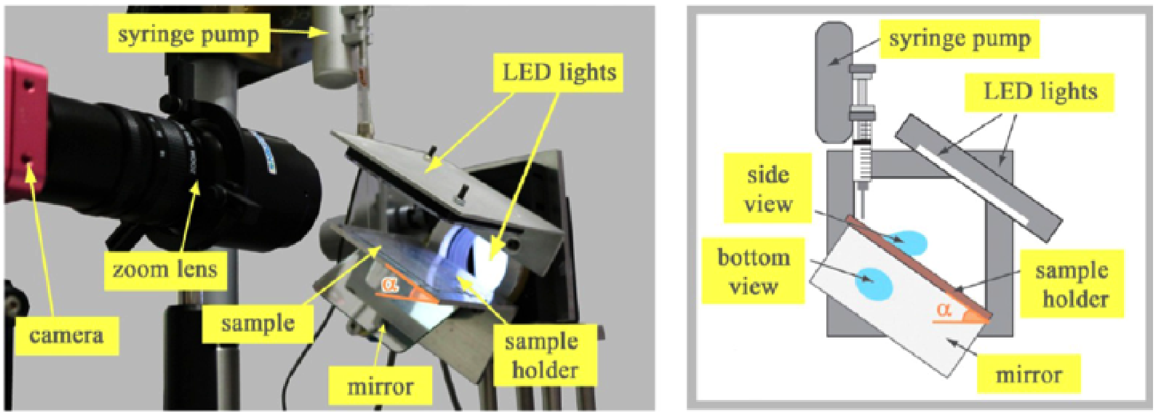

Figure 2.2 : Left: Photograph of the optical setup used to observe the sliding of water drops. Right: Cartoon of the setup where the contact line and the lateral side of the drop are seen simultaneously.

- camera Pulnix, TM1402CL, with a CCD sensor formed by 1392x1040 pixels and working at fixed frame rate (30 frame per second). This camera has a very good resolution and provides excelent quality images, but is limitated by the acquisition rate, as a consequence it is useful for the recording of static or very slow drops;

- camera CMOS MV-D1024E Camera Link, featuring a 1" sensor with resolution of 1024x1024 pixel. This camera offers the advantage to set the acquisition rate between a few to almost 120 fps at full frame and for this reason it is the most widely used in our experiments;

- camera PHANTOM, v7.3, with a resolution of 800x600 pixel. The maximum frame rate of this fast camera is 8 kHz full frame and is exploited for the study of very fast fenomena, as for example the motion of drops on vibrating surfaces (see Chapter 8);

- telecentric 2X objective, necessary for precise measurements of contact angles;

- macro zoom lens Navitar 7000, with an adjustable magnification allowing to see the whole motion of the drops (just from the side view or both side and bottom view), but also to focus on a droplet detail as, for instance, the contact angles, even if with lower quality images than using the telecentric objective.

§ 2.3. Images analysis

Acquired images are analyzed through two home made programs, written in *LabVIEW*8.2.1 [177]:

- **contact_angles.vi,** a program which analyses singular frames and finds drops contact angles;

- **sliding.vi,** a program processing image sequences, yelding front and rear contact points for every frame, so that motion law and drop length behavior can be reconstructed.

These softwares are very similar: both of them first find the drop contour and then fit its points with a polynomial function, subsequently used to obtain contact angles and contact points.

Preliminary image treatment: the first step of both programs allows an image correction, if it is necessary to improve its quality, by adjusting BCG values in the *LabVIEW* tool **IMAQ BCGLookup** [178]:

- **Brightness** defines the brightness of the frame. This value is used as the x intercept of the transfer function in the lookup table. The neutral value 128 does not modify the image, a higher value returns a brighter image and a lower value decreases its overall brightness;
- **Contrast** sets the contrast of the image. This parameter is the slope of the transfer function in the lookup table (expressed in degrees). The neutral value is 45, a greater value increases image contrast and a value smaller than 45 returns a less contrasted frame;
- **Gamma** means the gamma correction applied to the image. The default value is 1. A higher value returns extended contrast for small pixel values and less contrast for large pixel values. On the contrary, a value lower than 1 gives a frame with less contrast for small pixel values and extended contrast for large pixel values.

Then the image must be rotated, so that the plane becomes horizontal, for a correct calculation of angles and in-plane coordinates. The rotation is performed by the two programs using a line drawn parallel to the surface as a reference. Finally programs require areas where contour points must be searched:

- for **contact_angles.vi** the areas to be selected are two rectangles on the two sides of the drop;
- **sliding.vi** needs a line as an input (drawn only on the first image of the sequence), intersecting drop profiles in all the images of the sequence.

Outline determination: programs scan selected areas of the images and choose outline points according to the *LabVIEW* function **IMAQ Edge Tool**. The filter used to detect the edges is defined by three parameters:

- **Contrast** specifies the threshold for the contrast of the contour: only edges with a contrast higher than this value are considered. **Contrast** is defined as the difference between the average pixel intensity before and after the boundary;
- **Filter width** represents the number of pixels that the program averages to find the contrast at either side of the contour;
- **Steepness** quantifies the slope of the edge: its values is the number of pixels that correspond to the transition area of the outline. Points where **Contrast** is reached in a pixel range larger than **Steepness** are discarded.

For other details about this function we refer to [178].
An example of the profile detection is shown in figure 2.3.

Polynomial fit: once the points forming the drop contour are determined, they are fitted with a polynomial function of the desired order (in our case 3 or 4). In the case of **contact_angles.vi** all

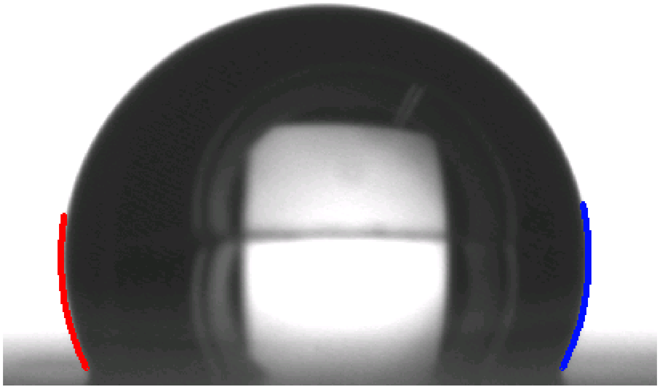

Figure 2.3 : Contour detection through the program **contact_angles.vi**.

the points in the selected rectangles are fitted; instead, in the case of **sliding.vi** only points under a red line (whose position can be adjusted to obtain a sufficient number of points) are considered for the interpolation, as depicted in figure 2.4.

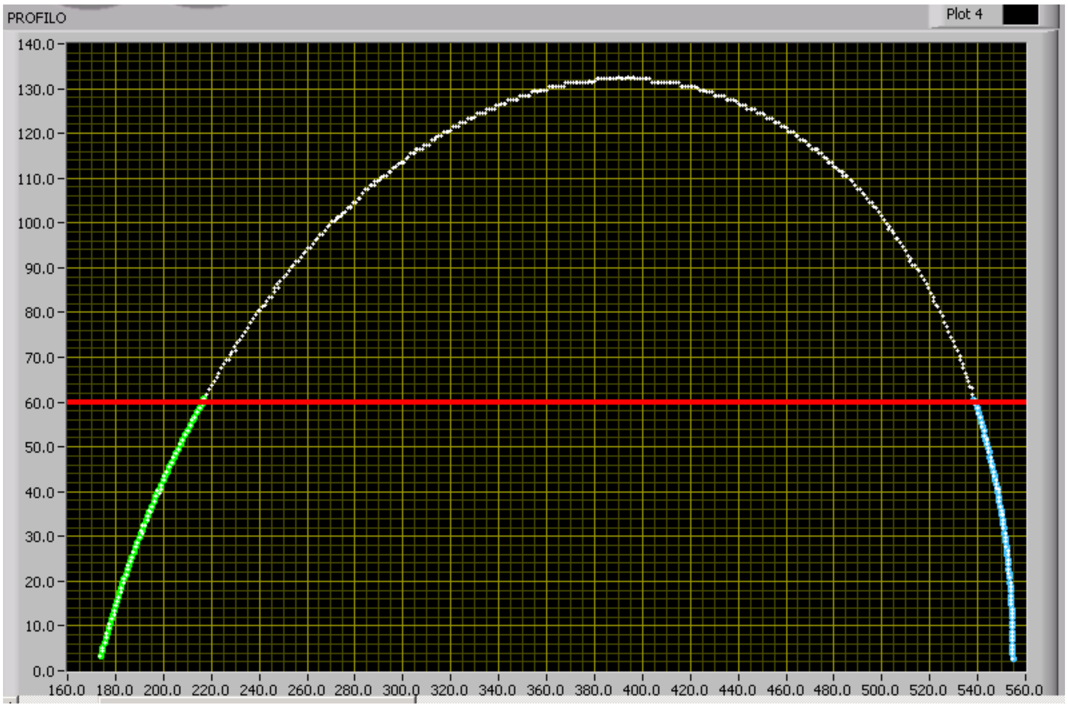

Figure 2.4 : Example of profile fitted by the **sliding.vi** program. White points are contour points, green and light blue points belong to fitting polynomial. Only outline under the settable red line are interpolated.

Interpolation polynomials are finally used in order to derive useful data (contact angles and contact points), calculating their tangents or intersections with the plane line.

Chapter 3

Hairy surfaces

Nature offers several examples of surfaces exhibiting different wettability properties, ranging between the water-repellent lotus leaf and the high adhesion of flower petals. In all these cases a suitable roughness at the micro-/nanoscale is necessary to achieve the particular wetting behavior. Inspired by such examples, we produced hairy samples of polymers having similar wettability but very different elasticity, in order to disentangle the contribution of texture morphology and stiffness to surface adhesion properties. This work is the object of the following chapter, beginning with an extended review of literarure about geometrically patterned surfaces (Section 3.1), then the fabrication protocols applied to realize our samples are described in Section 3.2 and the corresponding morphological and wettability analysis are reported in Section 3.3. the adhesion properties are discussed in section 3.4 and lastly conclusions are summarized in section 3.5.

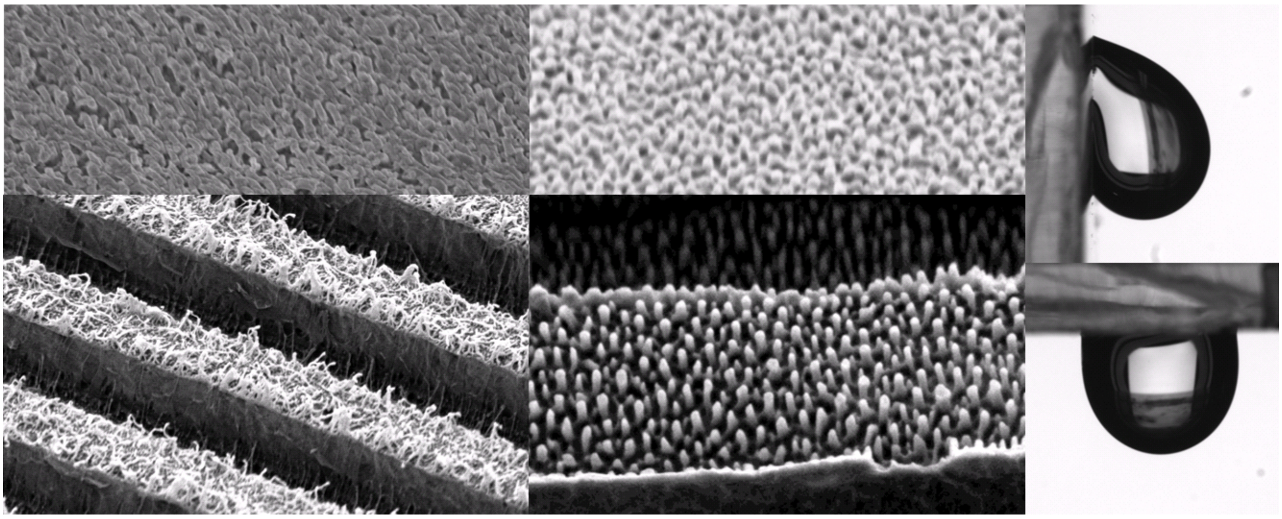

§ 3.1. Introduction

Various methods have been devised for the realization of rough surfaces at the micro-/nanoscale to produce low-adhesion superhydrophobic surfaces, including fractal growth of wax by solidification [179], nanocasting [180],nanoimprint lithography, wet etching and plasma etching [181], photolithography and reactive ion etching [182], surface micromachining combined with chemical modification [183] and silica sol-gel nanoimprint lithography [184]. Attention has also been devoted to the fabrication of smart coatings which can change their wettability when subject to specific external stimuli, like light [55,185,186], temperature [187,188], pH [189,190]. More recently, sticky surfaces [41,50,191,192] and surfaces with switchable adhesion [193–201] have also been obtained.

One simple and reproducible method of fabricating sticky hairy surfaces relies on replica molding of suitable templates by polymers. The rose-petal surface structure was replicated by employing a UV molding process using polyurethane acrylate (PUA) for the first replica and perfluoropolyether (PFPE) for the second replica [202]. As a result, PFPE micro-nanostructures, which were identical to the rose-petal hierarchical structure, were formed on a glass substrate. A water contact angle of 144° and contact angle hysteresis of 83° were found. Adhesive superhydrophobic surfaces were obtained by casting poly(dimethylsiloxane) (PDMS) on silicon carbide paper characterized by a rough texture at the micron scale [203]. Two-level polymer fibril structures with high aspect ratio were fabricated using stacked porous polycarbonate membranes as a template with nanoscale pores [204]. Structures in polypropylene were created with different diameters and density of fibers. By changing the densities and diameter of nanofibers, superhydrophobic surfaces with either Lotus effect or gecko effect were obtained. Self-ordered nanoporous alumina membranes (AAO) constitute a particularly attractive template characterized by regularly arranged, parallel nanopores with narrow diameter distribution and uniform depth [205,206]. Sticky hairy surfaces were obtained by casting i) hard PDMS in these alumina membranes and peeling off the molded PDMS from the alumina template [49] and ii) polystyrene (PS) followed by dissolution of the template in an etching solution [50]. Water contact angles as high as 150° (162°) were observed on the hairy PDMS (PS) surface, and the maximum water volume they could hold while kept in a vertical position was of 12 μL (6 μL). Polymeric nanopillars of controlled length were fabricated using a two-step wetting method [207]. Firstly, by filling uncured PDMS into the nanopores of an alumina template and then dissolving partially the uncured PDMS, the depth of the nanopores is adjusted and increases with the dissolving time. Subsequently, the second wetting step by polymeric liquid with the PDMS filled alumina template yields length-controlled nanopillars. Polystyrene nanopillars of average height varying between 200 and 1200 nm were obtained and the water contact angle was found to increase from 90° to 150° on the longest hairs. Controllable adhesive superhydrophobic PDMS surfaces presenting arrays of regular micrometric pillars made by standard photo and soft-lithography [208] have been recently investigated. Square pillars with sides of a few micrometers and height up to 20 μm were prepared with two different mixing ratios (MR) of base to curing agent which alter the pillar stiffness. When the pillar height was larger than 3.3 μm, the patterned PDMS surfaces made with the standard MR=10:1 exhibited slippery superhydrophobic behavior while those of MR=20:1 were sticky. This different response was explained by the collapse of the softer PDMS (e.g., MR=20:1) pillars due to the deposition of water drops.

§ 3.2. Microfabrication protocol

The following section describes the microfabrication protocol adopted to produce hairy surfaces with two polymers chosen in order to maximize the difference in their elastic mechanical properties while maintaining similar morphological structure and nominal wetting characteristics such as contact angle with water: hard polydimethylsiloxane (h-PDMS) and polypropylene (PP). At room temperature, h-PDMS haves a modulus of $\sim$ 10 MPa [209] while PP a modulus of $\sim$1 GPa [210], ie. $\sim$ 100 times larger. The relative stiffness of the surfaces felt by a droplet contact line will be principally governed by this difference in modulus, modulated somewhat by differences in hairs height.

§ 3.2.1. Fabrication of silicon mold for micropatterned samples

Silicon molds were fabricated using standard photolithography techniques and reactive ion etching [211].

Photolithography is a microfabrication process used to selectively remove parts of a substrate. It exploits the properties of a photoresist, which is a light sensitive substance with different characteristics, depending on whether it is exposed to light or not. By means of light the mask pattern is transferred on the photoresist:

- if the resist is positive, the part exposed to light becomes soluble and can be removed;
- if the resist is negative, its exposed portion becomes insoluble to the photoresist developer and the unexposed part can be dissolved by the photoresist developer (see figure 3.1).

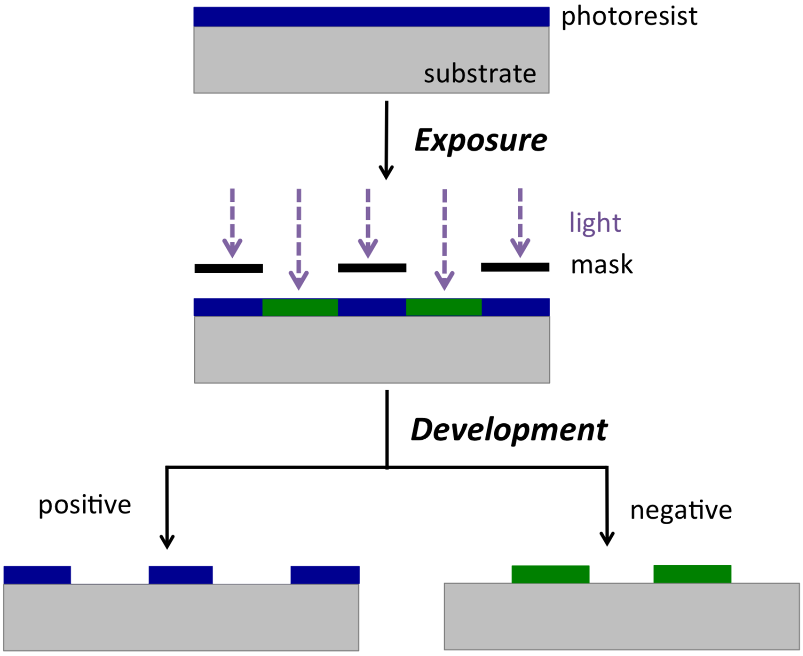

Figure 3.1 : Two types of photoresist: positive resist in the left hand side and negative resist in the right hand one.

The main steps of the production of grooved masters are sketched in figure 3.2. First of all, silicon samples (6 p type -100 oriented silicon wafers diced in 3x3 cm^2 pieces) are prebaked at 150° C for 5

minute to remove moisture and then spin coated using a positive photoresist (S1813 PR, Shipley) at 5000 round per minute (rpm) for 45 seconds. Subsequently, a 115° C soft bake for 90 seconds makes the solvent evaporate from the resist. The coated substrate is exposed for 3 seconds to UV radiation under a chromium glass mask with OAI Mask Aligner (Model MBA800). After the exposure, the non-polymerized parts of the resist layer are removed with the developer MF 319.
Using the patterned resist as an etch mask, the silicon is etched by reactive ion etching (Oxford ICP etcher) for 8 minutes. Finally, the remaining photoresist is removed with acetone in ultra-sound bath for 20 minutes.

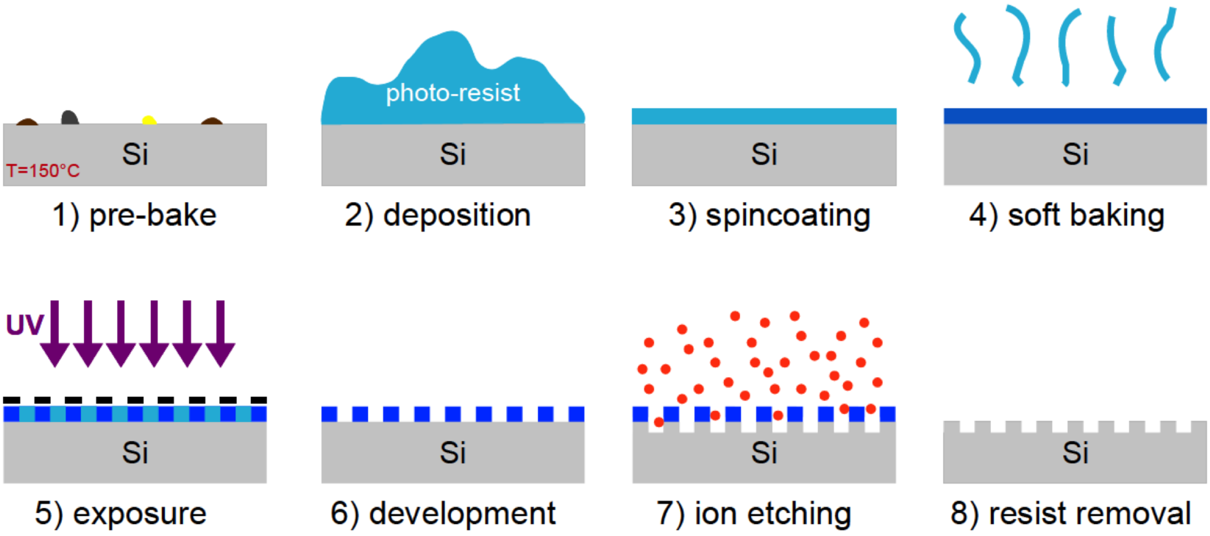

Figure 3.2 : Steps of the protocol adopted for the production of microgrooved silicon masters.

The resulting master consists of a 1.5 x 1.5 cm^2 silicon mold, containing line grating with 4 μm pitch (2 μm lines and grooves) with $\sim$ 2 μm groove depth (see figure 3.3).

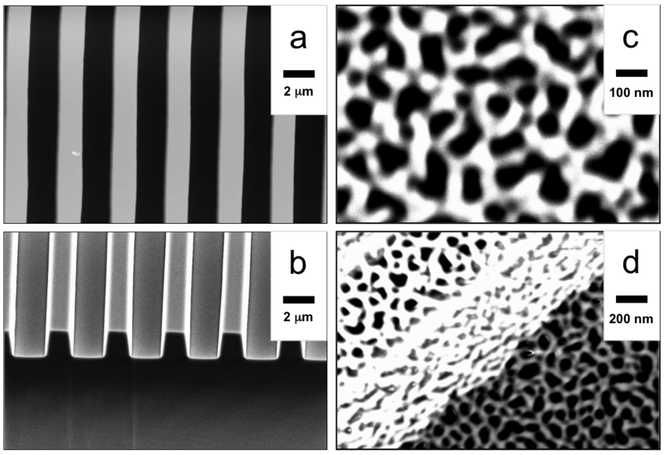

Figure 3.3 : Top view (a) and inclined view (b) of microgrooved silicon masters realized by means of a conventionalphotolithography process. An electro-chemical anodization procedure provides nanoscale pore production of tunable dimension on flat (c) and micropatterned (d) Si surfaces.

§ 3.2.2. Pore generation on Al films

Flat and micropatterned Si substrates were coated with Al using a metal evaporator system. The Al films deposited were of various thicknesses: 200 nm, 300 nm, 400 nm and 600 nm to produce polymer hairs of varying heights. An electro-chemical anodization process with different anodization voltages and different electrolyte solutions were used to produce pores of tunable dimensions [206, 212]. For this work, pores of 80 ± 40 nm diameter and 150 ± 50 nm pitch were formed (see figure 3.3). These Anodic Aluminum Oxide (AAO) molds were finally silanized with a Octadecyltrichlorosilane (OTS) solution to obtain a low energy surface (see Section 4.2 for more details). Silanization provides good anti-sticking surface properties to the molds that allow easy and smooth detachment of the patterned replica from the stamp surface. This helps preventing damage of both the molds and the patterned replica as well.

§ 3.2.3. Patterning of PP surfaces

Thermal nanoimprinting is applied to pattern the polypropylene surfaces. PP substrates (2 x 2 cm^2) are cut from 1 mm thick foils (Goodfellow Cambridge Ltd., product code: 425-485-97) and imprinted with the AAO templates using a Specac Hydraulic Press (15 T & 25 T) at a temperature of 200° C to soften the polymer. At lower temperatures, the polymer does not become soft enough for viscous flow to be achieved for molding. When the plates reach the set temperature value, the stamp is placed on the polymer and a pressure of 4 MPa is applied for 20 minutes before cooling down to 24° C. Conventionally, the de-molding temperature should be below glass transition temperature of PP (0° C), but in this case cooling down the system close to room temperature seemed to work well for de-molding of the hairy PP surface from the Si mold. Finally pressure is released and the stamp is detached from the master carefully.

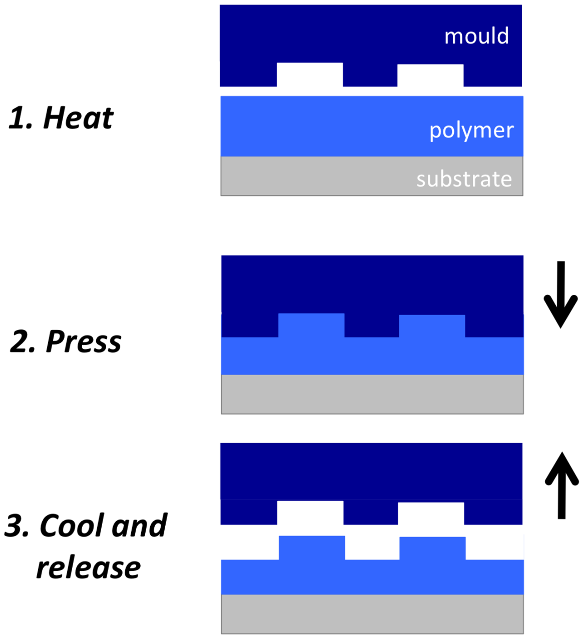

Figure 3.4 : Nanoimprinting to produce PP surfaces.

§ 3.2.4. Patterning of h-PDMS surfaces

A two layer stamp production method has been adopted to produce h-PDMS hairs [213], as depicted in figure 3.5. To prepare h-PDMS, 3.4 g of a vinyl PDMS prepolymer (VDT-731, Gelest Corp., www.gelest.com), 18 μL of a Pt catalyst (platinum divinyltetramethyldisiloxane, SIP6831.1, Gelest Corp.), and one drop of a modulator (2,4,6,8-tetramethyl-tetravinylcyclotetrasiloxane, 87927, Sigma-Aldrich, www.sigmaalrich. com) are mixed and degassed for 1-2 min. Then, 1 g of a hydrosilane prepolymer (HMS-301, Gelest Corp.) is gently stirred into this mixture. Immediately (i. e. within 3 minutes), a thin layer of h-PDMS is spin-coated onto the textured master at 1000 rpm for 40 s to obtain a thickness around 30-40 μm. The subsequent curing at 60°C for 30 minutes promotes polymerization, but leaves h-PDMS still slightly tacky for the bonding with the other part of the stamp: a liquid pre-polymer layer (about 3 mm) of Sylgard 184 PDMS (Dow Corning) is poured onto the h-PDMS layer and the whole sample is cured for at least an hour at 60°C to complete the polymerization process. The composite stamp is released from the master by cutting and carefully peeling the PDMS sample from the surface while still warm.

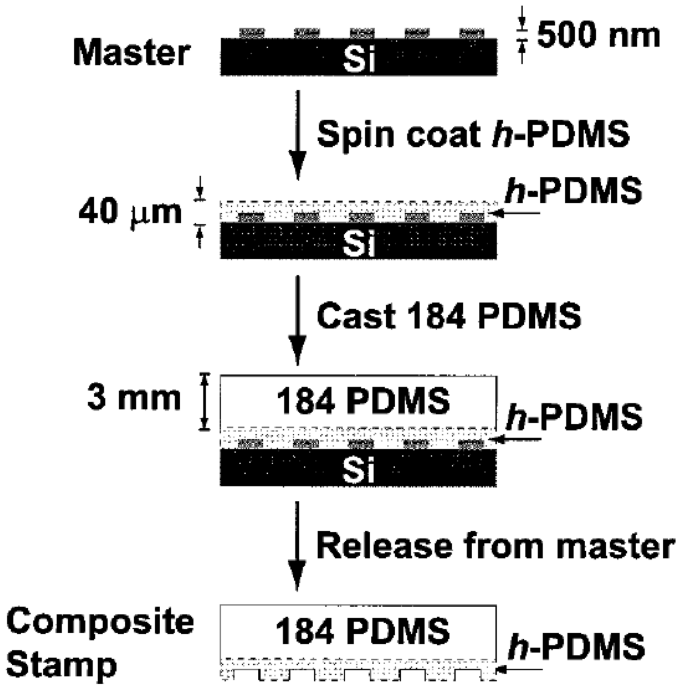

Figure 3.5 : Procedure for fabricating a two-layer composite stamp with hard PDMS and PDMS Sylgard 184 [213].

§ 3.2.5. Produced samples

The different samples are identified by the acronym of the material (PDMS or PP), followed by the letter n (for nanostructured) and an increasing number indicating each individual sample. We have also studied the behavior of flat samples, which are listed with the label flat. Following the same general scheme, microstructured samples are identified by the acronym of the material, followed by the letters μ and n (for microstructured and nanostractured), and an increasing number. As a comparison, we have also fabricated microstructured samples with smooth walls. Tables 3.1 and 3.2 list the investigated samples with the corresponding parameters adopted for the fabrication.

Table 3.1 : Fabrication parameters of the flat and hairy samples. Quantitative assessment of PDMS hair length was not possible due to SEM image charging.

Sample ID	**Al thickness (nm)**	**Anodization voltage (V)**	**Hairs height (nm)**
PP_flat_1	-	-	-
PP_flat_2	-	-	-
PDMS_flat_1	-	-	-
PDMS_flat_2	-	-	-
PP_n_1	200	100	95-120
PP_n_2	400	100	140-370
PP_n_3	400	150	260-400
PP_n_4	400	150	290-405
PP_n_5	600	80	collapsed
PP_n_6	600	100	collapsed
PDMS_n_1	200	100	short
PDMS_n_2	200	150	short
PDMS_n_3	300	150	short-medium
PDMS_n_4	300	100	short-medium
PDMS_n_5	400	150	medium
PDMS_n_6	400	100	medium
PDMS_n_7	600	150	medium

Table 3.2 : Fabrication parameters of the microgrooved samples.

Sample ID	**Al thickness (nm)**	**Anodization voltage (V)**	**Hairs height (nm)**
PP_μ_1	-	-	-
PP_μ_2	-	-	-
PDMS_μ_1	-	-	-
PDMS_μ_2	-	-	-
PP_μ_n_1	300	100	260-440
PP_μ_n_2	300	150	270-430
PP_μ_n_3	300	150	270-430
PP_μ_n_4	400	100	170-400
PP_μ_n_5	400	100	170-350
PDMS_μ_n_1	200	100	not observed
PDMS_μ_n_2	300	150	not observed
PDMS_μ_n_3	300	100	120-190
PDMS_μ_n_4	300	150	not observed
PDMS_μ_n_5	300	100	95-130
PDMS_μ_n_6	400	100	120-200
PDMS_μ_n_7	400	150	80-180
PDMS_μ_n_8	600	80	not observed
PDMS_μ_n_9	600	80	90-140
PDMS_μ_n_10	600	80	not observed
PDMS_μ_n_11	600	100	not observed
PDMS_μ_n_12	600	100	70-130

§ 3.3. Sample characterization

PDMS and PP surfaces have been morphologically characterized through Scanning Electron Microscopy (SEM) and the wettability features have been evaluated by measuring the static and dynamic contact angles.

§ 3.3.1. Scanning Electron Microscopy analysis

The morphology of hairy surfaces has been evaluated by means of SEM images, as shown in figure 3.6. The corresponding measurement of hair height is reported in tables 3.1 and 3.2. High resolution SEM imaging of our PDMS samples was not possible due to charging, and thus we only report a relative assessment of hair length.

Generally, even if similar stamps are used for producing PP and h-PDMS samples, the hair height is found to be higher for PP than h-PDMS (see figure 3.6 a-d). In addition, surfaces replicated from stamps featuring thicker Al films (e.g. 600 nm) and higher anodization voltages (e.g. 150 volts) are covered by hairs so long that they tend to bend under solvation and/or surface forces, such as Van der Waals interactions (see figure 3.6 e-f). For PP, hairs longer than about 400 nm collapse and lie randomly in a highly open network. This appears to occur for PDMS as well, but with a different, much less open morphology.

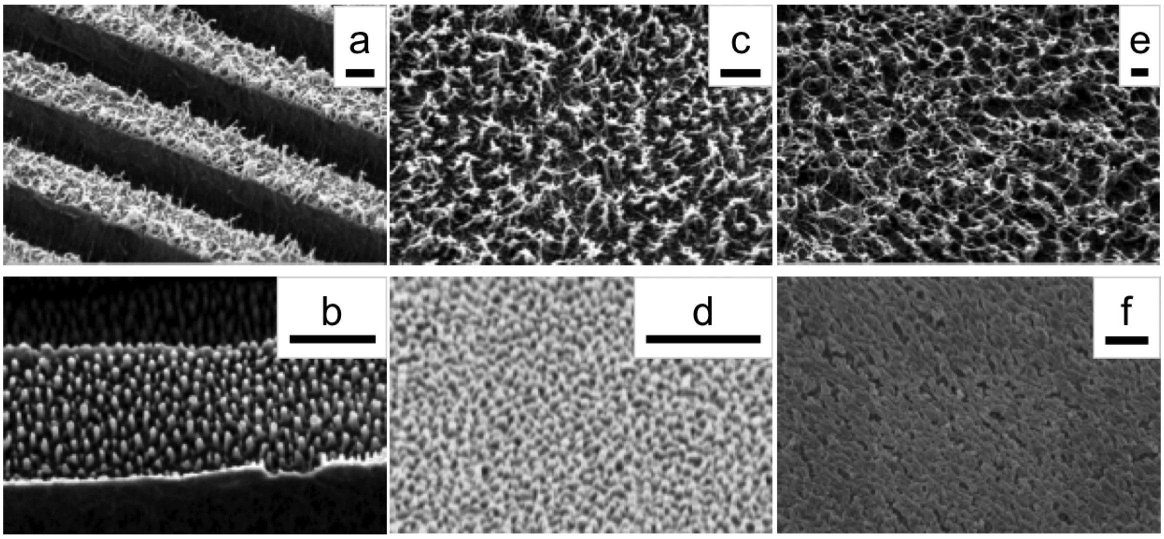

Figure 3.6 : Multi scale hairy surface production in micropatterned PP (a) and h-PDMS (b). Hairy surface production in flat PP (c) and h-PDMS (d). Similar anodization parameters were used in both cases to generate the mold but the hair heights seem to be larger for PP as compared to h-PDMS. Longer hairs tend to bend for both PP (e) and h-PDMS (f) flat surfaces.

§ 3.3.2. Wettability measurements

Static contact angle measurements are performed depositing 0.5 μL distilled water drops on the horizontal samples and taking profile pictures (see figure 3.7) by means of the setup described in Section 2.1. Data are collected from at least five droplets placed in different positions. The final contact angle is expressed by the mean of the various values and the error is the standard deviation which we take to be representative of the surface uniformity. In the case of the microstructured samples, the drops cover at least 150 grooves and are simultaneously viewed by two high-resolution cameras from two orthogonal directions: parallel and perpendicular to the grooves, as defined in figure 3.7

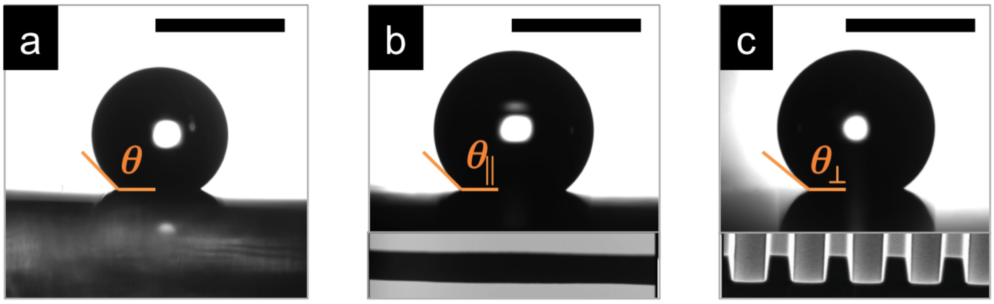

Figure 3.7 : Typical drop profiles taken on hairy PDMS surfaces: a) sessile drop on a hairy sample; simultaneous parallel b) and perpendicular c) views of a sessile drop on a micropatterned sample (substrate micrographs are not in scale). The horizontal bars correspond to 1 mm.

Advancing (θ_A) and receding (θ_R) contact angles are measured through the dynamic sessile drop method by injecting and removing water from a drop having an initial volume of almost 0.5 μL. For every surface this measurement has been performed at least in three different positions. The final dynamic contact angles are expressed as the mean and standard deviation of the three values. From these data we can also extract the value of the contact angle hysteresis, i.e. the difference between the advancing and the receding contact angle. Again, in the case of the micropatterned surfaces both the advancing and receding angles are simultaneously measured in the direction parallel and perpendicular to the stripes.

The graphs of figure 3.8 display the contact angle θ and the contact angle hysteresis $\Delta\theta$ for the flat and hairy samples of table 3.1. The static behavior is very similar for PDMS and PP: both flat samples show a static contact angle $\theta \sim 105°$, which is typical of the two hydrophobic materials [204, 214]. The presence of nanoscopic hairs on the flat surface raises the contact angle to more than 130° for h-PDMS and about 140° for the stiffer PP. As for the contact angle hysteresis $\Delta\theta$, it is less than 20° on the flat surfaces but becomes much higher than 40° on the hairy ones. For both static contact angle and hysteresis, the effect of nanostructuring the flat PP was slightly stronger (~20-30%) than for h-PDMS. An increase both in θ and $\Delta\theta$ with respect to the flat values is suggestive that drops on the PP and h-PDMS hairy surfaces are in the Wenzel state, where water is in contact with the rough surface without air pockets forming a homogeneous interface (see Section 1.2.3). According to this model, on a rough hydrophobic surface $\theta^* > \theta > 90°$. More importantly, the drops in the Wenzel state show a large hysteresis. However, the so-called Cassie impregnating state, where a water drop displays high contact angle, greater than about 150°, and adhesion, has been also invoked to explain the observed wetting behavior of sticky superhydrophobic surfaces [41]. This regime is intermediate

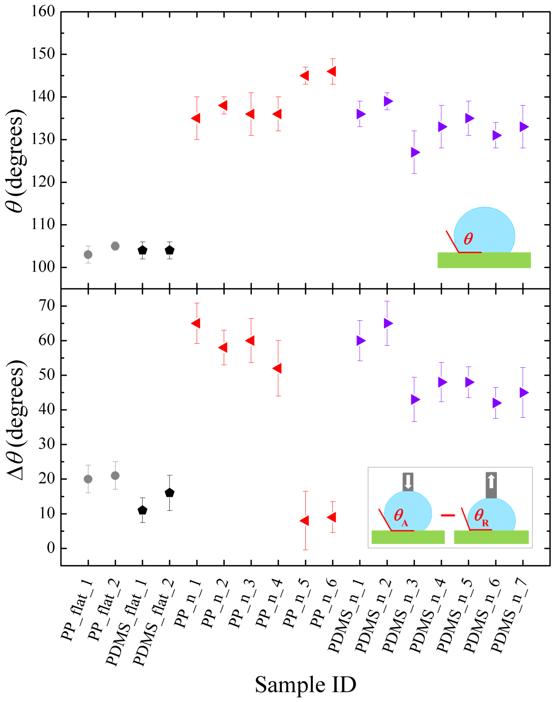

Figure 3.8 : Contact angle (top graph) and contact angle hysteresis (bottom graph) measured on flat and hairy surfaces (from table 3.1).

between the Wenzel and the Cassie state, where air fills the texture [126]. The Cassie impregnating state may arise on surfaces with hierarchical surfaces where droplets are pinned on the microscale asperities while the air remains entrapped in nanoscale asperities [41]. The high pinning on the PP and h-PDMS hairy surfaces could be the result of the Wenzel or the Cassie impregnating state of the droplet. The precise state, however, can be established only by knowing the contact line morphology of the drop with respect to the random texture of the surface [215] or by detecting the presence of air pockets at the interface [216].

The first observation deriving from pictures of sessile droplets on the micropatterned samples is about morphology: the shape of water drops is slightly elongated in the direction of the grooves, as found on rough, not isotropic surfaces formed by parallel channels with smooth walls [157, 217]. If a drop is deposited on such surfaces, the liquid tends to expand in every direction, but it finds periodically energy barriers in its motion across the channels, while it can move along the parallel direction. As shown in figure 3.9, for such drops the apparent static contact angles in the direction perpendicular to the grooves $\theta_\perp$ and that in the direction parallel to the grooves $\theta_\parallel$ are different with $\theta_\perp > \theta_\parallel$, and both are larger than the intrinsic value of the non-microstructured samples. On the hairy, microstructured surfaces both $\theta_\perp$ and $\theta_\parallel$ are larger (by $\sim 10^\circ$) than the corresponding values on the smooth, microstructured surfaces. If we define $\delta\theta = \theta_\perp$ - $\theta_\parallel$ as the degree of wetting anisotropy, we get $\delta\theta < 10^\circ$, about a factor two smaller than on the flat, microstructured surfaces probably because the edges of the smooth microgrooves are sharper than the ones covered by hairs and pin drop contact line more effectively. These values refer to a drop volume of 0.5 μL. By increasing the drop volume, we expect a significant rise in $\delta\theta$ as reported in the literature [157, 216].

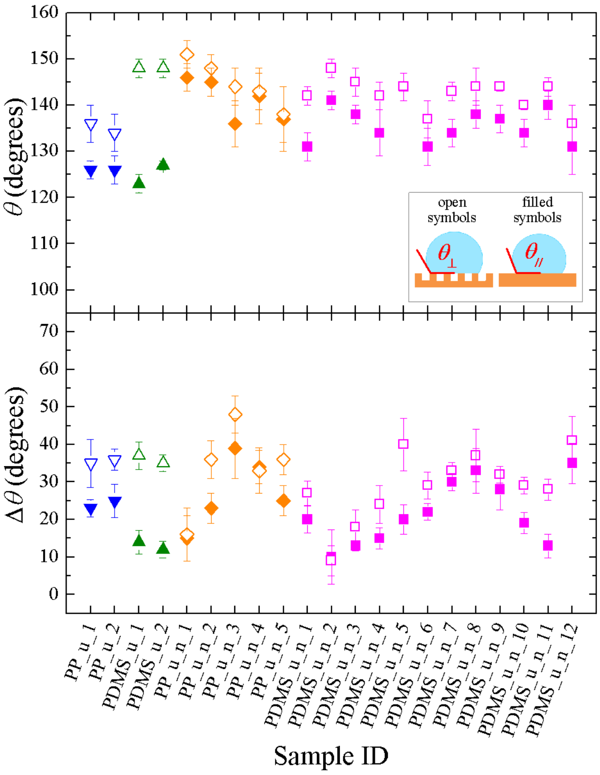

Figure 3.9 : Contact angle (top graph) and contact angle hysteresis (bottom graph) measured on smooth and hairy, microstructured surfaces (from table 3.2).

§ 3.4. Adhesion measurements

The stickiness of these hairy surfaces is evaluated through the maximum volume supported by the sample surfaces. More precisely, the maximum volume (V_{max}) is measured by placing distilled-water drops of increasing volume on the horizontal surface and then tilting the surface vertically with a motor controlled by a computer at a small rate (see Section 2.2).

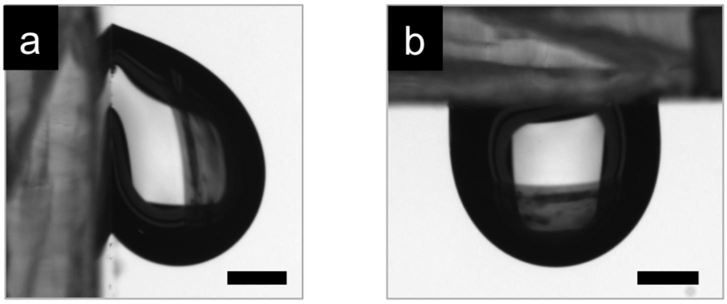

Figure 3.10 : Maximum volume held by a PDMS hairy surface kept in the vertical position a) and after tilting the surface upside down b). The horizontal bars correspond to 1 mm.

Drops having a volume larger than V_{max} are found to fall down during the tilt, while drops of volume $V \leq V_{max}$ remain attached to the surface even though it is tilted fully upside down, as shown in figure 3.10. For the micropatterned samples this procedure is applied twice: with the grooves parallel and perpendicular to the gravity force.

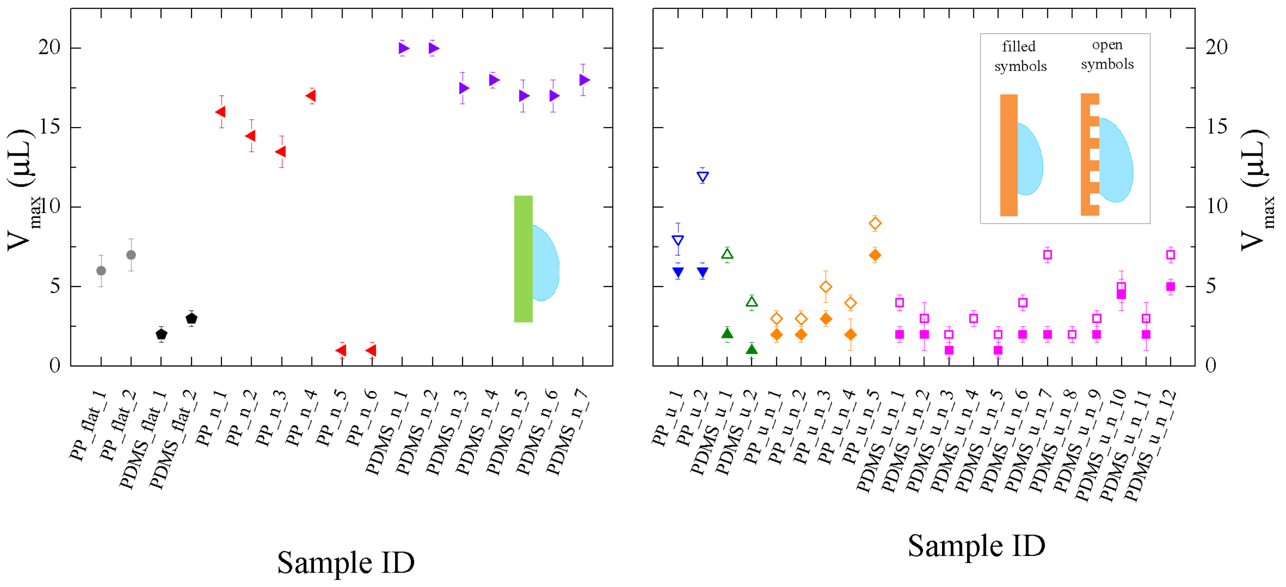

Figure 3.11 : Maximum supported volume measured on flat and hairy surfaces (left graph) and on microstructured, hairy surfaces (right graph). Supported volume was lower in the direction of microstructured lines (solid symbols, lower graph).

On flat surfaces, V_{max} is of a few μL, which goes up to $\sim$ 15 μL on hairy PP and a little higher $\sim$ 18 μL on hairy PDMS. These volumes, which correspond to a spherical drop having a diameter of about 3 mm, are quite similar to those obtained with different sticky, hairy surfaces prepared in different ways and materials [41,49,50,191,194,218,219]. There seems to be no apparent dependence of V_{max} on hair length, probably because in these samples the hairs height does not change enough to give an appreciable effect. Instead, the hair elasticity does seem to play a role, although not very dramatic. From PDMS to PP the Young's modulus increases by a factor $\sim$100, while V_{max} decreases by $\sim$20%, indicating that a softer contact favors drop pinning. Interestingly, samples PP_n_5 and PP_n_6 behave differently. They display the highest θ (close to 150°) while $\Delta\theta$ and V_{max} are lower than the flat surfaces. Morphologically, these two samples present the longest hairs (length $\sim$700 nm) which are not straight but rather are all collapsed forming a complex network of intermingled nanofibers (see figure 3.6e). The wettability data suggest that the superficial crevices trap air very effectively and the deposited drops are in a Cassie state characterized by high contact angles but low adhesion. Actually, if we slightly press on the deposited drop, water penetrates into the crevices forming a more impregnating state characterized by larger adhesion ($V_{max} \sim$ 8 μL) [220].

The grooved samples are characterized by an anisotropic behavior also in the adhesion property, as shown in the bottom panel of figure 3.11. When the hairy grooves are oriented parallel to the gravity force, V_{max} is comparable to the values measured on flat surfaces, while, when the grooves are perpendicular to the gravity force, V_{max} increases due to pinning action exerted by the edges of the rectangular pillars. However, the resulting values are a factor $\sim$4 smaller than those observed on hairy surfaces indicating that water does not fill the rectangular grooves and forms a Cassie contact, which is characterized by low adhesion to the patterned surface (see Section 1.2.3. This is also consistent with the analysis of the contact angle in terms of the Cassie-Baxter equation 1.14. In this case, $f_1 = f_2 = 1/2$, $\theta_1 = 180°$ on air and θ_2 is assumed equal to the contact angle measured on the hairy

surfaces produced with the same alumina templates. If we consider $\theta_2 \sim 133°$, a value typical of hairy PDMS, we get $\theta_{CB} \sim 147°$, which is very close to the angles $\theta_{||}$ measured on hairy, microstructured PDMS. The same holds for the PP samples.
A complete overview of the relation between V_{max} and $\Delta\theta$ is given in figure 3.12, collecting the dta about all the investigated samples. In particular, this graph reports V_{max}/R (where R is the radius of the contact area) as a function of $(\cos\theta_R - \cos\theta_A)$ to check the linear scaling 1.28. In spite of the scattering present in our data we can observe an increasing trend in agreement with the theoretical prediction 1.28 based on the balance between gravity and retentive capillary forces [130, 131].

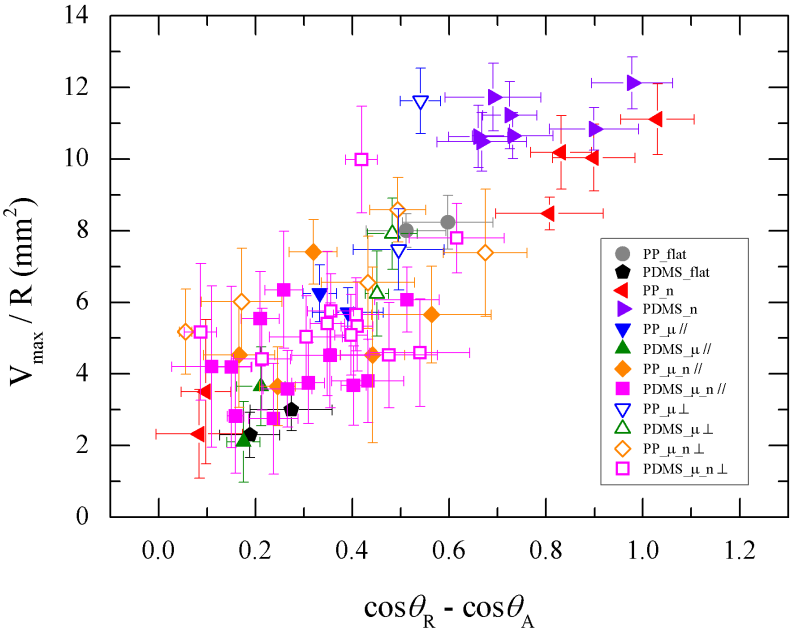

Figure 3.12 : Relation between V_{max}/R and $(\cos\theta_R - \cos\theta_A)$ to check the linear scaling 1.28 derived from the balance between weight and retentive capillary forces.

Finally, figure 3.13 summerizes the ability to tailor wetting behaviour on PP flat samples, by explicitly considering hair length and morphology. Our data reported in figure 3.13a reproduce the three zones in the trend of θ_A and θ_R on an increasingly rough hydrophobic wax surface, first qualitatively identified by Johnson and Dettre [221]. In figure 3.13b we show, as a function of hair length, the evolution of drop adhesion through progressive stickiness to a sudden transition to the Cassie water-repellent state related to hair bending. We note that this direct fabrication-induced wettability change of the surface may also be realized if the morphology is altered by further processing steps (eg. heating or mechanical shearing), or in fact may arise during service due to mechanical contact, etc [222]. On the other hand, a similar trend was not observed for the PDMS hairy surfaces: hair collapse, if it did occur, did not seem to produce the Cassie state.

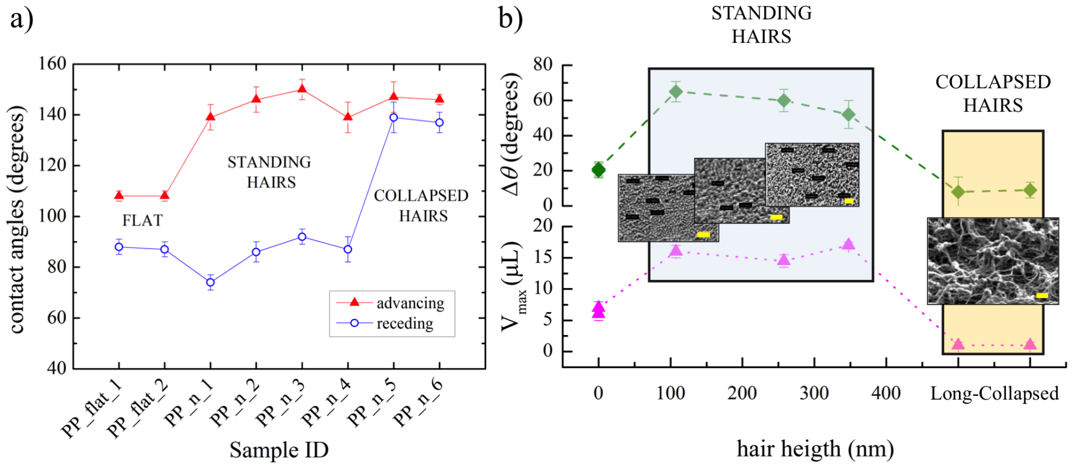

Figure 3.13 : Summary of PP dynamic contact angles (a); hysteresis and maximum pinned volume evolution (b) as a function of hair morphology as manufactured by anodized alumina nanoimprint. Scale bars in SEM snapshots correspond to 500 nm.

§ 3.5. Conclusion

We have fabricated hairy, micropatterned surfaces in h-PDMS and PP by nanoimprinting of porous alumina stamps. The hairs have a characteristic diameter of 80 nm and height comprised between 100 and 600 nm. The two polymers have quite different elastic properties and similar hydrophobic nature. The static wetting behavior of the hairy surfaces is quite similar for the two polymers. Both contact angle and contact angle hysteresis are increased with respect to flat surfaces, indicating that the water drops are partially impregnating the nanostructure. Furthermore, the hairy surfaces are more adhesive than the flat ones: the maximum drop volume they can hold when standing vertically can be up to 10 times larger than that of a flat surface. More interesting, the more rigid PP samples are less sticky than PDMS, suggesting that soft materials favor water adhesion. In addition, stiff PP hairs are much more fragile and easier to damage than PDMS ones, as we could observe simply by handling the samples for the measurements. Probably this is the reason why nanostructures on petals or gecko's feet are usually elastic rather than rigid. We have also imprinted micropatterned stamps covered by the porous alumina layer to produce multi-scale polymer surfaces consisting of a nanometric hairy layer superposed onto micrometric grooves. Water drops are suspended by the micrometric pillars and the resulting adhesion is intermediate between that on flat and on hairy surfaces. This results in a robust technique to tailor the wetting behavior of polymeric surfaces.

Chapter 4

Drops sliding down homogeneous surfaces

Drops sliding down homogeneous substrates have been extensively studied both experimentally [132, 133, 139, 152] and theoretically/numerically [135, 137, 150, 223–225]. However, some aspects of this phenomenon have not been systematically analysed yet. In this chapter we present original results about water drops sliding on homogeneous surfaces differing by static wettability. First of all, Section 4.1 reports a review of the main literature works about drops sliding on partially wetted surfaces. Section 4.2 describes the procedure followed to obtain different kinds of silane coatings and lists the realized samples. Experimental results are shown and compared with theoretical predictions in Section 4.3. Finally the study of drops on homogeneous inclined surfaces is summarized in the conclusion (Section 4.4).

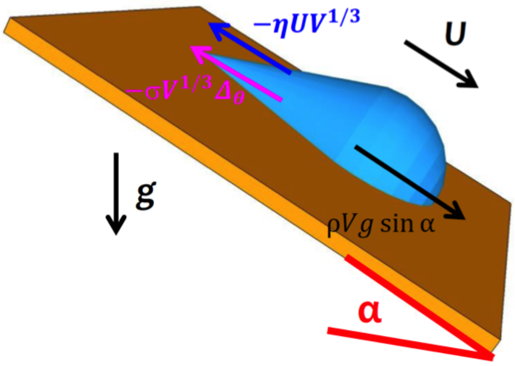

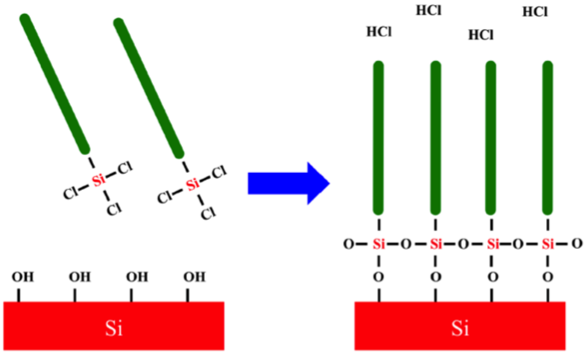

§ 4.1. Introduction

A drop sliding down a partially wetted homogeneous surface assumes, after the initial transient, a stationary velocity U determined by the balance of gravity, viscous and capillary forces (see figure 4.1), leading to a linear scaling between Capillary and Bond number:

$$Ca \simeq Bo_\alpha - Bo_c \tag{4.1}$$

where

- $Ca = \dfrac{\eta U}{\sigma}$, with η and σ viscosity and surface tension of the liquid, respectively;
- $Bo = V^{2/3}\dfrac{\rho g}{\sigma}\sin\alpha$, where V is drop volume, ρ the liquid density, g the gravity acceleration and α the inclination angle;
- Bo_c is a constant depending on the wetting hysteresis.

However, this basic approach does not give any information about the dependence of the scaling 4.1 on parameters such as the static contact angle θ on the surface or drop size.

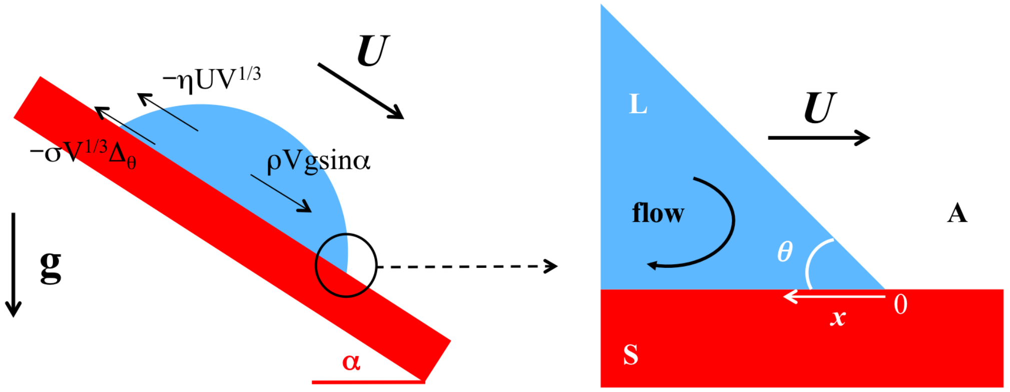

Figure 4.1 : Sketch of a sliding drop subject to gravity gravity, viscous and capillary forces. The wedge region is indicated by the circle and zoomed in the right panel showing the flow near the contact line of the drop.

In addition, the simplified description of the viscous force $F_v \sim \eta UV^{1/3}$ leads to a shear stress singularity [150] due to the no-slip condition: in the wedge region represented in figure 4.1 there is a strong velocity gradient and the resulting viscous force is

$$\begin{aligned} F_v &\sim \int_{corner} \eta \frac{U}{\theta x} R dx && (4.2)\\ &\sim \eta U R \int_0^R \frac{1}{\theta}\frac{dx}{x} && (4.3)\\ & && (4.4)\end{aligned}$$

where x is the horizontal distance from the contact point and R is drop radius. This integral diverges and a way to solve such a problem is to change the integration rangestarting from a, the molecular size, instead of 0:

$$F_v \sim \eta U R \frac{1}{\theta} ln \frac{R}{a} \tag{4.5}$$

In literature there are different theoretical works studying the moving contact line with boundary conditions chosen to determine the behavior of the contact angle and to remove the shear stress singularity. For instance, Hocking [223] analyzed the sliding of a bidimensional drop featuring small fixed advancing and receding contact angles and adopted a Navier slip model [226] where the velocity is linearly proportional to the velocity gradient in order to avoid the singularity. Dussan and coworkers [224, 225] examined the asymptotic solution of a drop moving in the limit of Capillary numbers approaching zero. In this case the contact line motion is obtained as a perturbation of the quasi-static solution of the Navier-Stokes equation neglecting the dynamic term and a linear dependence between the dynamic contact angles and the velocity of the contact line is assumed. Kim et al. [152] overcame the limits of such models studying the functional dependence of drop sliding velocity on various parameters through the energy balance and the evaluation of the dissipation occurring during drop motion. Indeed their results hold for drops partially wetting a solid substrate with an almost circular contact area and when either the dynamic contact angles or their aritmetic mean are close to the equilibrium contact angle θ. Furthermore, two distinct viscous dissipation mechanisms have been investigated: the wedge dissipation and the bulk dissipation. The wedge dissipation is due to the Stokes flow in the edge of a large drop or in a whole small drop. The bulk contribution arises from the lubrication flow associated to the fluid motion in the central part of a large drop. The distinction between small and large drops is based on the definition of a critical radius R_c resulting to be almost always over 10 mm: actually large drops where bulk dissipation is important are usually not experimentally investigated, above all from the dynamic point of view. However, the steady sliding velocity can be theoretically determined for drops of any size according to the balance between the rate of decrease of gravitational energy and the dissipation, including both the viscous term due to the velocity field inside the drop and the dissipation near to the contact line related to the motion of fluid molecules between adsorption sites on the solid surface, i. e. associated to the surface tension acting on the contact line.
For a small drop the resulting steady velocity U is:

$$U \sim \frac{\rho V g sin\alpha - \sigma w (cos\theta_R - cos\theta_A)}{\eta L c(\theta) ln(\Lambda/\lambda)} \tag{4.6}$$

where w is the width of the contact area, Λ is the length scale where the wedge flow approximation holds, λ is a cutoff length introduced to prevent a blowup of the dissipation and $c(\theta) = (1-cos^2\theta)/(\theta - sin\theta cos\theta)$.
On the other hand, in the case of large drops

$$U \sim \frac{\rho V g sin\alpha - \sigma w (cos\theta_R - cos\theta_A)}{\eta [V_b/h^2 + L c(\theta) ln(\Lambda/\lambda)]} \tag{4.7}$$

where V_b is the volume of the central part of the drop (bulk) and h is the height of the drop.
Relation 4.6, expressed in terms of the dimensionless Capillary and Bond numbers, becomes

$$Ca \sim \frac{Bo - Bo_c}{c(\theta)} = \frac{\theta - sin\theta cos\theta}{1 - cos^2\theta}(Bo - Bo_c) \tag{4.8}$$

where now the dependence on the static contact angle is explicit. In particular, the slope of the Ca vs. Bo curve is related to the static wettability, while the intercept to the contact angle hysteresis.

The sliding of drops partially wetting a homogeneous substrate has been experimentally observed only in a few important works [132, 133, 152]. Kim and coworkers [152] investigated the behavior of different viscous liquids (ethylene glycol and glycerin) and different volumes (ranging between 15 and 80 μL) on polycarbonate plates. The predicted linear scaling between Ca and Bo (4.8) has been verified for low Ca values and for small drop deformation due to inclination, confirmed by an almost insignificant change in the dynamic contact angles. Podgorski et al. [132] and Le Grand et al. [133] considered silicon oil droplets sliding down a glass plate coated with fluoropolymers or water droplets on a polyacylate substrate. The shape of the contact line of such droplets is quite complex because the rear part of the drop is different at varying inclination angle, featuring three different regimes (see image 4.2) [132]:

- for small angles the drop is round;
- for bigger angles the rear forms a corner;
- for further higher angles corners becomes cusps emitting smaller droplets (pearling) and shape is no more constant.

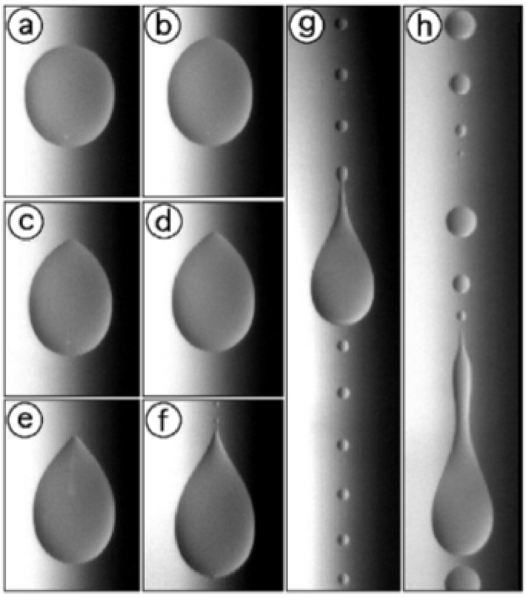

Figure 4.2 : Shape of drops on a homogeneous surface at different inclination angles [132]. In these photographs liquid is a silicon oil: water droplets photos are not showed in the article but authors refer of similar shape transitions also in the case of water. a) and b) rounded shape, c)-e) corner, f)-h) cusp and pearling.

The relation between Ca and Bo is found to be linear untill the production of satellite droplets is reached. In addition, a very accurate and systematic study of drop morphology has been reported [132, 133]:

- drops elongate and flatten as the sliding velocity increases;
- the shape of the rear depends on the Capillary number;
- the advancing angle increases as the Ca increases with a power law dependence, while the receding contact angle decreases for increasing Ca with a similar power law.

To the best of our knowledge, the experimental works present in literature consider only one homogeneous substrate, possibly focusing on the choice of different fluids, whereas a systematic analysis of the same liquid on surfaces differing for static wettability still lacks and is the aspect we decided to investigate as described in the next sections of this chapter.

§ 4.2. Production of homogeneous coatings

To obtain surfaces featuring different wettability we realized coatings on glass slides with different silanes and deposition techniques.

Before silane exposure, glass slides are rinsed with distilled water, acetone and ethanol and successively are placed in the UVO cleaner (Jelight Inc.) for at least 30 minutes. In this device organic contaminant molecules are removed from the solid surface by means of the excitation or dissociation caused by the absorption of a short-wavelength UV radiation. In addition, after this treatment the surface of glass is rich of hydroxyl groups important for the silanization process sketched in figure 4.3.

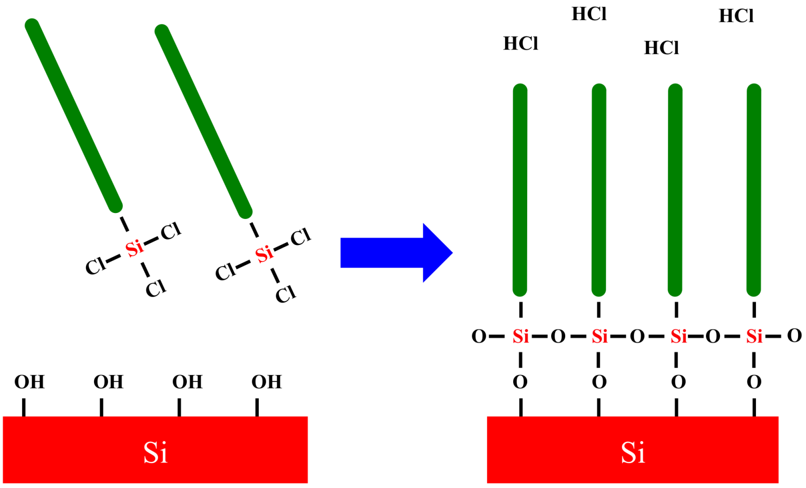

Figure 4.3 : Silanization process to coat a silicon or glass substrate with a silane layer (in this example a trichlorosilane).

In the case of trichlorosilanes, the formation of a silane layer covering the glass surface is due to the following reactions:

1. hydrolisis of the Si-Cl bonds and alkylsilane formation:

$$RSiCl_3 + 3H_20 \rightleftarrows 3HCl + RSi(OH)_3 \tag{4.9}$$

2. condensation reactions between alkylsilanes or with hydroxyl groups present on the substrate:

$$2nRSI(OH)_3 \rightleftarrows -(RSiOH - O - RSiOH)_n - +2nH_2O \tag{4.10}$$
$$RSI(OH)_3 + SiOH_{substr} \rightleftarrows RSi(OH)_2 - O - Si_{substr} + H_2O \tag{4.11}$$
$$\tag{4.12}$$

The resulting network is sketched in figure 4.3. In the case of a trimethoxysilane, the realization of a silane layer on a glass or silicon substrate is accompanied by the production of methanol and involves a more complex mechanism well detailed in [227].

The silane deposition can be realized either by immersion of the sample in a 5 mM silane/toluene solution or from the vapour phase in a vacuum chamber at almost 4 mbar.

The produced samples are listed in Table 4.1, including fabrication details and the resulting wettability. Different contact angles are due to the silane chain, for instance the Trichloro(1H,1H,2H,2H-perfluorooctyl)silane (TFS) gives a more hydrophobic coating for the presence of flourine atoms. On the other hand also the compactness of the silane layer is important, indeed we have Octadecyltrichlorosilane (OTS) samples featuring different static contact angles depending on the deposition technique: coatings obtained through vapour deposition are less hydrophobic than the ones realized by immersion. The OTS silanization by evaporation actually provides a sort of "fluffy" layer where silane chains are not densely packed, contrary to the samples realized by substrate immersion.

Table 4.1 : Specs of the produced homogeneous samples characterized by different wettability. OTS, TMS and TFS stand for Octadecyltrichlorosilane, N-octyltrimethoxysilane and Trichloro(1H,1H,2H,2H-perfluorooctyl)silane respectively.

Sample ID	θ	**Molecule**	**Deposition method**	**Exposure time**
1	$71° \pm 2°$	OTS	vapour phase	3 hours
2	$86° \pm 3°$	OTS	vapour phase	5 hours
3	$94° \pm 4°$	OTS	solution in toluene	1 day
4	$102° \pm 2°$	OTS	solution in toluene	2 days
5	$105° \pm 3°$	TMS	solution in toluene	7 days
6	$109° \pm 3°$	OTS	solution in toluene	3 days
7	$115° \pm 2°$	TFS	vapour phase	4 hours

§ 4.3. Experimental results and comparison with theory

To compare the sliding on different omogeneous surfaces we measured the velocity assumed by 30 μL water drops at several plane inclinations α. An example of the relation between velocity and inclination expressed in terms of the dimensionless Capillary and Bond numbers is reported in figure 4.4.

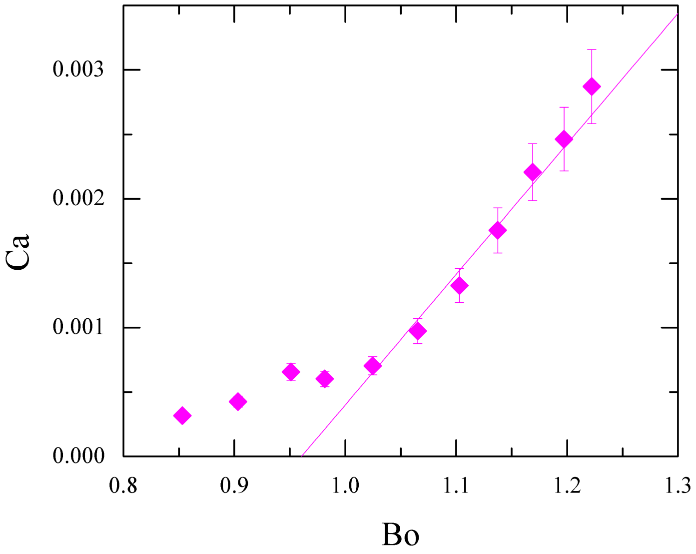

Figure 4.4 : Example of Ca *vs* Bo trend for a 30 μL water drop sliding down a glass slide coated with N-octyltrimethoxysilane (sample 5 in table 4.1)

Usually, for inclinations near the sliding angle the curves deviate from the linear scaling predicted by equation (1.29), probably because in this case drop dynamics is governed by capillary forces. The part of the curve considered for the comparison between different samples is the linear trend followed starting from the critical Bond number Bo_c, deduced by extrapolating the linear fit of the sliding points to Ca = 0, as shown in figure 4.4. Accordingly, in order to facilitate data understanding, the left graph in figure 4.5 reports the Ca as a function of Bo-Bo_c, because the Bo_c is different for all the samples, due to differences in contact angle hysteresis. The slope of these curves clearly increases as the hydrophobicity of the surfaces increases, with a dependence better reveald in the right panel of figure 4.5. In particular the agreement between the experimental data and the angular dependent prefactor of equation (4.8) is quite reasonable for all the investigated surfaces, meaning that our system can be well described by a theory based on wedge dissipation as the dominant dissipative contribution.

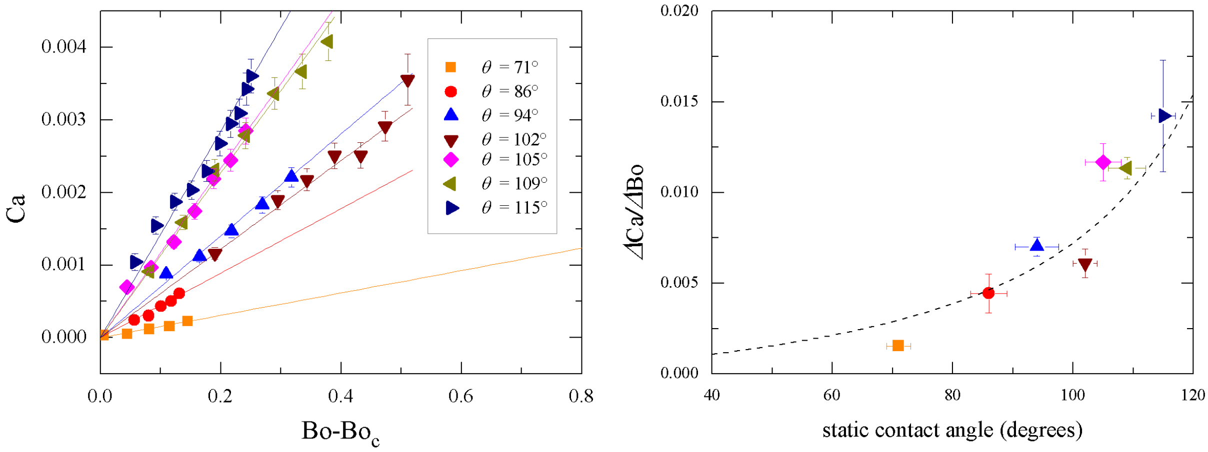

Figure 4.5 : Left panel: Ca vs. $(\mathrm{Bo} - \mathrm{Bo}_c)$ curves for water drops sliding on the homogeneous samples listed in table 4.1. Right panel: corresponding slope of the Ca vs. Bo curve, plotted as a function of the equilibrium contact angle. The dashed line is the scaling law predicted by (4.8), calculated for small drops sliding down homogeneous surfaces with a wedge dissipation as the dominant dissipative contribution.

§ 4.4. Conclusion

In conclusion, we produced homogeneous surfaces featuring different wettability by coating glass slides with different kinds of silane through immersion or by means of deposition from the vapour phase. The sliding of water drops has been observed at several inclination angles in order to derive the Ca vs Bo curves. The corresponding slope of the linear trend follows the theoretical prediction based on the wedge dissipation: for drops od millimetric size (volumes of the order of 10 μL) the bulk dissipation is negligible and the main mechanism of viscous dissipation is related to the flow in the wedge region.

Chapter 5

Chemically heterogeneous surfaces

Chemically heterogeneous surfaces formed by regions featuring different wettability can be easily produced through photolithography or sof-lithography, e. g. UV exposure under a mask or microcontact printing. Such techniques are suitable to obtain samples with domains of different shapes (stripes [101,228], squares [229], triangles [230], circles [231], ...) and dimensions ranging between 0.15 and 500 μm.

The dynamics of drops on an inclined heterogeneous sample is quite interesting: the front and rear contact points undergo a stick-slip regime due to the pinning/depinning transition of the drop contact line at the edges between a hydrophilic and a hydrophobic region; as a consequence the mean sliding velocity is highly dependent on the geometry and the arrangment of the tiles forming the pattern.

The following chapter begins with an introduction on the state of the art about droplets on heterogeneous surfaces (Section 5.1), then describes the microcontact printing protocol adopted for the realization of our samples (Section 5.2) and the sliding experiments on such surfaces (Section 5.4). Experimental results have been supported and completed with lattice Boltzmann simulations (by prof. Sbragaglia's group) reported in Section 5.5). At the end of the chapter conclusions summarize the main findings about drops sliding down heterogeneous patterns.

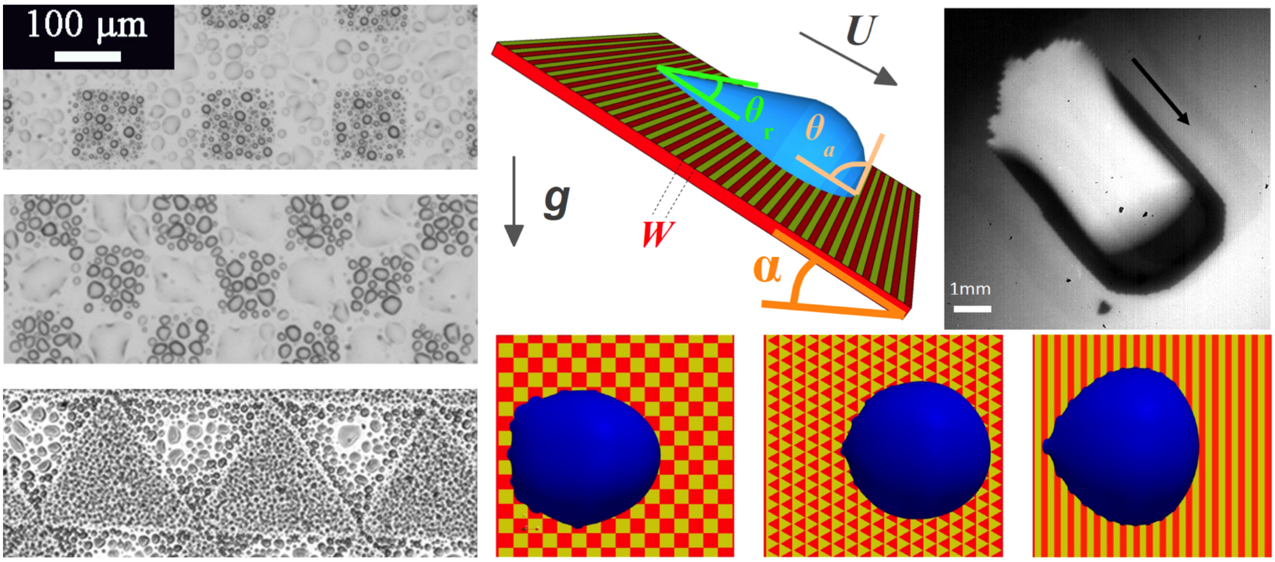

§ 5.1. Introduction

The two most widespread techniques applied to realize chemically heterogeneous surfaces are microcontact printing [211,232,233] and film or SAM (Self Assembled Monolayer) deposition combined with photolithography [101, 234–236]. These patterning methods allow the production of samples formed by domains of different shape (stripes [101, 228], squares [229], triangles [230], circles [231], ...) with dimensions ranging between 0.15 and 500 μm. Composite samples have been produced with a large variety both of substrates and of functionalizing molecules. Examples of printed materials are Si [237] , SiO_2 [229], Au [238], Al [239], glass [240] and borosilicate glass [241]. Instead OTS (Octadecylthriclorosilane) [237], DTS (docosyltrichlorosilane) [228], APTES [242], EG6 [243] or diaphorase [244] were used, as regards functionalizing molecules. The wettability contrast between the two materials forming such heterogeneous surfaces can vary from $\delta\theta \sim 10°$ [101] up to $\delta\theta \sim 100°$ [236], where $\delta\theta = \theta_1$-θ_2 is the difference between the contact angles characterizing the two homogeneous materials.

The static contact angle assumed by a drop deposited on these haterogeneous samples varies according to its size: if a drop contact area is smaller than surface tiles, the contact angle depends on the precise position where the drop is deposited [245]; on the other hand, for a drop covering a large number of domains, i. e. an area representative of the whole sample, the static contact angle is the weighted average of the wettability characterizing the different materials forming the surface. In addition, drop shape and contact angle are found to depend also on the geometry of the texture. In particular, drops deposited on striped surfaces may assume elongated shapes, which are characterized by different contact angles in the directions perpendicular and parallel to the stripes [236, 246–248].

The dynamics of the contact line is expected to be highly affected by the presence of regions featuring different wettability. Indeed a first observation in the spreading of a drop of increasing volume on a striped surface reports steps of the contact line moving in a sort of stick-slip dynamics along the direction orthogonal to the stripes, while in the other direction the contact line moves at a constant speed [249]. Studies about the sliding of drops on striped surfaces also report an anisotropic behavior: drops slide more easily along the alternating stripes than across them [101, 236], and periodic variations in the contact angles, possibly accompanied by fluctuations in the drop velocity, take place along this latter direction [101], although an actual stick-slip motion has not been seen probably because the sliding occurred across stripes having a small wettability contrast ($\sim 10°$). Recently, an anisotropic behavior has been found in a work concerning drops sliding down hydrophobic silane coatings patterned with small hydrophilic triangular domains arranged in a regular hexagonal lattice [230].

The problem of the contact line dynamics and drop motion on structured substrates has been investigated in a number of theoretical and numerical studies [159, 163, 249–256]. In a series of works by Thiele and coworkers [252, 253, 257], the depinning process corresponding to the loss of stability of drops moving over a heterogeneous pattern has been studied in the limit of small contact angles and small wettability contrasts, with the emergence of a *stick-slip* motion during which the contact line jumps from one wetting defect to another [249, 254]. Using lattice Boltzmann (LB) numerical simulations, Kusumaatmaja and coworkers [254, 255] explored the feasibility of using chemical patterning to control the size and polydispersity of micrometer sized drops: in agreement with other authors [249] the stick-slip motion of the contact line was recorded in the simulations. Wang and coworkers [256] simulated the moving contact line in two-dimensional chemically patterned channels using a diffuse-interface model with the generalized Navier boundary condition: the motion of the fluid-fluid interface has been found to be modulated by the chemical pattern on the surfaces, leading to a stick-slip behaviour of the contact line. In addition molecular-dynamics simulations [159] and the Stokes equations employing a boundary element method [163] have been applied to the problem.

§ 5.2. Microfabrication protocol

This chapter describes the whole procedure necessary to produce chemically patterned surfaces which present hydrophilic and hydrophobic domains. The first step is to fabricate masters characterized by pillars of different geometry, using suitable masks. Then the masters are replicated to make the molds for the microcontact printing technique. The stamps are soaked in a solution containing the molecules that make the surface hydrophobic and then are put in contact with the glass surface to be patterned: only the parts really in contact with the mold are functionalized and the final result is a glass hydrophilic surface with hydrophobic domains.

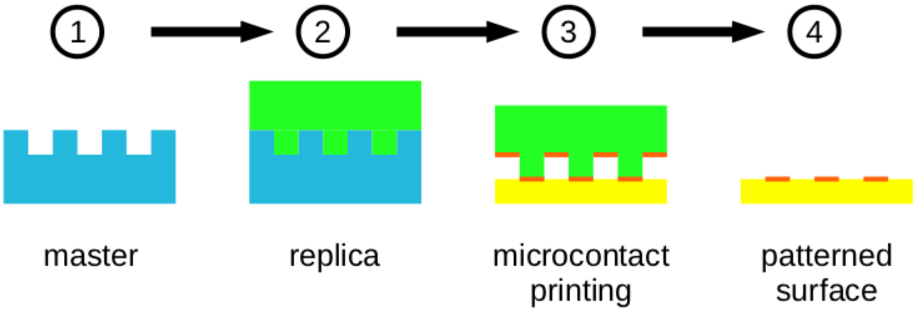

Figure 5.1 : Scheme of the entire fabrication procedure: principal steps.

§ 5.2.1. Masks

Masks are the drawing being reproduced on the masters: depending on whether the photoresist is positive or negative (see Section 3.2), mask pattern becomes a relief structure or is dug in the resist layer. In our case the mask drawings are printed on transparent sheets by a laser inkjet printer with a 3600 DPI resolution. As shown in figure 5.2, we considered patterns formed by domains of different shape (stripes, squares and triangles) but with a fixed periodicity $W \sim 200$ μm.

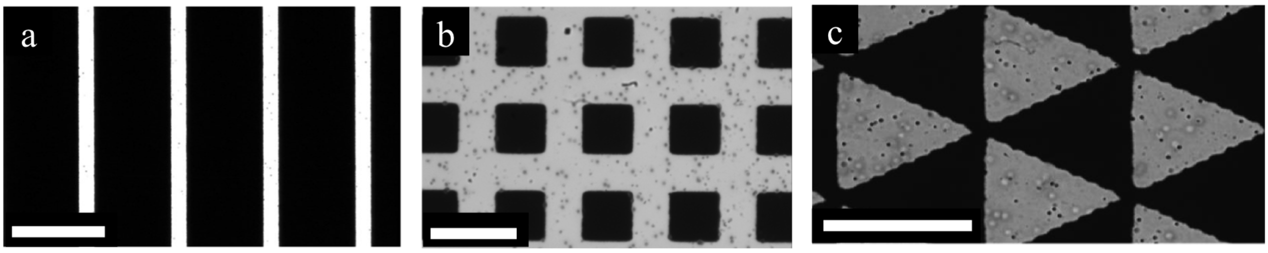

Figure 5.2 : Examples of masks for photolithography: a) stripes, b) squares and c) triangles. The drawing is printer with toner on transparent sheets. The horizontal bars correspond to 200 μm.

§ 5.2.2. Master production using photo-lithography

Masters are produced adopting a photolithographic technique [211] with SU-8-2050 (MicroChem Corporation), a negative photoresist (see Section 3.2.1) whose peak of absorption is in the ultraviolet light at a wavelength of 365 nm. This type of SU-8 is a very viscous polymer that can be spread over a thickness ranging between 10 and 200 μm. To prepare a master, SU-8 must be poured on a solid substrate that in our case is a silicon wafer (Silicon materials) properly cut in pieces of the right dimension. Silicon surface is preferable to other materials such as glass because of its lower roughness: the high flatness facilitates subsequently the adhesion between resist and substrate, making it more homogeneous and stronger.

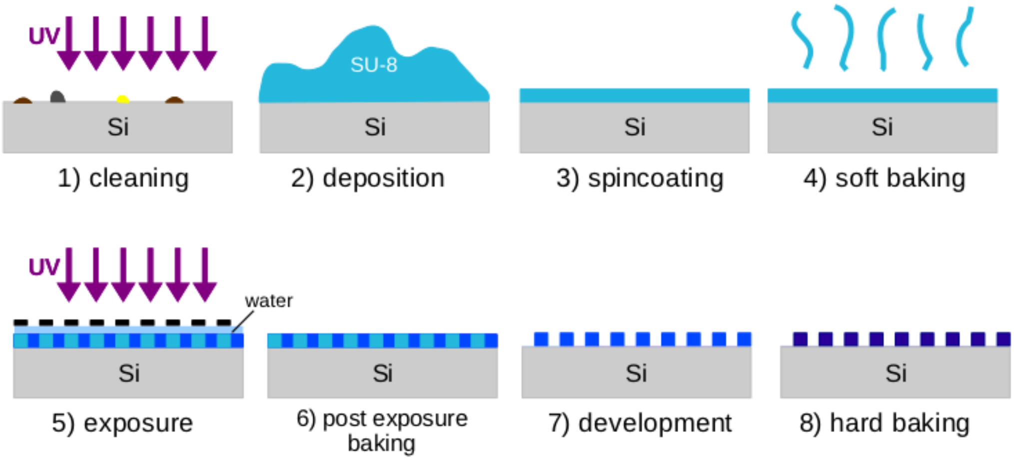

Figure 5.3 : Scheme of the principal phases in masters fabrication.

The first step of masters fabrication procedure (schematized in figure 5.3) is the substrate cleaning: silicon samples are rinsed with distilled water and isopropanol and then are set in the UVO cleaner (Jelight Inc.) for at least 30 minutes. In this device organic contaminant molecules are removed from the solid surface by means of the excitation or dissociation caused by the absorption of a short-wavelength UV radiation. Thereafter SU-8 is deposited on the substrate and spincoated using a Specialty Coating System (P 6708/6712). Because of the centrifugal force, most of the viscous liquid is expelled and only a thin homogeneous layer remains on the substrate. A spinning cycle consists of three steps, as schematized in figure 5.4.

The rotation velocity in the first two steps is set according to the velocity chosen for the last

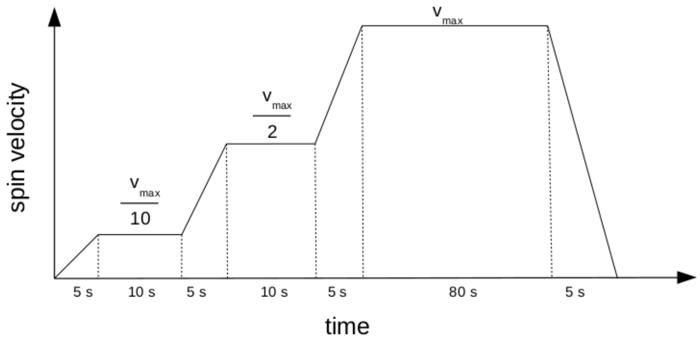

Figure 5.4 : Velocity steps in a spinning cycle. The first two velocity values are set according to the value chosen for the last one: the first one is one order of magnitude lower and the second one is its half.

one: the first one is an order of magnitude lower and the second one is its half (the velocity values we refer to in the following are the values at the third constant step). Moreover the first two steps lasts for 10 seconds, the third one for 80 seconds and to pass from a stage to the following there are ramps of 5 seconds at varying velocity. In order to extend the surface area characterized by a constant thickness layer, the sample needs two subsequent spinning cycles. In spite of this, some SU-8 backlogs form on the surface edges and it is necessary to remove them by hand using a cutter or a pair of tweezers. After this operation the coated surface has to rest for at least 2 or 3 hours, so that the resist layer becomes as uniform and homogeneous as possible. The spin velocity affects the final SU-8 layer thickness according to the relation plotted in figure 5.5 . [1]

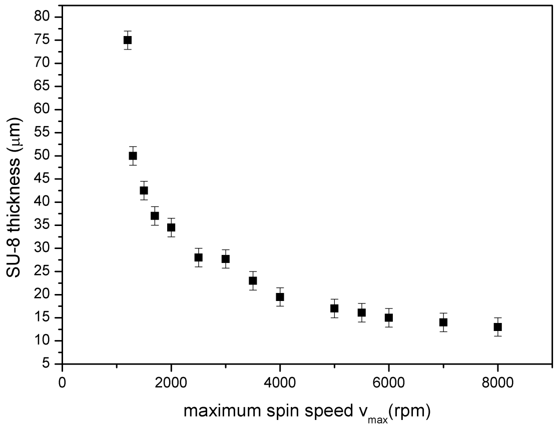

Figure 5.5 : Relation between the maximum spin velocity and the SU-8-2050 thickness obtained after 2 spin cycles and a pause of 2 or 3 hours.

The next step is a pre-bake at 60°C for 5 minutes followed by a ramp up to 90°C, temperature maintained for 20 minutes after which it is decreased to 40°C. This soft baking phase allows the evaporation of the excess of photoresist solvent and a partial hardening of the SU-8 which promotes the successive polymerization. Once the sample reaches room temperature, it is placed under the

---

[1] The coating height is chosen so that the aspect ratio H/L (where H represents the height and L the width of the spaces between the structures as shown in figure 5.6) to stand between 0.2 and 2 for ensuring the stability of the replicas made of PDMS (see section 5.2.3 and [232]).

mask putting a water layer between them to reduce unwanted diffraction effects. Afterwards mask and coated wafer are exposed to the collimated beam of an UV mercury arc lamp (Osram HBO) mounted on a flood exposure system (Reinraumtechnik Lanz UV400) with a working area having a diameter of about 10 cm [258]. The exposure time is a crucial parameter:

- if it is too short also the exposed parts can be removed by the developer;
- if it is too long it can cause the formation of structures which do not faithfully reproduce the mask pattern.

In our case the optimal exposure time is 30 s.
To avoid the solvent to erode the exposed zones, the sample undergoes a post exposure bake at the same temperatures as in the soft bake step. This baking grows and stabilizes the cross linking formed in the polymerized area. The unexposed part is definitively removed shaking the samples in the SU-8 developer. Master fabrication finishes with a hard baking at 100°C for at least 30 minutes which makes the structures stronger. The entire procedure takes place in a cleanroom (ISO 7 class) to guarantee a high level of cleaning necessary for an optimal fabrication of micro devices.

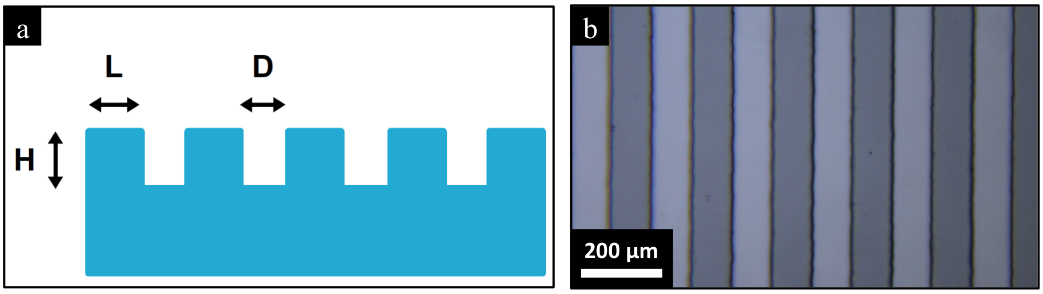

Figure 5.6 : SU-8 master with grooves almost 100μm wide and 70 μm high. a) profile sketch or pattern b) microscopy image.

In figure 5.6 we show an example of a master with grooves almost 100 μm wide and 75 μm high. All the other masters we fabricated are similar, but with different geometry.
Before proceeding with masters replica, their surface must be treated with a chemical vapour deposition (CVD) process facilitating replica peeling from its master: the surface is covered by organofunctional alkoxysilane molecules arranged in a monolayer forming an anti-adhesive film. Masters are left in a trichlorosilane atmosphere for at least 2 hours so that the whole surface is evenly coated. For further information about silanization protocol we refer to Section 4.2 and [259].
At this point our masters are ready to be replicated.

§ 5.2.3. Replica molding

The replica molding protocol we adopted is summarized in figure 5.7.

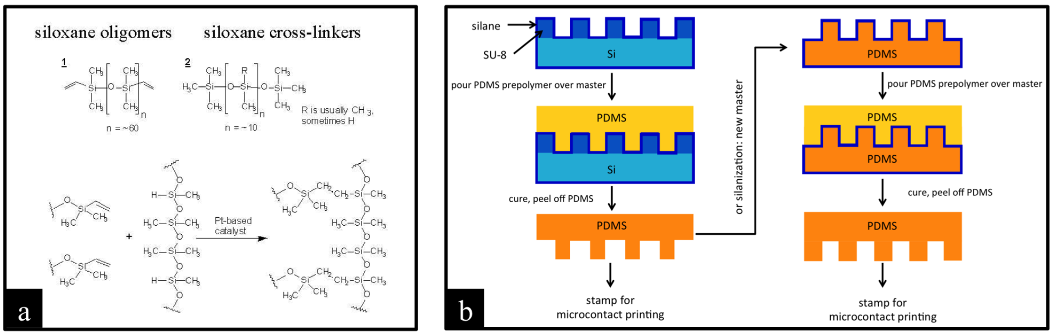

Figure 5.7 : (a) PDMS polymerization (b) Scheme of the replica molding (left column) and double replica molding (right column) procedure.

Liquid PDMS and its catalyst (Sylgard 184) are mixed together in 10:1 w/w ratio. During the blending some air bubbles form in the mixture and must be removed degassing the fluid with a rotative pump. Once PDMS is completely degassed, it can be poured on the master paying attention not to produce any bubble during the shedding. PDMS polymerization (see figure 5.7a) is sped up by heat, so the master covered by PDMS is put in the oven at 80°C for one hour. Once solidified, the replica can be peeled off delicately and then can be used as a stamp for the printing. An example of the built replicas is represented in figure 5.8.

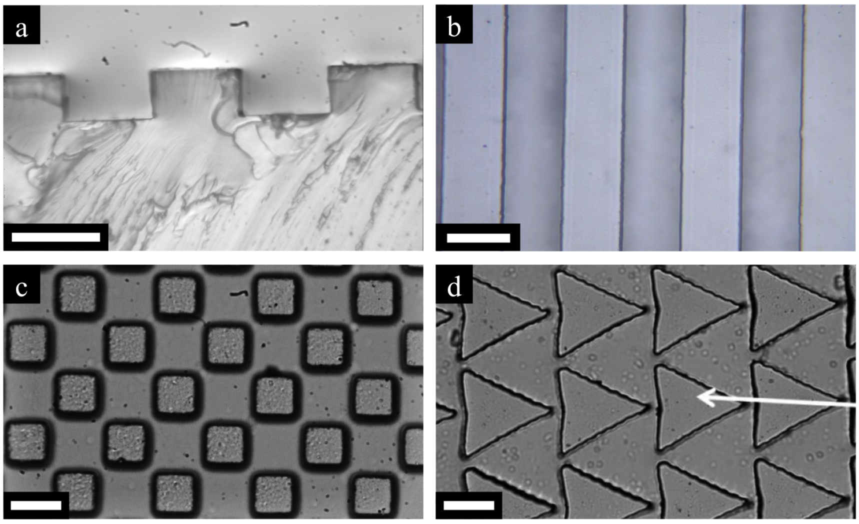

Figure 5.8 : Photographs PDMS stamps: a) lateral view of a stamp with grooves 100 μm wide, b) reflection microscope view of the same sample, c) stamp with squared pillars and d) double replica in PDMS of an initial SU-8 master with triangular geometry. The white arrow indicates the structure in relief in the PDMS stamp. The horizontal bars correspond to 100 μm.

In addition, the first replica in PDMS can be used, once silanized, as a master for a new PDMS stamp (double replica molding). Starting from a silicon master both its negative and its identical copy can be produce in order to have two complementary stamps.

§ 5.2.4. Microcontact printing

Microcontact printing (μCP) [233] is a soft lithographic technique for chemically patterning a surface: a PDMS mold is used as a stamp, being wetted with an "ink" consisting of a solution containing molecules which functionalize the substrate forming a self assembled monolayer (SAM) in the contact area between stamp and substrate. The drawing in relief of the stamp is reproduced on the substrate after contact, thanks to the adhesion between the molecules and the surface. This kind of selective patterning is very stable and time resistant because the carbon chains of these molecules align each other creating a strong and compact layer (see figure 5.9).

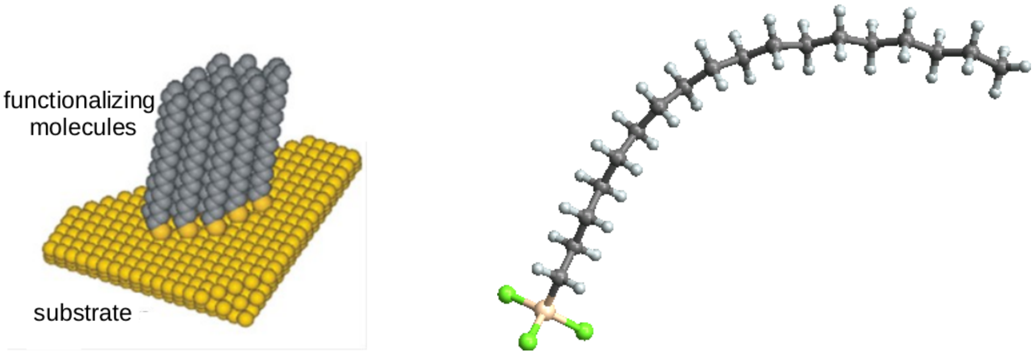

(a) (b)

Figure 5.9 : (a) Arranging of functionalizing molecules in a monolayer (b) OTS, the molecula we used: it is formed by 3 Cl atoms (green), 1 Si atom (pale yellow), 18 C atoms (dark grey) and 37 H atoms (white).

μCP has been realized with a large variety both of substrates and of functionalizing molecules. Examples of microcontact printed materials are Si [237] , SiO_2 [229], Au [238], Al [239], glass [240] and borosilicate glass [241]. Instead OTS (Octadecylthriclorosilane) [237], DTS (docosyltrichlorosilane) [228], APTES [242], EG6 [243] or diaphorase [244] were used, as regards functionalizing molecules.
In our case:

- **stamps** are PDMS molds described in section 5.2.3;
- **ink** is a 0,5 mM solution of OTS (octadecyltrichlorosilane, $CH_3(CH_2)_{17}SiCl_3$, Sigma Aldrich) in toluene (Sigma Aldrich);
- **substrates** are microscope glasses cleaned immediately before the printing with distilled water, isopropanol and left in the UVO cleaner for at least 30 minutes.

PDMS samples are completely soaked in the OTS and toluene solution for 30-60 seconds. They are consequently dried and put in contact with the cleaned glass substrate. Finger pressure [237], [233] is exerted for 40 seconds paying attention not to move the stamp and to give an homogeneous pressure [2]. Time is an important parameter because:

---

[2] We tried also to impress pressure placing a weight on the PDMS sample, but in this way it is easier to move the stamp on the substrate.

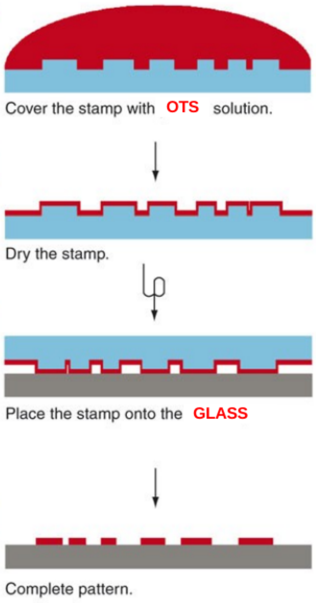

Figure 5.10 : Microcontact printing procedure.

- a too short time prevent the formation of a thick and homogeneous layer;
- a too long time cause OTS molecules to adhere also on areas not touched by the stamp.

After having removed delicately the mold, patterned glasses are placed on a hot plate at 70℃ in order to make the solvent evaporate. Funcionalized areas are not only covered by an OTS monolayer, but there are molecules buildups which are washed off rinsing samples in toluene for 8-10 minutes. Also this protocol is realized in the cleanroom for the high cleanness degree required for a good result.

§ 5.2.5. PDMS swelling

When the stamp is soaked in the OTS solution, toluene swells PDMS [260] and deforms the structures in relief, as shown in figure 5.11. Fortunately, the transformation is reversible and structures come back to the original shape as the solvent evaporates (see figure 5.11).

In addition, PDMS swelling, usually representing a problem in microfluidics, can be exploited as a useful advantage in the case of triangles and chessboard geometry: the pillars of the stamp are well separated (see figure 5.8d) and the corresponding printed surface would feature a larger fraction of glass, but thanks to swelling, the corners of the pillars meet, allowing the production of the desired pattern formed by almost the same fraction of glass and OTS, by starting contact at the suitable moment (see sequence in figure 5.11).

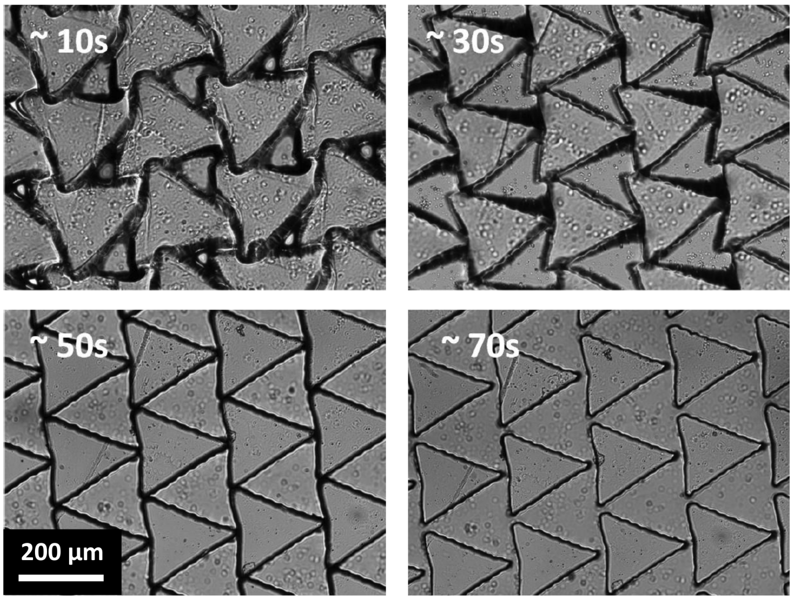

Figure 5.11 : Swelling of triangular PDMS stamps.

§ 5.3. Sample characterization

Such heterogeneous surfaces were characterized through three different techniques described in this section:

- the condensation figure method, based on the different condensation on hydrophilic and hydrophobic regions;
- Atomic Force Microscopy, sensitive to different roughness and fiction on different surfaces;
- wettability measurements aimed at testing the agreement with the Cassie-Baxter prediction.

§ 5.3.1. Condensation figure method

The final output of the microcontact printing procedure is a surface presenting hydrophobic OTS regions alternated with hydrophilic glass uncoated areas. This chemical difference can be exploited in order to characterize and to observe samples features with the condensation figure method [261]: water vapour condensation on hydrophobic and hydrophilic surfaces is different and, as a result, two different areas can be distinguished according to the size and distribution of the droplets.

As shown in figure 5.12, there are some regions characterized by bigger droplets (hydrophilic glass surface), as well as areas covered by smaller droplets (hydrophobic OTS layer). This is a simple and fast technique to measure the size of the domains and to check whether the patterned surface is affected by defects. The results of this optical characterization are summarized in table 5.1, where the samples are labeled with an acronym indicating the pattern geometry.

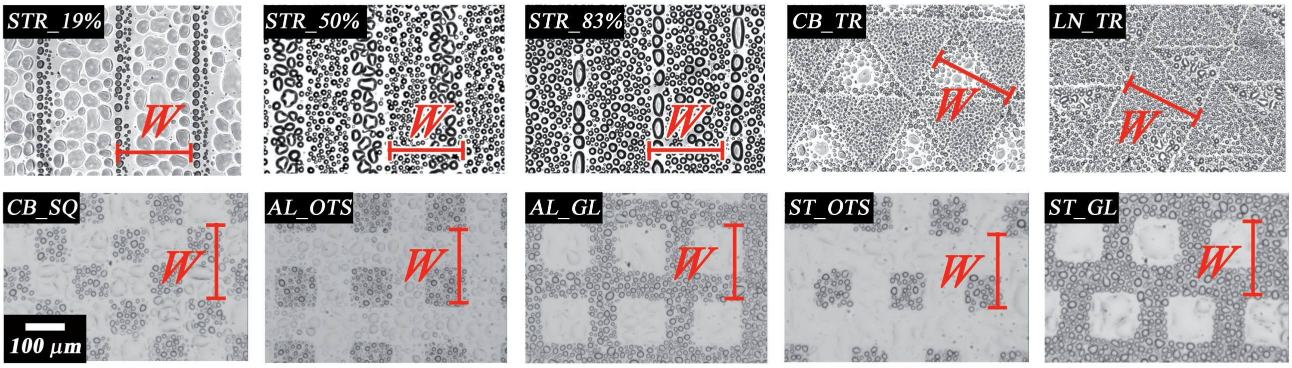

Figure 5.12 : Condensation figures of the ten patterns of heterogeneous surfaces produced: bigger droplets condense on the hydrophilic areas, whereas smaller droplets form on the hydrophobic domains. All the patterns feature the same periodicity W=200 μm but different fractions of hydrophilic uncoated glass and hydrophobic OTS layers. Bars indicating W show also the sliding direction (see Section 5.4).

Table 5.1 : Geometric specifications of the ten patterns as derived through the condensation figure method. The length parameters W, L and B are defined in figure 5.13. The striped samples are labeled with STR, standing for stripes, and the corresponding OTS percentage, whereas the acronym chosen for the other patterns refers to the geometry of the domains (TR → triangle, SQ → square, CB → chessboard, LN → linear, AL → aligned and ST → staggered).

sample ID	pattern description	dimensions (μm)	OTS fraction f_1	glass fraction f_2
STR_19%	stripes	L = 38 ± 3 W = 200 ± 3	0.19 ±0.02	0.81±0.02
STR_50%	stripes	L= 100 ± 3 W = 200 ± 3	0.50 ± 0.02	0.50 ± 0.02
STR_83%	stripes	L = 166 ± 4 W = 200 ± 3	0.83 ±0.03	0.17 ±0.03
CB_TR	isosceles triangles in chessboard arrangement	B = W =200 ± 3	0.54 ± 0.03	0.46 ± 0.03
LN_TR	isosceles triangles in linear arrangement	B = W =200 ± 3	0.58 ± 0.02	0.42 ± 0.02
CB_SQ	squared chessboard	L = 100 ± 6 W = 200 ± 4	0.50 ± 0.03	0.50 ± 0.03
AL_OTS	aligned squares	L = 110 ± 3 W = 200 ± 3	0.30 ± 0.02	0.70 ± 0.02
AL_GL	aligned squares	L = 119 ± 4 W = 200 ± 4	0.65 ± 0.03	0.35 ± 0.03
ST_OTS	staggered squares	L = 104 3 W = 200 ± 3	0.27 ± 0.02	0.73 ± 0.02
ST_GL	staggered squares	L = 123 ± 4 W = 201 ± 4	0.63 ± 0.03	0.37 ± 0.03

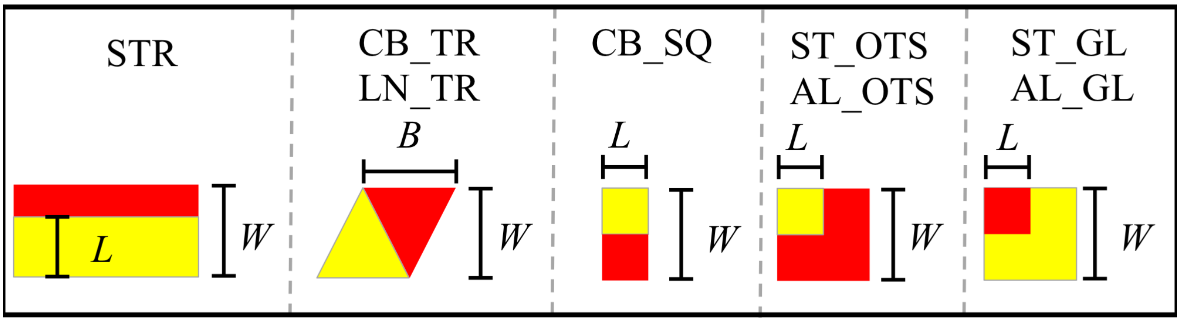

Figure 5.13 : Cartoon of the fundamental cells composing the periodic patterns used to define the characteristic lengths. Red (dark) regions represent uncoated glass areas, and yellow (light) regions represent OTS domains.

§ 5.3.2. AFM scans

In order to study our surfaces we employed an Atomic Force Microscope (Park scientific instruments autoprobe cp) both in topography mode and in lateral force mode [262].

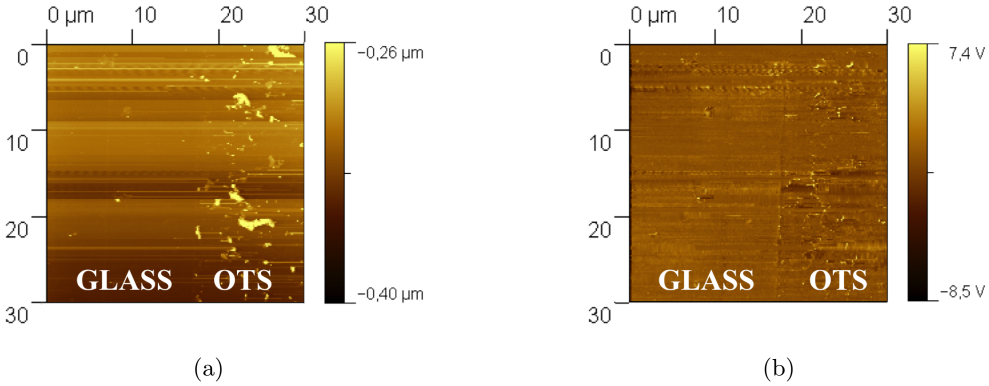

(a)

(b)

Figure 5.14 : AFM scanning image showing the border between two stripes: (a) topographic mode, (b) lateral force mode.

An example of a scanning output is depicted in figure 5.14. With the AFM in topography mode, the printed areas can be distinguished only for the presence of molecular accumulations instead of a single OTS monolayer. However these buildups are not higher than 100 nm, much smaller than the dimensions of the drops sliding down the patterned surface, so that these OTS layer irregularities do not affect drops motion. In addition, a net step between the printed area and the glass substrate cannot be identified because the thickness of the OTS layer is negligible with respect to the native roughness of the glass slide (mean roughness less than 10 nm, but much larger than 2.5 nm, the length of an OTS molecule). On the other hand, the printed areas can be better identified with lateral force microscopy, as shown in figure 5.14b, where the border between coated and bare glass regions is clear and well defined. In conclusion, the samples can be assumed to be flat and the drop sliding is affected only by chemical heterogeneities and not by geometrical pinning effects.

§ 5.3.3. Wettability measurements

The printed pattern is also analyzed in terms of static contact angle measurements through the Cassie-Baxter equation (1.14). The static contact angle θ has been measured with the experimental apparatus described in Section 2.1 by placing above the horizontal sample 4 μL water drops, whose contact area covers at least 100 fundamental cells composing the triangular or square patterns and 20-30 stripes in order to average on a region representative of the whole sample composition. To characterize the surface wettability, data are collected from at least five droplets placed in different positions. The final contact angle is expressed as the mean of the various values, and the standard deviation is representative of the surface uniformity. The main results of this analysis are listed in Table 5.2. The experimental determination of the static contact angle on the surfaces patterned with triangles and squares agrees very well with the Cassie-Baxter predictions, calculated from the material fractions of glass and OTS, evaluated through the condensation figures, and from the static contact angles of a homogeneous bare glass slide (rinsed in toluene to reproduce the same treatment applied to the patterned samples) and a homogeneous OTS coating, obtained by immersing a glass slide in an OTS/toluene solution (5 mM) for 3 days. In the case of striped samples we found an anysotropy between the equilibrium contact angle parallel ($\theta_{||}$) and perpendicular ($\theta_{\perp}$) to the stripes (see cartoons in Table 5.2): in agreement with Refs. [236, 247, 248], only the equilibrium contact angle parallel to the stripes is compatible with the theoretical prediction calculated through the Cassie-Baxter equation (see Table 5.2) and the asymmetry is more pronounced in the case of the more hydrophilic surfaces. The good agreement between theoretical and experimental values constitutes not only the confirmation of the Cassie-Baxter law (1.14), but also an indirect validation of the microfabrication protocol and of the quality and uniformity of the patterned surfaces.

Table 5.2 : Static contact angles of both homogeneous and heterogeneous surfaces of glass (red/dark) and OTS (yellow/light). For comparison also the Cassie-Baxter prediction θ_{CB} is reported.

ID	**Cartoon**	f_{OTS}	f_{glass}	**Equilibrium contact angle**		θ_{CB}
GLASS		0	1	$32° \pm 3°$		-
OTS	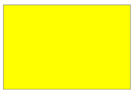	1	0	$110° \pm 3°$		-
CB_SQ	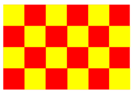	0.50	0.50	$76° \pm 4°$		$75° \pm 2°$
AL_OTS	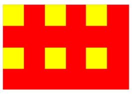	0.30	0.70	$61° \pm 3°$		$61° \pm 2°$
AL_GL	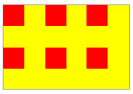	0.65	0.35	$85° \pm 4°$		$85° \pm 2°$
ST_OTS	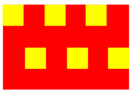	0.27	0.73	$59° \pm 3°$		$58° \pm 2°$
ST_GL	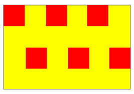	0.63	0.37	$86° \pm 6°$		$84° \pm 3°$
CB_TR	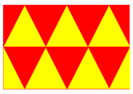	0.54	0.46	$83° \pm 6°$		$78° \pm 2°$
LN_TR	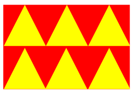	0.58	0.42	$84° \pm 5°$		$81° \pm 2°$
				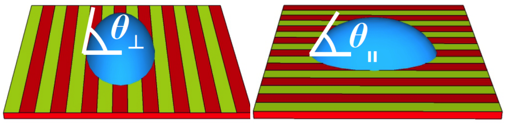		
STR_19%	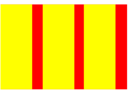	0.19	0.81	$\theta_\perp = 74° \pm 3°$	$\theta_{\|\|} = 58° \pm 4°$	$52° \pm 2°$
STR_50%		0.50	0.50	$\theta_\perp = 83° \pm 2°$	$\theta_{\|\|} = 72° \pm 2°$	$75° \pm 2°$
STR_83%		0.83	0.17	$\theta_\perp = 100° \pm 3°$	$\theta_{\|\|} = 100° \pm 3°$	$98° \pm 2°$

§ 5.4. Experimental results

This section collects all the main experimental results about the sliding of drops on heterogeneous surfaces formed by domains of different shape.

§ 5.4.1. Sliding measurements

We observed the sliding of 30 or 40 μL water drops down the heterogeneous samples in the direction indicated in figure 5.12, i. e. parallel to the pattern periodicity W, as depicted in the example in figure 5.15 related to a striped surface [167, 263, 264].

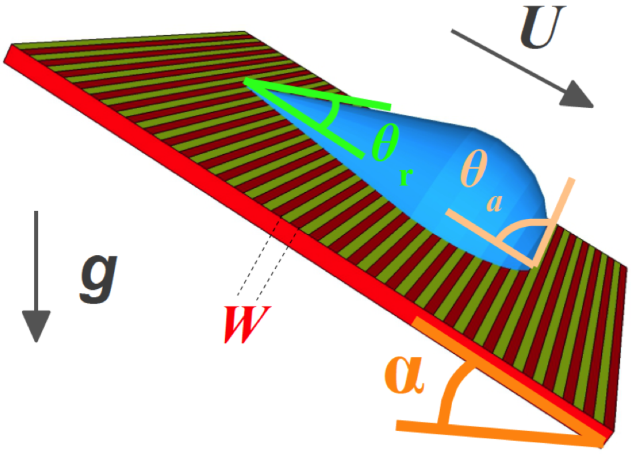

Figure 5.15 : Sliding drop on an inclined plane tilted by an angle α. The surface is functionalized with stripes (or square and triangular domains) of alternating wettability with periodicity W, much smaller than drop size (typically the drop contact area covers tens of W). The sliding direction is parallel to W, i. e. perpendicular to the stripes (or to the raws of squares and triangles, as indicated in figure 5.12.

In the case of surfaces with wider stripes of glass (sample STR_19% in figure 5.12), drops assume an asymmetric shape, elongated in the direction of the stripes, and get pinned for every inclination angle up to 90° so that sliding measurements are not possible. Drops on all the other heterogeneous surfaces are not affected by this pronounced asymmetry and the motion is studied for various inclinations α of the sample. In addition, to extend the range of static wettability on the striped samples, we also studied the sliding of ethanol in water drops (30% w/w, $\rho = 954$ kg/m^3, $\eta = 2.5$ cP, $\sigma = 35.5$ mN/m [265]) down the surface with stripes of equal width.

§ 5.4.2. Stick-Slip

An example of the particular drop dynamics on the surface formed by stripes of equal width (sample STR_50% in figure 5.12) is shown in figure 5.16.

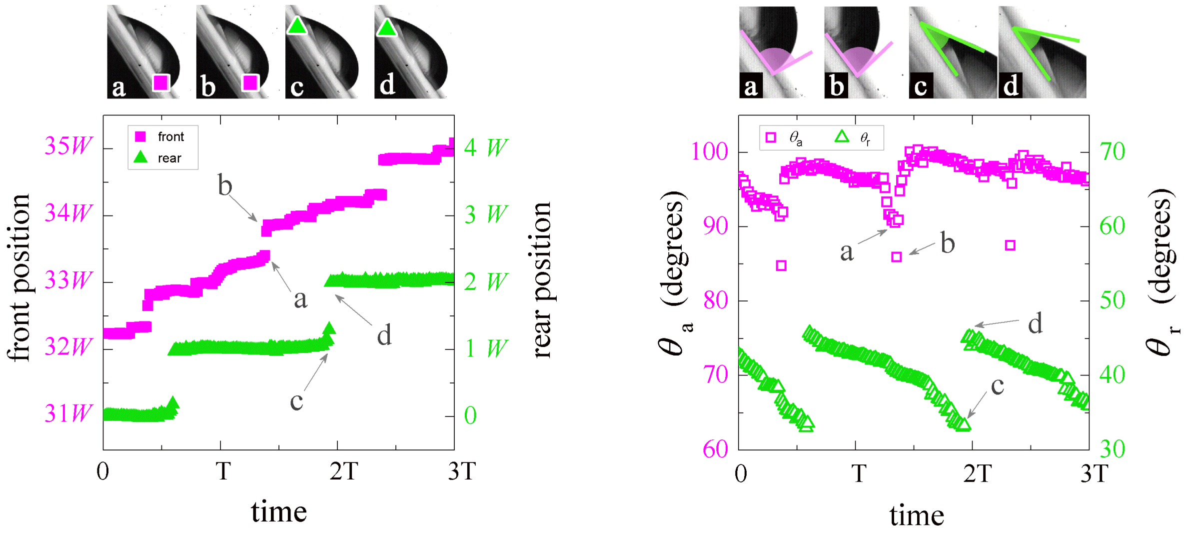

Figure 5.16 : Dynamics of a 30 μL water drop moving on sample STR_50% in the direction perpendicular to the stripes. Left graph: position of the front contact point (left axis) and rear contact point (right axis). Space is expressed in units of the pattern periodicity W and time in units of the period T (the time required for a step of the stick-slip dynamics). Right graph: time evolution of the advancing contact angle (left axis) and receding contat angle (right axis). The snapshot sequences show the contact points (left) and the contact angles (right) in the points indicated in the corresponding plots.

The drop clearly advances with a stick-slip behavior, with jumps on the order of the pattern periodicity W. The time period T is defined as the time required to a drop for a step of the stick-slip dynamics (in this case a displacement equal to W). Considering point (a) in the left graph of figure 5.16 as the beginning of T, at point (b) the front of the drop suddenly jumps forward by a distance almost equal to $W/2$, while the rear contact line is pinned. After the jump, the front line slowly advances and subsequently the rear line jumps by a distance equal to W, corresponding to points (c) and (d). The period T ends when the front contact point covers a length of $W/2$ before performing the next jump. The process then repeats itself. In correspondence to the leap of the front line, a fall in θ_a occurs, whereas θ_r reaches the minimum value just before the depinning of the rear contact point, then jumps to the maximum value in correspondence of the crossing of W and finally, during the subsequent pinning, gradually decreases (see the right graph in figure 5.16). We point out that the pinning-depinning transition occurs through a discontinuity both in the position and in the contact angle resulting more pronounced in the case of the rear of the drop.

This behavior is observed both in the case of ethanol in water and pure water drops on the same surface (sample STR_50%), differing only by the contact angle values that are higher in the case of water drops (see figures 5.16 and 5.17). On the other hand, the behavior of water drops on surfaces with larger stripes of OTS is quite different (see the bottom panel of figure 5.17): even if drop motion is characterized by the same space periodicity W, the trend of the front and the rear contact points is smoother and does not feature any net jump. Also θ_a and θ_r exhibit only oscillations without any marked discontinuity.

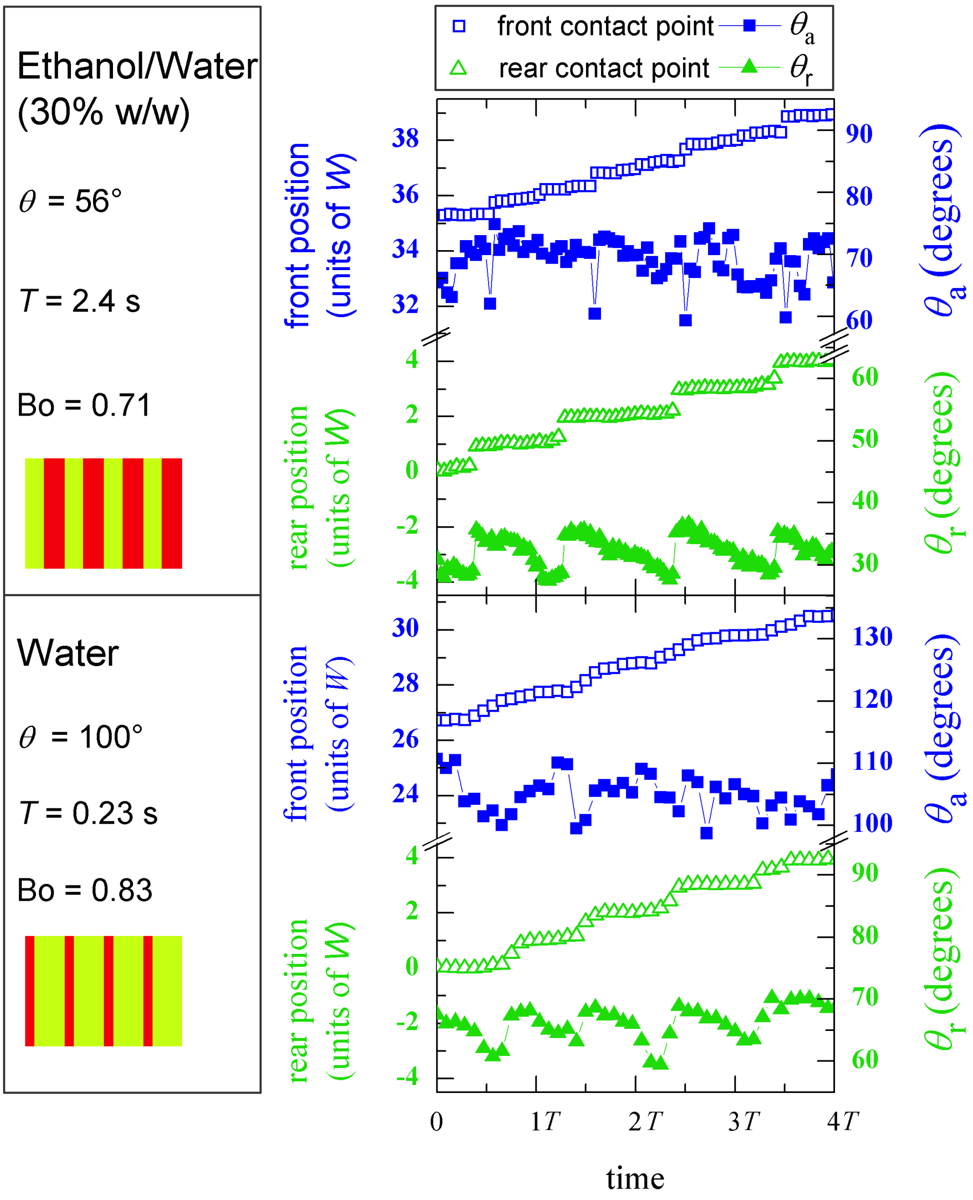

Figure 5.17 : Time dependence of the front and rear contact points (left axis) and the advancing and receding contact angles (right axis). Space is expressed in units of the pattern periodicity W and time in units of the period T (the time required for a step of the stick-slip dynamics). Top panel: measurement about a 30 μL drop of ethanol in water (30% w/w) sliding down the sample with stripes of equal width (STR_50%); bottom panel: measurement about a 30 μL water drop on the sample STR_83% featuring larger stripes of OTS (the hydrophobic part) with $f_1 = 0.83$, $f_2 = 0.17$. Boxes on the left report corresponding experimental details.

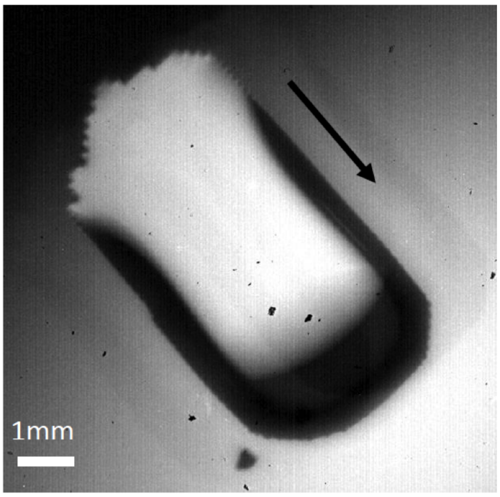

Figure 5.18 : Bottom view of a water drop on a triangular pattern. The contact line assumes a fragmentary shape to follow the borders of the triangles because of the pinning exerted by the presence of regions featuring different wettabilities.

On the square and triangular patterns the drop undergoes a stick-slip motion characterized by a continuous deformation of the entire contact line, which pins and depins at the edges between domains of different wettability, as shown in the photograph of the drop contact area in figure 5.18 and evidenced by the numerical snapshots reported in Section 5.5. As observed with the striped surfaces, the front and rear contact points move alternatively and the jumps forward do not occur simultaneously. However, on the triangular geometry, the jumps are less sharp than those observed in the case of hydrophilic and hydrophobic stripes of equal width (see figure 5.16). Instead, they resemble those found on striped surfaces with wider hydrophobic stripes, as arises from the comparison between the bottom panel of figure 5.17 and the graph of figure 5.19 displaying typical stick-slip motions in the direction ▲ ↓ (see below) on the linear and chessboard triangular configurations. These general features do not depend on the symmetry of the surface patterns or the sliding direction. The spatial periodicity of the stick-slip dynamics is equal to the height of the triangles or to the pattern periodicity W for all the square arrangements except for the chessboard configuration (sample CB_SQ), where the motion periodicity is $W/2$, as depicted in 5.19. For this geometry, the jumps of the contact points are compatible with the side of the squares, meaning that pinning and depinning occur at every row of squares. Again, this is also evidenced by the snapshots of the density contours reported in the numerical simulations (see Section 5.5).

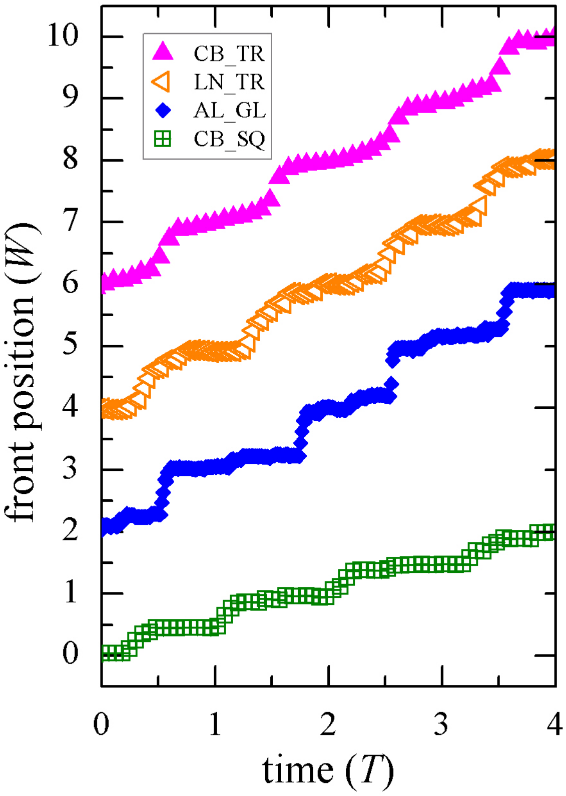

Figure 5.19 : Stickslip dynamics of the front contact point of water drops moving on the patterns with triangular domains arranged in chessboard (CB_TR) and linear (LN_TR) configurations and on two patterns formed by squares: aligned glass squares (AL_GL) and squared chessboard (CB_SQ). Time is expressed in units of the time period T, defined as the time required for a step of the stickslip dynamics, equal to W in all cases except on the squared chessboard pattern, where it is compatible with $W/2$. The front position is expressed in units of the pattern period W. Curves are vertically shifted for clarity.

§ 5.4.3. Stripes

By performing sliding measurements we can derive the relationship between the drop mean velocity U and the inclination angle α of the surface. Figure 5.20 reports data of water drops sliding on striped surfaces STR_50% and STR_83% and on homogeneous surfaces with similar wettabilities (see Chapter 4). The sliding velocity U scales linearly with $\sin\alpha$, as described by equation (4.6), for inclinations above the critical angle α_c, which is indeed determined by extrapolating the linear trend in the dissipative sliding up to zero velocity. We point out that experimentally we still observe motion even for tilt a few degrees ($\lesssim 5°$) smaller than α_c, a condition in which the drop is moving at low velocity where the viscous dissipation is negligible and the prediction of Equation (4.6) is no more applicable. Furthermore, the stick-slip regime is typically well observed close to α_c. Considering the heterogeneous and homogeneous surfaces with similar equilibrium contact angle, we observe two distinctive features: *i*) at the same inclination α, the velocity is always lower on the heterogeneous surface than on the homogeneous one and the angle α_c is higher for the heterogeneous surfaces which are characterized by a larger pinning; *ii*) the slope of the curve U *vs.* $\sin\alpha$ is the same for similar wettability, regardless of the composition of the surface, and is higher for the surfaces characterized by higher equilibrium contact angle.

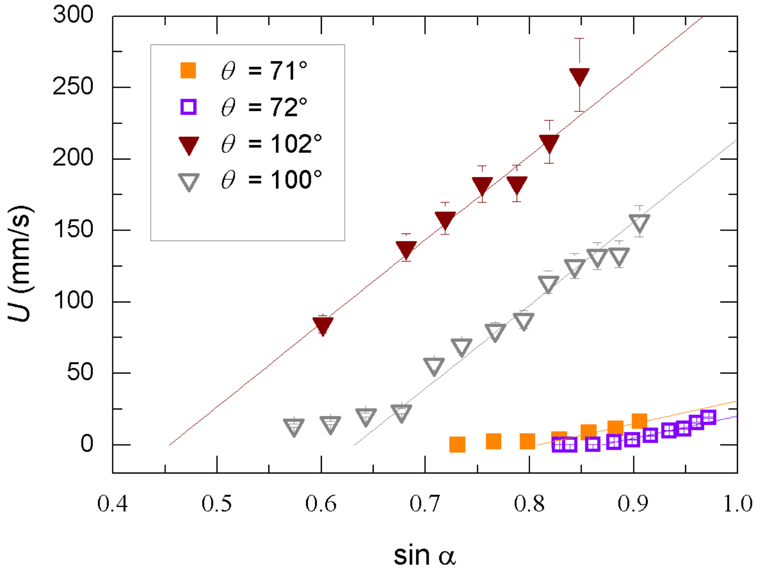

Figure 5.20 : Mean velocity of 30 μl water drops sliding down the heterogeneous (open symbols) surfaces STR_50% ($f_1 = f_2 = 0.5$, $\theta_{hete} = 72°$) and STR_83% ($f_1 = 0.83$, $f_2 = 0.17$, $\theta_{hete} = 100°$) and down homogeneous (filled symbols) surfaces of similar wettabilities, inclined by several angles α. Lines are linear fit to the data taken on a range where viscous dissipation is not negligible. The intercept at $U = 0$ defines the critical angle α_c.

§ 5.4.4. Squares

From the time evolution of the front contact point position, the mean velocity U has been determined through linear fits for different inclination angles α. The results obtained on the square patterns are summarized in the graphs of figure 5.21 in terms of the dimensionless Capillary number (Ca=$\eta U/\sigma$, where η and σ are the viscosity and the surface tension of the fluid, respectively) versus Bond number (Bo=$\rho V^{2/3} g \sin\alpha/\sigma$ where ρ is the density of the liquid and g the gravity acceleration). The onset of drop motion is found to be strongly affected by the arrangement of the domains. Actually, the critical Bond number Bo$_c$ (defined as the value at Ca=0 of the linear fit of the data) is the same for patterns with the same configuration but different wettability and is higher for the staggered squares than for the aligned ones. The critical Bo related to the chessboard geometry assumes an intermediate value between the other two pattern configurations. Above Bo$_c$, the data feature a linear trend with a slope clearly related to the static wettability of the samples: the slope is similar for surfaces characterized by the same contact angle, independently from the domain arrangement, and increases as the hydrophobicity of the sample increases.

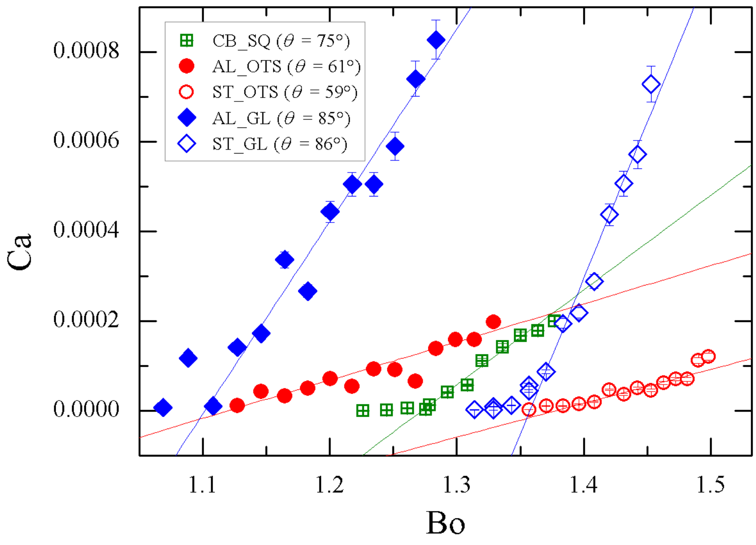

Figure 5.21 : Dependence of Ca (e. g. mean velocity) on Bo (e. g. plane inclination) for the 5 different configurations of patterns with squared domains: chessboard formed by squares (CB_SQ), aligned and staggered OTS squares (AL_OTS and ST_OTS, respectively) and aligned and staggered glass squares (AL_GL and ST_GL, respectively).

§ 5.4.5. Triangles

In contrast to square and striped surfaces, patterns formed by triangular domains are anisotropic: two main different directions of sliding can be defined, as sketched in figure 5.22. Direction ▲ ↓ indicates that the drop is moving from the apex to the base of the hydrophilic triangles, while direction ▼ ↓ is the opposite [230]. Sliding measurements have been performed along these two possible directions for several sample inclinations, with 40 μL drops which cover approximately 30-35 rows formed by 15 triangles each. The results obtained are summarized in the graphs of figure 5.22 in terms of the dimensionless Ca number versus Bo number. Both on the linear and on the chessboard patterns the velocity is different in the two sliding directions for the same plane inclination. Drops slide down faster along the direction ▼ ↓, the difference with respect to the opposite direction ▲ ↓ ranging from about 15% up to 50%. Furthermore, drops move faster on the chessboard pattern than on the linear one along both sliding directions.

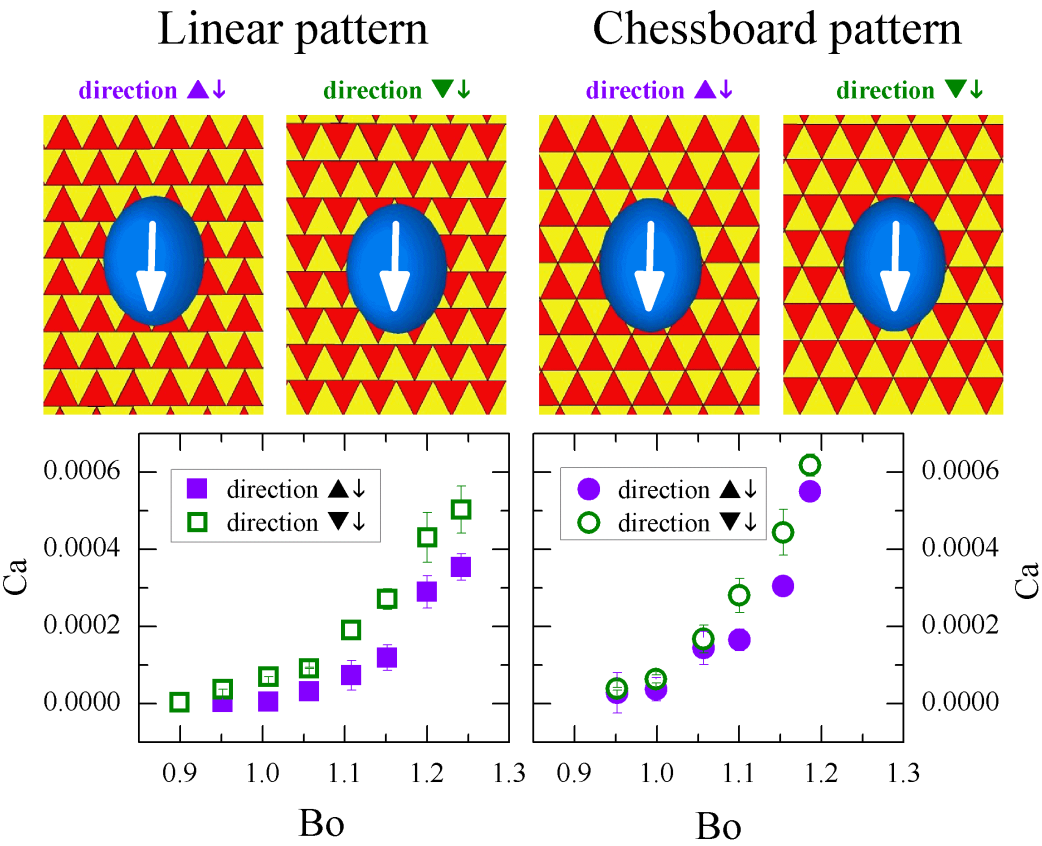

Figure 5.22 : Top cartoons: definition of the two possible directions of sliding (▲ ↓ and ▼ ↓) on the two patterns with triangular tiles: left, linear packing, right chessboard packing. Red (dark) areas represent glass hydrophilic parts, while yellow (light) areas symbolize OTS hydrophobic regions. The dimension of the drop, represented by the blue (dark) oval, is not in scale with respect to the size of the triangles: in a typical experiment drops cover almost 30-35 rows formed by 15 triangles. Bottom graphs: Ca number (e.g. mean velocity) as a function of Bo number (e.g. plane inclination α) on the linear (left) and chessboard (right) triangle arrangement.

The anisotropic behavior found between the ▲ ↓ and ▼ ↓ directions is consistent with the results of a recent study [230] concerning drops sliding down hydrophobic silane coatings patterned with small hydrophilic triangular domains arranged in a regular hexagonal lattice. However, the absolute values are much different because the hydrophilic triangles are a factor about 10 smaller than those in our study and are more sparsely packed, resulting in a hydrophilic fraction f_2=0.1. Accordingly, the pinning effects are less pronounced and the drops start moving at much smaller Bond numbers (∼0.12-0.15) than in our case (∼0.35-0.37). More interestingly, no stick-slip is observed on these patterns probably because f_2 is too small.

§ 5.4.6. Comparison between all the patterns

The graph in figure 5.23 collects the Ca *vs* Bo curves derived from the sliding on heterogeneous samples featuring similar wettability, but domains of different shape (stripes, aligned squares, squares and triangles arranged in a chessboard) in order to investigate the role played by texture geometry in affecting drop dynamics. Overall, the critical Bond number, that is, the critical dimensionless force needed to depin the drop, is found to be strongly affected by the shape and the spatial arrangement of the domains. Indeed the Bo_c is related to the distribution of the contact angle along the perimeter of the drop and is intimately connected to the pinning/depinning of the contact line at the edges of the domains. The drops are found to slide at lower Bo on the triangular configuration and the aligned squares, then on stripes and finally the sliding on the chessboard (and staggered) squares requires higher inclinations. On the contrary, the slopes of such curves are similar (eccept for the higher slope of data about sample AL_SQ, being actually more hydrophobic than the others), meaning that away from the critical Bond number, the dynamic regime depends mainly on the static contact angle and weakly on the real surface pattern: the viscous dissipation is given by an average on the domains independent of geometry details.

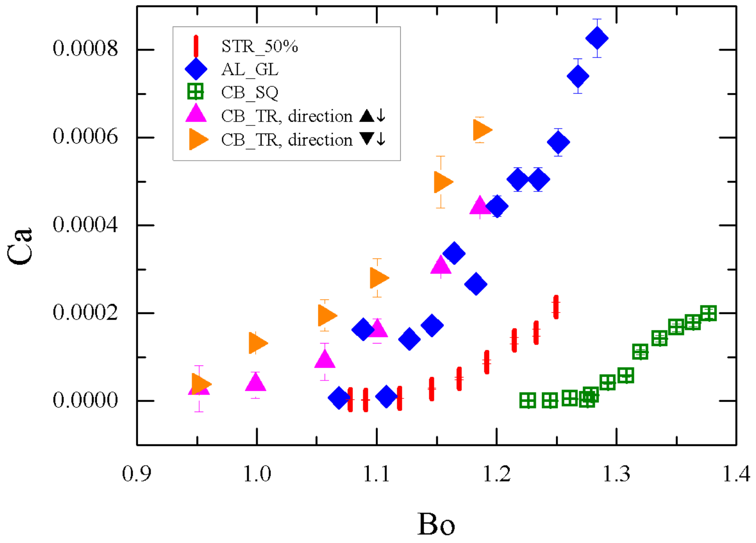

Figure 5.23 : Experimental Ca vs Bo relation for different surface patterns: stripes, aligned squares (AL_SQ), squares in the chessboard configuration (CB_SQ), and triangles with chessboard symmetry (CB_TR).

§ 5.5. Lattice Boltzman simulations

The experimental results are corroborated and completed with the use of numerical simulations based on the lattice Boltzmann models (see Section 1.6.1), which solve the diffuse-interface hydrodynamic equations of a binary mixture of two components (see refs [254] and [164] and references therein) d and o: d indicates the rich phase inside the droplet, corresponding to the liquid phase in the experiments, and o is the outer phase featuring a different viscosity (corresponding to the vapor phase in the experiments). We remark that fluids d and o differ from water and air in a real experiment both for the interface thickness and for the viscous ratio: this model considers a diffuse interface much wider

than in the experiment and the viscosity ratio between d and o phases is lower than the real viscosity ratio between water and air, to avoid numerical instabilities (see below for more details).
This method reproduces the Navier-Stokes equation for a binary mixture with densities ρ_d and ρ_o ($\rho = \rho_d + \rho_o$), with a body force density, $\rho_d g \sin\alpha$, applied to the rich phase inside the droplet (ρ_d) along the x-direction

$$\partial_t(\rho u_i) + \partial_j(\rho u_i u_j) = -\partial_j P_{ij} + \partial_j \tau_{ij} + \rho_d g \sin\alpha \delta_{x,i} \tag{5.1}$$

where τ_{ij} is the viscous stress tensor $\tau_{ij} = \eta(\partial_i u_j + \partial_j u_i)$, with η the dynamic viscosity, and u_i the velocity of the mixture. The pressure tensor P_{ij} accounts for the surface tension [266] at the interface between the two fluids, as well as the capillary forces at the contact line via a suitable imposition of wetting boundary conditions [254].
The patterning details can be easily changed by imposing mixed wetting boundary conditions. The numerical simulations refer to a flat hydrophilic surface (contact angle $\theta_2 \sim 50°$) patterned with different hydrophobic structures (contact angle $\theta_1 \sim 115°$). Initially 2D simulations were considered to model a drop on the striped samples, due to the symmetry of the problem, then 3D simulations were implemented to compare drop sliding on surfaces featuring different geometry: hydrophobic triangles on a hydrophilic plane with chessboard symmetry, aligned hydrophilic squares on a hydrophilic plane, squares arranged in chessboard symmetry, and alternating hydrophilic and hydrophobic stripes of equal width. In all cases, the hydrophilic and hydrophobic area fractions are assumed to be the same (i.e., $f_1 = f_2 = 0.5$), and the diameter of the droplet covers about 10 domains. More technical details about the numerical method can be found in Section 1.6.1 and in the studies [156, 166, 167, 266] and references therein.

§ 5.5.1. Stick-Slip

The stick-slip motion is well captured in the numerical simulations of a 2D drop on a surface with the same fraction of hydrophilic and hydrophobic areas, as shown in figure 5.24, which displays the time evolution of the positions of the front and rear contact points normalized to W, and T indicates the time period required for a displacement equal to W.

From the density snapshots, it is possible to determine precisely the positions where the contact line pins and depins with a resolution that is impossible to achieve in an experiment. The rear contact line gets pinned (snapshots a) before entering the hydrophobic area (yellow region at the base of the drop). A sudden jump makes it overcome the local energy barrier and enter the hydrophilic area (red region at the base of the drop) (snapshots b). The front contact line, in turn, stops before entering the hydrophobic regions. As the drop pins with an increasing advancing angle, it slowly penetrates through the hydrophobic area (snapshots c), similarly to what is observed in the experimental results reported in figure 5.16. A sudden jump follows when the front enters the hydrophilic area (snapshots d). We have also extended the simulations to the heterogeneous surface investigated in [101], which presents a lower wettability contrast of 10°, and found only periodic oscillations in the velocity without the occurrence of a stick phase in agreement with the experiment.
A further insight into the stick-slip mechanism can be given considering the balance equation obtained

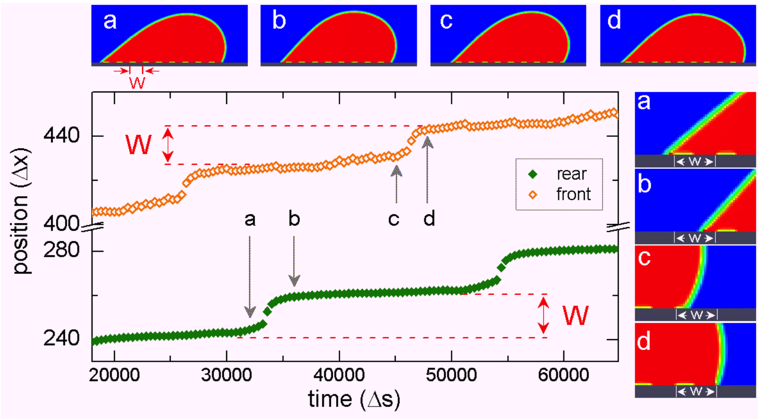

Figure 5.24 : Time evolution in dimensionless units (see text for details) of the front (left axis) and rear (right axis) contact points of a 2D drop on the heterogeneous substrate. The horizontal sequence of snapshots shows the whole drop motion. Color map on top is the density in Lattice Boltzmann units. Low density regions appear dark (blue) while high density regions are light (red). The vertical sequence (on the right) reports the corresponding enlargements to better appreciate the position of the contact line. Consistently, light (yellow) areas at the drop base represent hydrophobic regions, while red (dark) stripes represent hydrophilic regions.

by integrating the diffuse interface time-dependent Stokes equation 5.1 over the drop volume (then made dimensionless with respect to the surface tension force Rσ):

$$Ma(t) = F_{cap}(t) + D(t) + F_g \tag{5.2}$$

where $a(t)$ is the acceleration of the drop with mass M and F_g is the down-plane component of the gravitational force. The term F_{cap} (calculated as the integral of the pressure tensor term) accounts for the nonuniform pressure and curvature distortion as well as the capillary force on the drop at the contact line. The function $D(t)$ (the integral of the viscous stress term) quantifies the drag force due to viscous shear.

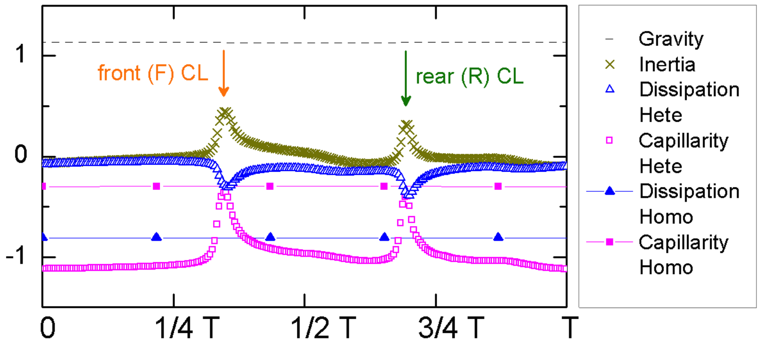

Figure 5.25 : Time evolution of the various terms in the balance equation (5.2) for the heterogeneous and the homogeneous case chosen to display the same static wettability.

Figure 5.25 presents the analysis of the balance equation (5.2) for a time frame of a period T of the stick-slip dynamics and compares it to the homogeneous case, for the same Bo. The gravitational force F_g is constant in time. When the drop is pinned, F_g is almost balanced by $F_{\rm cap}$ (snapshots c). Immediately after, the front contact line jumps forward and the drop depins ($F_{\rm cap} \rightarrow 0$): the drop experiences a localized acceleration $a(t)$ with a consistent dip in the dissipation function. The drop gets pinned again until the rear contact line jumps forward. The homogeneous case is instead stationary: the energy provided by F_g is almost entirely transferred into dissipation, apart from the deformation of the interface which causes a term F_{cap} smaller by a factor $\approx$10 with respect to the heterogeneous case. Overall, we see that the effective dissipation in the heterogeneous case is strongly suppressed as compared with the stationary homogeneous case. This is because the large wettability contrast causes additional energy to be stored in the non-equilibrium configuration of the drop which can pin before the contact lines jump forward.

§ 5.5.2. Comparison between all the patterns

Figure 5.26 shows top-view snapshots taken at equal times and at the same Bo $\sim$ 0.35 for four different geometries. We can clearly see that the slowest motion occurs on the stripes and the square chessboard pattern. This is likely a consequence of the elongation of the drop along the stripes in a direction perpendicular to the motion, which causes enhanced energy to be stored in the nonequilibrium configuration of the droplet. As evident from figure 5.26, for the same Bo number, the deformation of the droplet is larger on the striped and chessboard patterns.

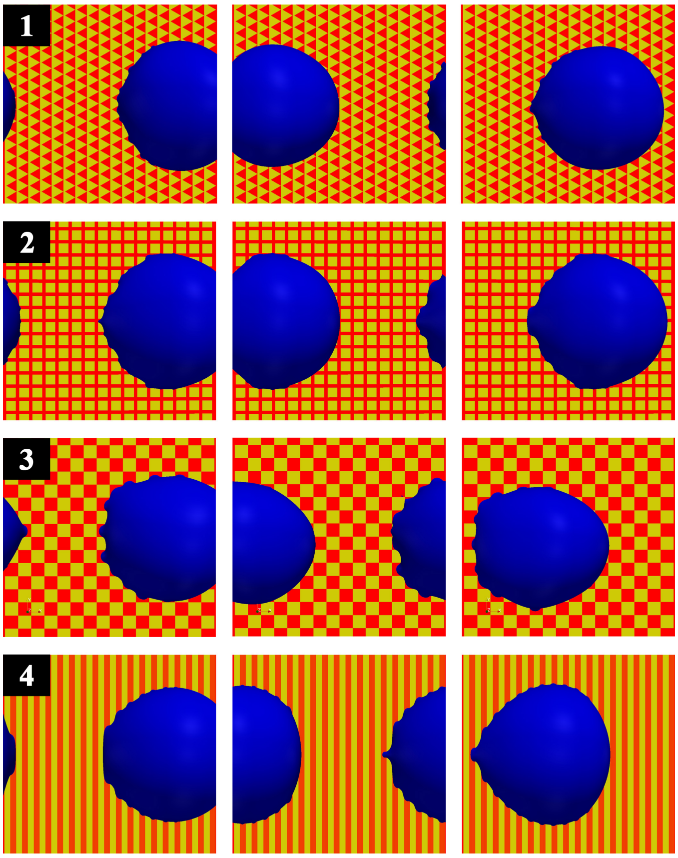

Figure 5.26 : Top-view snapshots showing the motion of droplets at equal times on four patterned surfaces all having $f_1 = f_2 = 0.5$: (1) triangles with chessboard symmetry (CB_TR), direction ▲ ↓; (2) aligned squares (AL_SQ); (3) square chessboard (CB_SQ); and (4) stripes. Droplet motion proceeds from left to right. Red (dark) areas represent hydrophilic parts, and yellow (light) areas symbolize hydrophobic regions.

Further insight can be gained by plotting the output of the numerical simulations in terms of Ca versus Bo numbers as done with the experimental data. Figure 5.27a shows the results corresponding to a viscosity ratio of $\chi = \eta_d/\eta_o = 20$, where η_d and η_o are the drop and the outer phase viscosity respectively. The choice of $\chi = 20$ is motivated by the necessity of producing data with a viscous ratio about an order of magnitude larger than $\chi = 1$ in order to approach the experimental value without undergoing numerical instabilities.

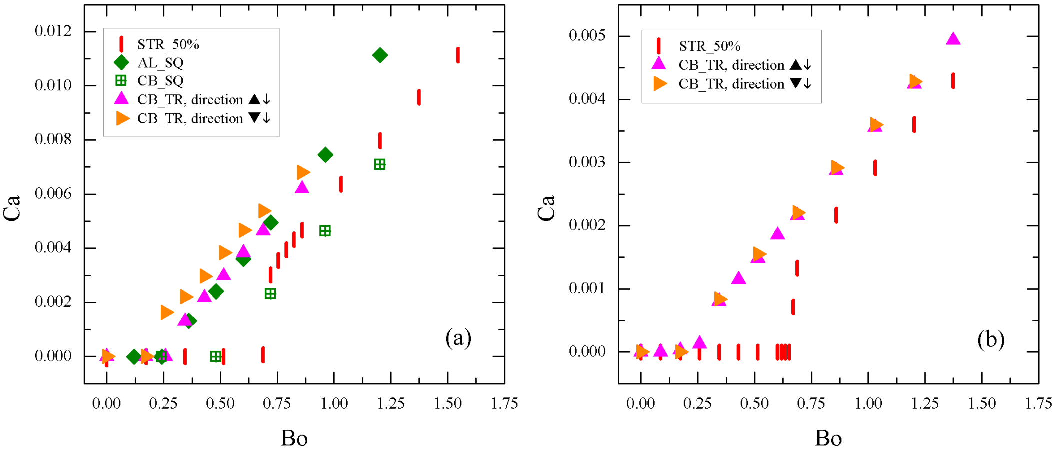

Figure 5.27 : Numerical Ca *vs* Bo relation for different surface patterns: stripes, aligned squares (AL_SQ), squares in the chessboard configuration (CB_SQ), and triangles with chessboard symmetry (CB_TR). a) viscous ratios $\chi = 20$ and b)$\chi = 1$.

The mean speed on the stripes and on the square chessboard is about 35% smaller than on the other patterns. Furthermore, the aligned squares produce the most slippery surface, confirming the experimental findings. In addition, for the triangular chessboard pattern the Bo_c in the ▲ ↓ direction is larger than that along ▼ ↓ ($\Delta\mathrm{Bo}_c \sim 0.05$). The Bo$_c$ of the aligned squares does not change appreciably with respect to the triangles. Instead, the Bo$_c$ of the stripes is larger than that of the triangles and squares. The slope $\Delta\mathrm{Ca}/Delta\mathrm{Bo}$ does not change appreciably (above Bo$_c$) for the four cases. This confirms that such a slope depends on the equilibrium contact angle θ, which is the same in these cases ($f_1 = f_2 = 0.5$ and θ_1, θ_2 fixed). To test the validity of this argument against a change in the viscous ratio between the inner and outer drop regions, a series of numerical simulations has been performed by changing the dynamic viscosity of the outer phase for both triangles and stripes. The graph of Figure 5.27b shows the results calculated for a viscous ratio of $\chi = 1$. Again, Bo$_c$ is larger in the case of stripes than in the case of triangles whereas the slope $\Delta\mathrm{Ca}/\Delta\mathrm{Bo}$ is the same above Bo$_c$. Moreover, for a viscous ratio of $\chi = 1$, the data on the triangles with chessboard symmetry display the same Ca versus Bo curve regardless of the drop direction, whereas for $\chi = 20$ there is a distinct difference in the corresponding Bo$_c$ values, as reported in figure 5.27a. This suggests that the observed anisotropy in the CB_TR pattern is intimately connected to the dissipation at the contact line. For a drop sliding down a homogeneous surface with equilibrium contact angle θ, a flow develops in the outer wedge angled by an angle $\pi - \theta$. Because the viscosities of the inner and outer phases are the same when χ =1, the dissipation for a system composed of a drop forming an angle θ is then the same as that of a drop with an angle $\pi - \theta$. Therefore, for a viscous ratio of χ =1, directions ▲ ↓ and ▼ ↓ become equivalent. These numerical findings are consistent with the experimental results presented in figure 5.23. The main quantitative difference concerns the value of Bo_c: the numerical value is much smaller than the experimental one. This is likely due to the reduced contact angle hysteresis in the numerical simulations because, at variance with the experimental data, the sliding on homogeneous surfaces in numerical simulations is by construction not affected by the hysteresis. From the numerical simulations we can therefore isolate the effect of the pattern by introducing a critical Bond number for the onset of motion, representing an increase in the static energetic barrier that must be overwhelmed by gravity before the drop starts to move.

§ 5.6. Comparison between the sliding on homogeneous and heterogeneous samples

To better understand the dependence of the curve Ca *vs.* Bo on the static wettability, we collected in the same plot in figure 5.28 the numerical data and the experimental results corresponding to the sliding on all the investigated samples, i. e. the homogeneous surfaces discussed in Chapter 4 and the heterogeneous samples formed by stripes, squares or triangles.

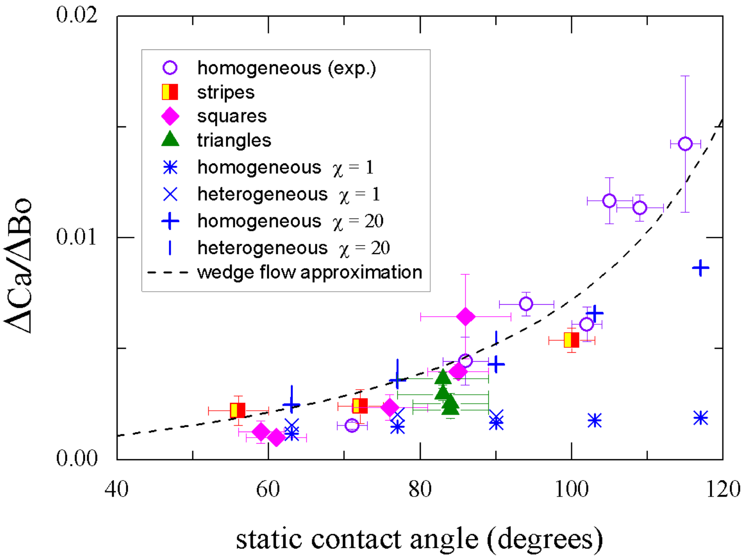

Figure 5.28 : Slope of the Ca *vs.* Bo curve as a function of the equilibrium contact angle. Filled symbols refer to the sliding on the homogeneous samples discussed in Chapter 4 (see figure 4.5). Open symbols are data derived from the experimental values reported in figures 5.20,5.21 and 5.22. Numerical simulations are performed with viscous ratios $\chi = 1$ and $\chi = 20$ between the drop phase and the outer phase for both homogeneous and striped surfaces. The dashed line is the scaling law predicted by (4.8), calculated for small drops sliding down homogeneous surfaces with a wedge dissipation as the dominant dissipative contribution [150, 152].

The numerical results with $\chi = 1$ do not show any appreciable variation of the slope $\Delta\mathrm{Ca}/\Delta\mathrm{Bo}$ with the equilibrium contact angle, indicating that the dissipation is unchanged at changing the equilibrium contact angle. For a drop sliding down a homogeneous surface with equilibrium contact angle θ, a flow develops in the outer wedge angled by an angle $\pi - \theta$. Being the viscosity of the inner and outer phase the same, the dissipation for a system composed of a drop with equilibrium contact angle θ is therefore the same as that of a drop with equilibrium contact angle $\pi - \theta$. This symmetry in changing the outer fluid with the inner fluid is responsible for the independence of $\Delta\mathrm{Ca}/\Delta\mathrm{Bo}$ on the contact angle. Repeating the simulations with the heterogeneous cases, we obtain the same value of $\Delta\mathrm{Ca}/\Delta\mathrm{Bo}$, witnessing that the average dissipation for the patterned surfaces grows in a similar way at increasing

the Bond number. To observe a variation of the slope with respect to a change in the equilibrium contact angle, we need to change the viscous ratio χ. Numerical results are shown for the case $\chi = 20$: the change in the slope that we achieve is not as large as the one that we get in the experiments, and the reason is probably because such viscous ratio is still smaller than the experimental values. Unfortunately, numerical simulations with very large χ are quite unstable and technical improvements are needed to cure such numerical instabilities. At very large viscous ratio the dependence of the slope $\Delta\mathrm{Ca}/\Delta\mathrm{Bo}$ as a function of the equilibrium contact angle θ can be described by the scaling law (4.8) with $c(\theta)$ calculated through the so called 'wedge flow approximation' [150, 152]: such scaling law is reported for comparison with the experimental and numerical data. Here we recall that the scaling of $\Delta\mathrm{Ca}/\Delta\mathrm{Bo}$ encodes the general feature that smaller contact angles are associated with higher viscous dissipation, indeed the slope $\Delta\mathrm{Ca}/\Delta\mathrm{Bo}$, being inversely proportional to the dissipation (see Chapter 4), clearly increases as the hydrophobicity of the surfaces increases. Overall, the agreement between the angular dependent prefactor of equation (4.8) and the experimental data are quite reasonable for all the investigated surfaces, including the heterogeneous one. This indicates that the effects of the heterogeneous patterning can be readsorbed in a renormalized value of the Bo_c, representing the increase of the static energetic barrier that must be overwhelmed by gravity before the drop starts to move, an observation that bears similarities with the results discussed in [163].
Furthermore, the numerical simulations provide evidence that the slope $\Delta\mathrm{Ca}/\Delta\mathrm{Bo}$ is well parametrized by the equilibrium contact angle, either homogeneous or heterogeneous, even in situations where the outer phase has a non negligible viscosity with respect to the drop phase, although numerical points do not well overlap the theoretical curve (4.8) because of the low viscosity ratio χ.

§ 5.7. Conclusion

We have characterized both experimentally and numerically the motion of drops sliding on heterogeneous surfaces formed by domains having a large wettability contrast. For Bond numbers close to a critical Bond number, these drops undergo a characteristic non linear stick-slip motion whose average speed can be up to an order of magnitude smaller than that measured on a homogeneous surface having the same equilibrium contact angle. The slow down is the result of the pinning-depinning transition of the contact line which causes energy dissipation to be localized in time and large part of the driving energy to be stored in the periodic deformations of the contact line when crossing the stripes. We have quantified the change of dissipation inside the drop as a function of the increasing Bond number, by comparing the motion of the drops on heterogeneous patterns with those on homogeneous substrates: the main effects of the heterogeneous patterning can be readsorbed in a renormalized value of the critical Bond number, representing the increase of the static energetic barrier that must be overcome by gravity before the drop starts to move. On the triangular patterns, an anisotropic behavior is found with drops sliding down faster when the tips of the glass hydrophilic triangles are pointing in the down-plane direction. The onset of drop motion is strongly affected by the shape and the spatial arrangement of the hydrophobic domains. Instead, in the dynamic regime, the slope $\Delta\mathrm{Ca}/\Delta\mathrm{Bo}$ mainly depends on the static equilibrium contact angle and weakly on the actual surface pattern. Our findings suggest practical criteria to use the chemical pattern printed on the surface to accurately tune the static and dynamic behavior of drops on surfaces. It is also worth to point out the essential role played by numerical simulations, which offer great flexibility in investigating a variety of load conditions and performing local measurements of capillary, viscous and body forces, otherwise impossible to obtain by experimental means. This would provide invaluable insights in the engineering of chemical patterns in open microfluidic devices.

Chapter 6

Drop motion through a chemical step

The sliding motion of a drop can be stopped by electro-wetting [267] or by sticky textures [49]. Also, drop trajectory can be deviated by means of chemically heterogeneous patterns [101, 268].

This chapter describes what happens when a drop sliding on a moderately hydrophilic surface meets a more hydrophobic region. Four distinct outcomes are possible: a) the drop is pinned at the step; b) the drop is deviated upon crossing the step; c) the drop moves along the chemical step and d) the drop starts deviating along the border but then stops after travelling a distance of 0.3-2 cm.

A brief introduction about techniques applied to affect drop sliding is given in Section 6.1. Section 6.2 reports the fabrication procedure and the characterization of samples formed by two chemically different regions. The experimental observations about drop interaction with the chemical step are the subject of Section 6.3. The corresponding numerical results obtained through Surface Evolver simulations are discussed in Section 6.4. Finally conclusions summarize this work (Section 6.5).

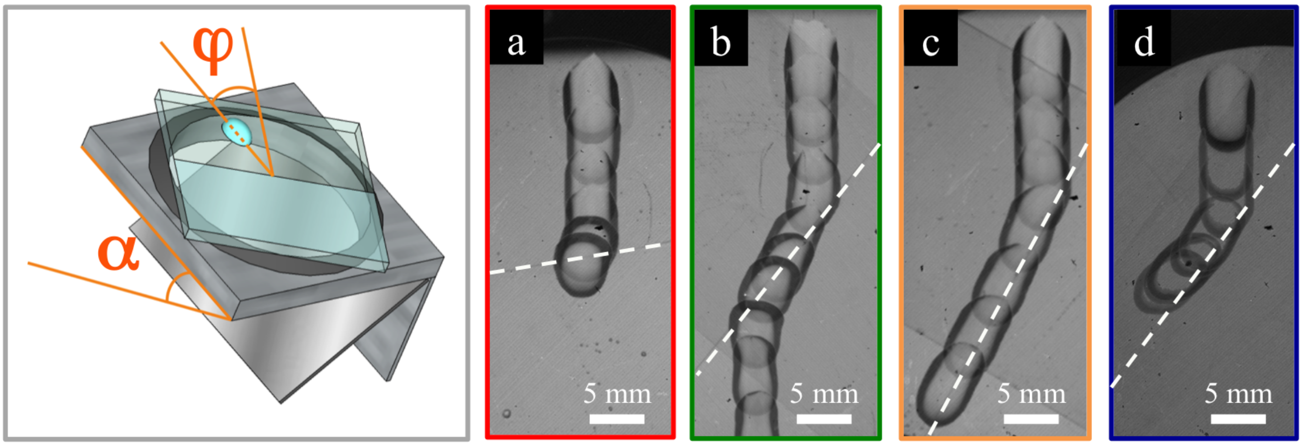

§ 6.1. Introduction

Different strategies have been devised in order to act on the sliding motion of a drop, including both passive and active methods. For instance, a drop moving very quickly on a superhydrophobic surface can suddenly stop when it enters a sticky hairy region [49]. A similar effect can be achieved by electrowetting as described in [267], where the trapping of a drop running on a superhydrophobic inclined plate is found to depend on its initial velocity and the applied voltage. The trajectory followed by a drop on a superhydrophobic sample can also be deflected by patterning the surface with regions characterized by a different contact angle hysteresis [268]. According to this study, drop deflection increases with increasing the difference in $\Delta\theta$ across the junction and depends also on the angle between the junction line and the direction of drop motion. In addition, both the velocity variation and the direction of deflection are different whether the transition occurs from a region with higher hysteresis to one with lower hysteresis or vice versa. This work includes the analysis of drop deflection induced by a step or single and multiple stripes. Surfaces patterned with stripes have been considered also in [101]. In this case the chemically heterogeneous sample is formed by hydrophobic stripes of different wettability. The surface is overall moderately hydrophobic and the wettability contrast between two different stripes is small (the corresponding static contact angles differ by around 10°). Again, such pattern is effective in deflecting the motion trajectory: drops tend to deviate along the inclined lines insted of following the direction of gravity.

The aim of our work is to further investigate the behavior of a sliding drop on a chemically heterogeneous surface formed by two extended regions of different wettability. Such a system can be thought as a pattern of chemical stripes (see Chapter 5), in the limit where the period is much larger than the drop diameter. This choice avoids the complication of having multiple pinning sites in the front and the rear of the drop [101], and allows to investigate the interplay between contour deformation and global pinning, disentangling the interference between drop size and pattern period. In contrast to [49, 267, 268], we focus on a situation where drop dynamics is governed by viscous dissipation and where inertial effects are minimized in order to examine the role of capillary forces and contact line distortion in the interaction of a drop with a chemical step. This regime is the prefereable choice to model the system through the Surface Evolver program providing a faithful description of the experiment even on a quantitative level.

§ 6.2. Production and characterization of a chemical step

For our study about the deviation of a sliding drop crossing a linear interface between two chemically homogeneous, hydrophobic surfaces the ideal wettability contrast of about 30°. Various methods have been explored to produce the patterned substrate. Next we briefly outline the most reliable procedure we devised. The substrate was a square slab in polycarbonate (PC) having a thickness of 5 mm and side of 5 cm. Half of the original protective cover was kept as a mask for the deposition from the vapor phase of a molecular layer of trichloro(1H, 1H, 2H, 2H-perfluorooctyl)silane (TFS). The removal of the cover produced two chemically distinct areas separated by a linear interface. The deposition of TFS did not affect the surface roughness, which was measured with a profilemeter to be about 20 nm in both areas. The wettability properties of the two regions are summarized in table 6.1, which reports the static θ, advancing θ_A and receding θ_R contact angles of droplets having a volume of 1 μL. Differently from usual, in this case the liquid used for the measurements is not distilled water, but a glycerol/water 80% (w/w) solution, which is chosen for this experiment because of its high viscosity ($\sim$ 50-60 cP), yielding a drop dynamics dominated by contact line friction so that inertial effects are negligible and the interaction of the drop with the chemical step is regulated by capillary forces and shape deformation.

Table 6.1 : Main parameters of the fluid used in this study. The concentration c is reported in w/w. Density, viscosity and surface tension are calculated from [269] for a tempertaure $T = 22°C$ and are labelled with ρ, η and σ respectively. Static (θ) and dynamic contact angles (θ_A and θ_R) and contact angle hysteresis ($\Delta\theta$) refer to sessile droplets on the substrate listed in the last column.

Fluid solution	c (w/w)	ρ (g/cm^3)	η (mPa s)	σ (mN/m)	θ (deg.)	θ_A (deg.)	θ_R (deg.)	$\Delta\theta$ (deg.)	substrate
glycerol in water	80%	1.2	55	65	86±2	88±1	63±3	25±3	PC
glycerol in water	80%	1.2	55	65	117±2	118±2	64±4	54±4	silanized PC

Besides this wettability characterization, based on the sessile drop method (see Section 2.1), we observed the sliding on the two homogeneous surfaces to derive the Capillary (Ca=$\eta U/\sigma$, where η and σ are the viscosity and the surface tension of the fluid, respectively) *vs* Bond number (Bo=$\rho V^{2/3} g \sin\alpha/\sigma$ where ρ is the density of the liquid and g the gravity acceleration) curve and the relation between the dynamic contact angles and the contact line velocity. The left graph of figure 6.1 reports the experimental values of Capillary number as a function of the Bond number for 40 μL drops. As discussed in Chapter 4, the scaling between Ca and Bo is almost linear and features a slope and a critical Bo depending on θ and $\Delta\theta$ respectively. In particular, on PC both the slope and Bo$_c$ are lower than on the silane coating because both the static angle and the contact angle hysteresis are smaller, as listed in table 6.1. The typical velocities of the drop steadily sliding on both regions range between $v \sim 0.1 mm/s$ and $v \sim 10 mm/s$. Accordingly, the Reynolds number was always smaller than $\sim$ 1, typical of a creeping motion, while the maximum capillary number was $\sim$ 0.01, characteristic of an over-damped dynamics which can be well described by the Surface Evolver simulations (see section 1.6.2). The right graph in figure 6.1 shows the relation between advancing and receding dynamic contact angles and the corresponding velocity of the contact line (positive for the front contact point and negative for the rear contact point). The error related to evaluation of the contact angles (typically between 2° and 4°) prevents to determine the precise exponent of the scaling between velocity and contact angle (see equation 1.48). Nevertheless, the threshold dynamic angles extrapolated from these data for $U = 0$ are compatible with the values measured by inflating and deflating a sessile drop (compare right graph in figure 6.1 and data in table 6.1). The experimental relation between velocity and contact angles is given as input to the Surface Evolver simulations to faithfully reproduce the behavior observed in the experiment (see Sections 1.6.2 and 6.4).

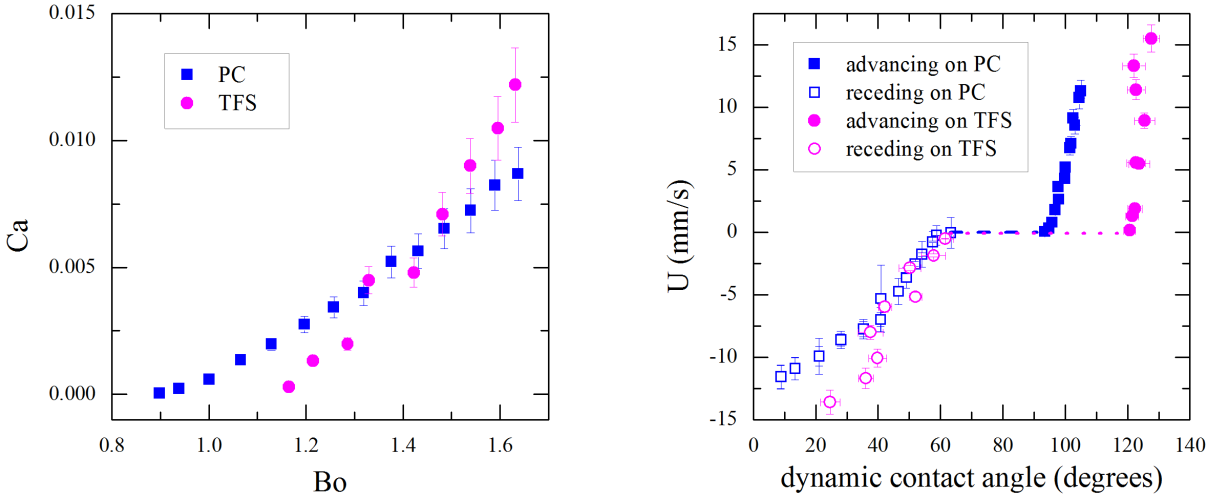

Figure 6.1 : Dynamic characterization about 40 μL glycerol/water droplets sliding on homogeneous PC and homogeneous TFS. Left graph: Ca *vs* Bo curve. Right graph: relation between the velocity of the contact points and the corresponding dynamic contact angles.

§ 6.3. Experimental results

For the study of drops interacting with a chemical step the setup described in Section 2.2 has been modified by introducing a manually rotating stage with a central hole allowing to change the inclination φ of the linear interface (more precisely, φ is defined as the angle between the in-plane component of gravity and the normal to the border delimiting the hydrophilic and hydrophobic regions). The stage is mounted on a motorized tilting support to incline the sample by the angle α, as sketched in figure 6.2.

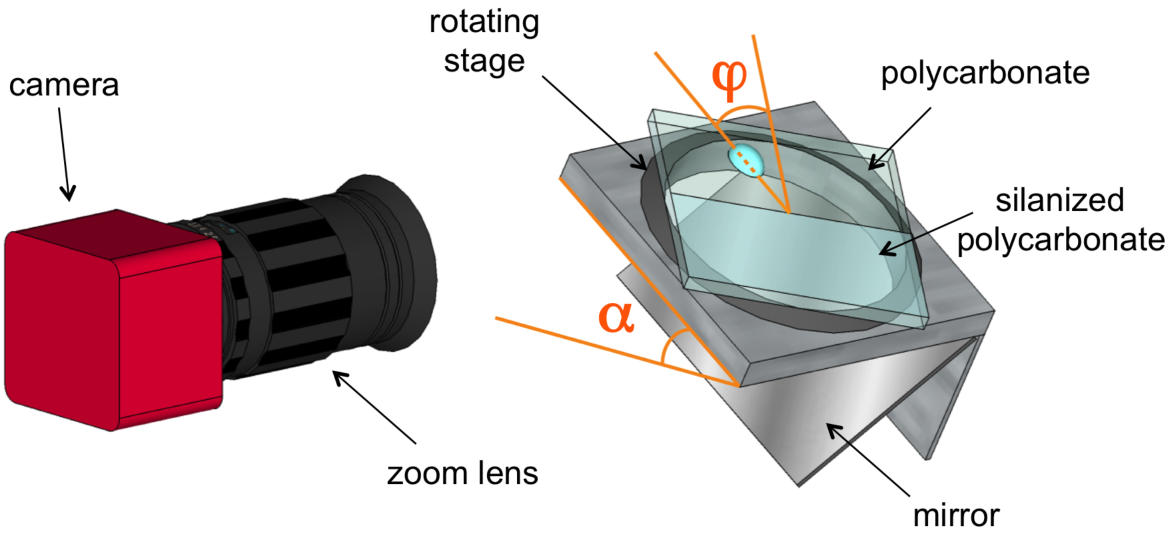

Figure 6.2 : Experimental setup to study the interaction of a sliding drop with a chemical step. The plane inclination is α and the inclination of the step interface is ϕ. The drop slides down from the more hydrophilic region (polycarbonate) to the more hydrophobic one (silanized polycarbonate) and its trajectory is observed from the bottom view seen in the mirror.

The crossing of the chemical step is studied by depositing drops of known volume on the polycarbonate region tilted by a constant angle α and following with the camera their trajectories observed from the bottom view reflected by the mirror. For each α, this procedure is repeated at different inclination angles φ, from 0° to 80°. Four distinct scenarios are observed as depicted in figure 6.3: a) the drop is pinned at the step; b) the drop is deviated upon crossing the step; c) the drop moves along the chemical step and d) the drop starts deviating along the border but then stops after travelling a distance of 0.3-2 cm.

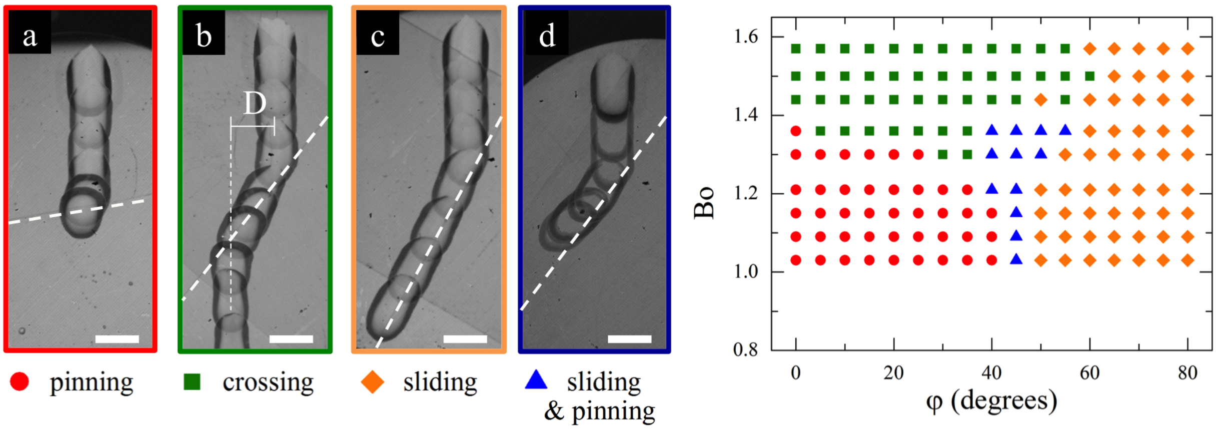

Figure 6.3 : Possible trajectories of a drop in proximity of a chemical step: a) pinning; b) crossing the interface; c) complete sliding along the interface and d) initial sliding along the border then interrupted. The dashed inclined line marks the chemical step and the horizontal scale bar corresponds to 5 mm. *D* represents the separation distance underwent by the drop after crossing the step in panel b). The right phase diagram reports the dynamical behavior assumed for different values of Bo number and interface inclination φ.

During the measurements, α was varied from $\sim 30°$ to $\sim 50°$ and $V = 40\mu$L. Smaller α yielded drops pinned to the surface; vice versa, $\alpha > 50°$ was not possible because it caused the run off of drops from the syringe needle during the infusion stage. In this way it was possible to map out a dynamical phase diagram as depicted in the right graph in figure 6.3. It shows the occurrence of the four regimes at different φ and Bond number. At sufficiently high interface inclination φ, the drops were always found to slide along the interface. Instead, for φ less than about 30° and small Bo, the drop got pinned at the interface. Increasing Bo above about 1.3 caused the drop to cross the chemical step. Unexpectedly, the minimum Bo required for passing in the more hydrophobic region does not correspond to $\varphi = 0$, i. e. when the interface is orthogonal to the sliding direction, but an inclination $30° < \varphi < 40°$ promotes drop crossing.

To quantify the interaction of a passing drop with the chemical step, we measured the lateral distance *D* separating the final trajectory from the incoming one as indicated in figure 6.3b. The left graph of figure 6.4 shows its variation with the product Bo $\cos\varphi$. A linear decrease is observed starting from an initial $D \sim$7 mm.

We also evaluated the transition time *T*, defined as the time lapse between the instant when the front contact point touches the chemical step and the instant in which the rear contact point passes it, so that the drop is entirely on the hydrophobic region. The dependence of *T* on the product Bo cos is reported in the right graph of figure 6.4 for different values of φ: for a fixed φ, *T* decreases as the Bond number is increased.

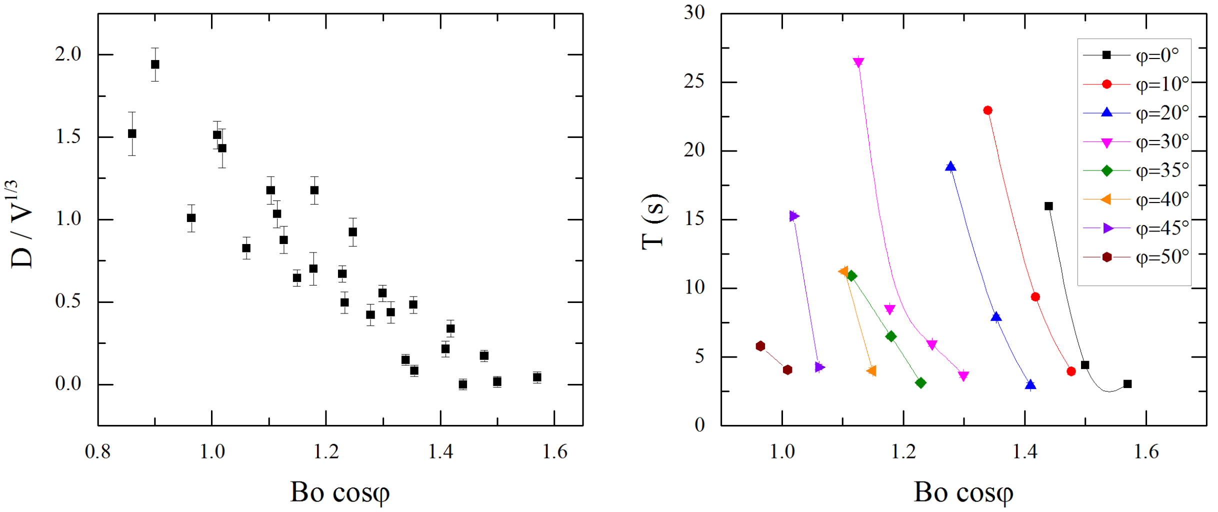

Figure 6.4 : Deviation D (left grapf) and transition time T (right graph) of a crossing drop as a function of the Bo number and the interface angle φ. Lines are not a fit of the data but just a guide for the eye.

§ 6.4. Numerical results

These experimental observations have been modelled through the simulations based on the Surface Evolver program described in Section 1.6.2. To match the experimental conditions, the input parameters adopted in the numerics are the same, i. e. the values related to the fluid listed in table 6.1 and the dependence between velocity and dynamic contact angles reported in figure 6.1, interpolated with a linear relation (β=1 in equation 1.48).
Similarly to the experiment, also the simulations detect the four possible dynamical behaviors described in figure 6.3. The graph in figure 6.5a compares experimental (symbols) and numerical (solid line) phase diagrams, displaying a good qualitative matching, even if the experimental pinning and crossing regions are respectively more and less extended than the corresponding numerical areas. Probably this discrepancies are due to defects of the interface which favour contact line pinning preventing contact line motion. However the key feature of the experimental diagram, i. e. the minimum of the crossing region corresponding to an inclination φ different from 0°, is evinced also by simulations. In addition, simulations allows us to further investigate the morphology of the phase diagram by changing the input parameters (in particular $\Delta\theta$) using also values non accessible in an experiment. For instance, figure 6.5b reports the contour of the crossing region in presence ($\Delta\theta \neq 0°$) and in absence of intrinsic hysteresis ($\Delta\theta = 0°$). In absence of intrinsic hysteresis the Bo required to cross the step is well described by Bo$\cos\varphi$, that is the Bond perpendicular to the step. On the other hand, in presence of intrinsic hysteresis the shape of the curve is completely different and develops a minimum for $\varphi \neq 0°$. This difference underlines and reveals the fundamental importance of the intrinsic hysteresis characterizing the substrates to faithfully describe and correctly explain the experimental observation.

In addition, simulations can provide the energy landscape of the system, as depicted in figure 6.6. Panels a-c report the footprints of a simulated drop at different values of φ and show the deformation of the contour line due to the interaction with the chemical step, revealing again a good qualitative

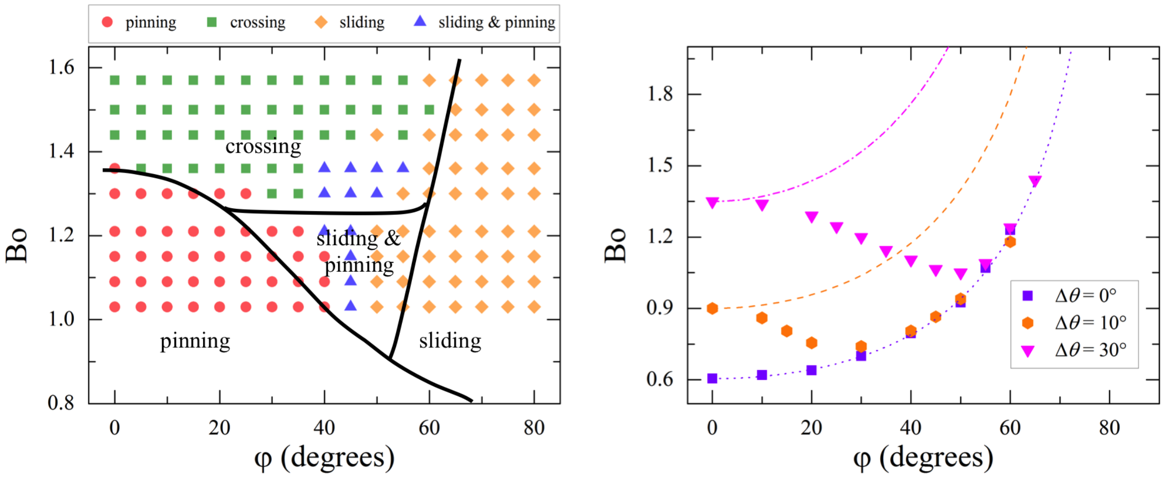

Figure 6.5 : Left panel: phase diagram where the black solid lines represent the boundaries between the different dynamic regimes evinced by the simulations and points refer to experimental values. Right panel: boundary of the crossing phase calculated with the simulations for different values of $\Delta\theta$. In this test $\Delta\theta$ is the same for both region, while the advancing contact angle is 90°/70° in the more hydrophobic/hydrophilic region. In absence of intrinsic hysteresis ($\Delta\theta$=0°) the Bo number required to cross the step is well described by Bo cos φ=Bo$_\perp$, where Bo$_\perp$ is the minimum Bo to have crossing orthogonally to the step (dashed curves). In presence of intrinsic hysteresis ($\Delta\theta$=10°, 30°) the Bond number required approaches the case without hysteresis at large φ.

agreement between the experiment and the numerical results. The corresponding plots d-f report the minimum force required to move the drop in terms of the Lagrange multiplier μ (see [85, 270] for more details). The value of such force is calculated at every position of the drop center of mass (x) for different inclinations φ and depends entirely on drop shape. When the drop meets the step, the force increases due to the chemical pinning. As φ increases, the force develops two peaks (see figures 6.6d and 6.6e) corresponding to the configurations marked in figures 6.6a and 6.6b: the first red peak is related to a partial penetration in the more hydrophobic region, while the second (blue) one is the force necessary for a complete transition in the hydrophobic area. As a consequence, if the Bo number is lower than the first peak, the drop gets pinned; if Bo is higher than the second peak, the drop crosses the interface; for Bo values ranging between the two peaks the drop initially slides, but later stops without passing in the hydrophobic region. The first red peak decreases as φ increases, disappearing when φ approaches 90° and the drop moves parallel to the step. For high enough φ, also the second blue peak disappears, as shown in figure 6.6f, but differently from the first peak, its value does not dimish: the second peak is asymtotically reached when x tends to infinity, describing the infinite sliding along the chemical interface shown in figure 6.6c. Figure 6.6g collects several energy landscapes for different values of φ, where the trend of the two peaks is indicated by a dashed line.

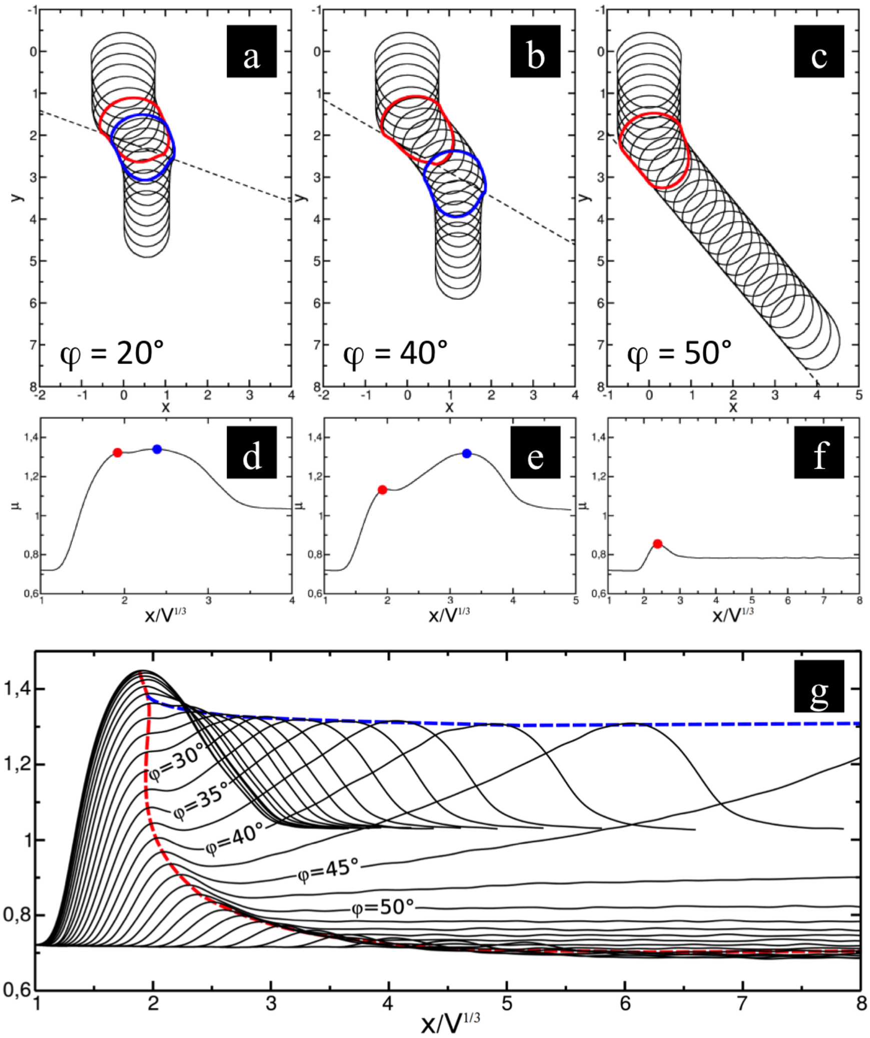

Figure 6.6 : a)-c) Numerical footprints of drops interacting with a chemical step for different values of φ; d)-f) corresponding energy landscapes showing the minimum force required to move the drop in terms of the Lagrange multiplier μ. The peaks refer to the configurations marked in panels a)-c). g) Summary of the energy landscapes computed for different values of φ, where the trend of the two peaks is indicated by a dashed line.

§ 6.5. Conclusion

In conclusion, we characterized the interaction of a highly viscous drop approaching a straight wettability step. To enhance the effect of the contact line distortion we oriented the chemical step with an arbitrary angle with respect to the direction of the in-plane body force, breaking the reflection symmetry. Four possible behaviors are observed by varying both the plane inclination and the inclination of the chemical interface: a) the drop gets pinned; b) the drop passes in the hydrophobic area; c) the drop deviates along the edge between the two regions, or d) the drop starts deviating along the border but then stops. The interesting morphology of the phase diagram including these dynamical regimes is related to the wettability properties of the two regions forming the surface and the complex shape of drop contact line meeting the step. Overall, our study demonstrates the fundamental role played by the intrinsic hysteresis present in the homogeneous portions of the substrate in determining the features of the dynamical regimes assumed by the drop. One of the major consequences is that, in order to precisely control drop motion by tuning the defect strength and geometry, the intrinsic hysteresis cannot be regarded as a minor correction and needs to be accounted in detail.

Chapter 7

Drops of non-Newtonian solutions

A large part of the fluids we experience in every-day life is non-Newtonian, i. e. has a complex response to shear stresses. The most common examples are toothpaste, shampoo, cosmetics, ketchup, mayonnaise, chocolate, paints... Despite the large diffusion of non-Newtonian fluids, the reasearch about non-Newtonian drops on open surfaces is quite recent and needs further investigation. The sliding of non-Newtonian drops down homogeneous substrates is the topic of this chapter: Sections 7.1 and 7.2 define and describe non-Newtonian fluids, Section 7.3 deals with the polymeric solutions considered in our experiments and the corresponding sliding results are reported in Section 7.4. The main features and findings of numerical simulations are presented and compared with the experimental observation in Section 7.5. Finally the study about non-Newtonian sliding droplets is summarized in Section 7.6.

§ 7.1. Non-Newtonian fluids

Non-Newtonian fluids [271] are complex fluids possessing mechanical properties intermediate between ordinary liquids and ordinary solids, usually having a non-linear relationship between stress and deformation. One of the fundamental feature discriminating between a solid and a liquid is the fact that liquids quickly assume the shape of their container, while solids maintain their shape indefinitely. Many complex fluids behave in a way intermediate between these two possibilities: they maintain their shape for a time and then eventually flow. Such fluids can be considered as solids at short times and liquids at long times and are defined as *viscoelastic*. The characteristic time required to change from solid to liquid behavior can vary from fractions of seconds to years, depending on the fluid. Non-Newtonian fluids with long relaxation times include polymer melts and solutions and micellar solutions. For some complex fluids the transition from solid-like to liquid-like (or the opposite one) can be induced by a modest deformation, as for polymeric gels, or by the application of electric or magnetic fields, as in the case of electrorheological and magnetorheological suspensions.
The rheological properties of a fluid, i. e. its response to external stresses, can be described through the stress tensor, defined as shown in figure 7.1a:

$$\tau = \begin{pmatrix} \tau_{1,1} & \tau_{1,2} & \tau_{1,3} \\ \tau_{2,1} & \tau_{2,2} & \tau_{2,3} \\ \tau_{3,1} & \tau_{3,2} & \tau_{3,3} \end{pmatrix} \tag{7.1}$$

where the element $\tau_{i,j}$ represents the stress (force per unit area) acting in the i-direction on the plane with a normal oriented in the j-direction. In an incompressible and isotropic system this tensor is symmetrical.

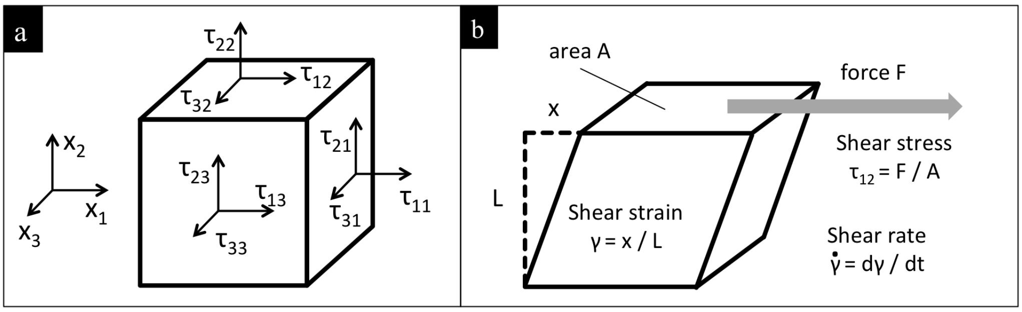

Figure 7.1 : a) Definition of the stress tensor. The element $\tau_{i,j}$ represents the stress (force per unit area) acting in the i-direction on the plane with a normal oriented in the j-direction. b) Shear stress causes a deformation described by the shear strain. The ratio between shear stress and shear rate in a fluid defines its viscosity (see equation 7.2).

For a Newtonian liquid all the diagonal elements are equal; on the contrary, non-Newtonian fluids can have different diagonal elements $\tau_{i,i}$ and the corresponding differences are defined as first normal stress difference $N_1 = \tau_{1,1} - \tau_{2,2}$ and second normal stress difference$N_2 = \tau_{2,2} - \tau_{3,3}$. Fluids where the normal stress differences are not negligible are viscoelastic fluids reacting with a normal deformation to a shear stress. For instance, in a parallel plate rheometer the fluid tends to expand perpendicularly to the plates when a shear stress is applied by rotating one plate; similarly, a rod rotating inside the complex fluid as shown in figure 7.2 makes the fluid climb up, while in the corresponding newtonian case the fluid moves away because of inertial forces. Examples of viscoelastic fluids featuring important normal stress difference effects are toothpaste, gelatine, the earth's mantle, blood clots, wormlike micellar fluids, amorphous polymers, semicrystalline polymers, biopolymers, solutions with elastic polymers, metals at very high temperatures and bitumen materials.

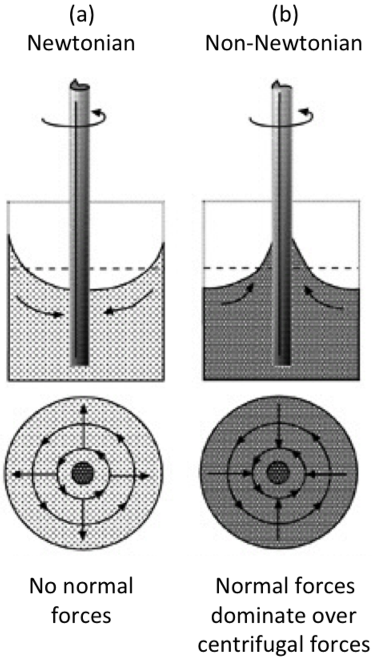

Figure 7.2 : Rod climbing (Weissenberg effect). (a) In Newtonian fluids, centrifugal forces generated by the rotation push the fluid away from the rod. (b) In non-Newtonian fluids, normal forces are stronger than centrifugal forces and drive the fluid inward toward the rod.

Another important rheological parameter is viscosity (η), which is related to shear stress $\tau_{1,2}$ and shear rate $\dot{\gamma}$ (see figure 7.1b) by the formula:

$$\tau_{1,2} = \eta\dot{\gamma}. \tag{7.2}$$

For a Newtonian fluid the viscosity is a constant value depending heavily on temperature and inner molecular structure, i. e. the strenght of links and interactions between neighbouring molecules (see figure 7.3. On the other hand, for a non-Newtonian fluid the viscosity often depends on the external forces acting on the fluid. Indeed, the vast majority of non-Newtonian fluids is classified according to the behavior of viscosity which can be evinced by the graphs in figure 7.3:

- the straight line corresponds to a constant viscosity, i. e. a linear relation between shear stress and shear rate, as for Newtonian fluids or non-Newtonian fluids exhibiting normal stress effects (Boger fluids);
- shear thickening (dilatant) fluids have a viscosity increasing with the shear rate and include, for instance, Silly Putty (made of silicone oil and boric acid), suspensions of corn starch in water or sand in water;

- shear thinning (pseudoplastic) fluids have a viscosity decreasing with the shear rate and are much more common. Such a behavior characterizes, for example, ketchup, whipped cream, blood, paint, nail polish, many polymer solutions and molten polymers.

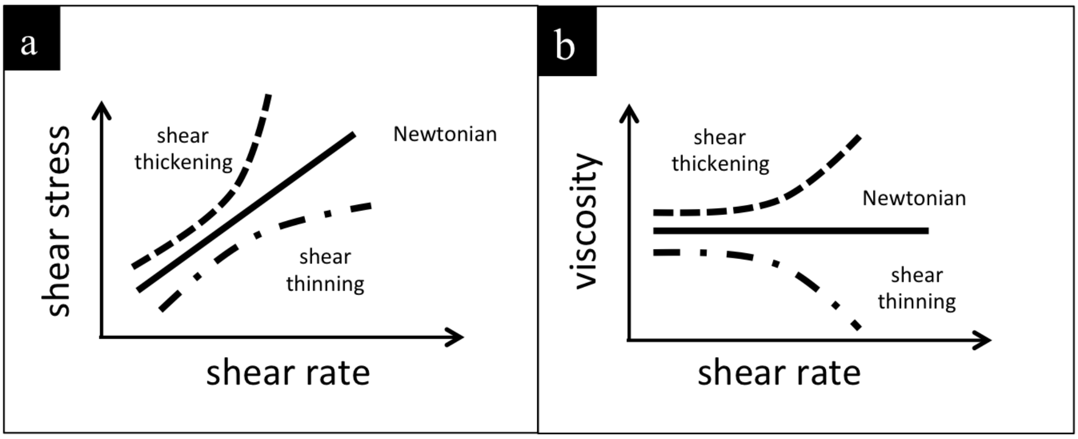

Figure 7.3 : Sketch of rheological curves for Newtonian, shear thinning and shear thickening fluids: a) shear stress *vs* shear rate dependence and b) corresponding viscosity trend as a function of shear rate. A Newtonian fluid has a constant viscosity, while for a shear thickening/thinning fluid the viscosity increases/decreases with the shear rate.

These are the main categories of comple fluids, however there is a huge variety of fluids with different rheological properties. For fluids exhibiting other non-Newtonian behaviors we refer to [271].

§ 7.2. Polymer solutions

Polymer solutions [272] feature non-Newtonian behaviors depending on the mechanical and elastic properties of polymeric chains and on polymer concentration. Polymers in a solution can be thought as random coiled chains interacting in three possible regimes according to the concentration of the solution, as shown in figure 7.4:

(a) in dilute solutions, polymer chains are well separated and behave more or less independently, interacting mainly with the solvent molecules;

(b) in semidilute solutions, the spheres including the coiled polymers are packed and chains are overlapped and entangled. Their mobility is greatly reduced compared with the chains in dilute solutions;

(c) at a higher concentration, in the concentrated regime, each segment of the polymer chain does not have a sufficient space available and a complex network of entangled polymer chins is formed.

Typically, for a polymer of a sufficiently high molecular weight (from $\sim 10^5$ g mol^{-1}), the semidilute regime covers a broad range of concentrations, with different degrees of overlapping, as depicted in figure 7.4.

The classification of these concentration regimes is based on the definition of the overlap concentration c^*, corresponding to the configuration where the spheres including the polymers touch each other and occupy the whole volume of the solution in a packed arrangment:

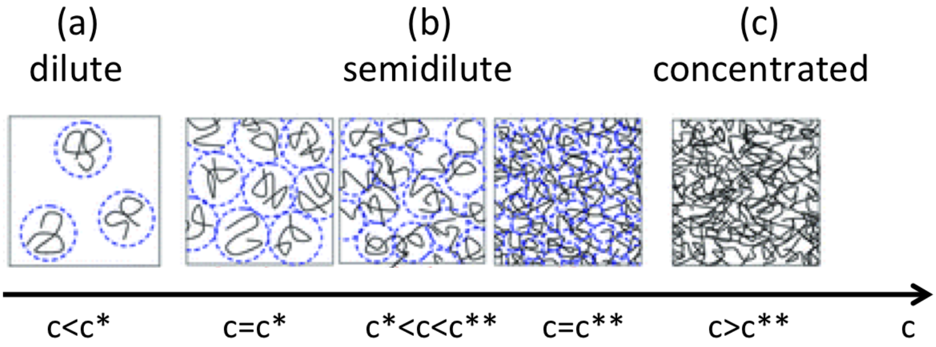

Figure 7.4 : Concentration regimes for polymer solutions: a) dilute; b)semidilute and c) concentrated. The overlap concentration delimiting the dilute phase is c^* and the critical concentration c^{**} marks the boundary between semidilute and concentrated regimes.

$$c^* = \frac{1}{\frac{4\pi}{3}R_g^3}\frac{M_w}{N_A} \tag{7.3}$$

where M_w/N_A is the mass of each chain, with N_A being the Avogadros number and R_g is the radius of gyration giving the size of the sphere including the polymer chain. The overlap concentration represents the limit between dilute and semidilute regime. The transition from semidilute to concentrated solutions occurs for a concentration c^{**} corresponding to a volume fraction of the polymer ranging between 0.2 and 0.3 (see figure 7.4).

§ 7.3. Chemical and physical properties of polymeric aqueous solutions

We have investigated acqueous solutions of two different polymers: i) Xanthan (molecular weight, $M_w \sim 10^6$ g mol^{-1} , Sigma Aldrich), a stiff rodlike polysaccaride depicted in figure 7.5a and ii) polyacrylamide (PAA, $M_w \sim 5 - 6 \times 10^6$ g mol^{-1}, Sigma Aldrich), a flexible polymer shown in figure 7.5b.

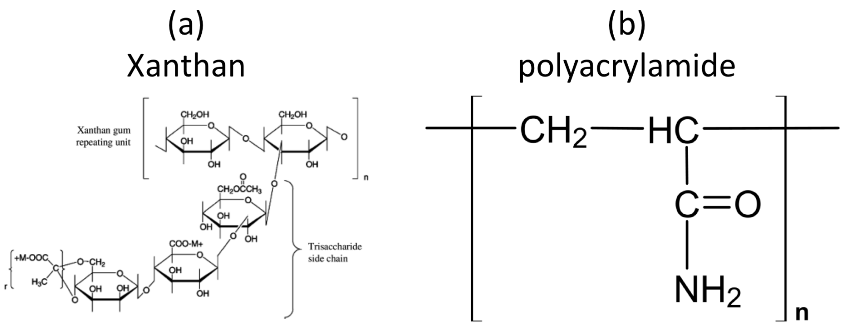

Figure 7.5 : Fundamental units forming the polymers considered in our study: a) Xanthan and b) polyacrylamide (PAA).

The solvent is distilled water and was chosen also as the reference Newtonian fluid. Since the overlap concentration c^* is 70 ppm (w/w) and 400 ppm (w/w) for Xanthan and PAA respectively [273], our solutions have concentrations ranging in the dilute or semi-dilute regime [273–275], as listed in table 7.1.

Table 7.1 : Viscosity parameters for the non-Newtonian Xanthan and PAA solutions: a and b are the parameters fitting the rheological data described by the power law $\eta_{xan}(\dot{\gamma})=a\ \dot{\gamma}^{-b}$; η_{os} is the direct measurement performed with an Ostwald viscometer.

Liquid	concentration (ppm w/w)	a (mPa s^{1-b})	b	η_{os} (mPa s)
Xanthan/water	400	33	0.41	
Xanthan/water	800	76	0.51	
Xanthan/water	1500	310	0.61	
Xanthan/water	2500	990	0.70	
PAA/water	250			1.09±0.03
PAA/water	1500			2.09±0.06
PAA/water	2500			4.0±0.1
PAA/water	5000			9.1±0.3
PAA/water	10000			77±2

Due to the different mechanical and elastic properties of the polymeric chains, Xanthan and PAA solutions exhibit different rheological non-Newtonian behaviors. In particular, Xanthan solutions are mainly characterized by a shear-dependent viscosity [273,276–285], but also normal stress effects have been reported, particularly at high enough ($\sim$ 1000 ppm) concentrations [276–280]. On the other hand, in some works [273, 274, 281, 283], where the behavior of Xanthan solutions was compared to other polymeric solutions (e.g. polyacrylamide), normal stresses were claimed to be negligible if compared to the strong shear rate dependence of the viscosity. Indeed, PAA solutions feature pronounced normal stress difference effects [273, 274, 279, 281, 285–289], while the viscosity varies weakly with the shear rate. Again, for high enough concentrations both normal stress effects and shear thinning are present. However we would like to remark the different origin of the elastic behavior of the solutions formed by these two polymers: for PAA it is related to the intrinsic elasticity of the polymer chain, whereas for Xanthan it is due to particle interaction and entanglement.

We characterized the rheological behavior of our solutions through a parallel plate rheometer (Advanced Rheometric Expansion System ARES, TA instruments) equipped with two 50 mm diameter disks. In the case of PAA/water solutions we measured the viscosity also with an Ostwald and a cup&bob (DV-II+PRO, Brookfield) viscometer because the viscosity of low concentrated solutions was out of the range accessible by the parallel plate rheometer.

As shown in figure 7.6a, the viscosity of Xanthan solutions varies with the shear rate $\dot{\gamma}$ according to the power law

$$\eta_{xan}(\dot{\gamma}) = a\dot{\gamma}^{-b}$$

with a and b dependent on the concentration, as listed in table 7.1 (see also [273]).

For PAA solutions with concentration up to 2500 ppm the viscosity actually does not depend on the shear rate, in agreement with [273, 286], and the corresponding value measured with the Ostwald viscometer (η_{os}) is reported in table 7.1. At higher concentrations, η slightly varies with $\dot{\gamma}$ and the decrease is much smaller than that observed with Xanthan solutions. This weak shear thinning effect is shown in figure 7.6a for a 10000 ppm solution: the viscosity is compatible with η_{os} for small shear rate ($\approx$ 1-10 s^{-1}) and then decreases. The dark blue continuous line is a second order polynomial fit to the data.

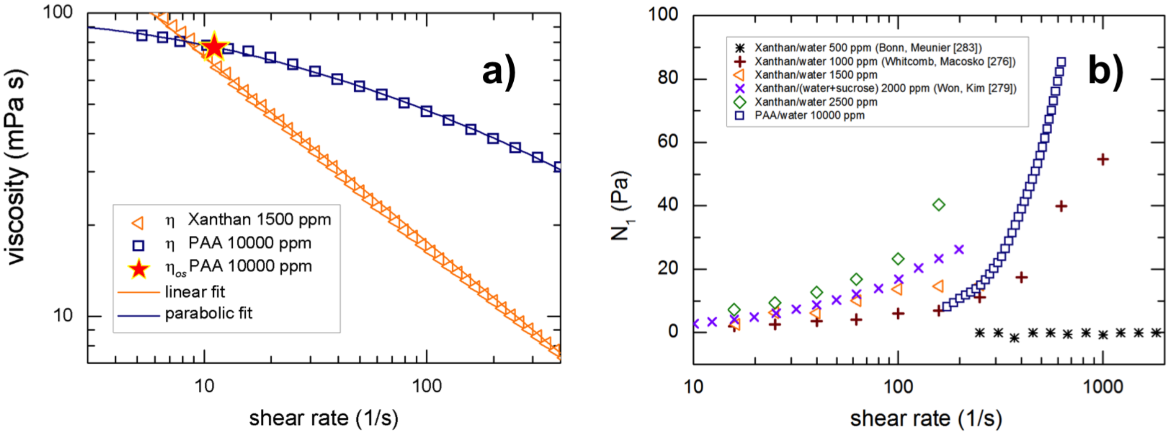

Figure 7.6 : Examples of rheological characterization of Xanthan and PAA solutions. a) Viscosity *vs* shear rate curves: Xanthan data follow a power law ($\eta_{xan}(\dot{\gamma}) = a\dot{\gamma}^{-b}$, with a and b dependent on the concentration as reported in table 7.1); on the other hand PAA solutions exhibit a much slighter shear thinning which can be described with a parabolic fit in the log-log plot of the 10000 ppm data (less concentrated solutions feature an even weaker thinning). For comparison we also report η_{os}, the viscosity measured for a single fixed shear rate with an Ostwald viscometer. b) N_1 *vs* $\dot{\gamma}$ measurement: 1500 and 2500 ppm Xanthan solutions show non negligible elastic effects in agreement with data [276, 279, 283]; PAA/water solutions reach higher values of N_1, confirming the viscoelastic nature reported in literature [273, 274, 279, 281, 285–289].

Figure 7.6b reports some examples of first normal stress difference curves. Our measurement about the 1500 and 2500 ppm Xanthan solutions indicates the presence of a measurable N_1 in agreement with [276,279], which investigate the rheology of Xanthan solutions of similar concentrations (see figure 7.6b). Values related to lower concentrations were found to be smaller, actually negligible below 1000 ppm [283], and also a bit more scattered than data at higher concentrations because near to the sensitivity limit of the instrument. On the other hand, solutions feature higher values of N_1, typical of viscoelastic fluids, confirming the behavior observed in many literature works [273,274,279,281,285–289].

The wetting properties of our polymer solutions have been analyzed through the sessile drop method with the experimental apparatus described in 2.1. The substrate chosen for all the measurements is a homogeneous, polycarbonate (PC) plate characterized by a static contact angle θ close to 90° and dynamic contact angles similar for all solutions, as reported in table 7.2. The comparison between contact angles of water and polymer solutions hints that the surface tension of such solutions is similar to water, as reported also in literature [273].

Table 7.2 : Static (θ), advancing (θ_A), receding (θ_R) contact angles and contact angle hysteresis ($\Delta\ \theta$) of all the investigated solutions on a homogeneous PC sample.

Liquid	concentration (ppm w/w)	θ (degrees)	θ_A (degrees)	θ_R (degrees)	$\Delta\ \theta$ (degrees)
water		81±3	91±2	66±3	25±4
Xanthan/water	400	86±2	89±2	64±2	24±3
Xanthan/water	800	87±2	92±2	67±3	26±3
Xanthan/water	1500	89±1	91±1	66±1	25±2
Xanthan/water	2500	87±3	89±1	63±2	25±2
PAA/water	250	87±2	92±1	68±2	24±3
PAA/water	1500	87±2	92±2	65±2	27±3
PAA/water	2500	82±5	89±2	60±4	29±4
PAA/water	5000	89±3	91±4	61±2	29±4
PAA/water	10000	86±1	87±2	57±4	31±4

§ 7.4. Non-Newtonian sliding drops

Sliding measurements of 30 μL droplets have been performed by means of the experimental setup described in Section 2.2. The main experimental results, consisting in the dependence of the stationary droplet velocity U on the inclination angle α of the PC surface, are shown in figures 7.7a and 7.8a for Xanthan and PAA solutions, respectively. In both cases, by comparing the results of the polymeric solutions with those of water, we observe a decrease of U as the polymer concentration increases due to the higher viscosity of the more concentrated solutions, which results in a smaller steady velocity at a fixed driving force [130,132,152,290]. As a consequence, in order to better compare the behavior of the different liquids, the data are plotted in terms of Capillary (Ca=$\eta U/\sigma$, where η and σ are the viscosity and the surface tension of the fluid, respectively) versus Bond number (Bo=$\rho V^{2/3} g \sin\alpha/\sigma$ where ρ is the density of the liquid and g the gravity acceleration).

The computation of the Ca number for non-Newtonian solutions requires the evaluation of the viscosity corresponding to the sliding velocity U. Since the rheological measurements of these solutions relate the viscosity to the shear rate, we have devised the following method to convert the data in viscosity versus U. We define an $effective$ viscosity η_{eff} such that the non-Newtonian data overlap the trend of the Newtonian points (i.e. water) in the Ca *vs.* $\mathrm{Bo}-\mathrm{Bo_c}$ curve:

$$\eta_{eff} = \frac{\sigma(m(\mathrm{Bo}-\mathrm{Bo_c})+\mathrm{q})}{U} \tag{7.4}$$

where m and q are the slope and the intercept of the straight line fitting the water data plotted in figure 7.7c. Two examples of the resulting η_{eff} are reported in figure 7.7b as a function of U for the 800 and 2500 ppm Xanthan solutions: the viscosity decreases as the velocity increases (with a trend typical of the shear thinning behavior), with some noise at the highest velocities reached by the droplet, particularly significant for the 2500 ppm solution, as shown in the inset. We then fit the η_{eff} data at low velocity according to the formula

$$\eta_{xan}(U) = a\left(\frac{U}{\lambda}\right)^{-b}$$

where a and b are the parameters reported in table 7.1 and λ is a characteristic length to be considered as the free parameter of the fit represented by a dashed line in figure 7.7b. In other words, we assume that non-Newtonian effects other than shear thinning be small at low U. The viscosity η_{eff} in equation (7.4) is then used to calculate the Ca for the Xanthan droplets and the corresponding values are plotted as a function of $\mathrm{Bo} - \mathrm{Bo_c}$ in figure 7.7c. Remarkably, a constant value of λ ($\sim 10\ \mu$m) for all the Xanthan concentrations investigated, allows to obtain a good collapse of the non-Newtonian data on the Newtonian ones for small Bo. The scale λ can be thought of as defining an effective gradient U/λ which is "representative" for viscous dissipation inside the droplet. Such a scale is indeed smaller than the macroscopic length scale (i.e. the capillary length) of the order of 1 mm and larger than the microscopic length (i.e. the slip length) ranging from 1 to 10^2 nm [291]. However, at larger $\mathrm{Bo} - \mathrm{Bo_c}$, non-Newtonian data systematically deviate from the reference Newtonian data, and even a plateau appears at the largest concentrations considered. We think there may be different reasons for these deviations. First, the characteristic scale λ may not be constant as a function of the velocity: the non constancy of the viscosity inside the droplet may well induce a variation of λ for larger velocities, with λ being an increasing function of the velocity. To shed some lights on this issue, we have carried out some numerical simulations with a power-law fluid and we have not found evidences of this velocity dependence in the characteristic scale λ. These results are described in section 7.5.1. We could, instead, relate the deviations from non-Newtonian data to the presence of normal stresses inside the droplet, which are more important at high shear rates [276–280, 285], i.e. at high velocities and Bo, while it is weaker at small inclinations where the behavior is similar to a Newtonian fluid. With the measured velocities and the used values for λ (10 μm), we indeed obtain $\dot{\gamma}_{eff} \sim 10^2 - 10^3\ \mathrm{s}^{-1}$ for the largest velocities of the more concentrated Xanthan solutions analyzed. This itself points to a representative value for the shear rate at which measured normal stresses are different from zero [276–280, 285], as shown in figure 7.6b. An elastic non-viscous effect has been observed also in the flow of Xanthan solutions through a porous medium and has been ascribed to the presence of normal stresses [277].

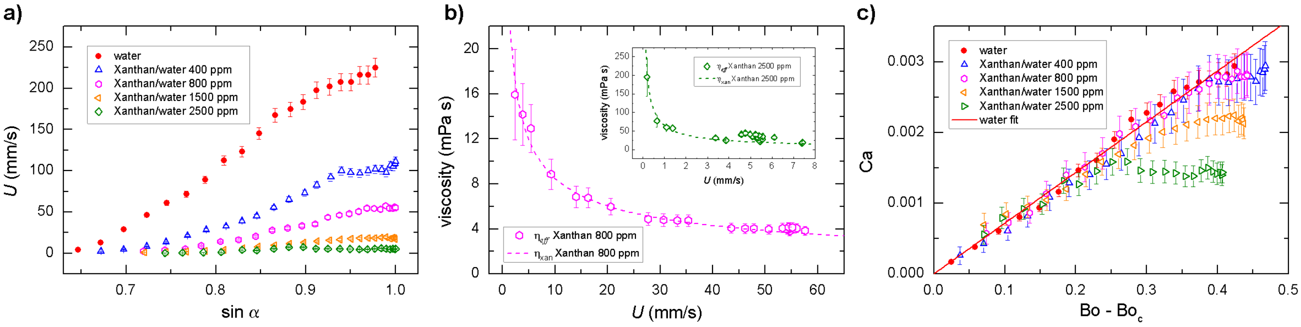

Figure 7.7 : a) Velocity of 30 μL droplets sliding down the homogeneous plane (PC) inclined by different angles α for water and Xanthan/water solutions. b) Viscosity evaluation as a function of droplet velocity for the 800 ppm Xanthan solution and 2500 ppm in the inset. Both the effective viscosity η_{eff} (obtained through the comparison with the Newtonian data) and the shear thinning viscosity (η_{xan}=a $(U/\lambda)^{-b}$) are plotted (see text for details). c) Dimensionless Ca *vs.* $\mathrm{Bo} - \mathrm{Bo_c}$ trend for water and Xanthan/water solutions with a Ca number calculated through the values of η_{xan}.

To better analyze the deviation from linearity of the Ca *vs.* $\mathrm{Bo} - \mathrm{Bo_c}$ curve we have decided to perform a new series of sliding measurements with PAA solutions, which are characterized mainly by normal stress difference effects and by a viscosity only slightly dependent on the shear rate [273, 286] as discussed in section 7.3. They are therefore good candidates to investigate whether the deviation from the linearity of the Ca *vs.* $\mathrm{Bo} - \mathrm{Bo_c}$ curve can be attributed to the presence of normal stresses, as argued in the analysis of the Xanthan solutions.

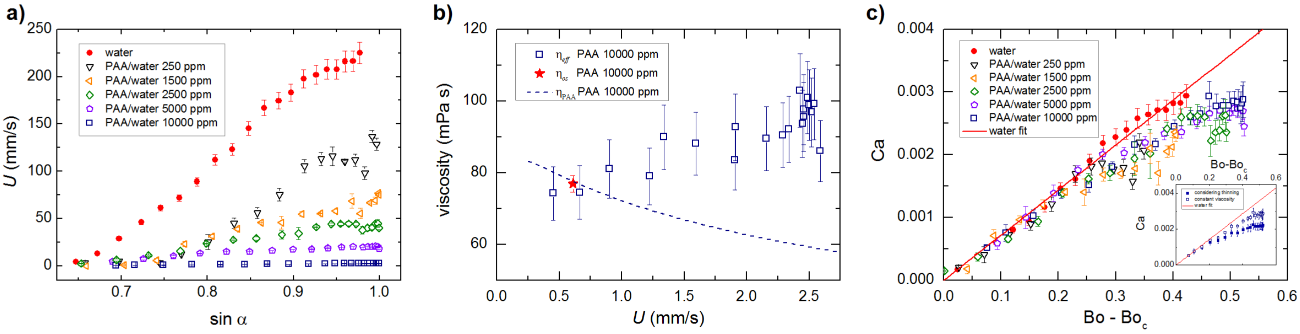

Figure 7.8 : a) Velocity of 30 μL droplets sliding down the homogeneous plane (PC) inclined by different angles α for water and PAA/water solutions. b) Viscosity evaluation as a function of U for the 10000 ppm PAA solution: i) The effective viscosity η_{eff} (open squares) is calculated through Eq. (7.4); ii) η_{os} (filled star) is the value measured for a single fixed shear rate with an Ostwald viscometer; iii) $\eta_{PAA}(U)$ (dashed line) is the fit to the experimental data obtained from the rheological measurement. c) Dimensionless Ca *vs.* $\mathrm{Bo} - \mathrm{Bo_c}$ trend for water and PAA/water solutions. The viscosity used to calculate the Ca number is η_{os}. Inset: Ca *vs.* $\mathrm{Bo} - \mathrm{Bo_c}$ trend for the 10000 ppm PAA solution, with a Ca number calculated through η_{os} (open symbols) and η_{PAA} (filled symbols).

Again, to determine the effective Ca number we need to know the fluid viscosity as a function of U. As before, we calculate η_{eff} assuming the PAA data overlap the trend of the water points in the Ca *vs.* $\mathrm{Bo} - \mathrm{Bo_c}$ curve. The results are plotted in figure 7.8b for the 10000 ppm solution. At low velocity they are almost constant and are in good agreement with the measurement obtained with the Ostwald viscometer, a further hint of the validity of the method devised to compute the viscosity of non-Newtonian sliding droplets. At higher U, η_{eff} increases and becomes noisy, probably because viscoelasticity starts being important. In addition, we plotted in the same graph the function $\eta_{PAA}(U/\lambda)$ calculated from the parabolic fit of the data reported in figure 7.6a, with a free parameter λ determined by matching $\eta_{PAA}(U)$ and η_{eff} at low velocity ($U \leq 1$ mm/s). Again the length λ results to be of the same order as that computed for Xanthan solutions. Given the weak dependence of η_{eff} on U, to determine the Ca number we have assumed the constant value of viscosity η_{os} reported in table 7.1. The results are plotted in the bottom plate of Figure 7.8. Similarly to Xanthan solutions, PAA points corresponding to low inclinations follow the Newtonian linear trend, while at higher $\mathrm{Bo} - \mathrm{Bo_c}$ the Ca number stops increasing linearly and shows a sublinear behavior, with a saturation in the Ca number at larger concentrations. Correspondingly, η_{eff} starts increasing at high inclination to yield the observed velocity saturation (see figure 7.8b). At variance with Xanthan solutions (shear thinning), where the Ca *vs.* $\mathrm{Bo} - \mathrm{Bo_c}$ plateau decreases as the polymer concentration is increased, PAA data collapse on the same curve, regardless of the polymer concentration. We point out that this analysis does not include shear thinning effects. Actually, if for the calculation of the Ca number we use the viscosity $\eta_{PAA}(U)$ deduced by our rheological measurements, the resulting curves will display a more pronounced plateau for the 5000 and 10000 ppm PAA solutions (see the inset in figure 7.8c), while those at lower concentration would be barely affected.

§ 7.5. Lattice Boltzmann simulations and discussion

This section gives some details about the implementation of the lattice Boltzmann model (see Section 1.6.1), adjust for the description of a pure shear thinning fluid (Section 7.5.1) and a normal stress fluid with constant viscosity similar to a Boger fluid (Section 7.5.2) in order to disentangle and understand the role played by these different non-Newtonian effects in the problem of a sliding drop.

§ 7.5.1. Shear Thinning Fluid

The numerical method, based on LBM, offers a unique advantage to simulate a shear thinning fluid, being able to integrate simultaneously the non-trivial interface dynamics (due to the diffuse interface nature of the method) and the non-Newtonian nature of the bulk phases, by making the relaxation times in LBM dependent on the local shear properties [292]. The equations solved in the outer (o) and droplet (d) phases are the NS equations

$$\rho_{o,d}\left[\partial_t \boldsymbol{u}_{o,d} + (\boldsymbol{u}_{o,d}\cdot\boldsymbol{\nabla})\boldsymbol{u}_{o,d}\right] = -\boldsymbol{\nabla}P_{o,d} + \boldsymbol{\nabla}\left(\eta_{o,d}(\boldsymbol{\nabla}\boldsymbol{u}_{o,d} + (\boldsymbol{\nabla}\boldsymbol{u}_{o,d})^T)\right). \tag{7.5}$$

Here, $\boldsymbol{u}_{o,d}$ and $\eta_{o,d}$ are the velocity and the dynamic viscosity of the outer and droplet phase, respectively. The corresponding densities and pressures are indicated with $\rho_{o,d}$ and $P_{o,d}$, while $(\boldsymbol{\nabla}\boldsymbol{u}_{o,d})^T$ indicates the transpose of $(\boldsymbol{\nabla}\boldsymbol{u}_{o,d})$.

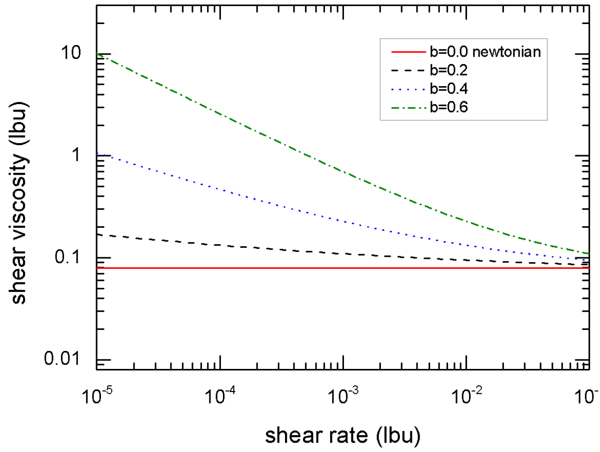

Figure 7.9 : Viscosity of the power-law fluid used in the numerical simulations. The exponent b regulates the degree of thinning. On average, dissipation is larger at increasing b, in qualitative agreement with the behavior of the viscosity of Xanthan solutions at changing the polymer concentration.

As plotted in Figure 7.9, the viscosity in the droplet phase is chosen to be

$$\eta_d(\dot\gamma) = \begin{cases} \eta_0 + a\dot\gamma_0^{-b} & \dot\gamma \le \dot\gamma_0 \\ \eta_0 + a\dot\gamma^{-b} & \dot\gamma > \dot\gamma_0 \end{cases} \tag{7.6}$$

where $a = 0.01$ (lbu, lattice Boltzmann units) and where the cut-off shear rate $\dot\gamma_0 = 10^{-5}$ lbu is introduced to prevent a divergence of the viscosity at small shear rates. The background viscosity

$\eta_0 = 0.07$ is chosen to avoid a zero viscosity in the high shear rate limit, which would cause numerical instabilities. For all practical purposes, in the range of shear rates relevant for our problem (see figure 7.9), we are actually simulating a power-law fluid. In the outer matrix phase the viscosity is kept constant to $\eta_0 = 0.07$ so that the viscous ratio between the droplet and the outer phase ranges in the interval $[1-10]$ for the results presented.

In figure 7.10a we report the stationary velocity measurement for 3 cases: a Newtonian case ($b = 0$) and two viscoelastic cases with $b = 0.2$ and $b = 0.4$. Consistently with the fact that the viscosity chosen (7.6) produces a more viscous fluid at increasing b, the stationary droplet velocity is smaller at increasing the thinning exponent. However, by following the same procedure explained for the experimental data, once we tune the scale λ to achieve good collapse on the Newtonian data for small velocities, a very good collapse is obtained also for higher Ca, as shown in figure 7.10b. This surely indicates robustness in this "practical" procedure. It is true that some tiny deviations emerge for the largest Ca, but they are really very small and surely not at all reminiscent of the plateau behavior observed for the experimental data on Xanthan.

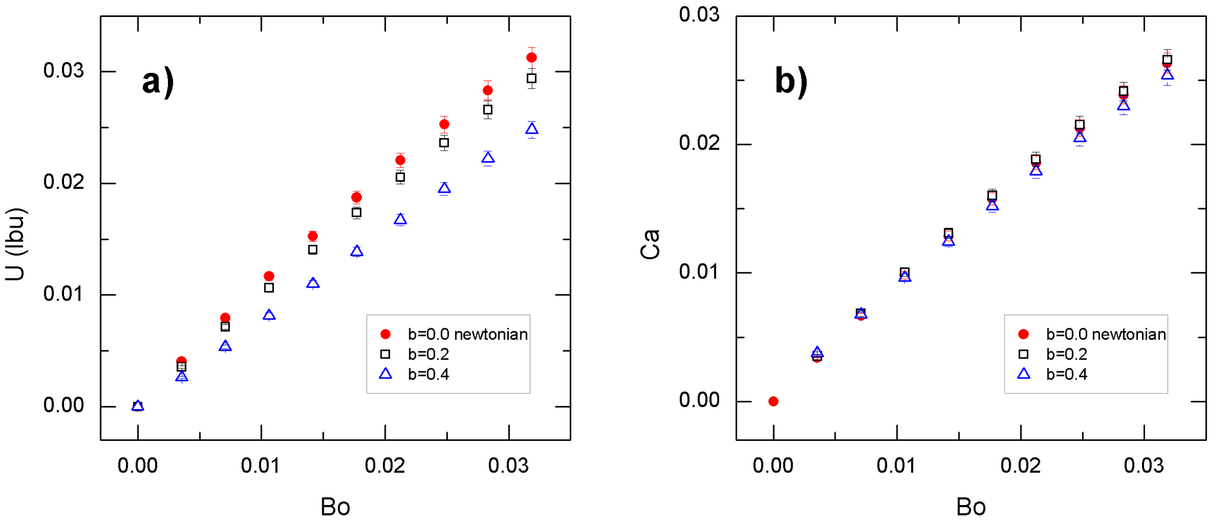

Figure 7.10 : a) Stationary velocity for sliding droplets at changing the thinning exponent b in (7.6). b) Rescaled data based on the lengthscale $\lambda = 0.3$ (lbu) in the definition of the shear rate $\dot{\gamma} = U/\lambda$ used in the viscosity to identify the "effective" viscosity of the thinning fluid. The rescaling is chosen in such a way that the non-Newtonian data overlap the Newtonian data for small Bond numbers. Good collapse is also found at larger Bond number.

§ 7.5.2. Normal Stress Fluid

The simulations implemented to introduce normal stresses in the droplet phase, are based on the FENE-P constitutive model, obtained via a pre-averaging approximation applied to a suspension of non interacting Finitely Extensible Nonlinear Elastic (FENE) dumbbells. This is well-adapted for dilute (and semidilute) polymeric solutions and was previously used to analyze filament thinning of polymeric fluids in macroscopic experiments [293, 294] and droplet breakup processes in microchannels [286]. FENE-P fluids exhibit normal stress effects with a quadratic dependence on the shear rate. Even if such dependence on the shear rate well describes the behavior of PAA solutions, but contrasts with the sub-linear scaling law found for rigid polysaccharide solutions like Xanthan [280], we rather use this numerical model to "generically" highlight the effect of Normal Stresses. The algorithm we use is based on a hybrid combination of LBM with finite difference schemes, as detailed in [295, 296]. The equations that we solve in the droplet phase are the Navier-Stokes (NS) equations coupled to the FENE-P constitutive equations

$$\rho_d \left[\partial_t \boldsymbol{u}_d + (\boldsymbol{u}_d \cdot \boldsymbol{\nabla})\boldsymbol{u}_d\right] = -\boldsymbol{\nabla} P_d + \boldsymbol{\nabla}\left(\eta_d(\boldsymbol{\nabla}\boldsymbol{u}_d + (\boldsymbol{\nabla}\boldsymbol{u}_d)^T)\right) + \frac{\eta_P}{\tau_P}\boldsymbol{\nabla}\cdot[f(r_P)\boldsymbol{C}]. \tag{7.7}$$

$$\partial_t \boldsymbol{C} + (\boldsymbol{u}_d \cdot \boldsymbol{\nabla})\boldsymbol{C} = \boldsymbol{C}\cdot(\boldsymbol{\nabla}\boldsymbol{u}_d) + (\boldsymbol{\nabla}\boldsymbol{u}_d)^T \cdot \boldsymbol{C} - \left(\frac{f(r_P)\boldsymbol{C} - \boldsymbol{I}}{\tau_P}\right). \tag{7.8}$$

where η_P is the viscosity parameter for the FENE-P solute, τ_P the polymer relaxation time, $\boldsymbol{C}$ the polymer-conformation tensor, $\boldsymbol{I}$ the identity tensor, $f(r_P) \equiv (L^2-3)/(L^2-r_P^2)$ the FENE-P potential that ensures finite extensibility, $r_P \equiv \sqrt{Tr(\boldsymbol{C})}$ and L is the maximum possible extension of the polymers [297, 298]. In the outer phase we just consider the NS equations with viscosity $\eta_P + \eta_d$, i.e. with the same shear viscosity as the droplet phase. The chosen value of L^2 is so large that the system only displays very weak thinning effects, while possessing normal stresses increasing with the squared shear rate (see figure 7.11). The value of the polymer relaxation time τ_P is chosen in such a way that the range of sliding velocity produces shear rate in the wedge which are of the order of magnitude of τ_P^{-1}. We expect that this choice allows us to appreciate the effects of the normal stresses on the Capillary-Bond curve. Further details on the algorithm used can be found in [295, 296].

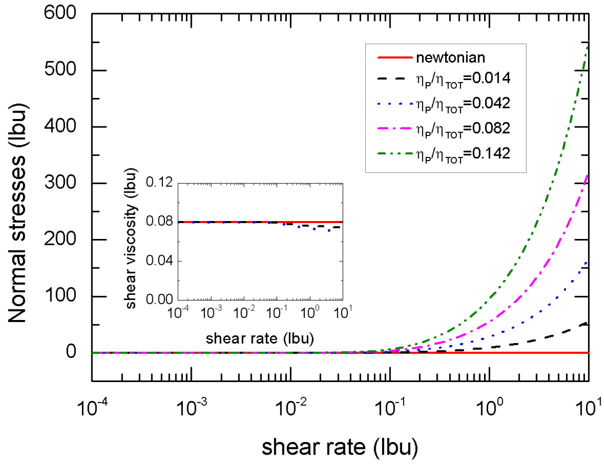

Figure 7.11 : Normal Stresses (main panel) and shear viscosity (inset) curves for the chosen viscoelastic solution. With the parameters chosen, the thinning effects are minimized while normal stresses are present for the range of shear rates relevant for our problem.

Results for the Ca *vs.* Bo curve are presented in figure 7.12. The concentration $\eta_P/\eta_{TOT} = \eta_P/(\eta_d + \eta_P)$ is systematically varied from 0.01 to 0.15. The viscosity ratio of the two fluids was chosen in such a way that $\chi = (\eta_d + \eta_P)/\eta_o = 1.0$. This allowed to study the properties of viscoelastic droplets ($\eta_P \neq 0$) and compare them with the corresponding Newtonian ($\eta_P = 0$) case. It is readily verified that the deviations from linearity first emerge with a slight sublinear behavior for the smallest concentrations, while they produce a plateau for the largest concentrations. The behavior observed in the presence of normal stresses points to the fact that effects other than viscous dissipation come into play to balance the work done by the external driving. The numerical simulations show that normal stresses provide an additional driving and accelerate the flow near the contact line [273], and the effect does so more strongly as the shear rate is increased. Parts closest to the rear wedge move faster and there the polymer feedback stress is enhanced to provide a counter force against sliding. This is the key mechanism explaining the observed drop slowing down.

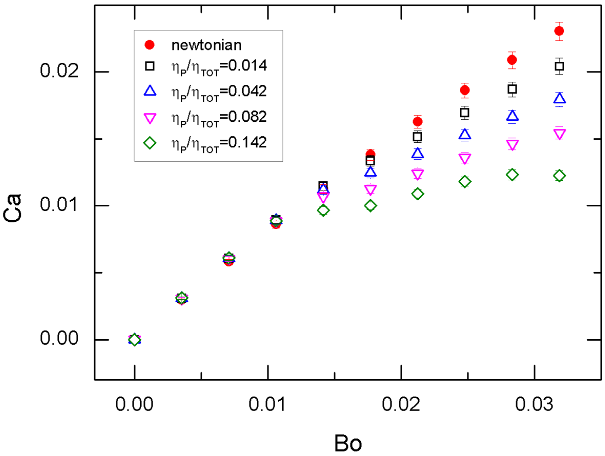

Figure 7.12 : Capillary *vs.* Bond number curve for viscoelastic fluid with rheological properties described in figure 7.11. The concentration $\eta_P/\eta_{TOT} = \eta_P/(\eta_d + \eta_P)$ is varied from 0.01 to 0.14.

§ 7.6. Conclusion

We have investigated non-Newtonian droplets made of polymers in water solutions, sliding on a homogeneous inclined surface. In particular, we considered i) shear thinning solutions of Xanthan, a stiff rodlike polysaccaride and ii) solutions of polyacrylamide (PAA), a flexible polymer, exhibiting normal stress difference effects. Polymer solutions feature concentrations ranging in the dilute or semi-dilute regime. The sliding of non-Newtonian droplets was systematically compared to the one of water through the relation between the Ca number (i.e. the dimensionless velocity) and the Bo number (i.e. the dimensionless volume force), as the driving force is changed by varying the plane inclination. The usual linear behavior of Newtonian solutions is found to well adapt to the non-Newtonian solutions only up to a given Bo number, above which deviations emerge, as the linear behavior is first replaced by a sublinear behavior (small concentrations) and then by a more visible plateau exhibiting a saturation in the Ca number. By properly rescaling the data, we argued that these effects can be mainly attributed to the presence of normal stress differences in the polymeric solutions. The experimental findings have been complemented with numerical simulations of an “idealized” two-dimensional droplet modelled as a shear thinning fluid or as a dilute polymeric solution of non interacting Finitely Extensible Nonlinear Elastic dumbbells (FENE-P model). Such a numerical study allowed to highlight the emergence of the observed experimental behaviors ascribing the reduction of sliding velocity to the presence of normal stres differences inside the drop. Simulations also validate the empirical method devised to analyze data about shear thinning fluids.

Chapter 8

Drop motion induced by acoustic vibrations

An active way to control drop motion on open surfaces relies on the application of vibrations to the substrate. The advantage of using acoustic waves with respect to the electro-wetting technique is the possibility to handle any kind of liquids, in particular not only polar fluids, thanks to the coupling with the liquid inertia. A net motion of the drop can be achieved through a combination of vertical (pumping mode) and horizontal (rocking mode) surface oscillations, for instance by using two independent orthogonal shakers [112] or by applying vibrations obliquely to the substrate, e. g. vertical vibrations to an inclined plane [113]. In the former case the direction of drop motion has been found to depend on the phase shift between the two vibrations. In the latter case, the drop can be pinned, slide down or climb up according to the amplitude and frequency of oscillation.
In this chapter we first give an overview about drops on oscillating substrates (Section 8.1), then we describe the details of our experiments and the corresponding results about droplets on inclined surfaces subject to vertical vibrations (Sections 8.2 and 8.3 respectively). This work has been complemented with 2D simulations performed by prof. Casciola's group (Sections 8.4 and 8.5). Finally the main observations and results are reported in the conclusion (Section 8.6).

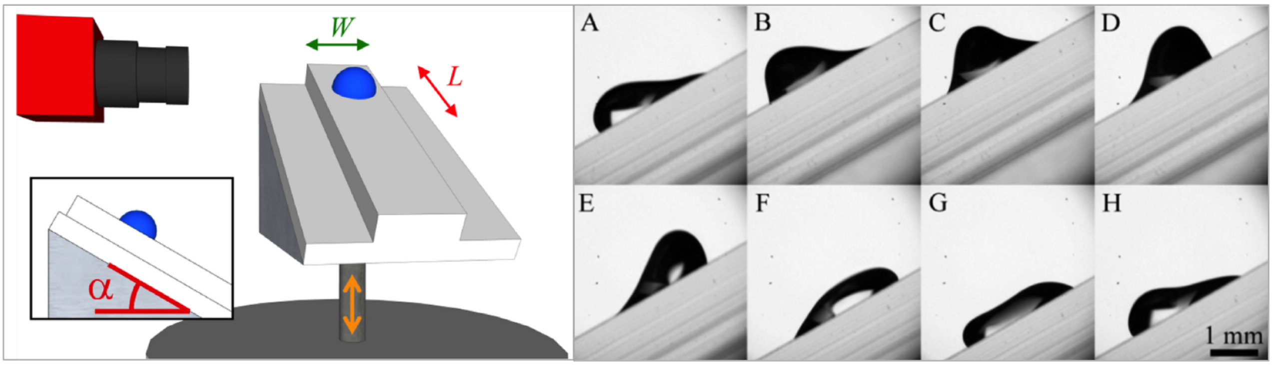

§ 8.1. Drops on oscillating surfaces

The following section describes the behavior of drops subject to different kinds of acoustic vibratios of the substrate: vertical and horizontal oscillations of a horizontal surface (Subsections 8.1.1 and 8.1.2 respectively) and combinations of such modes on horizontal or inclined substrates (Subsection 8.1.3).

§ 8.1.1. Vertical oscillations: pumping mode

A sessile drop placed on a vertically oscillating substrate ia subject to a periodic acceleration:

$$a(t) = (2\pi f)^2 x_0 \cos(2\pi f t), \tag{8.1}$$

where f and x_0 are frequency and maximum amplitude of oscillation, respectively. Such vibrations can induce deformations of the drop interface in two different regimes: 1) with the contact line completely pinned, typically at small acceleration; 2) with oscillating movement of the contact line, at higher accelerations. The steady surface waves, i. e. the oscillation modes of the liquid/air interface, are classified according to the index j or k (for pinned or moving contact line) equal to half the number of nodes appearing in the profile of the drop during the oscillation, as depicted in figure 8.1.

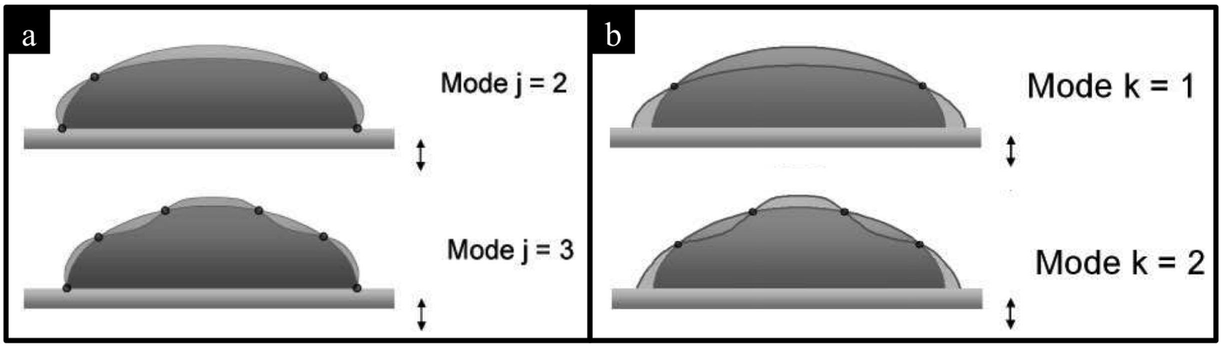

Figure 8.1 : Schematic representation of the drop profiles to define the modes when the contact line is pinned (a) or moves (b). Modes $j = 2$ and $j = 3$ correspond to 4 and 6 nodes, while modes $k = 1$ and $k = 2$ have 2 and 4 nodes respectively. Nodes are emphasized with black spots [299].

The oscillation modes have been experimentally investigated by Noblin *et al.* [299], who measured the resonance frequency of different modes with a pinned contact line (see figure 8.2a) and analyzed the transition from pinned to moving contact line (see figure 8.2b). From a theoretical point of view, an analitical description of this system is impossible because of the complexity of the wave pattern formed on drop surface by oscillations. In literature there are only simplified models and we refer to [299] for more details.

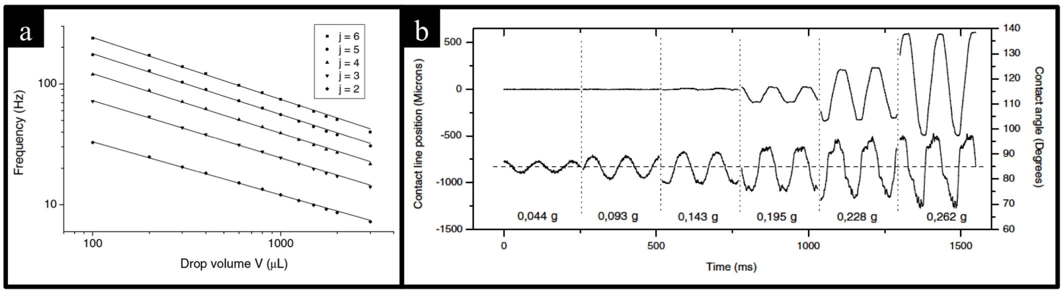

Figure 8.2 : (a) Resonance frequencies as a function of drop volume for different modes. The trends are well described by a power law with an exponent close to 0.5. The resonance frequency decreases with drop volume and increases as the mode number increases;(b) Transition between stick and stick-slip motions of the contour. Lower curves are contact angle variations versus time, the dashed line represents the equilibrium angle θ. Higher curves are the contact line position around the starting position before vibrations. The six curves for different acceleration amplitudes are joined together in the same plot for comparison. In these plots f = 9 Hz, V = 1 mL [299].

§ 8.1.2. Horizontal oscillations: rocking mode

A drop subject to horizontal vibrations of the plane oscillates in the direction of the force and its shape deforms by increasing and decresing the contact angles. For a high enough acceleration, the contact angle can overcome the advancing or receding threshold and the contact line can move, but the symmetry of the oscillation does not produce a net displacement. Again, the phenomenon is quite complex and a complete description can be found only for particular simple cases.
If the external force is weak and drop deformation are small, the contact line remains pinned and the system can be represeneted as in figure 8.3a [300].

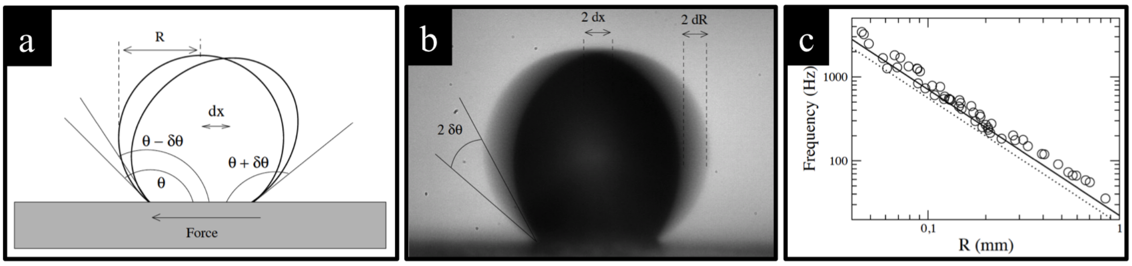

Figure 8.3 : (a) Schematic representation of the droplet shape under the influence of an external force. The deformation induces a displacement dx of the center of mass and a variation $\delta\theta$ of the advancing and receding wetting angles; (b) experimental snapshot of a vibrating mercury drop with radius R=0.192 mm. The measure of the ghost radius variation dR permits to calculate both $\delta\theta$ and dx; (c) relation between the resonance frequency and drop size. Circles are experimental points, the dashed line is the result derived from equation 8.6 with θ=140° , finally the dashed line is the evaluation obtained considering the *effective* angle θ_{eff}=130° to take into account the inertial force transmitted from the plane to the drop [299].

In this model the deformation is characterized by a displacement of the mass center, dx and a variation of the contact angle $\delta\theta$ so that $\theta_a = \theta + \delta\theta$ and $\theta_r = \theta - \delta\theta$. The corresponding surface variation ΔS with respect to the equilibrium surface S_0 is

$$\Delta S = S_0 f(\theta)(\delta\theta)^2 \tag{8.2}$$

where $f(\theta)$ is related to the shape of the drop. The displacement of drop center of mass is

$$dx = g(\theta)R\delta\theta \tag{8.3}$$

where R is the radius of the spherical cap and $g(\theta)$ is another function depending on drop geometry. Merging equations 8.2 and 8.3 we obtain:

$$\Delta S = \frac{S_0 h(\theta)}{R^2} dx^2 \tag{8.4}$$

where $h(\theta) = f(\theta)/g(\theta)^2$. The deformation of drop interface is opposed by a force due to the surface tension σ:

$$F = -\frac{\sigma \Delta S}{dx} = -\frac{\sigma S_0 h(\theta)}{R^2} dx. \tag{8.5}$$

The linear dependence between force and displacement allows us to define an elastic constant k_e and a characteristic frequency $\omega_0 = \sqrt{k_e/(\rho V)}$ whose expression obtained considering the geometrical formulas of a spherical cap is:

$$\omega_0 = \sqrt{\frac{6\sigma h(\theta)}{\rho(1-\cos\theta)(2+\cos\theta)}} R^{-3/2}. \tag{8.6}$$

This law has been verified by measuring the resonance frequency (i. e. the frequency corresponding to the maximum dR) of a mercury drop through pictures acquired at high exposure time, as shown in figure 8.3b [300]. The experimental relation between resonance frequency and drop radius plotted in figure 8.3c well reproduces the expected power law, even if 8.6 slightly underestimates the absolute value of ω_0. A better agreement is found considering the momentum transfert to the drop from the plane and introducing an $effective$ contact angle $\theta_{eff} < \theta$.

§ 8.1.3. Combinations of different oscillation modes

Although the modes described in the prevous sections can induce a displacement of the contact line, a net motion of the drop cannot be achieved because of the symmetry of the system. Such symmetry can be broken, for instance, by applying vertical harmonic oscillation to a surface featuring a wettability gradient [94, 95], by using vertical asymmetrical vibrations [301] or combinations of horizontal and vertical oscillations [112]. In this latter work, two independent shakers have been used as sketched in figure 8.4a to apply horizontal (h) and vertical (v) harmonic oscillations with amplitude:

$$\begin{cases} x_h(t) = A_h \cos(2\pi f_h t) \\ x_v(t) = A_v \cos(2\pi f_v t + \Delta\Phi) \end{cases}, \tag{8.7}$$

where A_h and A_v are the maximum oscillations amplitudes, f_h and f_v are the oscillation frequencies and $\Delta\Phi = f_v - f_h$ is the phase shift. Such a combination of vibrations can induce a net motion of the drop, as shown in figures 8.4b and 8.4c. The rocking mode drives the displacement along the horizontal direction, while the pumping mode breaks the symmetry producing a different deformation of the drop so that the contact point does not come back to the initial position after a cycle, but progressively moves in one direction, as reported in figure 8.4c. The displacement can be either towards left (velocity

< 0) or towards right (velocity > 0) according to the value of $\Delta\Phi$, once fixed the amplitude A_h (see figure 8.4d). The velocity of the drop is found to depend both on $\Delta\Phi$ and on A_h, as plotted in figures 8.4d and 8.4e.

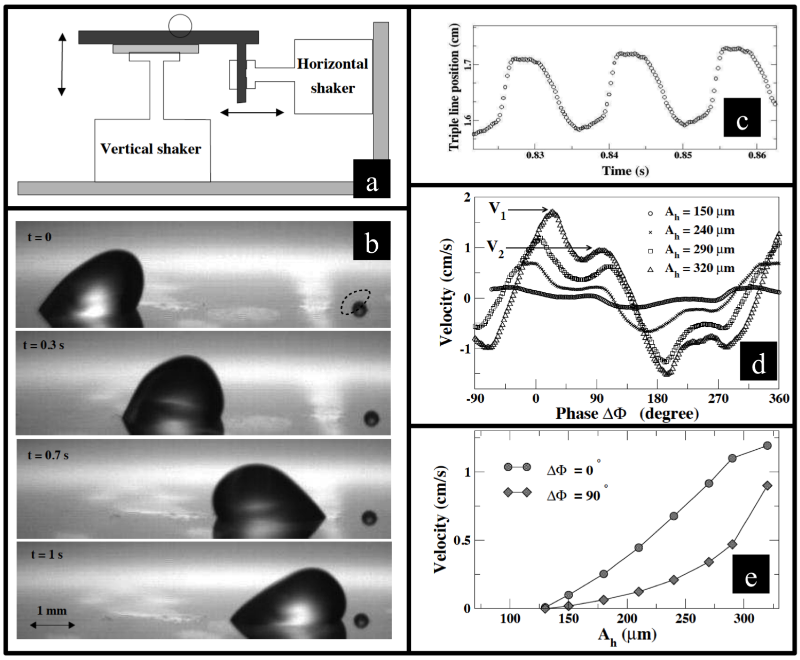

Figure 8.4 : (a) cartoon of the setup used to combine vertical and horizontal oscillations; (b) drop images taken from different vibration cycles at various oscillation phases; (c) position of the right contact point as a function of time; (d) droplet velocity as a function of the phase shift for different A_h; (e) dependence between drop velocity and horizontal amplitude [112].

An analogous combination of oscillations in different directions consists in the vertical vibration of an inclined substrate [113]. Differently from the horizontal plate subject to two two independent oscillations, in this case the phase shift is fixed and gravity favours downward motion breaking the left-right symmetry of the horizontal configuration (see figure 8.5a). Also on the oscillating inclined surface the drop can move in two opposite direction, i. e. drop can slide down but also climb up the surface against gravity. Drop dynamic behavior depends on the combination of amplitude and frequency of oscillation as reported in the phase diagram in figure 8.5b [113].

The surprising drop climbing was originally explained as a breaking of the front-back symmetry of the oscillating drop and a nonlinear friction law between the drop and the plane [113]. This phenomenon was also studied theoretically assuming thin, two-dimensional drops. John and Thiele [302] examined the limit of low Reynolds numbers and modeled the drops contact line by precursor films due to van der Waals forces. They found that the component of the vibration orthogonal to the plate induces a nonlinear response in the drop shape that causes an anharmonic response of the drop to the parallel vibration component. Benilov and Billingham [303] analyzed the opposite limit of low viscosity, with contact lines governed by a contact-line law and observed that the climbing motion is due to an interaction of oscillatory modes induced by vibrations. These studies were then extended to a first 3D modelling of climbing drops on oscillating substrates under the assumptions of weak vibrations, low viscosity and inertia of the liquid, thin drops and contact-line law [304]. The main

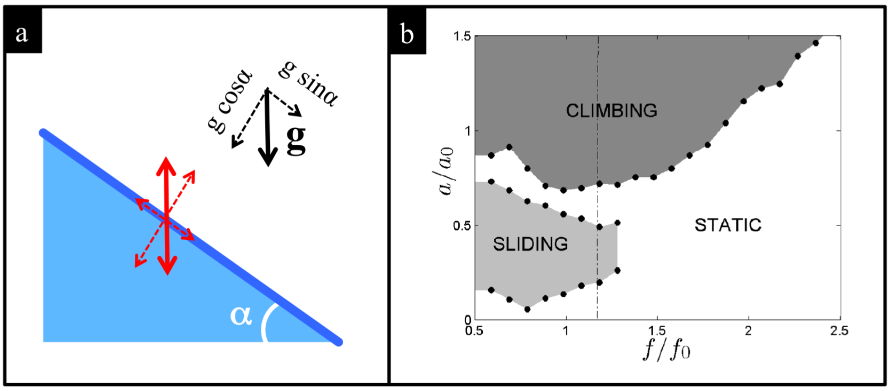

Figure 8.5 : (a) sketch of the verically oscillating inclined surface where the oscillation and the gravity acceleration are deconposed in vectors parallel and orthogonal to the plane; (b) phase diagram of drop motion for V = 5 μL, α=45° and kinematic viscosity ν=31 mm^2/s. The normalization factors are f_0= 50.77 Hz and a_0=174 m/s^2 [113].

conclusion was that, at low frequency, the 2D model [303] is qualitatively incorrect because it predicts that 2D drops can climb only for a very large acceleration of the plate, whereas, for 3D drops, the acceleration can be finite.

§ 8.2. Experimental details

We have studied the dynamics of drops deposited on inclined poly(methyl methacrylate) (PMMA) wedges attached to the moving shaft of an electromagnetic shaker (LDS V101 Brel & Kjr) as shown in the schematic diagram of figure 8.6. After a series of experiments [305–307] with different inclination angles α (30°, 45° and 60°), we decided to fix the inclination at 30°, to make droplets climb more easily and for a wider combination of amplitude and frequency (at high slopes as 60° climbing is almost always not possible because of the prevalent role of gravity [306]).

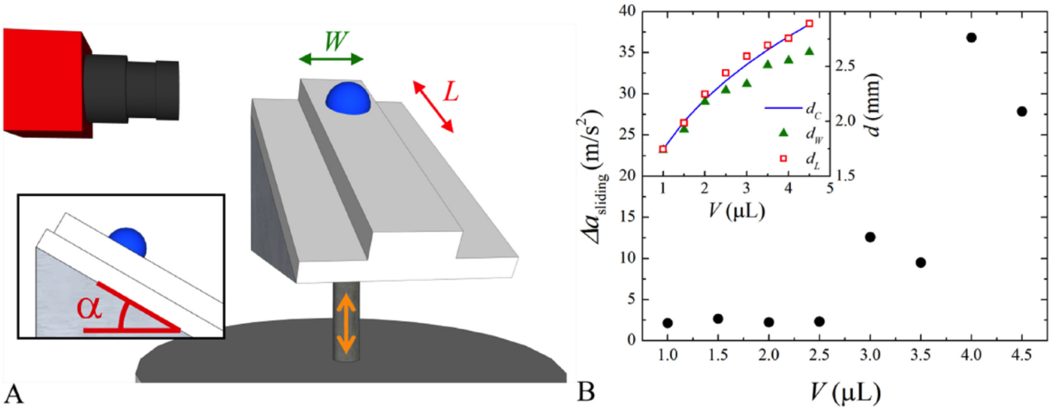

Figure 8.6 : A: Schematic drawing of the experimental set-up. B: Dispersion of the acceleration threshold for sliding $\Delta\ a_{sliding}$ as a function of the drop volume for a ridge with a width of 3 mm oscillating at a frequency of 80 Hz. Inset: comparison of the expected diameter d_C of a hemispherical sessile drop of volume with the measured longitudinal d_L and transversal d_W elongations of the contact line.

The shaker oscillates vertically in the frequency range 10 Hz -10 KHz with a maximum amplitude

of 2.5 mm and the maximum force it can exert is 8.9 N.
A mismatch in the location of the wedge mass center with the shaker axis may cause horizontal oscillations at certain resonance frequencies that can significantly affect the drop dynamics. To avoid this problem, we took particular care to balance the wedge on the axis by adding some extra little loads at specific points. Figure 8.7 shows the results of this tuning operation. The top image represents a portion of the screw attached to the wedge with the shaker off. The middle image shows the screw vibrating at a frequency of 65 Hz and amplitude of 100 μm during an exposure time of 50 ms. The shadows of the contour clearly indicate that there is a horizontal oscillation with an amplitude of about 200 μm superimposed to the vertical vibration. The bottom image refers to the shaker driven at the same conditions as above but after the tuning the center of mass of the wedge. The motion is now purely along the vertical direction. Similar tests have been carried at different frequencies and amplitudes, in particular close to the maximum driving amplitude.

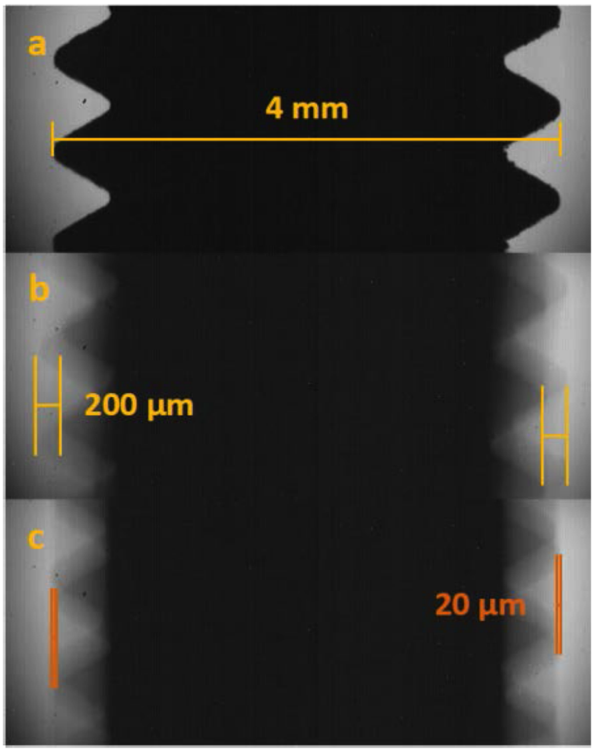

Figure 8.7 : a) Shaker off. b) Shaker driven at a frequency of 65 Hz and amplitude of 100 μm. Vertical and lateral vibrations can be detected from the shadows at the contour. c) Shaker driven at the same conditions as above but after the tuning the center of mass of the wedge.The horizontal vibrations are now highly reduced.

In order to constrain the drop motion to one dimension, we have sculpted channels of different cross-sections (circular, triangular and rectangular) and different widths (from about 0.2 mm to 4 mm) along the direction of the tangential component of the acceleration of gravity [307]. The one we found most effective is a square ridge having height of 2 mm and width of 3 mm (see figure 8.6A). Its vertical extension allowed us to more easily focus the side-view camera to the drop backlighted by the diffuse LED source. For the detection of drop shape, contact angles and contact points during vibrations we exploited a fast camera (PHANTOM, v7.3) working up to 8 kHz, equipped with a telecentric objective

2X.

To find the most appropriate drop volume, we have systematically investigated the reproducibility of the drop dynamics. Water drops of increasing volume are deposited with a syringe pump (Ultra-MicroPump UMP3, WPI) at the center of the ridge. The drops are initially pinned to the surface. Vertical oscillations of the substrate above a given acceleration $a_{sliding}$ cause a downward sliding of the drop. The graph of figure 8.7 shows the dispersion of the acceleration threshold for sliding Δ $a_{sliding}$ measured as a function of the drop volume for a ridge with a width of 3 mm and an oscillating frequency of 80 Hz. The dispersion Δ $a_{sliding}$ is the root mean square deviation calculated from a statistical ensemble of at least five data points acquired at the same nominal conditions. The graph shows a sudden increase in Δ $a_{sliding}$ just above 2.5 μL. We explain it as due to the interaction of the drop contact line with the lateral, irregular edges of the ridge. Actually, the inset compares the expected diameter d_C of a hemispherical sessile drop of volume V with the measured longitudinal d_L and transversal d_W elongations of the contact line. At small volumes, these three quantities coincide confirming that the contact line is circular. Above 2.5 μL, d_W lies below d_C confirming that one side of the contact touches the edge. The fact that d_L remains equal to d_C means that the lateral contact angle is increased because of the geometric pinning at the edge [308]. In our study we have then used drops of 2 μL because they can be easily and accurately detected with our optical set-up. Furthermore, the lateral extension of the ridge guarantees that during their motion the lateral displacement amounts to no more than 0.4 mm, otherwise they will pin to or fall down the edges. In this way, we can accurately track the (one-dimensional) motion of drops by using only one video camera. We have also compared the sliding of 2 μL water drops on the ridge with that on a flat surface and could not detect any appreciable difference between the two substrates.

Besides distilled water, we have also studied different aqueous solutions of glycerol, ethanol and isopropanol. In addition, we have modified the wettability of the PMMA by coating it with trichloro(1H,1H,2H,2H-perfluorooctyl)silane. Their main physical parameters are listed in table 8.1. The values of density ρ, viscosity η and surface tension σ refer to a temperature of 25°C and have been deduced from literature [265,269]. The addition of ethanol and isopropanol mainly decreases the surface tension of the mixture, while that of glycerol increases the viscosity. The kinematic viscosities ν of these mixtures cover the range 1-39 mm^2/s, much wider than the interval between 31 and 55 mm^2/s of the glycerol-water mixtures originally studied by Brunet et al. [113]. The equilibrium contact angle θ and the advancing (receding) contact angle θ_A (θ_R) are determined using the optical apparatus described in Section 2.1. In particular, θ_A and θ_R are measured, respectively, by inflating and deflating a drop deposited on the horizontal surface with the syringe pump and observing the profile when the contact line starts moving. This study is completed with the determination of the contact angle hysteresis $\Delta\theta = \theta_A$ - θ_R, which quantifies the surface pinning. All these data are listed in table 8.1. We have also measured the surface roughness of the top face of the PMMA ridge with a profilemeter and got an rms value less than a couple of nm.

Table 8.1 : Main parameters of the different aqueous solutions used in this study. The concentration c is reported in w/w. Density, viscosity and surface tension are labelled with ρ, η and σ respectively. Static (θ) and dynamic contact angles (θ_A and θ_R) and contact angle hysteresis ($\Delta\theta$) refer to sessile droplets on the substrate listed in the last column.

Fluid solution	c (w/w)	ρ (g/cm^3)	η (mPa s)	σ (mN/m)	θ (deg.)	θ_A (deg.)	θ_R (deg.)	$\Delta\theta$ (deg.)	substrate
water		0.997	0.89	72	71±2	87±2	66±3	21±5	PMMA
ethanol in water	9%	0.98	1.35	52.4	63±3	79±3	62±3	17±6	PMMA
ethanol in water	17%	0.97	1.83	48.8	57±3	72±1	50±3	22±4	PMMA
isopropanol in water	5%	0.988	1.12	49.6	64±3	75±3	43±3	32±5	PMMA
isopropanol in water	10%	0.981	1.41	40.4	61±2	71±3	34±3	37±5	PMMA
glycerol in water	60%	1.15	9	67.2	69±1	78±1	67±3	11±4	PMMA
glycerol in water	80%	1.2	47	65	70±1	79±2	67±2	12±4	PMMA
water		0.997	0.89	72	115±2	118±2	69±2	49±4	silanized PMMA

§ 8.3. Experimental results

The motion of the drop is found to depend on the acceleration a and on the frequency f of the vertical vibrations. Figure 8.8 displays the dynamical phase diagrams of the 5 aqueous solutions obtained by scanning, at different constant frequencies, the vertical acceleration. To better compare them, the oscillating frequency is normalized [113] to the resonance frequency of the drops rocking mode corresponding to a supported drop vibrated in a direction parallel to the substrate [300]:

$$f_0 = \frac{1}{2\pi R^{3/2}} \sqrt{\frac{6\sigma h(\theta)}{\rho(1-\cos\theta)(2+\cos\theta)}} \tag{8.8}$$

where R is the radius of the truncated spherical drop of volume V and h(θ) is a dimensionless geometric function of the equilibrium contact angle θ. For droplets on PMMA, θ is always less than 90° and then h=1, while for water droplets on silanized PMMA h(θ=115°)=0.4. The radius R can be calculated from [308]:

$$R^3 = \frac{3V}{\pi} \frac{1}{(1-\cos\theta)^2(2+\cos\theta)} \tag{8.9}$$

The acceleration is determined from the formula:

$$a = 4\pi^2 f^2 A \tag{8.10}$$

where A is the oscillating amplitude, which is deduced from the maximum displacement of the ridge measured with the high frequency camera. The characteristic acceleration is taken as

$$a_0 = 4\pi^2 f_0^2 V^{1/3} \tag{8.11}$$

since $V^{1/3}$ is a measure of the deformation [113]. For 2 μL water drops on PMMA, the two characteristic parameters are f_0 =70 Hz and a_0=241 m/s^2, while on silanized PMMA f_0 = 47 Hz and a_0=110 m/s^2. For the other liquids on PMMA these values become smaller and are comprised in the ranges f_0 =34-59 Hz and a_0=59-173 m/s^2. As can be evinced from the comparison with figure 8.5b, the phase diagrams of glycerol/water mixtures look quite similar to that originally reported for a drop of water-glycerol having V=5 μL and ν=31 mm^2/s deposited on an inclined plane with α = 45° [113] (the parabolic dashed lines in the diagrams of figure 8.8 represent the relative acceleration corresponding to the maximum oscillating amplitude of our shaker equal to 2.5 mm). On the static ridge, the drops are always pinned to the surface. Vertically vibrating the ridge above a certain relative acceleration a/a_0 ~0.2, very similar to that found by Brunet el al. [113], yields sliding of the drop. Furthermore, sliding can be induced only for relative frequencies f/f_0 smaller than ~1.5, which is close to the cut-off of ~1.3 reported in figure 8.5 for a 5 μL glycerol/water drop for α = 45° [113]. At variance with previous experiments that could not detect sliding for drops of volume smaller than 5 μL [113, 309], we always observed a sliding region for all the 2 μL drops we investigated, an indication that our surfaces were not too defective. Also, no evidence of drop breaking was found during our measurements in contrast to what reported by Brunet et al. [113, 309], probably because of the smaller drops we used.

We now discuss in more detail the single phase diagrams, starting from that of pure water on PMMA that presents a pronounced sliding region at moderate accelerations: for f/f_0 =0.9 and a/a_0=0.4 the sliding velocity is about 6.4 mm/s. Further increasing the oscillating amplitude moves the drop upwards against gravity: for f/f_0 =1.1 and a/a_0=1.1 the climbing velocity is 4.3 mm/s. As expected, the overall phase diagram closely resembles those of mixtures of 9% (w/w) of ethanol in water and 5% (w/w) of isopropanol in water (not shown because it has fewer points) because these solutions have essentially the same viscosity and wetting properties of pure water. More interesting, it is also very similar to those of glycerol/water mixtures in spite of a variation in ν greater than a factor 10. This finding is consistent with the observation that the threshold for climbing with liquids of similar surface tensions does not depend on the liquid viscosity [309]. If instead we compare it with that of water on silanized PMMA, we notice that the sliding and climbing regions have been shifted to higher relative accelerations to balance the higher capillarity forces due to contact-angle hysteresis that, on silanized PMMA, is more than twice the value measured on PMMA, as reported in table 8.1. Arguably, the most interesting and original result of our experimental study is that drops of 17% (w/w) of ethanol in water and of 10% (w/w) of isopropanol in water do not climb within the a/a_0 range accessible to the experiment clearly indicating that a wettable ridge favors sliding only.

With a fast camera we have analyzed the drop evolution during sliding and climbing. Figure 8.9 shows a sequence of side view snapshots taken over an oscillating period. They clearly show that the instantaneous drop profile varies differently in the two situations. The evolution of the climbing drop experiences a bigger variation in the profile: the peak becomes sharper (see E-D) and the bump is wider and shallower (see F-G).

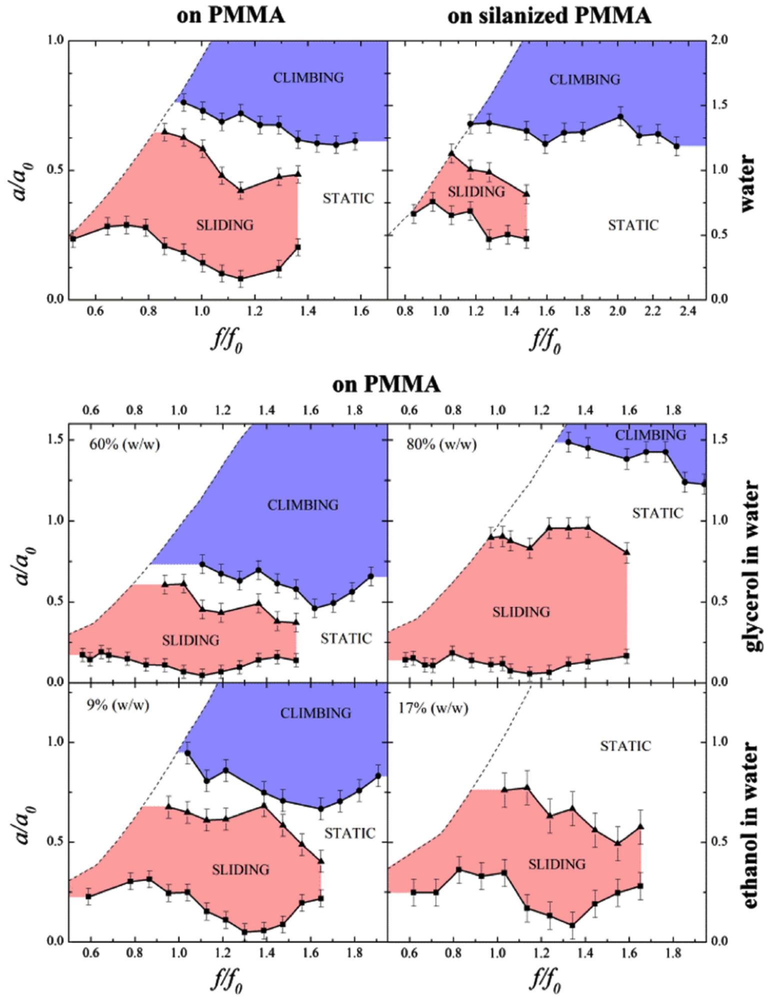

Figure 8.8 : Dynamical phase diagrams of drops of different aqueous solutions corresponding to V=2 μL and $\alpha = 30°$. The normalization factors are a_0=241 m/s^2 and f_0=70 Hz for water on PMMA and a_0=110 m/s^2 and f_0=47 Hz for water on silanized PMMA. For the other liquids they are comprised in the ranges a_0=117-173 m/s^2 and f_0= 48-59 Hz.

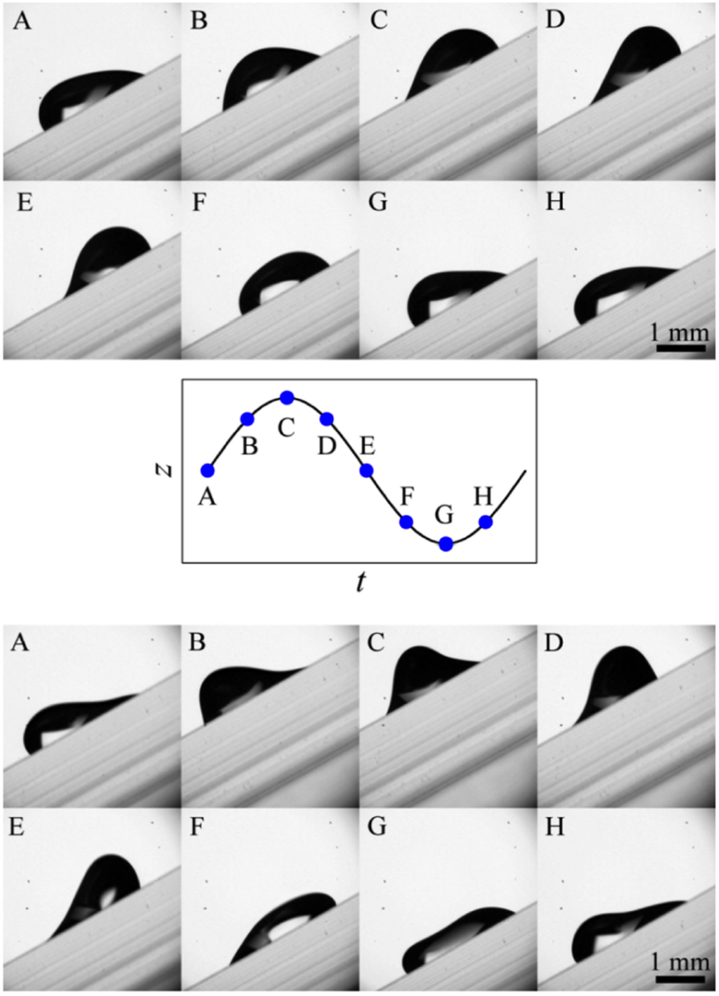

Figure 8.9 : Side views of a sliding (top) and climbing (bottom) water drop taken at different instants of a vibrating cycle of frequency f=65 Hz, e.g. f/f_0=0.9 for sliding (f=80 Hz, e.g. f/f_0=1.1 for climbing) as indicated in the middle panel. The vertical accelerations are a=100 m/s^2 (a/a_0=0.4) for the sliding drop and a=260 m/s^2 (a/a_0=1.1) for the climbing drop.

From the analysis of these images, we have extracted the evolution of the upper and lower instantaneous contact angles, θ_{up} and θ_{down} respectively, which are shown in figure 8.10 for the two cases just discussed. In the same graphs, the corresponding positions of the contact points are also plotted. All quantities oscillate periodically over time. In particular, the positions display an oscillatory behavior around a mean value that slowly moves downward (upward) when the drop slides (climbs). It is clearly evident that the lower (upper) contact point of a sliding drop moves downward when the corresponding contact angle is above (below) the advancing (receding) contact angle, as shown by the shaded areas in figure 8.10. Similarly, the upper (lower) contact point of a climbing drop moves upward when the corresponding contact angle is above (below) the advancing (receding) contact angle.

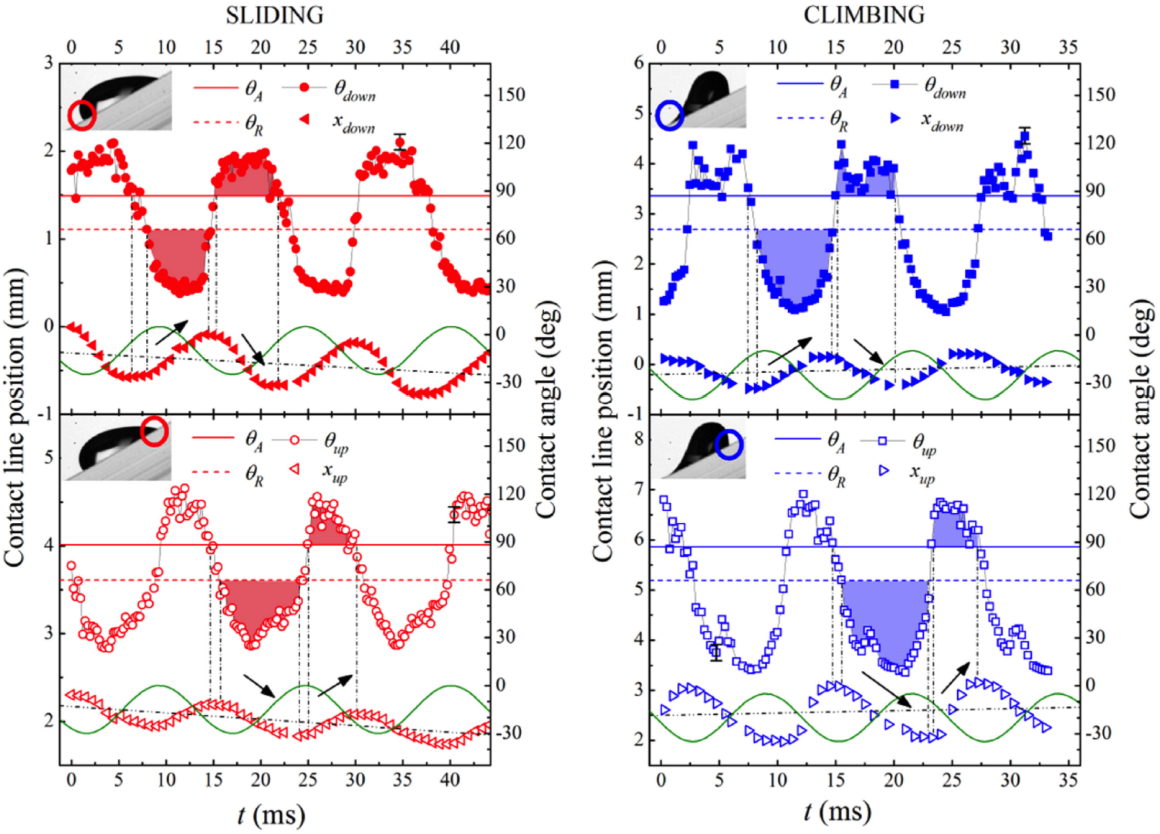

Figure 8.10 : Time evolution of the upper and lower contact angles for a water drop sliding down (left panels) and climbing up (right panels) the inclined ridge. The corresponding contact line positions along the x direction of the inclined ridge are also plotted. Frequency and acceleration are $f = 65$ Hz and $a = 100$ m/s^2 for the sliding drop and $f = 80$ Hz and $a = 260$ m/s^2 for the climbing drop, respectively. The advancing (receding) contact angle is indicated by a continuous (dashed) horizontal line. The continuous sinusoidal lines represent the oscillation of the vertical position z of the inclined plate (in arbitrary units). The error on the contact angle is about 5°. For the sake of clarity , the corresponding error bars are reported only in one point for each contact angle. Instead, the error bars on the position are smaller than the symbols.

Furthermore, the contact angles, as well as the contact line positions, are out of phase with the oscillation of the inclined plate. The phase shift δ_{down} (δ_{up}) between the lower (upper) contact point velocity and the lower (upper) contact angle for sliding and climbing drops driven at different frequencies are reported in figure 8.11. It results that the upper contact point velocity are always in phase with respect to the upper contact angle, while the lower contact point velocity is out of phase with the lower contact angle.

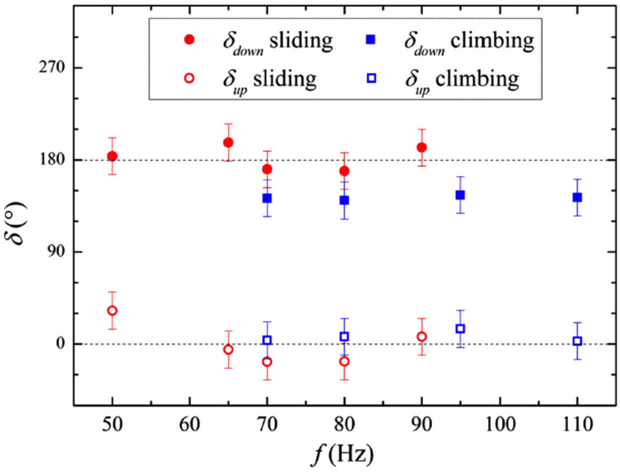

Figure 8.11 : Phase shift δ_{down} (δ_{up}) between the lower (upper) contact point velocity and the lower (upper) contact angle for the sliding drop and the climbing drop. In the sliding case the peak acceleration is fixed at $a = 80$ m/s^2, while in the climbing one it is fixed at $a = 200$ m/s^2.

§ 8.4. Numerical simulations

The numerical simulations modelling a drop on an oscillating surface are based on a diffuse interface approach, the Cahn-Hilliard / Navier-Stokes (CHNS) model, described in Section 1.6.3. In particular, in this case equation 1.52 has to include the term related to the oscillation of the substrate. In the reference frame of the plate, the vibration corresponds to a time dependent body force which originates a buoyancy term that, for small density difference, can be approximated *à la* Boussinesq to yield $\mathbf{g}(t) = -\sin(2\pi t)(\sin(\alpha)\hat{\mathbf{e}}_\mathbf{x} + \cos(\alpha)\hat{\mathbf{e}}_\mathbf{z})(\Phi+1)/2$, with $\hat{\mathbf{e}}_{\mathbf{x},\mathbf{z}}$ the unit vectors in the two directions, parallel and perpendicular to the plate. The consequent equation is:

$$\frac{D\mathbf{u}}{Dt} = -\frac{1}{\rho}\boldsymbol{\nabla} p + \frac{1}{\mathrm{We\,Cn}}\mu_c \boldsymbol{\nabla}\Phi + \frac{1}{\mathrm{Re}}\nabla^2\mathbf{u} + \frac{1}{\mathrm{Fr}}\mathbf{g}\,, \tag{8.12}$$

where $\dfrac{D(\cdot)}{Dt} = \partial(\cdot)/\partial t + \mathbf{u}\cdot\boldsymbol{\nabla}(\cdot)$ is the material derivative, $\mathrm{Re} = \rho L^2 f/\mu$ is the Reynolds number with μ the dynamic viscosity and f the frequency of the vibrating plate, $\mathrm{We} = 3\rho f^2 L^3/(\sqrt{8}\sigma)$ is the Weber number, $\mathrm{Fr} = L\rho/(4\pi^2 A\Delta\rho)$ is the Froude number, with A the amplitude of the plate oscillation and $\Delta\rho = \rho_A - \rho_B$.

The system of equations (1.50, 1.51 and 8.12) is completed with the following boundary conditions:

$$\mathbf{u} = 0\,, \tag{8.13}$$

$$\boldsymbol{\nabla}\mu_c \cdot \mathbf{n} = 0\,, \tag{8.14}$$

implying the no-slip and no mass flux conditions at the wall, respectively, and

$$\frac{D\Phi}{Dt} = -\frac{\mathrm{Re}}{\mathrm{Dw\,We\,Cn}}\left(\Phi^2 - 1\right)\cos\theta_e - \frac{\mathrm{Re}}{\mathrm{Dw\,We}}\frac{\partial\Phi}{\partial n}\,, \tag{8.15}$$

where $\mathrm{D_w} = \mu_f/\mu$, with μ_f an effective friction of the contact line, represents the ratio of the typical relaxation time in reaching the equilibrium contact angle to the macroscopic time scale [176]. Eq. (8.15) represents the non-equilibrium boundary condition for the contact angle and links together the velocity of the contact line and the instantaneous contact angle.

In order to reach the sharp interface limit $\mathrm{Cn} = 0.025$ and $\mathrm{M} = \mathrm{Cn}^2$ has been used throughout the simulations. The equilibrium contact angle has been chosen slightly hydrophobic, $\theta = 97.5^\circ$ and, following [176], $D_w = 100$. The values chosen for density, viscosity and surface are the typical parameters for water reported in table 8.1. We considered a 1 mm radius drop and, in order to compare the numerical results with the experiments, we used $\Delta\rho/\rho = 1$ relying on the ability of the Boussinesq approximation to qualitatively reproduce the correct physics. More details about these simulations can be find in [164, 310].

§ 8.5. Numerical results and comparison with experiments

Extensive numerical simulations have been performed by changing the frequency and the amplitude of the vibrating plate. Before discussing the results, we point out that several significant differences exist between the systems we have numerically simulated and the corresponding experiments: i) the simulations are two dimensional; ii) the two fluids (corresponding to droplet liquid and surrounding air, in the experiment) have the same viscosity and almost identical densities. More precisely, the Boussinesq approximation is adopted, which implies that the density is constant apart from the buoyancy term; iii) no pinning of the contact lines is considered; iv) the plate is hydrophobic (E =97.5). Clearly, assumptions i) and ii) have been introduced for simplicity. Assumption iii) is due to the lack of reliable models for pinning in the context of diffuse interface models. Finally, drop climbing has been found only by assuming iv). We cannot exclude that a more complete search could identify climbing also on slightly hydrophilic surfaces.

Despite these differences, the dynamical phase diagram in figure 8.12 reproduces the main features observed in the experiments (see figure 8.8). At high acceleration the drop climbs. Reducing the oscillating amplitude at fixed frequency, a non-pinned static droplet is found. Because of the lack of pinning in the model, in this region the droplet periodically moves up and down without a mean displacement. Further decreasing a/a_0, the drop starts sliding. The numerical simulations cannot reproduce the static region found in the experiments at very low accelerations again because of the lack of pinning in the model. At very high accelerations, the drop detaches from the plane or, in some cases, breaks-up due to the extreme deformations. In the phase diagram in figure 8.12 the dashed curve identifies this breaking region. This sequence of dynamic transitions is found for all frequencies below a threshold value $\simeq 2f_0$, beyond which climbing disappears because the drop dynamics at high a/a_0 is dominated by detachment and break-up. This behavior, not observed in our experiments, is likely due to the 2D nature of the drops since the reduced capillary stress (in 2D simulations the second main curvature is zero) leads to greater elongations that facilitate the drop break-up. Similarly, the numerical transitions are found at higher relative accelerations than the experimental ones. Notwithstanding these discrepancies, the overall qualitative behavior is reproduced which means that neither the contact line pinning due to contact angle hysteresis, nor the density difference between the droplet and the ambient fluid, seems to be of crucial importance to describe the climbing mechanism.

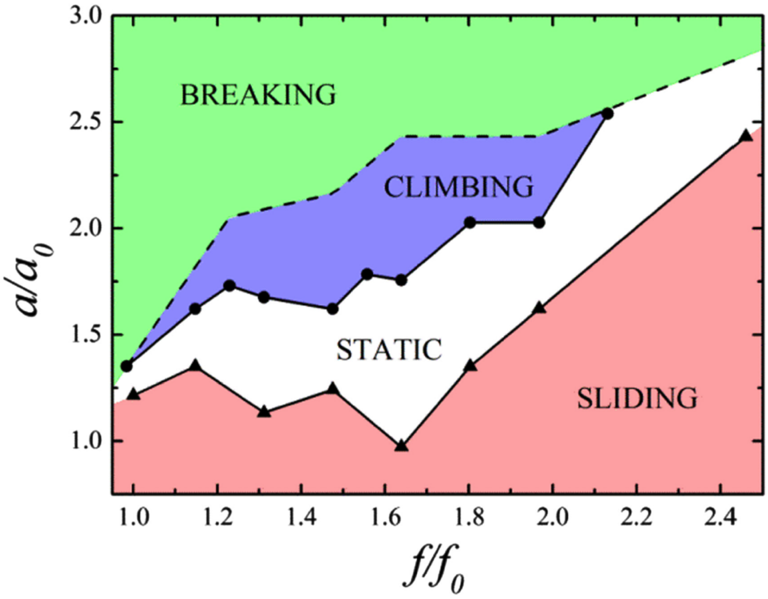

Figure 8.12 : Dynamical phase diagram of water obtained by numerical simulations. The data correspond to $\alpha = 30°$ and θ=97.5°. The normalization factors are a_0=185 m/s^2 and f_0=61 Hz.

The drop shape and the velocity field at different instants of the plate oscillating period are shown in figure 8.13 during both sliding and climbing. In agreement with the experiments (see figure 8.9), during sliding the drop undergoes smaller deformations: the border is more rounded and the maximum horizontal and vertical elongations are smaller. Furthermore the periodicity of the sliding drop is the same as that of the plate. Instead, the climbing drop shows a sub-harmonic response with twice the periodicity of the oscillating plate, which does not seem to be confirmed by the experiments and is probably related to the approximations introduced in the model (see Supplemental Material of [310] for a more complete discussion).

The time evolution of the contact line positions and of both upper and lower contact angles can be derived from the analysis of the droplet shape. Figure 8.14 compares the sliding (left panels) and the climbing (right panels) cases and the double period is again apparent in the upper front of the climbing drop. Full symbols correspond to the lower contact line, empty symbols to the upper contact line. As a reference, the vertical position of the plate is represented by a solid green line. In agreement with the experiments (see figure 8.10), the simulations of the sliding drop clearly show a phase shift of the contact line motion: when the plate goes up, the drop squeezes down and the lower contact line moves down while the other one goes up. The maximum tangential elongation is reached slightly before the plate reaches its maximum height. Overall, the capillary stresses act like a spring to restore the equilibrium shape. A similar dynamics is observed when the plate descends: the drop retracts and elongates vertically with the lower contact line moving up and the upper one going down. Again, the capillary stresses act against the strong deformation and the motion of the contact lines before the plate reaches its minimum height. The dynamic of the climbing drop is far more complicated as a result of the higher deformation experienced during the plate oscillation (see again the snapshots in

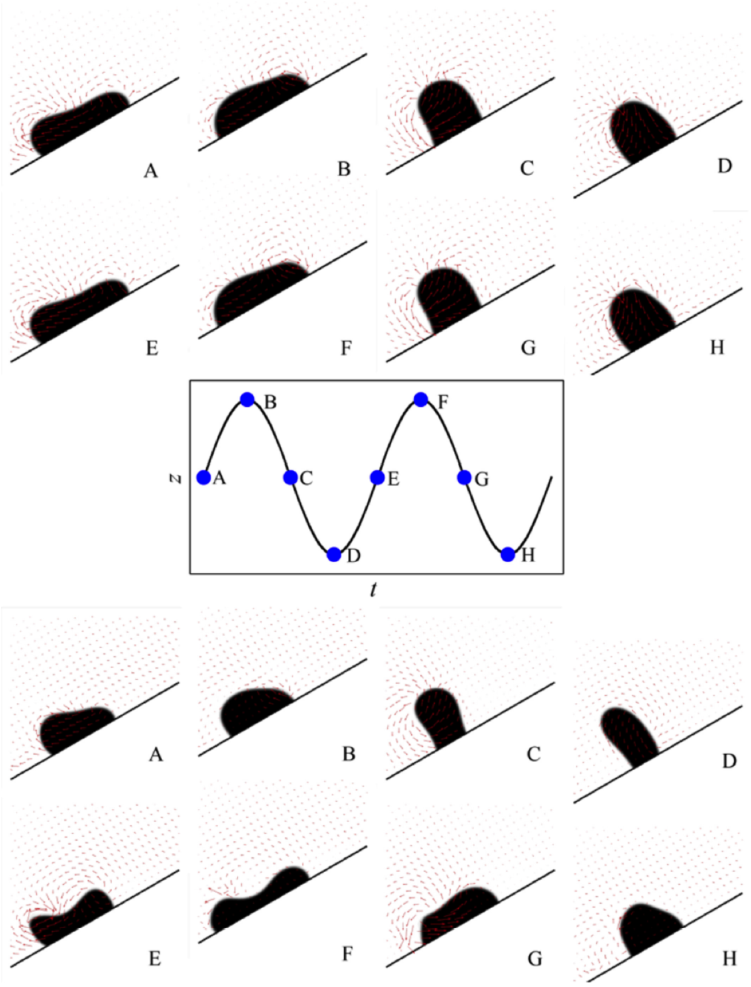

Figure 8.13 : Snapshots of a sliding (top) and climbing (bottom) 2D water drop taken at different instants of a vibrating cycle as indicated in the middle panel. The sliding drop corresponds to the case with a/a_0=1 and f/f_0=1.33, while the climbing drop to a/a_0=1.9 and f/f_0=1.67. The arrows represent the calculated velocity in both fluids.

figure 8.13). The phase shift is still present, but in the case shown in figure 8.14 it is not so pronounced. Moreover, the upper contact line stops sliding down during the plate descent, in a sort of dynamical pinning that enhances the climbing.

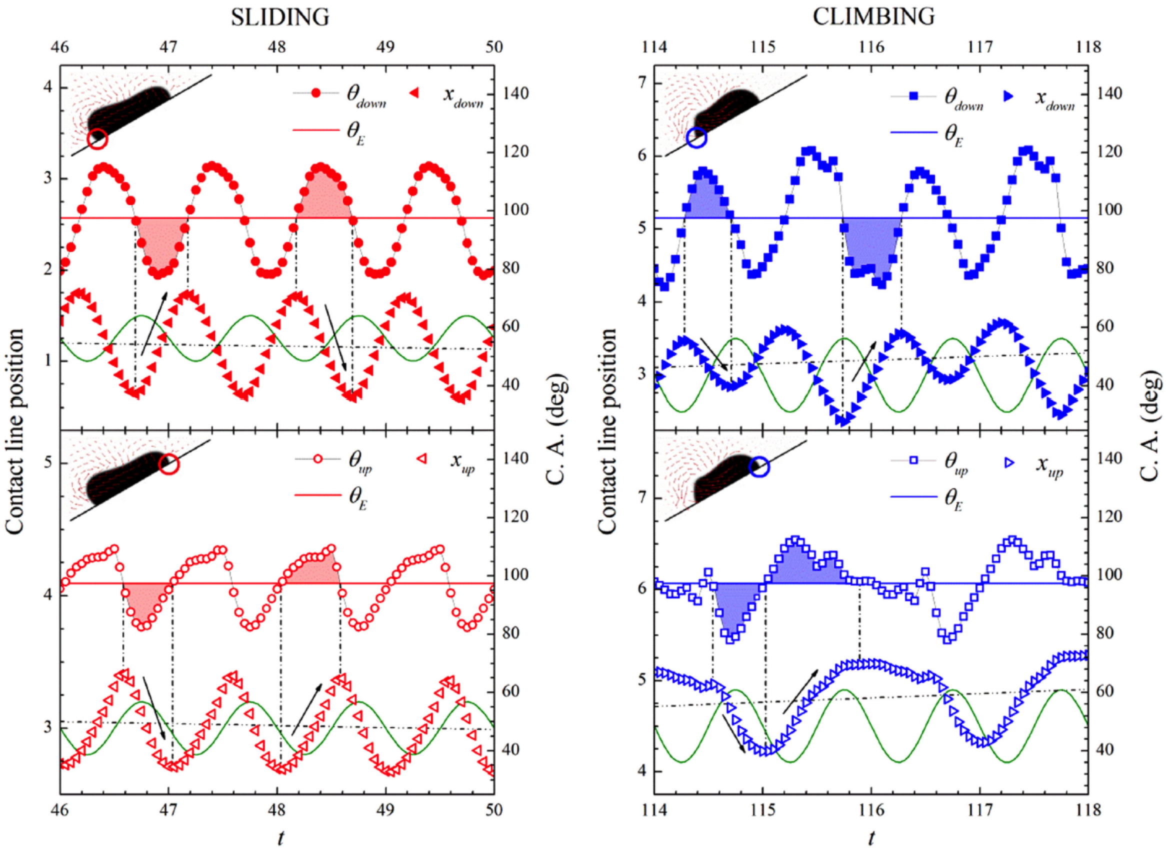

Figure 8.14 : Time evolution of the lower (full symbols) and upper (empty symbols) contact line positions (triangles) and of the contact angles (circles and squares) both in the sliding (left panels) and in the climbing (right panels) regime. The vertical position of the plate is indicated by a sinusoidal green solid line. The contact line position is expressed in unit of the resting drop radius (1 mm) and the time unit is the oscillation period.

Besides the analysis of the drop shape, the numerical simulations provide details about the stress distribution. In particular, by numerical integration of equation 8.12 over the entire domain it is possible to extract the total force acting on the fluid (see [310] for more details):

$$F_{tot} = F_{visc}(t) + F_{cap}(t) + W(t), \tag{8.16}$$

where $W(t)$ is the integral of the buoyancy force in the x direction due to the plate vibration and $F_{visc}(t)$ and $F_{cap}(t)$ are the viscous and capillary forces, respectively. Figure 8.15 shows the time evolution of the viscous and capillary forces during two consecutive plate oscillations. The left panel refers to a sliding drop, the right one to a climbing drop. In both cases the two forces are not in phase with respect to the plate position. The time average of the resulting force equals zero since, on average, the motion is a steady sliding or climbing. The main difference between sliding or climbing is in the sign of the individual forces. We would like to remark that the mean viscous force always acts in the direction of the mean motion.

This result suggests a possible mechanism for droplet motion: following the sketch in figure 8.16, a

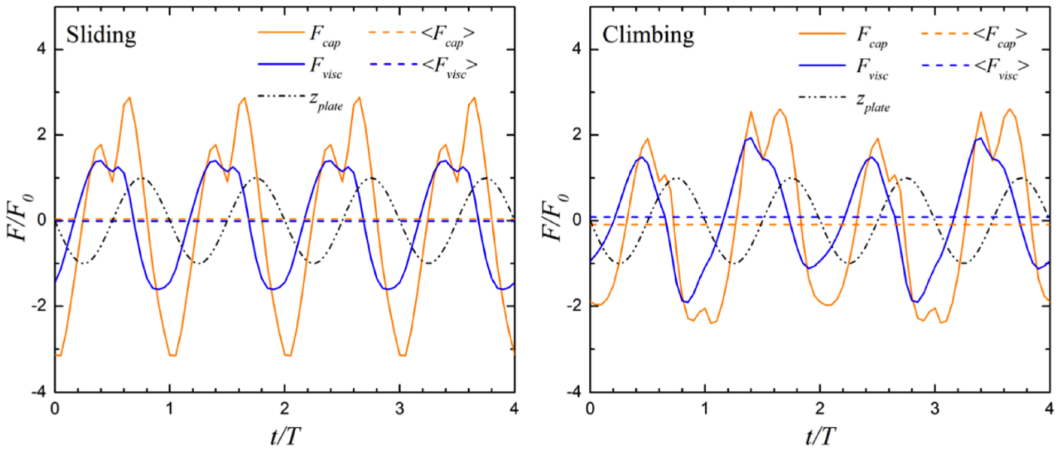

Figure 8.15 : Time evolution of the capillary and viscous forces acting on the drop. T is the period of the plate oscillation and F_0 is a reference force defined as $F_0 = \rho R^3/T^2$, with ρ density of the liquid and R radius of the drop. The left panel represents the sliding case, the right panel the climbing one. The vertical oscillation of the inclined plate z plate is represented in arbitrary unit.

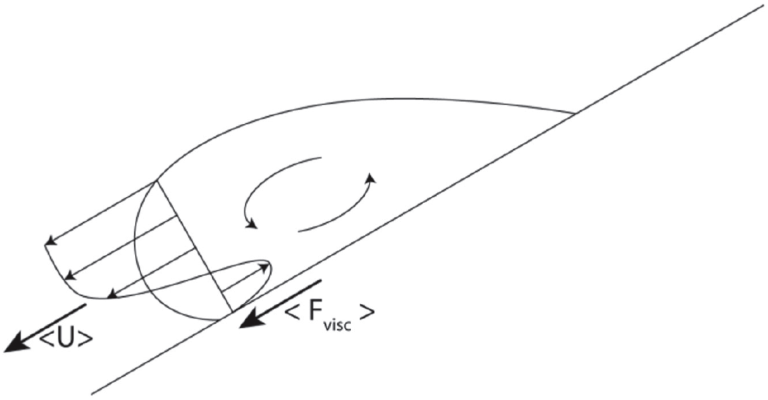

Figure 8.16 : Sketch of the rolling mean motion inside of a sliding droplet. Both the mean velocity and the mean viscous force are directed downhill.

downhill-directed viscous force on the drop together with a mean motion in the same direction can be obtained by a circulatory motion of the fluid inside the drop. As a consequence, the droplet rolls down. On the contrary, when the drop climbs the plate, the circulatory motion reverts sign (up-hill rolling). To be more quantitative, we evaluated the mean circulation in the droplet interface by integrating the mean vorticity:

$$\langle\Gamma\rangle = \frac{1}{2T}\int_{2T}\oint_{\partial S}\mathbf{u}\cdot d\mathbf{l} = \frac{1}{2T}\int_{2T}\int_{S}\nabla\times\mathbf{u}dSdt \tag{8.17}$$

where the drop is identified as the region where $\Phi > 0$. All the sliding drops show positive values of $\langle\Gamma\rangle$ while climbing drops have $\langle\Gamma\rangle < 0$, confirming the conjectured rolling motion.

§ 8.6. Conclusion

In conclusion, we have systematically studied the dynamics of liquid drops on an inclined plate subject to vertical vibrations. The liquids comprised distilled water and different aqueous solutions of glycerol, of ethanol and of isopropanol spanning the range 1-39 mm^2/s in kinematic viscosity and 40 - 72 mN/m in surface tension. At sufficiently low oscillating amplitudes, the drops are always pinned to the surface. Vibrating the plate above a certain amplitude yields sliding of the drop. Further increasing the oscillating amplitude drives the drop upward against gravity. The viscosity of the liquid solution does not seem to affect significantly the dynamical phase diagrams, at least in the explored range 1-39 mm^2/s. Instead, low surface tensions, i.e. low contact angles, are found to hinder climbing and favor sliding of drops. Complementary numerical simulations of 2D drops based on a diffuse interface approach essentially confirm the experimental findings. The overall qualitative behavior is reproduced suggesting that the contact line pinning due to contact angle hysteresis is not necessary to explain the drop climbing. Images taken with a fast camera show that the drop profile evolves in a different way during sliding and climbing as also confirmed by the numerical simulation. The direction of motion is related to the circulation (i. e. vorticity) inside the drop and shape deformations induced by plane oscillations.

The exploitation of these effects offer the possibility to control and manipulate droplets on a substrate by tuning frequency and acceleration of the vertical vibration. Since the phase diagram depends on drop volume and kind of fluid, drops of different size and/or composition subject to the same oscillation cane move in opposite directions up to meet and react together (see Movie3 in supplemental maririal of [310]).

Conclusions

This PhD research analyzed the behavior of drops, with volumes on the order of microliters, on inclined surfaces. Different kinds of surfaces have been considered to passively control drop motion: hairy samples and chemically heterogeneous surfaces.

In particular, the adhesion properties of hairy surfaces are heavily affected by their morphology but also, even if in a minor role, by structure elasticity. More precisely, hairy surfaces are sticky except when hairs are so long that they collapse, making the sample water-repellent. Surfaces formed by nanohairs overlapping microgrooves are found to be water repellent too. These sticky surfaces can be exploited for liquid transfer with small volume losses or to stop moving drops.
The sliding velocity of drops on inclined homogeneous surfaces varies according to the static wettability and the contact angle hysteresis of the samples: drops start sliding at low inclination if the hysteresis is small and move faster on hydrophobic surfaces. A tool to passively tune sliding velocity consists of chemically patterning surfaces with hydrophilic and hydrophobic domains of different shapes, like for instance stripes, squares and triangles. Drops on these heterogeneous samples undergo a stick-slip motion with jumps of the front and rear contact points corresponding to the pattern periodicity. Energy dissipation related to the pinning/depinning transition of the contact line at the edges of the domains affects drop mean velocity, which is found to depend on the geometry and arrangement of the texture tiles.
A chemical step formed at the junction between two regions of different wettability can be exploited to control drop trajectories: when a sliding drop finds a more hydrophobic area, it can stop, pass or deviate following the border between the two parts of the surface, according to the combination of plane inclination and inclination of the step with respect to the gravity direction.
In order to actively handle drops on inclined homogeneous substrates, acoustic vibrations have been applied to the surface. In particular, different combinations of oscillation amplitude and frequency can make droplets slide down, be pinned or even climb upward against gravity. Furthermore, this manipulation is effective with any kind of liquid thanks to the direct coupling with fluid inertia and could be exploited to make different droplets react together. Indeed the direction of motion under vibration depends on drop volume: droplets of different size can move in opposite directions until they meet and merge together. Because the internal motion induced by plane oscillations favors mixing, the resulting reaction times are significantly reduced, differently from droplets in closed channels.
In these experiments pure liquids, Newtonian solutions and complex fluids have been investigated. Marked differences are found in the behavior of Newtonian and complex fluids.

There is an ample variety of possible ways to extend this research. For example, studying the sliding of other types of non-Newtonian solutions or ferrofluids subject to modulated magnetic fields, or the dynamics of drops on different kinds of surfaces, such as geometrically textured samples. Also vibrations can be applied to complex fluids or to patterned surfaces. The results will be very important to realize a digital microfluidic open device for chemical or biomedical applications.

Bibliography

[1] K. Liu, X. Yao, and L. Jiang. Recent developments in bio-inspired special wettability. *Chemical Society Reviews*, 39(8):3240–3255, 2010.

[2] C. Neinhuis and W. Barthlott. Characterization and distribution of water-repellent, self-cleaning plant surfaces. *Annals of Botany*, 79(6):667–677, 1997.

[3] D. Quéré. *Wetting and roughness*, volume 38 of *Annual Review of Materials Research*, pages 71–99. 2008.

[4] J. Genzer and A. Marmur. Biological and synthetic self-cleaning surfaces. *Mrs Bulletin*, 33(8):742–746, 2008.

[5] B. Bhushan, Y. C. Jung, and K. Koch. Micro-, nano- and hierarchical structures for superhydrophobicity, self-cleaning and low adhesion. *Philosophical Transactions of the Royal Society a-Mathematical Physical and Engineering Sciences*, 367(1894):1631–1672, 2009.

[6] O. Sato, S. Kubo, and Z.-Z. Gu. Structural color films with lotus effects, superhydrophilicity, and tunable stop-bands. *Accounts of Chemical Research*, 42(1):1–10, 2009.

[7] S. Kim, E. Cheung, and M. Sitti. Wet self-cleaning of biologically inspired elastomer mushroom shaped microfibrillar adhesives. *Langmuir*, 25(13):7196–7199, 2009.

[8] C. R. Crick and I. P. Parkin. A single step route to superhydrophobic surfaces through aerosol assisted deposition of rough polymer surfaces: duplicating the lotus effect. *Journal of Materials Chemistry*, 19(8):1074–1076, 2009.

[9] L. Qu, L. Dai, M. Stone, Z. Xia, and Z. L. Wang. Carbon nanotube arrays with strong shear binding-on and easy normal lifting-off. *Science*, 322(5899):238–242, 2008.

[10] V. Zorba, E. Stratakis, M. Barberoglou, E. Spanakis, P. Tzanetakis, S. H. Anastasiadis, and C. Fotakis. Biomimetic artificial surfaces quantitatively reproduce the water repellency of a lotus leaf. *Advanced Materials*, 20(21):4049, 2008.

[11] K. Liu, J. Zhai, and L. Jiang. Fabrication and characterization of superhydrophobic sb_2o_3 films. *Nanotechnology*, 19(16), 2008.

[12] D. Nystrom, J. Lindqvist, E. Ostmark, P. Antoni, A. Carlmark, A. Hult, and E. Malmstrom. Superhydrophobic and self-cleaning bio-fiber surfaces via atrp and subsequent postfunctionalization. *Acs Applied Materials & Interfaces*, 1(4):816–823, 2009.

[13] B. Bhushan, K. Koch, and Y. C. Jung. Biomimetic hierarchical structure for self-cleaning. *Applied Physics Letters*, 93(9), 2008.

[14] B. Bhushan, Y. C. Jung, and K. Koch. Self-cleaning efficiency of artificial superhydrophobic surfaces. *Langmuir*, 25(5):3240–3248, 2009.

[15] K. Koch, B. Bhushan, and W. Barthlott. Multifunctional surface structures of plants: An inspiration for biomimetics. *Progress in Materials Science*, 54(2):137–178, 2009.

[16] Z. Luo, Z. Zhang, L. Hu, W. Liu, Z. Guo, H. Zhang, and W. Wang. Stable bionic superhydrophobic coating surface fabricated by a conventional curing process. *Advanced Materials*, 20(5):970, 2008.

[17] Z.-G. Guo, W.-M. Liu, and B.-L. Su. A stable lotus-leaf-like water-repellent copper. *Applied Physics Letters*, 92(6), 2008.

[18] E. Stratakis, V. Zorba, M. Barberoglou, E. Spanakis, S. Rhizopoulou, P. Tzanetakis, S. Anastasiadis, and C. Fotakis. Laser structuring of water-repellent biomimetic surfaces. *SPIE Newsroom*, 10(2.1200901):1441, 2009.

[19] A. Marmur. The lotus effect: Superhydrophobicity and metastability. *Langmuir*, 20(9):3517–3519, 2004.

[20] A. Tuteja, W. Choi, J. M. Mabry, G. H. McKinley, and R. E. Cohen. Robust omniphobic surfaces. *Proceedings of the National Academy of Sciences of the United States of America*, 105(47):18200–18205, 2008.

[21] W. Choi, A. Tuteja, S. Chhatre, J. M. Mabry, R. E. Cohen, and G. H. McKinley. Fabrics with tunable oleophobicity. *Advanced Materials*, 21(21):2190, 2009.

[22] M. Le Merrer. *Dissipation aux interfaces : caléfaction, sillages, filaments visqueux.* Phd thesis, Ecole Polytechnique X, 2010.

[23] A. L. Biance, C. Clanet, and D. Quéré. Leidenfrost drops. *Physics of Fluids*, 15(6):1632–1637, 2003.

[24] M. Liu, S. Wang, Z. Wei, Y. Song, and L. Jiang. Bioinspired design of a superoleophobic and low adhesive water/solid interface. *Advanced Materials*, 21(6):665, 2009.

[25] L. Chen, M. Liu, H. Bai, P. Chen, F. Xia, D. Han, and L. Jiang. Antiplatelet and thermally responsive poly(n-isopropylacrylamide) surface with nanoscale topography. *Journal of the American Chemical Society*, 131(30):10467–10472, 2009.

[26] H. Meng, S. Wang, J. Xi, Z. Tang, and L. Jiang. Facile means of preparing superamphiphobic surfaces on common engineering metals. *Journal of Physical Chemistry C*, 112(30):11454–11458, 2008.

[27] J. Xi, L. Feng, and L. Jiang. A general approach for fabrication of superhydrophobic and superamphiphobic surfaces. *Applied Physics Letters*, 92(5), 2008.

[28] K. Zhao, K. S. Liu, J. F. Li, W. H. Wang, and L. Jiang. Superamphiphobic cali-based bulk metallic glasses. *Scripta Materialia*, 60(4):225–227, 2009.

[29] W. Wu, X. Wang, D. Wang, M. Chen, F. Zhou, W. Liu, and Q. Xue. Alumina nanowire forests via unconventional anodization and super-repellency plus low adhesion to diverse liquids. *Chemical Communications*, (9):1043–1045, 2009.

[30] X. Liu, W. Wu, X. Wang, Z. Luo, Y. Liang, and F. Zhou. A replication strategy for complex micro/nanostructures with superhydrophobicity and superoleophobicity and high contrast adhesion. *Soft Matter*, 5(16):3097–3105, 2009.

[31] T. Darmanin and F. Guittard. Molecular design of conductive polymers to modulate superoleophobic properties. *Journal of the American Chemical Society*, 131(22):7928–7933, 2009.

[32] T. Darmanin and F. Guittard. One methylene unit to control super oil-repellency properties of conducting polymers. *Chemical Communications*, (16):2210–2211, 2009.

[33] J. Zimmermann, M. Rabe, G. R. J. Artus, and S. Seeger. Patterned superfunctional surfaces based on a silicone nanofilament coating. *Soft Matter*, 4(3):450–452, 2008.

[34] A. Steele, I. Bayer, and E. Loth. Inherently superoleophobic nanocomposite coatings by spray atomization. *Nano Letters*, 9(1):501–505, 2009.

[35] A. Ahuja, J. A. Taylor, V. Lifton, A. A. Sidorenko, T. R. Salamon, E. J. Lobaton, P. Kolodner, and T. N. Krupenkin. Nanonails: A simple geometrical approach to electrically tunable superlyophobic surfaces. *Langmuir*, 24(1):9–14, 2008.

[36] T. Kim, D. Tahk, and Hong H. Lee. Wettability-controllable super water- and moderately oil-repellent surface fabricated by wet chemical etching. *Langmuir*, 25(11):6576–6579, 2009.

[37] G. Lagubeau, M. Le Merrer, C. Clanet, and D. Quéré. Leidenfrost on a ratchet. *Nature Physics*, 7(5):395–398, 2011.

[38] D. Quéré. Leidenfrost dynamics. *Annual Review of Fluid Mechanics, Vol 45*, 45:197–215, 2013.

[39] K. Piroird, C. Clanet, and D. Quéré. Magnetic control of leidenfrost drops. *Physical Review E*, 85(5), 2012.

[40] K. Piroird, B. D. Texier, C. Clanet, and D. Quéré. Reshaping and capturing leidenfrost drops with a magnet. *Physics of Fluids*, 25(3), 2013.

[41] L. Feng, Y. Zhang, J. Xi, Y. Zhu, N. Wang, F. Xia, and L. Jiang. Petal effect: A superhydrophobic state with high adhesive force. *Langmuir*, 24(8):4114–4119, 2008.

[42] K. Autumn, M. Sitti, Y. C. A. Liang, A. M. Peattie, W. R. Hansen, S. Sponberg, T. W. Kenny, R. Fearing, J. N. Israelachvili, and R. J. Full. Evidence for van der waals adhesion in gecko setae. *Proceedings of the National Academy of Sciences of the United States of America*, 99(19):12252–12256, 2002.

[43] K. Autumn, Y. A. Liang, S. T. Hsieh, W. Zesch, W. P. Chan, T. W. Kenny, R. Fearing, and R. J. Full. Adhesive force of a single gecko foot-hair. *Nature*, 405(6787):681–685, 2000.

[44] W. R. Hansen and K. Autumn. Evidence for self-cleaning in gecko setae. *Proceedings of the National Academy of Sciences of the United States of America*, 102(2):385–389, 2005.

[45] H. Lee, B. P. Lee, and P. B. Messersmith. A reversible wet/dry adhesive inspired by mussels and geckos. *Nature*, 448(7151):338–U4, 2007.

[46] Z. L. Wang. Sticky but not messy. *Nature Nanotechnology*, 4(7):407–408, 2009.

[47] J. Davies, S. Haq, T. Hawke, and J. P. Sargent. A practical approach to the development of a synthetic gecko tape. *International Journal of Adhesion and Adhesives*, 29(4):380–390, 2009.

[48] W.-H. Ting, C.-C. Chen, S. A. Dai, S.-Y. Suen, I. K. Yang, Y.-L. Liu, F. M. C. Chen, and R.-J. Jeng. Superhydrophobic waxy-dendron-grafted polymer films via nanostructure manipulation. *Journal of Materials Chemistry*, 19(27):4819–4828, 2009.

[49] W. K. Cho and I. S. Choi. Fabrication of hairy polymeric films inspired by geckos: Wetting and high adhesion properties. *Advanced Functional Materials*, 18(7):1089–1096, 2008.

[50] M. H. Jin, X. J. Feng, L. Feng, T. L. Sun, J. Zhai, T. J. Li, and L. Jiang. Superhydrophobic aligned polystyrene nanotube films with high adhesive force. *Advanced Materials*, 17(16):1977, 2005.

[51] X. Hong, X. Gao, and L. Jiang. Application of superhydrophobic surface with high adhesive force in no lost transport of superparamagnetic microdroplet. *Journal of the American Chemical Society*, 129(6):1478, 2007.

[52] J. A. Howarter and J. P. Youngblood. Self-cleaning and anti-fog surfaces via stimuli-responsive polymer brushes. *Advanced materials*, 19(22):3838–3843, 2007.

[53] J. A. Howarter and J. P. Youngblood. Self-cleaning and next generation anti-fog surfaces and coatings. *Macromolecular Rapid Communications*, 29(6):455–466, 2008.

[54] L. Zhang, Y. Li, J. Sun, and J. Shen. Mechanically stable antireflection and antifogging coatings fabricated by the layer-by-layer deposition process and postcalcination. *Langmuir*, 24(19):10851–10857, 2008.

[55] R. Wang, K. Hashimoto, A. Fujishima, M. Chikuni, E. Kojima, A. Kitamura, M. Shimohigoshi, and T. Watanabe. Light-induced amphiphilic surfaces. *Nature*, 388(6641):431–432, 1997.

[56] F. C. Cebeci, Z. Z. Wu, L. Zhai, R. E. Cohen, and M. F. Rubner. Nanoporosity-driven superhydrophilicity: A means to create multifunctional antifogging coatings. *Langmuir*, 22(6):2856–2862, 2006.

[57] D. Lee, M. F. Rubner, and R. E. Cohen. All-nanoparticle thin-film coatings. *Nano Letters*, 6(10):2305–2312, 2006.

[58] X. Du, X. Liu, H. Chen, and J. He. Facile fabrication of raspberry-like composite nanoparticles and their application as building blocks for constructing superhydrophilic coatings. *Journal of Physical Chemistry C*, 113(21):9063–9070, 2009.

[59] X. Gao, X. Yan, X. Yao, L. Xu, K. Zhang, J. Zhang, B. Yang, and L. Jiang. The dry-style antifogging properties of mosquito compound eyes and artificial analogues prepared by soft lithography. *Advanced Materials*, 19(17):2213, 2007.

[60] M. Srinivasarao. Nano-optics in the biological world: Beetles, butterflies, birds, and moths. *Chemical Reviews*, 99(7):1935–1961, 1999.

[61] A. R. Parker and H. E. Townley. Biomimetics of photonic nanostructures. *Nature Nanotechnology*, 2(6):347–353, 2007.

[62] P. Vukusic and J. R. Sambles. Photonic structures in biology. *Nature*, 424(6950):852–855, 2003.

[63] Y.-F. Huang, S. Chattopadhyay, Y.-J. Jen, C.-Y. Peng, T.-A. Liu, Y.-K. Hsu, C.-L. Pan, H.-C. Lo, C.-H. Hsu, Y.-H. Chang, C.-S. Lee, K.-H. Chen, and L.-C. Chen. Improved broadband and quasi-omnidirectional anti-reflection properties with biomimetic silicon nanostructures. *Nature Nanotechnology*, 2(12):770–774, 2007.

[64] C.-H. Sun, A. Gonzalez, N. C. Linn, P. Jiang, and B. Jiang. Templated biomimetic multifunctional coatings. *Applied Physics Letters*, 92(5), 2008.

[65] G. S. Watson and J. A. Watson. Natural nano-structures on insects - possible functions of ordered arrays characterized by atomic force microscopy. *Applied Surface Science*, 235(1-2):139–144, 2004.

[66] G. Zhang, J. Zhang, G. Xie, Z Liu, and H. Shao. Cicada wings: A stamp from nature for nanoimprint lithography. *Small*, 2(12):1440–1443, 2006.

[67] G. Xie, G. Zhang, F. Lin, J. Zhang, Z. Liu, and S. Mu. The fabrication of subwavelength anti-reflective nanostructures using a bio-template. *Nanotechnology*, 19(9), 2008.

[68] G. Kostovski, D. J. White, A. Mitchell, M. W. Austin, and P. R. Stoddart. Nanoimprinted optical fibres: Biotemplated nanostructures for sers sensing. *Biosensors & Bioelectronics*, 24(5):1531–1535, 2009.

[69] M. Ebner, T. Miranda, and A. Roth-Nebelsick. Efficient fog harvesting by stipagrostis sabulicola (namib dune bushman grass). *Journal of Arid Environments*, 75(6):524–531, 2011.

[70] J. Ju, H. Bai, Y. Zheng, T. Zhao, R. Fang, and L. Jiang. A multi-structural and multi-functional integrated fog collection system in cactus. *Nature communications*, 3:1247, 2012.

[71] J. Ju, X. Yao, S. Yang, L. Wang, R. Sun, Y. He, and L. Jiang. Cactus stem inspired cone-arrayed surfaces for efficient fog collection. *Advanced Functional Materials*, 24(44):6933–6938, 2014.

[72] P. Comanns, C. Effertz, F. Hischen, K Staudt, W. Böhme, and W. Baumgartner. Moisture harvesting and water transport through specialized micro-structures on the integument of lizards. *Beilstein journal of nanotechnology*, 2(1):204–214, 2011.

[73] A. R. Parker and C. R. Lawrence. Water capture by a desert beetle. *Nature*, 414(6859):33–34, 2001.

[74] L. Zhai, M. C. Berg, F. C. Cebeci, Y. Kim, J. M. Milwid, M. F. Rubner, and R. E. Cohen. Patterned superhydrophobic surfaces: Toward a synthetic mimic of the namib desert beetle. *Nano Letters*, 6(6):1213–1217, 2006.

[75] R. P. Garrod, L. G. Harris, W. C. E. Schofield, J. McGettrick, L. J. Ward, D. O. H. Teare, and J. P. S. Badyal. Mimicking a stenocara beetle's back for microcondensation using plasmachemical patterned superhydrophobic-superhydrophilic surfaces. *Langmuir*, 23(2):689–693, 2007.

[76] C. Dorrer and J. Ruehe. Mimicking the stenocara beetle-dewetting of drops from a patterned superhydrophobic surface. *Langmuir*, 24(12):6154–6158, 2008.

[77] Y. Zheng, H. Bai, Z. Huang, X. Tian, F.-Q. Nie, Y. Zhao, J. Zhai, and L. Jiang. Directional water collection on wetted spider silk. *Nature*, 463(7281):640–643, 2010.

[78] B. S. Lalia, S. Anand, K. K. Varanasi, and R. Hashaikeh. Fog-harvesting potential of lubricant-impregnated electrospun nanomats. *Langmuir*, 29(42):13081–13088, 2013.

[79] T. L. Sun, L. Feng, X. F. Gao, and L. Jiang. Bioinspired surfaces with special wettability. *Accounts of Chemical Research*, 38(8):644–652, 2005.

[80] P. Tabeling and S. Chen. *Introduction to Microfluidics.* Oxford University Press, USA, 2006.

[81] G. M. Whitesides. The origins and the future of microfluidics. *Nature*, 442:368–373, 2006.

[82] M. Rauscher, S. Dietrich, and J. Koplik. Shear flow pumping in open micro- and nanofluidic systems. *Phys. Rev. Lett.*, 98:224504, 2007.

[83] R. Ledesma-Aguilar, R. Nistal, A. Hernández-Machado, and I. Pagonabarraga. Controlled drop emission by wetting properties in driven liquid filaments. *Nature Materials*, 10:367–371, 2011.

[84] R. Seemann, M. Brinkmann, E. J. Kramer, F. F. Lange, and R. Lipowsky. Wetting morphologies at microstructured surfaces. *Proceedings of the National Academy of Sciences of the United States of America*, 102(6):1848–1852, 2005.

[85] D. Ferraro, C. Semprebon, T. Tóth, E. Locatelli, M. Pierno, G. Mistura, and M. Brinkmann. Morphological transitions of droplets wetting rectangular domains. *Langmuir*, 28(39):13919–13923, 2012.

[86] P. Brunet and J. H. Snoeijer. Star-drops formed by periodic excitation and on an air cushion - a short review. *European Physical Journal-Special Topics*, 192(1):207–226, 2011.

[87] K. Ohno, K. Tachikawa, and A. Manz. Microfluidics: applications for analytical purposes in chemistry and biochemistry. *Electrophoresis*, 29(22):4443–4453, 2008.

[88] S. K. Sia and G. M. Whitesides. Microfluidic devices fabricated in poly (dimethylsiloxane) for biological studies. *Electrophoresis*, 24(21):3563–3576, 2003.

[89] D. B. Weibel and G. M. Whitesides. Applications of microfluidics in chemical biology. *Current opinion in chemical biology*, 10(6):584–591, 2006.

[90] D. J. Beebe, G. A. Mensing, and G. M. Walker. Physics and applications of microfluidics in biology. *Annual review of biomedical engineering*, 4(1):261–286, 2002.

[91] G. Dupeux, P. Bourrianne, Q. Magdelaine, C. Clanet, and D. Quéré. Propulsion on a superhydrophobic ratchet. *Scientific reports*, 4, 2014.

[92] N. Moumen, R. S. Subramanian, and J. B. McLaughlin. Experiments on the motion of drops on a horizontal solid surface due to a wettability gradient. *Langmuir*, 22(6):2682–2690, 2006.

[93] R. S. Subramanian, N. Moumen, and J. B. McLaughlin. Motion of a drop on a solid surface due to a wettability gradient. *Langmuir*, 21(25):11844–11849, 2005.

[94] S. Daniel, M. K. Chaudhury, and J. C. Chen. Past drop movements resulting from the phase change on a gradient surface. *Science*, 291(5504):633–636, 2001.

[95] S. Daniel, S. Sircar, J. Gliem, and M. K. Chaudhury. Ratcheting motion of liquid drops on gradient surfaces. *Langmuir*, 20(10):4085–4092, 2004.

[96] Y. Ito, M. Heydari, A. Hashimoto, T. Konno, A. Hirasawa, S. Hori, K. Kurita, and A. Nakajima. The movement of a water droplet on a gradient surface prepared by photodegradation. *Langmuir*, 23(4):1845–1850, 2007.

[97] M. K. Chaudhury and G. M. Whitesides. How to make water run uphill. *Science*, 256(5063):1539–1541, 1992.

[98] H. Bouasse. *Capillarité: phénomènes superficiels*. Librairie Delagrave, 1924.

[99] F. Brochard. Motion of droplets on solid-surfaces induced by chemical or thermal-gradients. *Langmuir*, 5(2):432–438, 1989.

[100] D. K. N. Sinz and A. A. Darhuber. Self-propelling surfactant droplets in chemically-confined microfluidics - cargo transport, drop-splitting and trajectory control. *Lab on a Chip*, 12(4):705–707, 2012.

[101] S. Suzuki, A. Nakajima, K. Tanaka, M. Sakai, A. Hashimoto, N. Yoshida, Y. Kameshima, and K. Okada. Sliding behavior of water droplets on line-patterned hydrophobic surfaces. *Applied Surface Science*, 254(6):1797–1805, 2008.

[102] A. Nakajima. Control of static and dynamic hydrophobicity of solid surface and its application. *Journal of the Ceramic Society of Japan*, 119(1394):711–719, 2011.

[103] N. J. Cira, A. Benusiglio, and M. Prakash. Vapour-mediated sensing and motility in two-component droplets. *Nature*, 519(7544):446, 2015.

[104] R. Shamai, D. Andelman, B. Berge, and R. Hayes. Water, electricity, and between... on electrowetting and its applications. *Soft Matter*, 4:38–45, 2008.

[105] S. C. C. Shih, H. Yang, M. J. Jebrail, R. Fobel, N. McIntosh, O. Y. Al-Dirbashi, P. Chakraborty, and A. R. Wheeler. Dried blood spot analysis by digital microfluidics coupled to nanoelectrospray ionization mass spectrometry. *analytical chemistry*, 84:3731–3738, 2012.

[106] N. A. Mousa, M. J. Jebrail, H. Yang, M. Abdelgawad, P. Metalnikov, J. Chen, A. R. Wheeler, and R. F. Casper. Droplet-scale estrogen assays in breast tissue, blood, and serum. *Science Translational Medicine*, 1(1):1ra2, 2009.

[107] S. Srigunapalan, I. A. Eydelnant, C. A. Simmons, and A. R. Wheeler. A digital microfluidic platform for primary cell culture and analysis. *Lab Chip*, 12:369–375, 2012.

[108] I. Barbulovic-Nad, S. H. Au, and A. R. Wheeler. A microfluidic platform for complete mammalian cell culture. *Lab on a Chip*, 10(12):1536–1542, 2010.

[109] J. V. I. Timonen, M. Latikka, L. Leibler, R. H. A. Ras, and O. Ikkala. Switchable static and dynamic self-assembly of magnetic droplets on superhydrophobic surfaces. *Science*, 341(6143):253–257, 2013.

[110] C.-Y. Chen and Z. Y. Cheng. An experimental study on rosensweig instability of a ferrofluid droplet. *Physics of Fluids*, 20(5), 2008.

[111] K. S. Khalil, S. R. Mahmoudi, N. Abu-dheir, and K. K. Varanasi. Active surfaces: Ferrofluid-impregnated surfaces for active manipulation of droplets. *Applied Physics Letters*, 105(4), 2014.

[112] X. Noblin, R. Kofman, and F. Celestini. Ratchetlike motion of a shaken drop. *Physical review letters*, 102(19):194504, 2009.

[113] P. Brunet, J. Eggers, and R. D. Deegan. Vibration-induced climbing of drops. *Phys. Rev. Lett.*, 99:144501, Oct 2007.

[114] P. Brunet, M. Baudoin, O. Bou Matar, and F. Zoueshtiagh. Droplet displacements and oscillations induced by ultrasonic surface acoustic waves: A quantitative study. *Physical Review E*, 81(3), 2010.

[115] M. Baudoin, P. Brunet, O. B. Matar, and E. Herth. Low power sessile droplets actuation via modulated surface acoustic waves. *Applied Physics Letters*, 100(15), 2012.

[116] X. Ding, P. Li, S.-C. S. Lin, Z. S. Stratton, N. Nama, F. Guo, D. Slotcavage, X. Mao, J. Shi, F. Costanzo, et al. Surface acoustic wave microfluidics. *Lab on a Chip*, 13(18):3626–3649, 2013.

[117] L. Y. Yeo and J. R. Friend. Surface acoustic wave microfluidics. *Annual Review of Fluid Mechanics*, 46:379–406, 2014.

[118] S. Daniel and M. K. Chaudhury. Rectified motion of liquid drops on gradient surfaces induced by vibration. *Langmuir*, 18(9):3404–3407, 2002.

[119] S. Daniel, M. K. Chaudhury, and P.-G. De Gennes. Vibration-actuated drop motion on surfaces for batch microfluidic processes. *Langmuir*, 21(9):4240–4248, 2005.

[120] R. W. Style, R. Boltyanskiy, Y. Che, J. S. Wettlaufer, L. A. Wilen, and E. R. Dufresne. Universal deformation of soft substrates near a contact line and the direct measurement of solid surface stresses. *Physical review letters*, 110(6):066103, 2013.

[121] R. W. Style and E. R. Dufresne. Static wetting on deformable substrates, from liquids to soft solids. *Soft Matter*, 8(27):7177–7184, 2012.

[122] A. B. D. Cassie and S. Baxter. Wettability of porous surfaces. *Transactions of the Faraday Society*, 40:546–551, 1944.

[123] R. N. Wenzel. Resistance of solid surfaces to wetting by water. *Industrial & Engineering Chemistry*, 28(8):988–994, 1936.

[124] J. Bico, C. Marzolin, and D. Quéré. Pearl drops. *EPL (Europhysics Letters)*, 47(2):220, 1999.

[125] J. Bico, C. Tordeux, and D. Quéré. Rough wetting. *EPL (Europhysics Letters)*, 55(2):214, 2001.

[126] P.-G. De Gennes, F. Brochard-Wyart, and D. Quéré. *Capillarity and wetting phenomena: drops, bubbles, pearls, waves.* Springer Science & Business Media, 2004.

[127] D. Quéré. Surface chemistry: Fakir droplets. *Nature Materials*, 1:14–15, September 2002.

[128] E. Bormashenko G. Whyman and T. Stein. The rigorous derivation of Young, Cassie-Baxter and Wenzel equations and the analysis of the contact angle hysteresis phenomenon. *Chemical Physics Letters*, 450(4-6):355 – 359, 2008.

[129] A. I. ElSherbini and A. M. Jacobi. Liquid drops on vertical and inclined surfaces: I. an experimental study of drop geometry. *Journal of Colloid and Interface Science*, 273(2):556 – 565, 2004.

[130] C.G.L. Furmidge. Studies at phase interfaces. i. the sliding of liquid drops on solid surfaces and a theory for spray retention. *Journal of Colloid Science*, 17(4):309 – 324, 1962.

[131] C. W. Extrand and Y. Kumagai. Liquid drops on an inclined plane: the relation between contact angles, drop shape, and retentive force. *Journal of colloid and interface science*, 170(2):515–521, 1995.

[132] T. Podgorski, J. M. Flesselles, and L. Limat. Corners, cusps, and pearls in running drops. *Physical Review Letters*, 87(3):036102, June 2001.

[133] N. Le Grand, A. Daerr, and L. Limat. Shape and motion of drops sliding down an inclined plane. *Journal of Fluid Mechanics*, 541:293–315, 2005.

[134] S. Suzuki, A. Nakajima, M. Sakai, J. Song, N. Yoshida, Y. Kameshima, and K. Okada. Sliding acceleration of water droplets on a surface coated with fluoroalkylsilane and octadecyltrimethoxysilane. *Surface Science*, 600(10):2214 – 2219, 2006.

[135] S. R. Annapragada, J. Y. Murthy, and S. V. Garimella. Prediction of droplet dynamics on an incline. *International Journal of Heat and Mass Transfer*, 55(5-6):1466 – 1474, 2012.

[136] Y. Y. Koh, Y. C. Lee, P. H. Gaskell, P. K. Jimack, and H. M. Thompson. Droplet migration: Quantitative comparisons with experiment. *The European Physical Journal - Special Topics*, 166:117–120, 2009.

[137] A. K. Das and P. K. Das. Simulation of drop movement over an inclined surface using smoothed particle hydrodynamics. *Langmuir*, 25(19):11459–11466, 2009.

[138] S. Suzuki, A. Nakajima, M. Sakai, Y. Sakurada, N. Yoshida, A. Hashimoto, Y. Kameshima, and K. Okada. Slipping and rolling ratio of sliding acceleration for a water droplet sliding on fluoroalkylsilane coatings of different roughness. *Chemistry Letters*, 37(1):58–59, 2008.

[139] M. Sakai, J. Song, N. Yoshida, S. Suzuki, Y. Kameshima, Yoshikazu, and A. Nakajima. Direct observation of internal fluidity in a water droplet during sliding on hydrophobic surfaces. *Langmuir*, 22(11):4906–4909, 2006.

[140] T. Furuta, A. Nakajima, M. Sakai, T. Isobe, Y. Kameshima, and K. Okada. Evaporation and sliding of water droplets on fluoroalkylsilane coatings with nanoscale roughness. *Langmuir*, 25(10):5417–5420, 2009.

[141] L. Gao and T. J. McCarthy. Contact angle hysteresis explained. *Langmuir*, 22(14):6234–6237, 2006.

[142] G. McHale, N. J. Shirtcliffe, and M. I. Newton. Contact-angle hysteresis on super-hydrophobic surfaces. *Langmuir*, 20(23):10146–10149, 2004.

[143] B. He, J. Lee, and N. A. Patankar. Contact angle hysteresis on rough hydrophobic surfaces. *Colloids and Surfaces A: Physicochemical and Engineering Aspects*, 248(1 - 3):101 – 104, 2004.

[144] P. Hao, C. Lv, Z. Yao, and F. He. Sliding behavior of water droplet on superhydrophobic surface. *EPL (Europhysics Letters)*, 90(6):66003, 2010.

[145] M. Miwa, A. Nakajima, A. Fujishima, K. Hashimoto, and T. Watanabe. Effects of the surface roughness on sliding angles of water droplets on superhydrophobic surfaces. *Langmuir*, 16(13):5754–5760, 2000.

[146] M. Sakai, H. Kono, A. Nakajima, X. Zhang, H. Sakai, M. Abe, and A. Fujishima. Sliding of Water Droplets on the Superhydrophobic Surface with ZnO Nanorods. Part of the "Langmuir 25th Year: Wetting and superhydrophobicity special issue". *Langmuir*, 25(24):14182–14186, 2009.

[147] D. Quéré. Non-sticking drops. *Reports on Progress in Physics*, 68(11):2495, 2005.

[148] M. Reyssat, D. Richard, C. Clanet, and D. Quéré. Dynamical superhydrophobicity. *Faraday discussions*, 146:19–33, 2010.

[149] E. Reyssat, F. Chevy, A.-L. Biance, L. Petitjean, and D. Quéré. Shape and instability of free-falling liquid globules. *EPL (Europhysics Letters)*, 80(3):34005, 2007.

[150] C. Huh and L. E. Scriven. Hydrodynamic model of steady movement of a solid/liquid/fluid contact line. *Journal of Colloid and Interface Science*, 35(1):85–101, 1971.

[151] L. Mahadevan and Y. Pomeau. Rolling droplets. *Physics of Fluids*, 11:2449–2453, September 1999.

[152] H. Kim, H. J. Lee, and B. H. Kang. Sliding of liquid drops down an inclined solid surface. *Journal of Colloid and Interface Science*, 247(2):372 – 380, 2002.

[153] M. R. Swift, W. R. Osborn, and J. M. Yeomans. Lattice boltzmann simulation of nonideal fluids. *Physical Review Letters*, 75(5):830, 1995.

[154] A. J. Briant, A. J. Wagner, and J. M. Yeomans. Lattice boltzmann simulations of contact line motion. i. liquid-gas systems. *Physical Review E*, 69(3), 2004.

[155] A. J. Briant and J. M. Yeomans. Lattice boltzmann simulations of contact line motion. ii. binary fluids. *Physical Review E*, 69(3), 2004.

[156] X. W. Shan and H. D. Chen. Lattice boltzmann model for simulating flows with multiple phases and components. *Physical Review E*, 47(3):1815–1819, 1993.

[157] C. Semprebon, G. Mistura, E. Orlandini, G. Bissacco, A. Segato, and J. M. Yeomans. Anisotropy of water droplets on single rectangular posts. *Langmuir*, 25(10):5619–5625, 2009.

[158] C. Semprebon and M. Brinkmann. On the onset of motion of sliding drops. *Soft matter*, 10(18):3325–3334, 2014.

[159] T. Qian, C. Wu, S. L. Lei, X.-P. Wang, and P. Sheng. Modeling and simulations for molecular scale hydrodynamics of the moving contact line in immiscible two-phase flows. *Journal of Physics-Condensed Matter*, 21(46), 2009.

[160] A. Giacomello, S. Meloni, M. Chinappi, and C. M. Casciola. Cassie–baxter and wenzel states on a nanostructured surface: phase diagram, metastabilities, and transition mechanism by atomistic free energy calculations. *Langmuir*, 28(29):10764–10772, 2012.

[161] L. W. Schwartz and R. R. Eley. Simulation of droplet motion on low-energy and heterogeneous surfaces. *Journal of colloid and interface science*, 202(1):173–188, 1998.

[162] J. H. Snoeijer, N. Le Grand-Piteira, L. Limat, H. A. Stone, and J Eggers. Cornered drops and rivulets. *Physics of Fluids*, 19(4):042104, 2007.

[163] D. Herde, U. Thiele, S. Herminghaus, and M. Brinkmann. Driven large contact angle droplets on chemically heterogeneous substrates. *EPL (Europhysics Letters)*, 100(1):16002, 2012.

[164] F. Magaletti, F. Picano, M. Chinappi, L. Marino, and C. M. Casciola. The sharp-interface limit of the cahn-hilliard/navier-stokes model for binary fluids. *Journal of Fluid Mechanics*, 714:95–126, 2013.

[165] D. M. Anderson, G. B. McFadden, and A. A. Wheeler. Diffuse-interface methods in fluid mechanics. *Annual review of fluid mechanics*, 30(1):139–165, 1998.

[166] K. N. Premnath and J. Abraham. Three-dimensional multi-relaxation time (mrt) lattice-boltzmann models for multiphase flow. *Journal of Computational Physics*, 224(2):539–559, 2007.

[167] M. Sbragaglia, L. Biferale, G. Amati, S. Varagnolo, D. Ferraro, G. Mistura, and M. Pierno. Sliding drops across alternating hydrophobic and hydrophilic stripes. *Physical Review E*, 89(1), 2014.

[168] X. Shan. Pressure tensor calculation in a class of nonideal gas lattice boltzmann models. *Physical Review E*, 77(6):066702, 2008.

[169] L. Scarbolo, D. Molin, P. Perlekar, M. Sbragaglia, A. Soldati, and F. Toschi. Unified framework for a side-by-side comparison of different multicomponent algorithms: lattice boltzmann vs. phase field model. *Journal of Computational Physics*, 234:263–279, 2013.

[170] K. A. Brakke. The Surface Evolver and the Stability of Liquid Surfaces. *Philosophical Transactions of the Royal Society A: Mathematical, Physical and Engineering Sciences*, 354(1715):2143–2157, 1996.

[171] M. Musterd, V. Van Steijn, C. R. Kleijn, and M. T. Kreutzer. Droplets on inclined plates: Local and global hysteresis of pinned capillary surfaces. *Physical Review Letters*, 113(6):066104, August 2014.

[172] T. D. Blake, A. Clarke, J. DeConinck, and M. J. DeRuijter. Contact angle relaxation during droplet spreading: Comparison between molecular kinetic theory and molecular dynamics. *Langmuir*, 13(7):2164–2166, 1997.

[173] O. V. Voinov. Hydrodynamics of wetting. *Fluid Dynamics*, 11(5):714–721, 1976.

[174] R. G. Cox. The dynamics of the spreading of liquids on a solid surface. Part 2. Surfactants. *Journal of Fluid Mechanics*, 168(-1):195, 1986.

[175] D. Jacqmin. Contact-line dynamics of a diffuse fluid interface. *Journal of Fluid Mechanics*, 402:57–88, 2000.

[176] A. Carlson, G. Bellani, and G. Amberg. Contact line dissipation in short-time dynamic wetting. *EPL (Europhysics Letters)*, 97(4):44004, 2012.

[177] E. Chiarello. *Analisi gocce 2010: Manuale utente*, 2010.

[178] National Instruments. *NI Vision for LabVIEW VI Reference Help*, 2007.

[179] T. Onda, S. Shibuichi, N. Satoh, and K. Tsujii. Super-water-repellent fractal surfaces. *Langmuir*, 12(9):2125–2127, 1996.

[180] M. H. Sun, C. X. Luo, L. P. Xu, H. Ji, O. Y. Qi, D. P. Yu, and Y. Chen. Artificial lotus leaf by nanocasting. *Langmuir*, 21(19):8978–8981, 2005.

[181] A. Pozzato, S. Dal Zilio, L. Bruschi, G. Mistura, and M. Tormen. Fabrication of substrates with extended nanostructured surface areas for wetting studies. *Microelectronic Engineering*, 86(4):1329–1332, 2009.

[182] W. Xu, R. Leeladhar, Y. T. Kang, and C.-H. Choi. Evaporation kinetics of sessile water droplets on micropillared superhydrophobic surfaces. *Langmuir*, 29(20):6032–6041, 2013.

[183] C. Dorrer and J. Rühe. Advancing and receding motion of droplets on ultrahydrophobic post surfaces. *Langmuir*, 22(18):7652–7657, 2006.

[184] A. Gauthier, M. Rivetti, J. Teisseire, and E. Barthel. Role of kinks in the dynamics of contact lines receding on superhydrophobic surfaces. *Physical review letters*, 110(4):046101, 2013.

[185] H. S. Lim, J. T. Han, D. Kwak, M. H. Jin, and K. Cho. Photoreversibly switchable superhydrophobic surface with erasable and rewritable pattern. *Journal of the American Chemical Society*, 128(45):14458–14459, 2006.

[186] D. Dattilo, L. Armelao, G. Fois, G. Mistura, and M. Maggini. Wetting properties of flat and porous silicon surfaces coated with a spiropyran. *Langmuir*, 23(26):12945–12950, 2007.

[187] T. L. Sun, H. A. Liu, W. L. Song, X. Wang, L. Jiang, L. Li, and D. B. Zhu. Responsive aligned carbon nanotubes. *Angewandte Chemie-International Edition*, 43(35):4663–4666, 2004.

[188] A. Podestà, G. Bongiorno, P. E. Scopelliti, S. Bovio, P. Milani, C. Semprebon, and G. Mistura. Cluster-assembled nanostructured titanium oxide films with tailored wettability. *The Journal of Physical Chemistry C*, 113(42):18264–18269, 2009.

[189] X. Yu, Z. Q. Wang, Y. G. Jiang, F. Shi, and X. Zhang. Reversible ph-responsive surface: From superhydrophobicity to superhydrophilicity. *Advanced Materials*, 17(10):1289, 2005.

[190] F. Xia, L. Feng, S. T. Wang, T. L. Sun, W. L. Song, W. H. Jiang, and L. Jiang. Dual-responsive surfaces that switch superhydrophilicity and superhydrophobicity. *Advanced Materials*, 18(4):432, 2006.

[191] X. Wang and R. A. Weiss. A facile method for preparing sticky, hydrophobic polymer surfaces. *Langmuir*, 28(6):3298–3305, 2012.

[192] J. B. K. Law, A. M. H. Ng, A. Y. He, and H. Y. Low. Bioinspired ultrahigh water pinning nanostructures. *Langmuir*, 30(1):325–331, 2014.

[193] M. J. Liu and L. Jiang. Switchable adhesion on liquid/solid interfaces. *Advanced Functional Materials*, 20(21):3753–3764, 2010.

[194] Xinjie Liu, Qian Ye, Bo Yu, Yongmin Liang, Weimin Liu, and Feng Zhou. Switching water droplet adhesion using responsive polymer brushes. *Langmuir*, 26(14):12377–12382, 2010.

[195] T. Pisuchpen, N. Chaim-ngoen, N. Intasanta, P. Supaphol, and V. P. Hoven. Tuning hydrophobicity and water adhesion by electrospinning and silanization. *Langmuir*, 27(7):3654–3661, 2011.

[196] M. K. Dawood, H. Zheng, T. H. Liew, K. C. Leong, Y. L. Foo, R. Rajagopalan, S. A. Khan, and W. K. Choi. Mimicking both petal and lotus effects on a single silicon substrate by tuning the wettability of nanostructured surfaces. *Langmuir*, 27(7):4126–4133, 2011.

[197] W. Lee, B. G. Park, D. H. Kim, D. J. Ahn, Y. Park, S. H. Lee, and K. B. Lee. Nanostructure-dependent water-droplet adhesiveness change in superhydrophobic anodic aluminum oxide surfaces: From highly adhesive to self-cleanable. *Langmuir*, 26(3):1412–1415, 2010.

[198] C. F. Wang, T. F. Wang, C. S. Liao, S. W. Kuo, and H. C. Lin. Using pencil drawing to pattern robust superhydrophobic surfaces to control the mobility of water droplets. *Journal of Physical Chemistry C*, 115(33):16495–16500, 2011.

[199] D. Wu, S. Z. Wu, Q. D. Chen, Y. L. Zhang, J. Yao, X. Yao, L. G. Niu, J. N. Wang, L. Jiang, and H. B. Sun. Curvature-driven reversible in situ switching between pinned and roll-down superhydrophobic states for water droplet transportation. *Advanced Materials*, 23(4):545, 2011.

[200] Y. K. Lai, F. Pan, C. Xu, H. Fuchs, and L. F. Chi. In situ surface-modification-induced superhydrophobic patterns with reversible wettability and adhesion. *Advanced Materials*, 25(12):1682–1686, 2013.

[201] J. L. Yong, F. Chen, Q. Yang, D. S. Zhang, H. Bian, G. Q. Du, J. H. Si, X. W. Meng, and X. Hou. Controllable adhesive superhydrophobic surfaces based on pdms microwell arrays. *Langmuir*, 29(10):3274–3279, 2013.

[202] S. Choo, H.-J. Choi, and H. Lee. Replication of rose-petal surface structure using uv-nanoimprint lithography. *Materials Letters*, 121:170–173, 2014.

[203] M. M. Stanton, R. E. Ducker, J. C. MacDonald, C. R. Lambert, and W. G. McGimpsey. Superhydrophobic, highly adhesive, polydimethylsiloxane (pdms) surfaces. *Journal of Colloid and Interface Science*, 367:502–508, 2012.

[204] H. Lee and B. Bhushan. Fabrication and characterization of hierarchical nanostructured smart adhesion surfaces. *Journal of Colloid and Interface Science*, 372:231–238, 2012.

[205] L. Bruschi, G. Fois, G. Mistura, K. Sklarek, R. Hillebrand, M. Steinhart, and U. Gösele. Adsorption hysteresis in self-ordered nanoporous alumina. *Langmuir*, 24(19):10936–10941, 2008.

[206] W. Lee and S.-J. Park. Porous anodic aluminum oxide: anodization and templated synthesis of functional nanostructures. *Chemical reviews*, 114(15):7487–7556, 2014.

[207] M. Wang, X. Ye, and J. Feng. Fabrication of length-controlled polymer nanopillars using poly (dimethylsiloxane) filled anodised aluminium oxide templates. *Micro & Nano Letters*, 8(10):713–717, 2013.

[208] Y. H. Yeh, K. H. Cho, and L. J. Chen. Effect of softness of polydimethylsiloxane on the hydrophobicity of pillar-like patterned surfaces. *Soft Matter*, 8(4):1079–1086, 2012.

[209] K. M. Choi and J. A. Rogers. A photocurable poly (dimethylsiloxane) chemistry designed for soft lithographic molding and printing in the nanometer regime. *Journal of the American Chemical Society*, 125(14):4060–4061, 2003.

[210] C. Brun, P. Delobelle, M. Fromm, F. Berger, A. Chambaudet, and F. Jaffiol. Mechanical properties determined by nanoindentation tests of polypropylene modified by he+ particle implantation. *Materials Science and Engineering: A*, 315(1):63–69, 2001.

[211] M. J. Madou. *Fundamentals of microfabrication: the science of miniaturization*. CRC Press, 2 edition, March 2002.

[212] H. Masuda, M. Watanabe, K. Yasui, D. Tryk, T. Rao, and A. Fujishima. Fabrication of a nanostructured diamond honeycomb film. *Advanced Materials*, 12(6):444–447, 2000.

[213] T. W. Odom, J. C. Love, D. B. Wolfe, K. E. Paul, and G. M. Whitesides. Improved pattern transfer in soft lithography using composite stamps. *Langmuir*, 18(13):5314–5320, 2002.

[214] J. Lee, M. J. Kim, and H. H. Lee. Surface modification of poly (dimethylsiloxane) for retarding swelling in organic solvents. *Langmuir*, 22(5):2090–2095, 2006.

[215] A. T. Paxson and K. K. Varanasi. Self-similarity of contact line depinning from textured surfaces. *Nature communications*, 4:1492, 2013.

[216] C. F. Wang and T. W. Hsueh. Patterning superhydrophobic surfaces to realize anisotropic wettability and to transport micro-liter-sized droplets to any type of surface. *Journal of Physical Chemistry C*, 118(23):12399–12404, 2014.

[217] Y. Chen, B. He, J. H. Lee, and N. A. Patankar. Anisotropy in the wetting of rough surfaces. *Journal of Colloid and Interface Science*, 281(2):458–464, 2005.

[218] E. Bormashenko, T. Stein, R. Pogreb, and D. Aurbach. ”petal effect” on surfaces based on lycopodium: High-stick surfaces demonstrating high apparent contact angles. *Journal of Physical Chemistry C*, 113(14):5568–5572, 2009.

[219] J. Peng, P. Yu, S. Zeng, X. Liu, J. Chen, and W. Xu. Application of click chemistry in the fabrication of cactus-like hierarchical particulates for sticky superhydrophobic surfaces. *Journal of Physical Chemistry C*, 114(13):5926–5931, 2010.

[220] A. Lafuma and D. Quéré. Superhydrophobic states. *Nature Materials*, 2(7):457–460, 2003.

[221] R. E. Johnson and R. H. Dettre. Contact angle hysteresis. *Advances in Chemistry Series (Contact Angle, Wettability, and Adhesion)*, 43:112, 1964.

[222] C.-H. Xue and J.-Z. Ma. Long-lived superhydrophobic surfaces. *Journal of Materials Chemistry A*, 1(13):4146–4161, 2013.

[223] L. M. Hocking. Sliding and spreading of thin two-dimensional drops. *The Quarterly Journal of Mechanics and Applied Mathematics*, 34(1):37–55, 1981.

[224] E. B. Dussan V. and R. T.-P. Chow. On the ability of drops or bubbles to stick to non-horizontal surfaces of solids. *Journal of Fluid mechanics*, 137:1–29, 1983.

[225] V. E. B. Dussan. On the ability of drops or bubbles to stick to non-horizontal surfaces of solids. part 2. small drops or bubbles having contact angles of arbitrary size. *Journal of Fluid Mechanics*, 151(FEB):1–20, 1985.

[226] H. Lamb. *Hydrodynamics*. Cambridge university press, 1932.

[227] C. A. Schlecht and J. A. Maurer. Functionalization of glass substrates: mechanistic insights into the surface reaction of trialkoxysilanes. *Rsc Advances*, 1(8):1446–1448, 2011.

[228] K. R. Finnie, R. Haasch, and R. G. Nuzzo. Formation and patterning of self-assembled monolayers derived from long-chain organosilicon amphiphiles and their use as templates in materials microfabrication. *Langmuir*, 16(17):6968–6976, 2000.

[229] H. Tu, C. E. Heitzman, and P. V. Braun. Patterned poly(n-isopropylacrylamide) brushes on silica surfaces by microcontact printing followed by surface-initiated polymerization. *Langmuir*, 20(19):8313–8320, 2004.

[230] A. Nakajima, Y. Nakagawa, T. Furuta, M. Sakai, T. Isobe, and S. Matsushita. Sliding of water droplets on smooth hydrophobic silane coatings with regular triangle hydrophilic regions. *Langmuir*, 29(29):9269–9275, 2013.

[231] Y. Xia, M. Mrksich, E. Kim, and G. M. Whitesides. Microcontact printing of octadecylsiloxane on the surface of silicon dioxide and its application in microfabrication. *Journal of the American Chemical Society*, 117(37):9576–9577, 1995.

[232] Y. Xia and G. M. Whitesides. Soft lithography. *Angewandte Chemie International Edition*, 37(5):550–575, 1998.

[233] J. L. Wilbur, A. Kumar, H. A. Biebuyck, E. Kim, and G. M. Whitesides. Microcontact printing of self-assembled monolayers: applications in microfabrication. *Nanotechnology*, 7(4):452, 1996.

[234] M. Winkelmann, J. Gold, R. Hauert, B. Kasemo, N. D. Spencer, D. M. Brunette, and M. Textor. Chemically patterned, metal oxide based surfaces produced by photolithographic techniques for studying protein–and cell–surface interactions i: Microfabrication and surface characterization. *Biomaterials*, 24(7):1133–1145, 2003.

[235] K. Lee, F. Pan, G. T. Carroll, N. J. Turro, and J. T. Koberstein. Photolithographic technique for direct photochemical modification and chemical micropatterning of surfaces. *Langmuir*, 20(5):1812–1818, 2004.

[236] M. Morita, T. Koga, H. Otsuka, and A. Takahara. Macroscopic-wetting anisotropy on the line-patterned surface of fluoroalkylsilane monolayers. *Langmuir*, 21(3):911–918, 2005.

[237] E. Färm, M. Kemell, M. Ritala, and M. Leskelä. Selective-area atomic layer deposition with microcontact printed self-assembled octadecyltrichlorosilane monolayers as mask layers. *Thin Solid Films*, 517(2):972 – 975, 2008.

[238] T. Burgin, V. Choong, and G. Maracas. Large area submicrometer contact printing using a contact aligner. *Langmuir*, 16(12):5371–5375, 2000.

[239] N. L. Jeon, K. Finnie, K. Branshaw, and R. G. Nuzzo. Structure and stability of patterned self-assembled films of octadecyltrichlorosilane formed by contact printing. *Langmuir*, 13(13):3382–3391, 1997.

[240] J. Kim, B. Lee, H. Kang, J. Kim, G. Chae, I. Kang, and I. Chung. Self-assembly of ag nanopowder on ots-patterned glass. *Applied Surface Science*, 255(23):9386 – 9390, 2009.

[241] L. Lu, L. Kam, M. Hasenbein, K. Nyalakonda, R. Bizios, A. Göpferich, J. F. Young, and A. G. Mikos. Retinal pigment epithelial cell function on substrates with chemically micropatterned surfaces. *Biomaterials*, 20(23 - 24):2351 – 2361, 1999.

[242] G. Arslan, M. Özmen, I. Hatay, I. H. Gübbük, and M. Ersöz. Microcontact printing of an alkylsilane monolayer on the surface of glass. *TURKISH JOURNAL OF CHEMISTRY*, 32(3):313–321, 2008.

[243] Y. Zhou, R. Valiokas, and B. Liedberg. Structural characterization of microcontact printed arrays of hexa(ethylene glycol)-terminated alkanethiols on gold. *Langmuir*, 20(15):6206–6215, 2004.

[244] H. Q. Luo, H. Shiku, A. Kumagai, Y. Takahashi, T. Yasukawa, and T. Matsue. Microcontact printed diaphorase monolayer on glass characterized by atomic force microscopy and scanning electrochemical microscopy. *Electrochemistry Communications*, 9(11):2703 – 2708, 2007.

[245] C. W. Extrand. Contact angles and hysteresis on surfaces with chemically heterogeneous islands. *Langmuir*, 19(9):3793–3796, 2003.

[246] J. Buehrle, S. Herminghaus, and F. Mugele. Impact of line tension on the equilibrium shape of liquid droplets on patterned substrates. *Langmuir*, 18(25):9771–9777, 2002.

[247] H. P. Jansen, K. Sotthewes, C. Ganser, C. Teichert, H. J. W. Zandvliet, and E. S. Kooij. Tuning kinetics to control droplet shapes on chemically striped patterned surfaces. *Langmuir*, 28(37):13137–13142, 2012.

[248] H. P. Jansen, O. Bliznyuk, E. S. Kooij, B. Poelsema, and H. J. W. Zandvliet. Simulating anisotropic droplet shapes on chemically striped patterned surfaces. *Langmuir*, 28(1):499–505, 2012.

[249] J. Léopoldès and D. G. Bucknall. Droplet spreading on microstriped surfaces. *The Journal of Physical Chemistry B*, 109(18):8973–8977, 2005.

[250] A. Moosavi, M. Rauscher, and S. Dietrich. Size dependent motion of nanodroplets on chemical steps. *Journal of Chemical Physics*, 129(4), 2008.

[251] M. Rauscher and S. Dietrich. Nano-droplets on structured substrates. *Soft Matter*, 5(16):2997–3001, 2009.

[252] U. Thiele and E. Knobloch. Driven drops on heterogeneous substrates: Onset of sliding motion. *Physical Review Letters*, 97(20), 2006.

[253] U. Thiele and E. Knobloch. On the depinning of a driven drop on a heterogeneous substrate. *New Journal of Physics*, 8, 2006.

[254] H. Kusumaatmaja and J. M. Yeomans. Modeling contact angle hysteresis on chemically patterned and superhydrophobic surfaces. *Langmuir*, 23(11):6019–6032, 2007.

[255] H. Kusumaatmaja, J. Léopoldès, A. Dupuis, and J. M. Yeomans. Drop dynamics on chemically patterned surfaces. *EPL (Europhysics Letters)*, 73(5):740, 2006.

[256] X.-P. Wang, T. Qian, and P. Sheng. Moving contact line on chemically patterned surfaces. *Journal of Fluid Mechanics*, 605:59–78, 2008.

[257] Ph. Beltrame, P. Haenggi, and U. Thiele. Depinning of three-dimensional drops from wettability defects. *Epl*, 86(2), 2009.

[258] M. Grison. *Fotolitografia mediante resist SU-8*. Bachelor thesis, Università degli Studi di Padova, 2009/2010.

[259] S. Begolo. *Fabrication of Microfluidic devices resistant to organic solvents*. Master thesis, Università degli Studi di Padova, 2006/2007.

[260] J. N. Lee, C. Park, and G. M. Whitesides. Solvent compatibility of poly(dimethylsiloxane)-based microfluidic devices. *Analytical Chemistry*, 75(23):6544–6554, 2003.

[261] G. P. López, H. A. Biebuyck, C. D. Frisbie, and G. M. Whitesides. Imaging of features on surfaces by condensation figures. *Science*, 260(5108):647–649, 1993.

[262] H. J. Butt, B. Cappella, and M. Kappl. Force measurements with the atomic force microscope: Technique, interpretation and applications. *Surface Science Reports*, 59(1 - 6):1 – 152, 2005.

[263] S. Varagnolo, D. Ferraro, P. Fantinel, M. Pierno, G. Mistura, G. Amati, L. Biferale, and M. Sbragaglia. Stick-slip sliding of water drops on chemically heterogeneous surfaces. *Physical Review Letters*, 111(6), 2013.

[264] S. Varagnolo, V. Schiocchet, D. Ferraro, M. Pierno, G. Mistura, M. Sbragaglia, A. Gupta, and G. Amati. Tuning drop motion by chemical patterning of surfaces. *Langmuir*, 30(9):2401–2409, 2014.

[265] I. S. Khattab, F. Bandarkar, M. A. A. Fakhree, and A. Jouyban. Density, viscosity, and surface tension of water+ethanol mixtures from 293 to 323k. *Korean Journal of Chemical Engineering*, 29(6):812–817, 2012.

[266] R. Benzi, M. Sbragaglia, S. Succi, M. Bernaschi, and S. Chibbaro. Mesoscopic lattice boltzmann modeling of soft-glassy systems: Theory and simulations. *Journal of Chemical Physics*, 131(10), 2009.

[267] D. 't Mannetje, S. Ghosh, R. Lagraauw, S. Otten, A. Pit, C. Berendsen, J. Zeegers, D. van den Ende, and F. Mugele. Trapping of drops by wetting defects. *Nature Communications*, 5, April 2014.

[268] M. A. Nilsson and J. P. Rothstein. Using sharp transitions in contact angle hysteresis to move, deflect, and sort droplets on a superhydrophobic surface. *Physics of Fluids*, 24(6):062001, 2012.

[269] Glycerine Producers' Association. *Physical Properties of Glycerine and Its Solutions*. Glycerine Producers' Association, 1963.

[270] C. Semprebon, P. Forsberg, C. Priest, and M. Brinkmann. Pinning and wicking in regular pillar arrays. *Soft matter*, 10(31):5739–5748, 2014.

[271] R. G. Larson. *The structure and rheology of complex fluids*, volume 33. Oxford university press New York, 1999.

[272] T. Iwao. Polymer solutions: An introduction to physical properties, 2002.

[273] S. Rafai, D. Bonn, and A. Boudaoud. Spreading of non-newtonian fluids on hydrophilic surfaces. *Journal of Fluid Mechanics*, 513:77–85, 2004.

[274] S. Rafai and D. Bonn. Spreading of non-newtonian fluids and surfactant solutions on solid surfaces. *Physica a-Statistical Mechanics and Its Applications*, 358(1):58–67, 2005.

[275] P. T. Callaghan and A. M. Gil. Rheo-nmr of semidilute polyacrylamide in water. *Macromolecules*, 33(11):4116–4124, 2000.

[276] P. J. Whitcomb and C. W. Macosko. Rheology of xanthan gum. *Journal of Rheology*, 22(2):493, 1978.

[277] A. Helmreich, J. Vorwerk, R. Steger, M. Muller, and P. O. Brunn. Non-viscous effects in the flow of xanthan gum solutions through a packed-bed of spheres. *Chemical Engineering Journal and the Biochemical Engineering Journal*, 59(2):111–119, 1995.

[278] M.A. Zirnsak, D.-V. Boger, and V. Tirtaatmadja. Steady shear and dynamic rheological properties of xanthan gum solutions in viscous solvents. *Journal of Rheology*, 43:627, 1999.

[279] D. Won and C. Kim. Alignment and aggregation of spherical particles in viscoelastic fluid under shear flow. *Journal of non-newtonian fluid mechanics*, 117(2):141–146, 2004.

[280] J.R. Stokes, L. Macakova, A. Chojnicka-Paszun, C.G. DeKruif, H. Harmen, and H.J. De Jong. Lubrication, adsorption, and rheology of aqueous polysaccharide solutions. *Langmuir*, 27:3474–3484, 2011.

[281] F. Varela López, L. Pauchard, M. Rosen, and M. Rabaud. Non-newtonian effects on ribbing instability threshold. *Journal of Non-Newtonian Fluid Mechanics*, 103:123–139, 2002.

[282] E. Choppe, F. Puaud, T. Nicolai, and L. Benyahia. Rheology of xanthan solutions as a function of temperature, concentration and ionic strength. *Carbohydrate Polymers*, 82(4):1228–1235, 2010.

[283] D. Bonn and J. Meunier. Viscoelastic free-boundary problems: Non-newtonian viscosity vs normal stress effects. *Physical Review Letters*, 79:2662–2665, 1997.

[284] N. B. Wyatt and M. W. Liberatore. Rheology and viscosity scaling of the polyelectrolyte xanthan gum. *Journal of Applied Polymer Science*, 114(6):4076–4084, 2009.

[285] H. W. Bewersdorff and R. P. Singh. Rheological and drag reduction characteristics of xanthan gum solutions. *Rheologica Acta*, 27(6):617–627, 1988.

[286] P.E. Arratia, L.-A. Cramer, J.P. Gollub, and D. J. Durian. The effects of polymer molecular weight on filament thinning and drop breakup in microchannels. *New J. Phys.*, 11:115006, 2009.

[287] P.E. Arratia, J.P. Gollub, and D.J. Durian. Polymeric filament thinning and breakup in microchannels. *Physical Review E*, 77:036309, 2008.

[288] B. Purnode and M.J. Crochet. Flows of polymer solutions through contractions. part 1: flows of polyacrylamide solutions through planar contractions. *Journal of Non-Newtonian Fluid Mechanics*, 65:269–289, 1996.

[289] A. Zell, S. Gier, S. Rafaï, and C. Wagner. Is there a relationship between the elongational viscosity and the first normal stress difference in polymer solutions? *Journal of Non-Newtonian Fluid Mechanics*, 165(19-20):1265, 2010.

[290] E. Rio, A. Daerr, B. Andreotti, and L. Limat. Boundary conditions in the vicinity of a dynamic contact line: Experimental investigation of viscous drops sliding down an inclined plane. *Physical Review Letters*, 94:024503, 2005.

[291] P. Yue and J. J. Feng. Phase-field simulations of dynamic wetting of viscoelastic fluids. *Journal of Non-Newtonian Fluid Mechanics*, 189:8–13, 2012.

[292] S. Gabbanelli, G. Drazer, and J. Koplik. Lattice boltzmann method for non-newtonian (power-law) fluids. *Physical Review E*, 72:046312, 2005.

[293] A. Lindner, J. Vermant, and D. Bonn. How to obtain the elongational viscosity of dilute polymer solutions? *Physica A*, 319:125–133, 2003.

[294] C. Wagner, Y. Amarouchene, D. Bonn, and J. Eggers. Droplet detachment and satellite bead formation in viscoelastic fluids. *Physical Review Letters*, 95:164504, 2005.

[295] A. Gupta, M. Sbragaglia, and A. Scagliarini. Hybrid lattice boltzmann/finite difference simulations of viscoelastic multicomponent flows in confined geometries. *Journal of Computational Physics*, 291:177–197, 2015.

[296] A. Gupta and M. Sbragaglia. Deformation and breakup of viscoelastic droplets in confined shear flow. *Physical Review E*, 90:023305, 2014.

[297] R. B. Bird, R. C. Armstrong, and O. Hassager. *Dynamics of polymeric liquids.* J. Wiley & Sons, 1987.

[298] M. Herrchen and H.C. Oettinger. A detailed comparison of various fene dumbell models. *Journal of Non-Newtonian Fluid Mechanics*, 68:17–42, 1997.

[299] X. Noblin, A. Buguin, and F. Brochard-Wyart. Vibrated sessile drops: Transition between pinned and mobile contact line oscillations. *The European Physical Journal E: Soft Matter and Biological Physics*, 14(4):395–404, 2004.

[300] F. Celestini and R. Kofman. Vibration of submillimeter-size supported droplets. *Physical Review E*, 73(4), 2006.

[301] S. Mettu and M. K. Chaudhury. Motion of liquid drops on surfaces induced by asymmetric vibration: role of contact angle hysteresis. *Langmuir*, 27(16):10327–10333, 2011.

[302] K. John and U. Thiele. Self-ratcheting stokes drops driven by oblique vibrations. *Physical Review Letters*, 104(10), 2010.

[303] E. S. Benilov and J. Billingham. Drops climbing uphill on an oscillating substrate. *Journal of Fluid Mechanics*, 674:93–119, 2011.

[304] E. S. Benilov. Thin three-dimensional drops on a slowly oscillating substrate. *Physical Review E*, 84(6), 2011.

[305] N. Galvanetto. *Studio preliminare del moto di una goccia indotto da vibrazioni del substrato.* Bachelor thesis, Università degli Studi di Padova, 2011/2012.

[306] D. Stefani. *Moto di una goccia indotto da vibrazioni del substrato.* Bachelor thesis, Università degli Studi di Padova, 2011/2012.

[307] V. Chilese. *Moto unidimensionale di una goccia indotto da vibrazioni del substrato.* Bachelor thesis, Università degli Studi di Padova, 2012/2013.

[308] T. Tóth, D. Ferraro, E. Chiarello, M. Pierno, G. Mistura, G. Bissacco, and C. Semprebon. Suspension of water droplets on individual pillars. *Langmuir*, 27(8):4742–4748, 2011.

[309] P. Brunet, J. Eggers, and R. D. Deegan. Motion of a drop driven by substrate vibrations. *The European Physical Journal - Special Topics*, 166:11–14, 2009.

[310] P. Sartori, D. Quagliati, S. Varagnolo, M Pierno, G. Mistura, F Magaletti, and C. M. Casciola. Drop motion induced by vertical vibrations. *New Journal of Physics*, 17(11):113017, 2015.

Ringraziamenti

E anche questa volta siamo giunti al momento dei ringraziamenti e non posso che partire ringraziando tutto il gruppo **LaFSI**, che mi ha permesso di lavorare serenamente in un clima positivo di collaborazione e confronto come non se ne trovano molti.
Prima di tutto un grazie davvero di cuore a **Giampaolo**, che mi ha dato tantissimi ottimi consigli e un grande aiuto sia per quanto riguarda l'attività di ricerca di dottorato che per il proseguimento. Grazie anche per aver avuto la pazienza di leggere e correggere tutta questa tesi e per la bellissima esperienza a Roma alla conferenza a cui abbiamo partecipato insieme.
Un grande ringraziamento è dedicato anche a **Matteo**, per le discussioni scientifiche, per tutte le mail che mi ha corretto, per avermi insegnato a fare le presentazioni e le figure con la giusta precisione e per aver reso più interessante la permanenza a Lisbona, a partire dalla cena con annesso concerto di Fado, ma anche con la visita al castello e i giri per la città.
Ringrazio particolarmente anche **Giorgio**, organizzatore dei LaFSI party e di tanti altri eventi mondani tra cui pizzate, cene, pranzi sui colli e la nostra festa di compleanno condivisa. Un grazie speciale anche perché con la sua simpatia contribuisce in modo fondamentale al clima piacevole che si trova al LaFSI.
Sono grata anche a **Davide**, che mi ha saputo dare davvero tantissimi consigli preziosi, soprattutto nei primi mesi del dottorato, ma che anche dopo, quando è andato a Parigi, si è sempre dimostrato molto disponibile in caso di bisogno.
Un ringraziamento speciale va anche ad **Emanuele**, che, forse inconsapevolmente, mi ha aiutata davvero tanto nel periodo emotivamente peggiore di questi tre anni e che è sempre stato un buon amico con cui parlare.
Grazie mille a **Paolone**, con cui è sempre interessante e piacevole confrontarsi, sia dal punto di vista scientifico che sul piano gastronomico, e con cui mi sono trovata benissimo ad organizzare i viaggi e ad andare alle conferenze.
Un forte ringraziamento è rivolto a **Daniele**, che mi ha fatta diventare un po' più scienziata dei materiali insegnandomi dei trucchi per fare bene le soluzioni e qualche nozione in più di chimica, e che è sempre stato pronto ad aiutarmi per qualsiasi cosa (e penso in particolare alle nostre lotte comuni per l'esperimento sul gradino chimico).
Ringrazio anche **Enrico**, come al solito per il suo lavoro informatico, senza il quale le cose sarebbero state molto più difficili, ma anche per avermi ospitata più di qualche volta a casa sua e per il suo humor che mi ha fatto ridere molte volte.
Sono grata a **Lacy** che, anche se per poco tempo, ha condiviso con me la sua esperienza dandomi dei

suggerimenti molto utili, e che è stato gentile e ospitale (ricordo particolarmente la bellissima festa a casa sua e la montagna di cioccolatini che ha portato al LaFSI).
Grazie mille anche al **grande Baz**, per tutte le serate e le feste che ha reso speciali e mi riferisco in particolare a cene e aperitivi a Milano, anche con Ema, ma soprattutto all'indimenticabile Mojito party.
Ringrazio enormemente anche **Luca**, grazie al quale ho potuto partecipare a molti eventi LaFSI, essendo stato per me un autista e un albergatore, oltre che un amico e qualche volta un "confessore".
Sono felice di ringraziare in modo speciale anche **Greshia**, che ha portato spesso al LaFSI il sorriso, la simpatia, l'allegria, ma soprattutto ottime torte!! E grazie anche per avermi convinta a usare qualche martelletto o qualche manina ogni tanto.
Poi grazie ai dottorandi e i post-doc degli altri gruppi con cui ho condiviso questa esperienza, in particolare **Giacomo e Gianluca**, **Massimo e Ruggero**, la **Vic** e la **Anna**, la **Maki**, le due **Valentine** e **Laura**.
Non posso dimenticare di ringraziare (quasi) tutti i tesisti triennali e magistrali che ho seguito durante questi anni. Vi ringrazio per avermi dato la possibilità di insegnarvi, forse, qualcosina di quello che so e spero di esservi stata utile. Tra tutti ringrazio in modo particolare **Gianluca dalle Rive, Veronica, Carlo, Luca Perlini, Rasa, Michele Minchio e Damiano** perchè il loro lavoro ha contribuito a realizzare alcune parti di questa tesi.
Non posso fare a meno di ringraziare anche tutti i collaboratori esterni che hanno partecipato in un modo o nell'altro ai vari lavori di cui mi sono occupata: **Nandita** e il gruppo del **prof. Cross** per le superfici pelose, il gruppo del **prof. Pisignano** per i campioni coperti da nanofibre, il gruppo del **prof. Martucci** per le misure di viscosità, il **prof. Lucchetta** per le misure reologiche a Rovigo, il gruppo del **prof Casciola** per le simulazioni sulle gocce che si muovono sulle superfici che oscillano.
Un pensiero speciale va a **Mauro** e **Ciro**, i teorici con cui ho interagito maggiormente e che si sono occupati dei progetti che mi hanno dato più soddisfazione, anche se a volte interagire con loro e riuscire a fare quello che chiedevano è stato un po' difficile e stressante.
Infine ringrazio tantissimo la mia **famiglia** per il supporto e il sostegno morale dimostrato in tutti questi anni e per avermi aiutata praticamente in qualsiasi cosa avessi bisogno nella vita fuori dall'università.

Spero di aver ringraziato tutti e se ho dimenticato qualcuno lo ringrazio adesso: **GRAZIE MILLE A TUTTI!!!**